

CHEMISTRY INSTITUTE
UNIVERSITY OF SÃO PAULO
Chemistry Graduation Program

JUAN SEBASTIAN AGUIRRE ARAQUE

**Development of supramolecular metal-organic type
systems and nanotechnology applications**

**Desenvolvimento de sistemas metal-orgânicos e suas aplicações
nanotecnológicas.**

Corrected Version

São Paulo

02/05/2019

JUAN SEBASTIAN AGUIRRE ARAQUE

**Development of supramolecular metal-organic type
systems and nanotechnology applications**

**Desenvolvimento de sistemas metal-orgânicos e suas aplicações
nanotecnológicas.**

Thesis presented to the Chemistry Institute
at University of São Paulo for Doctor in
Science-Chemistry Title

Advisor: Professor Henrique Eisi Toma PhD

São Paulo

02/05/2019

*To my family who always supported me
and the love of my life for the patience and understanding.*

Acknowledgements

Five years have passed since a young chemist obtained his degree and started to wonder what he wanted to become and where he wanted to be. Now I am excited to look back and realize that I made the right decision.

Coming to a new country with a different language, different customs all by yourself is always a frightening endeavor. Luckily, I found great people who gifted me with their friendship and made this journey much easier. There were people who taught me many things about chemistry but the most important were the ones who came into my life and never left, those who made an indelible print, for you there will be my eternal gratitude.

I would like to thank my family who always supported me in every way they could, from studying chemistry to living abroad in order to become a better professional and human being away from them. To my mother Maria Nohelia and my father Jose Jesus that even in the distance always stood by my side, supporting me in my worst times and giving me force to continue and realize my dreams is dedicated this thesis. To my brother Santiago Jose who was always there and gave me lessons about strength and focus in his goals. To my grandmother Elodia who passed away while I was here in Brazil and could not say good bye thank you for all the time together, we will meet again.

Half way into this five-year journey, destiny allowed me to encounter one of the best human beings I have ever met. Today I am lucky to call her the love of my life and without her I don't know where I would be. To Aliny de Fatima, your love transformed my life and allowed me to see life with different eyes. Your support and understanding through our hardest hours made this possible.

I truly thank my advisor Professor Henrique Eisi Toma for the opportunity of becoming a better scientist and human being. The lessons learned from you will never be forgotten.

To Professor Koiti Araki for his help and the scientific discussions.

To Manuel Fernando and Carol for welcoming me into Brazil and receiving me in their home.

To Maria Rosana for the lessons given, the synthesis training and portuguese classes in the chemistry restaurant but above all for her friendship.

To Josue for his friendship and the successful collaborations performed throughout the graduation. Obrigado meu chapa!

To Julio, Alexander, Paola, Ana Paula, Bruno and Bill for the enriching discussions and friendship.

To the most important person in the LQSN because without him none of us could ever finish our theses. Alceu!!! Thank you for your patience and disposition to help and aid with anything I needed.

To Marcelo for his collaboration and disposition to help with AFM, Raman and other experiments needed.

To the laboratory colleagues for welcoming me and making me feel at home: Geovane, Sabrina, Daiana, Mayara, Helton, Delmarcio, Daniel G, Daniel (Peru), Thiago, André, Hiago, Lucas, Fernando, Rodrigo and Mariana.

To Lucas, Pamela and Abischek for their collaborations.

To the institute's analytic center analysts for their disposition to perform NMR, CHN and MS experiments.

Finally, I would like to thanks CNPq and Brazil government for the fellowship granted.

"I, a Universe of atoms. An atom in the Universe."

Richard Feynman

"The scientist is not a person who gives the right answers, he is one who asks the right questions."

Claude Lévi-Strauss

Abstract

AGUIRRE-ARAQUE, J.S. *Development of supramolecular metal-organic type systems and nanotechnology applications*. PhD Thesis, 2019. 201 p. Chemistry graduation program, Chemistry Institute, University of São Paulo.

Polypyridine ruthenium complexes have attracted attention due to their remarkable photoelectronic properties and being employed as electron injection compounds in DSSCs, photo catalysts in water splitting among others.

The first two chapters of this thesis present a comprehensive study of two novel ruthenium polypyridine and pyridine based complexes for DSSCs and for the study of an outer sphere intervalence electron transfer respectively.

Porphyrins are organic structures commonly found in nature. Their outstanding chemical versatility, structural and electronic properties have made these compounds object of continuous research. Among these properties are enzymatic catalysis, transport and photoelectron generation.

For these reasons the last two chapters of this thesis tried to focus in the development of supramolecular porphyrin arrangements capable of exploit and generate a synergistic effect of metallated cobalt porphyrins and polypyridine ruthenium complexes with opposite electronic properties -depending upon their π -accepting or donating nature- and their interaction with GO as nanocomposites for effective tetraelectronic dioxygen reduction and isoniazid oxidation. These catalytic studies showed promising results as possible sensors for dioxygen and isoniazid when compared with reported methodologies.

Key words: Supramolecular porphyrins, nanocomposites, ruthenium polypiridin complexes, intervalence charge transfer.

Resumo

AGUIRRE-ARAQUE, J.S. *Development of supramolecular metal-organic type systems and nanotechnology applications*. Tese de Doutorado, 2019. 201 p. Programa de Pós-Graduação em Química, Instituto de Química, Universidade de São Paulo.

Os complexos polipiridínicos de rutênio têm atraído muita atenção devido às suas notáveis propriedades foto eletrônicas, os quais têm sido empregados como compostos injetores de elétrons em DSSCs, fotocatalisadores na oxidação de água entre outros.

Os dois primeiros capítulos desta tese apresentam um estudo abrangente de dois novos complexos polipiridínicos e piridínicos de rutênio para DSSCs e no estudo de uma transferência eletrônica de intervalência de esfera externa respectivamente.

As porfirinas são estruturas orgânicas comumente encontradas na natureza. Sua excelente versatilidade química, propriedades estruturais e eletrônicas fizeram desses compostos objeto de intensa pesquisa. Entre essas propriedades estão a catálise enzimática, transporte e geração de fotoelétrons.

Por estas razões, os dois últimos capítulos desta tese tentaram se concentrar no desenvolvimento de arranjos porfirínicos supramoleculares capazes de explorar e gerar um efeito sinérgico entre porfirinas de cobalto e complexos polipiridínicos de rutênio com propriedade eletrônicas opostas -dependendo da natureza π -acceptor ou doador- e sua interação com GO como nano compósitos para a efetiva redução tetra eletrônica de oxigênio e oxidação de isoniazida. Os estudos catalíticos mostraram

resultados promissores como possíveis sensores para oxigênio e isoniazida quando comparados com metodologias na literatura.

Palavras chave: Porfirinas supramoleculares, nanocompositos, complexos polipiridínicos de rutênio, intervalencia.

Table of Content

INTRODUCTION	31
<i>Ruthenium</i>	31
<i>Ruthenium Clusters</i>	34
<i>Ruthenium Polypyridine Complexes</i>	35
<i>Metallated and Polymetallated Porphyrins</i>	41
<i>Supramolecular Porphyrins</i>	46
<i>Polymetallated Porphyrins in Photochemistry and Photobiology</i>	50
<i>Polymetallated Porphyrins in Redox Catalysis</i>	52
<i>Polymetallated Hetero-Hybrid Catalysts</i>	57
OBJECTIVES.....	61
EXPERIMENTAL SECTION.....	63
<i>Equipment</i>	63
SYNTHESES.....	66
<i>Synthesis of [2,2':6',2''-terpyridine]-4'-carboxylic acid (McTerpy)</i>	66
<i>Synthesis of [Ru^{II}(McTerpy)(H₂O)Cl₂].H₂O</i>	67
<i>Synthesis of [Ru^{II}(McTerpy)(dmbpy)Cl]Cl</i>	68
<i>Synthesis of [Ru^{II}(McTerpy)(dmbpy)(H₂O)](PF₆)₂</i>	69
<i>Synthesis of [Ru^{II}(McTerpy)(dmbpy)(TMT)]PF₆</i>	70
<i>Preparation of [Ru^{II}(McTerpy)(dmbpy)(TMT)]PF₆ deprotonated species</i> 70	70
<i>Synthesis of [Ru^{II}(NH₃)₅(dpypn)](PF₆)₂.3H₂O</i>	71
<i>Synthesis of [Ru^{III}(NH₃)₅(μ-dpypn)Fe^{II}(CN)₅].4H₂O</i>	71
<i>Synthesis of [Ru^{III}(NH₃)₅{μ-(dpypn-β-CD)}Fe^{II}(CN)₅]</i>	72
<i>Synthesis of [Ru^{II}(NH₃)₅(μ-dpypn)Ru^{II}(NH₃)₅](PF₆)₄</i>	73
<i>Synthesis of Na₆[Fe^{II}(CN)₅(μ-dpypn)Fe^{II}(CN)₅]</i>	74
<i>Synthesis of cis-[Ru^{II}(dmbpy)₂Cl₂]</i>	74
<i>Synthesis of cis-[Ru^{II}(H₂dcbpy)₂Cl₂]</i>	76
<i>Synthesis of Co^{II}TPyP</i>	76
<i>Synthesis of Co^{III}TRP(dmbpy)</i>	77

Synthesis of Co^{III}TRP(H₂dcbpy)	78
Preparation of Co^{III}TRP(dmbpy)/nGO composite	79
Preparation of Co^{III}TRP(dcbpy)-Ni/ GO composite	80
Electrode modification with Co^{III}TRP(dmbpy)/nGO composite	81
Electrode modification with Co^{III}TRP(H₂dcbpy)-Ni/ GO composite	81
Anatase TiO₂ nanoparticles synthesis	81
TiO₂ electrode preparation	82
TiO₂ film dye functionalization	82
Counter electrode preparation	82
Electrolyte preparation	82
DSSCs assemble	83
RESULTS AND DISCUSSION	84
CHAPTER I: Synthesis and Characterization of [Ru^{II}(McTerpy)(dmbpy)(TMT)]PF₆ and DSSC Application.	85
McTerpy characterization	85
[Ru^{II}(McTerpy)(H₂O)Cl₂].H₂O characterization	86
¹ H-NMR spectra	86
EPR spectra.....	88
Mass spectrometry.....	89
UV-Vis spectra.....	90
[Ru^{II}(McTerpy)(dmbpy)Cl]Cl characterization	92
¹ H-NMR spectra	92
UV-vis spectra	93
[Ru^{II}(McTerpy)(dmbpy)(TMT)]PF₆ characterization	93
¹ H-NMR spectra	93
Mass spectrometry.....	95
UV-Vis spectra.....	96
Electrochemistry.....	97
Spectroelectrochemistry	98
Spectrophotometric Titration	99
Emission and excitation studies.....	105
Efficiency and IPCE measurements	107

IPCE measurements.....	110
Chapter I conclusions.....	112
CAPTER II: Synthesis and Characterization of [Ru^{III}(NH₃)₅(μ-dpypn)Fe^{II}(CN)₅].4H₂O Complex.	113
[Ru^{II}(NH₃)₅(dpypn)](PF₆)₂.3H₂O characterization.....	113
UV-vis spectra.....	113
Mass spectrometry.....	114
[Ru^{III}(NH₃)₅(μ-dpypn)Fe^{II}(CN)₅].4H₂O characterization.....	116
FTIR spectroscopy.....	116
Electrochemistry.....	117
UV-vis spectra.....	118
Vis-NIR spectra.....	120
DFT calculations.....	122
Chapter II conclusions.....	123
CHAPTER III: Synthesis and Characterization of Co^{III}TRP(dmbpy) and its GO Composite for Dissolved Oxygen Sensors.	125
cis-[Ru^{II}(dmbpy)₂Cl₂] characterization.....	125
UV-vis spectra.....	125
Co^{II}TPyP characterization.....	125
UV-vis spectra.....	125
Co^{III}TRP(dmbpy) characterization	126
UV-vis spectra.....	126
Raman spectra.....	127
Electrochemistry.....	128
Spectroelectrochemistry.....	129
Co^{III}TRP(dmbpy)/4GO composite characterization.....	132
UV-vis spectra.....	132
Raman spectra.....	133
Co ^{III} TRP(dmbpy)/4GO composite electrochemical behavior.....	134
Chapter III conclusions	136
CHAPTER IV: Synthesis and Characterization of Co^{III}TRP_(dcbpy)-Ni Coordination Polymer and its GO Composite for Isoniazid Sensing.....	138

<i>cis-[Ru^{II}(H₂dcbpy)₂Cl₂] characterization</i>	138
UV-vis spectra	138
¹ H-NMR spectra	138
<i>Co^{III}TRP(H₂dcbpy) characterization</i>	139
¹ H-NMR and 2D ¹ H- ¹ H COSY NMR spectra	139
UV-vis spectra	141
Spectrophotometric titration	143
FTIR spectra	145
Raman spectra	146
Electrochemistry.....	147
Spectroelectrochemistry	148
<i>Co^{III}TRP(dcbpy)-Ni/GO composite characterization</i>	150
X-ray Powder Diffraction measurement	151
FTIR spectra	152
Raman spectra	153
Co ^{III} TRP(dcbpy)-Ni/GO composite electrochemical behavior.....	155
Chapter V conclusions	160
APPENDICES	162
<i>Appendix 1: [Ru^{II}(McTerpy)(dmbpy)(TMT)]PF₆ molar extinction coefficients.</i>	162
<i>Appendix 2: I-V plots of the [Ru^{II}(McTerpy)(dmbpy)(HTMT)] and (N-Bu₄)[Ru^{II}(McTerpy)(dmbpy)(TMT)] DSSCs.</i>	163
<i>Appendix 3: Electrostatic bending and outer-sphere intervalence transfer in a flexible ligand-bridged ruthenium(III)-iron(II) complex paper first page.</i>	164
<i>Appendix 4: CoTRP/Graphene oxide composite as efficient electrode material for dissolved oxygen sensors paper first page.</i>	166
<i>Appendix 5: GO composite encompassing a tetraruthenated cobalt porphyrin-Ni coordination polymer and its behavior as isoniazid BIA sensor paper first page.</i>	167
<i>Appendix 6: Parallel Collaborations</i>	168
Bromination of 5,15-diisopentiloxylporphyrin (DIPP) with NBS	168
Characterization of Br-DIPP	170
Characterization of Br ₂ -DIPP	172

Synthesis and characterization of 5,15-dioctyloxyphenylporphyrin (DOPP).	
.....	175
<i>Synthesis and characterization of 1,3-dioctyloxybenzene</i>	175
<i>Synthesis and characterization of 2,6-dioctyloxybenzenaldehyde</i>	177
<i>Synthesis and characterization of DOPP</i>	178
Chapter V conclusions	180
<i>Full ¹H NMR spectrum of DOPP</i>	181
BIBLIOGRAPHY	182

Table of Figures

Figure 1. Schematic representation of the Creutz-Taube ion.	33
Figure 2. Schematic representations of $[\text{Ru}_3\text{O}(\text{RCO}_2)_6\text{L}_3]_n$ (left) and $\text{Ru}_3(\text{CO})_{12}$ (right).	35
Figure 3. Schematic representations of the $[\text{Ru}(\text{bpy})_3]^{2+/3+}$ (top left), $[\text{Ru}(\text{phen})_3]^{2+/3+}$ (top right) and $[\text{Ru}(\text{terpy})_2]^{2+/3+}$ (bottom).	36
Figure 4. Schematic structures of commonly employed dyes for DSSCs.	39
Figure 5. Schematic representation of a porphirin ring.	42
Figure 6. UV-vis spectra of H ₂ TPyP (a) and ZnTPyP (b).	43
Figure 7. Synthetic pathway for –meso substituted porphyrins.	44
Figure 8. Schematic representation of 5,10,15,20-tetrapyridylporphirine (TPyP).	47
Figure 9. Schematic representation of H ₂ (4-TCP) left and H ₂ (3-TCP) right.	49
Figure 10. Schematic representation of the synthetic pathway for McTerpy. ...	67
Figure 11. Schematic representation of $[\text{Ru}^{\text{II}}(\text{McTerpy})(\text{H}_2\text{O})\text{Cl}_2] \cdot \text{H}_2\text{O}$ synthesis.	68
Figure 12. Schematic representation of $[\text{Ru}^{\text{II}}(\text{McTerpy})(\text{dmbpy})\text{Cl}]\text{Cl}$ synthesis.	69
Figure 13. Schematic representation of $[\text{Ru}^{\text{II}}(\text{McTerpy})(\text{dmbpy})(\text{H}_2\text{O})](\text{PF}_6)_2$ synthesis.	69
Figure 14. Schematic representation of $[\text{Ru}^{\text{II}}(\text{McTerpy})(\text{dmbpy})(\text{TMT})]\text{PF}_6$ synthesis.	70
Figure 15. Schematic representation of $[\text{Ru}^{\text{II}}(\text{NH}_3)_5(\text{dpypn})](\text{PF}_6)_2 \cdot 3\text{H}_2\text{O}$ synthesis.	71
Figure 16. Schematic representation of $[\text{Ru}^{\text{III}}(\text{NH}_3)_5(\mu\text{-dpypn})\text{Fe}^{\text{II}}(\text{CN})_5] \cdot 4\text{H}_2\text{O}$ synthesis.	72
Figure 17. Schematic representation of $[\text{Ru}^{\text{III}}(\text{NH}_3)_5\{\mu\text{-}(\text{dpypn} \cdot \beta\text{-CD})\}\text{Fe}^{\text{II}}(\text{CN})_5]$ synthesis.	73
Figure 18. Schematic representation of $[\text{Ru}^{\text{II}}(\text{NH}_3)_5(\mu\text{-dpypn})\text{Ru}^{\text{II}}(\text{NH}_3)_5](\text{PF}_6)_4$ synthesis.	74
Figure 19. Schematic representation of $\text{Na}_6[\text{Fe}^{\text{II}}(\text{CN})_5(\mu\text{-dpypn})\text{Fe}^{\text{II}}(\text{CN})_5]$ synthesis.	74
Figure 20. Schematic representation of cis- $[\text{Ru}^{\text{II}}(\text{dmbpy})_2\text{Cl}_2]$ synthesis.	75
Figure 21. Schematic representation of cis- $[\text{Ru}^{\text{II}}(\text{H}_2\text{dcbpy})_2\text{Cl}_2]$ synthesis.	76
Figure 22. Schematic representation of Co ^{II} TPyP synthesis.	77
Figure 23. Schematic representation of Co ^{III} TRP(dmbpy) synthesis.	78

Figure 24. Schematic representation of Co ^{III} TRP(H ₂ dc bpy) synthesis.	79
Figure 25. Image of assembled DSSCs employing N719 and a porphyrin-based dye.	83
Figure 26. ¹ H-NMR spectrum of MCTerpy in D ₂ O/NaOD.	86
Figure 27. ¹ H-NMR spectrum of [Ru ^{II} (McTerpy)(H ₂ O)Cl ₂].H ₂ O in DMSO-d ₆	87
Figure 28. EPR spectra of [Ru ^{II} (McTerpy)(H ₂ O)Cl ₂].H ₂ O in DMF at 77 K.	89
Figure 29. ESI-MS from [Ru ^{II} (McTerpy)(H ₂ O)Cl ₂].H ₂ O. Nebulizer: 0.8 Bar, dry gas: 5 L min ⁻¹ , temp: 200 °C, HV: 4500 V.	89
Figure 30. Molecular orbital energy diagram for octahedral RuL ₆ complexes. .	91
Figure 31. UV-vis absorption spectra of [Ru ^{II} (McTerpy)(H ₂ O)Cl ₂].H ₂ O in DMF.	91
Figure 32. ¹ H-NMR spectra of [Ru ^{II} (McTerpy)(dmbpy)Cl]Cl in MeOD-d ₄	92
Figure 33. UV-vis absorption spectra of [Ru ^{II} (McTerpy)(dmbpy)Cl]Cl in MeOH.	93
Figure 34. ¹ H-NMR spectra of [Ru ^{II} (McTerpy)(dmbpy)(TMT)]PF ₆ in MeOD-d ₄ .	94
Figure 35. ESI-MS from [Ru ^{II} (McTerpy)(dmbpy)(TMT)]PF ₆ . Nebulizer: 0.4 Bar, dry gas: 4 L min ⁻¹ , temp: 200 °C, HV: 4500 V.	96
Figure 36. UV-vis spectra from [Ru ^{II} (McTerpy)(dmbpy)(TMT)]PF ₆ in MeOH....	97
Figure 37. Cyclic voltammetry of [Ru ^{II} (McTerpy)(dmbpy)(TMT)]PF ₆ in CH ₃ CN.	98
Figure 38. Spectroelectrochemistry spectrum from [Ru ^{II} (McTerpy)(dmbpy)(TMT)]PF ₆ in DMF.	99
Figure 39. Spectrophotometric titration of [Ru ^{II} (McTerpy)(dmbpy)(TMT)]PF ₆ complex in basic (left) and acid (right) pH window.	103
Figure 40. Absorbance at 302 nm vs pH (a), sigmoidal fitting for the first equilibrium (b) and second derivative for the fitting (c).	104
Figure 41. Absorption (blue) and emission spectra (red) of [Ru ^{II} (McTerpy)(dmbpy)(TMT)]PF ₆ in MeOH.	106
Figure 42. Energy diagram comparison for anatase TiO ₂ , [Ru ^{II} (McTerpy)(dmbpy)(TMT)]PF ₆ and I ⁻ /I ₃ ⁻ redox couple.	107
Figure 43. Image of anatase TiO ₂ sensitized anodes.	108
Figure 44. I-V curves for [Ru ^{II} (McTerpy)(dmbpy)(H ₂ TMT)]PF ₆ (left) and N719 (right) assembled DSSCs.	109
Figure 45. IPCE measurements of [Ru ^{II} (McTerpy)(dmbpy)(H ₂ TMT)]PF ₆ (a), [Ru ^{II} (McTerpy)(dmbpy)(HTMT)] (b) and (N-Bu ₄)[Ru ^{II} (McTerpy)(dmbpy)(TMT)] (c).	111

Figure 46. UV-vis spectra from $[\text{Ru}^{\text{III}}(\text{NH}_3)_5\text{Cl}]\text{Cl}_2$ (black line) and $[\text{Ru}^{\text{II}}(\text{NH}_3)_5(\text{dpypn})](\text{PF}_6)_2 \cdot 3\text{H}_2\text{O}$ (red line) in water.	114
Figure 47. ESI-MS from $[\text{Ru}^{\text{II}}(\text{NH}_3)_5(\text{dpypn})](\text{PF}_6)_2 \cdot 3\text{H}_2\text{O}$. Nebulizer: 0.4 Bar, dry gas: 4 L min^{-1} , temp: $200 \text{ }^\circ\text{C}$, HV: 4500 V.	115
Figure 48. FTIR spectrum of the mixed-valence complex $[\text{Ru}^{\text{III}}(\text{NH}_3)_5(\mu\text{-dpypn})\text{Fe}^{\text{II}}(\text{CN})_5] \cdot 4\text{H}_2\text{O}$ in KBr pellets.	116
Figure 49. CV measurements of $\text{Ru}^{\text{II}}\text{LRu}^{\text{II}}$ and $\text{Fe}^{\text{II}}\text{LFe}^{\text{II}}$ (a), $\text{Ru}^{\text{II}}\text{LFe}^{\text{II}}$ (b) and DPV of $\text{Ru}^{\text{II}}\text{LFe}^{\text{II}}$ (c) at 50 mV s^{-1} in aqueous 0.1 mol L^{-1} KCl.	118
Figure 50. UV-vis spectra from $[\text{Ru}^{\text{II}}(\text{NH}_3)_5(\mu\text{-dpypn})\text{Fe}^{\text{II}}(\text{CN})_5]^-$ ($\text{Ru}^{\text{II}}\text{LFe}^{\text{II}}$), $[\text{Ru}^{\text{II}}(\text{NH}_3)_5(\text{dpypn})]^{2+}$ ($\text{Ru}^{\text{II}}\text{L}$) and $[\text{Fe}^{\text{II}}(\text{CN})_5(\text{dpypn})]^{3-}$ ($\text{Fe}^{\text{II}}\text{L}$) in water.	119
Figure 51. UV-vis spectra from $\text{Fe}^{\text{II}}\text{L}$ and $\text{Fe}^{\text{II}}\text{LFe}^{\text{II}}$ (a), $\text{Ru}^{\text{II}}\text{L}$ and $\text{Ru}^{\text{II}}\text{LRu}^{\text{II}}$ (b) and $\text{Ru}^{\text{II}}\text{LFe}^{\text{II}}$ in water under N_2 atmosphere.	120
Figure 52. Vis-NIR spectra of $\text{Ru}^{\text{II}}\text{LFe}^{\text{II}}$ (black line) and $\text{Ru}^{\text{III}}\text{LFe}^{\text{II}}$ (red line) in the solid state. *Instrumental artifact.	121
Figure 53. Vis-NIR spectra of $\text{Ru}^{\text{III}}\text{LFe}^{\text{II}}$ (black line) and $[\text{Ru}^{\text{III}}(\text{NH}_3)_5\{\mu\text{-}(\text{dpypn } \beta\text{-CD})\}\text{Fe}^{\text{II}}(\text{CN})_5]$ (red line).	122
Figure 54. DFT structures of $\text{Ru}^{\text{III}}\text{LFe}^{\text{II}}$ (a), $\text{Fe}^{\text{II}}\text{LFe}^{\text{II}}$ (b) and $\text{Ru}^{\text{II}}\text{LRu}^{\text{II}}$ (c).	123
Figure 55. UV-vis spectra of the cis- $[\text{Ru}^{\text{II}}(\text{dmbpy})_2\text{Cl}_2]$ complex in MeOH.	125
Figure 56. Uv-vis spectra of $\text{Co}^{\text{II}}\text{TPyP}$ in DMF.	126
Figure 57. UV-vis spectra of $\text{Co}^{\text{III}}\text{TRP}(\text{dmbpy})$ in MeOH.	127
Figure 58. Raman spectra of $\text{Co}^{\text{III}}\text{TRP}(\text{dmbpy})$	128
Figure 59. Cyclic voltammograms of $\text{Co}^{\text{III}}\text{TRP}(\text{dmbpy})$ in DMF (a) and water (b).	129
Figure 60. Spectroelectrochemistry spectra of $\text{Co}^{\text{III}}\text{TRP}(\text{dmbpy})$ in DMF.	130
Figure 61. Spectroelectrochemistry spectra of $\text{Co}^{\text{III/II}}\text{TRP}(\text{dmbpy})$ in DMF.	131
Figure 62. UV-vis/scattering spectra of $\text{Co}^{\text{III}}\text{TRP}(\text{dmbpy})$ (blue line), GO (red line) and $\text{Co}^{\text{III}}\text{TRP}(\text{dmbpy})/4\text{GO}$ composite (black line).	132
Figure 63. Raman spectra of GO, $\text{Co}^{\text{III}}\text{TRP}(\text{dmbpy})$ and $\text{Co}^{\text{III}}\text{TRP}(\text{dmbpy})/4\text{GO}$ (a), confocal Raman images of $\text{Co}^{\text{III}}\text{TRP}(\text{dmbpy})/4\text{GO}$ generated from $\text{Co}^{\text{III}}\text{TRP}(\text{dmbpy})$ spectra (b), from GO (c) and convoluted image (d). Raman profile contribution of $\text{Co}^{\text{III}}\text{TRP}(\text{dmbpy})$ and GO along	133
Figure 64. Cathodic region of cyclic voltammograms of GC (black line), GO/GC (red line), $\text{Co}^{\text{III}}\text{TRP}(\text{dmbpy})/\text{GC}$ (green line), $\text{Co}^{\text{III}}\text{TRP}(\text{dmbpy})/4\text{GO}$ (blue line) modified electrodes of an O_2 saturated aqueous solution.	136

Figure 65. UV-vis spectra from cis-[Ru ^{II} (H ₂ dcbpy) ₂ Cl ₂] in DMF.....	138
Figure 66. ¹ H-NMR spectra of cis-[Ru ^{II} (H ₂ dcbpy) ₂ Cl ₂] in DMSO-d ₆	139
Figure 67. ¹ H-NMR spectrum of Co ^{III} TRP(dcbpy) in D ₂ O/NaOD.....	140
Figure 68. 2D ¹ H- ¹ H NMR COSY spectrum of Co ^{III} TRP(dcbpy) in D ₂ O/NaOD.....	141
Figure 69. UV-vis spectra of Co ^{III} TRP(dcbpy) in MeOH/H ₂ O/NaOH.	142
Figure 70. Spectrophotometric titration of Co ^{III} TRP(dcbpy) (a), sigmoidal fitting for absorbance at 436 nm (b) and second derivative of the sigmoidal function (c).....	144
Figure 71. FTIR spectrum of Co ^{III} TRP(H ₂ dcbpy) in KBr pellet.	146
Figure 72. Raman spectra of Co ^{III} TRP(H ₂ dcbpy).	147
Figure 73. Cyclic voltammogram of Co ^{III} TRP(dcbpy) in DMF/H ₂ O/NaOH mixture.	148
Figure 74. Spectroelectrochemistry spectra of Co ^{III} TRP(dcbpy) in DMF.....	149
Figure 75. Spectroelectrochemistry spectra of Co ^{III/II} TRP(dcbpy) in DMF.....	150
Figure 76. X-ray powder diffractograms of Co ^{III} TRP(dcbpy)-Ni/GO (red line) and GO (black line).	152
Figure 77. FTIR spectra of Co ^{III} TRP(H ₂ dcbpy) (black line), GO (red line) and Co ^{III} TRP(dcbpy)-Ni/GO composite (blue line) in KBr pellets.	153
Figure 78. Raman comparative spectra of Co ^{III} TRP(H ₂ dcbpy) (black line), GO (red line) and Co ^{III} TRP(dcbpy)-Ni/GO composite (blue line) λ _{exc} 532 nm.	154
Figure 79. Raman microscopy images from 1350 cm ⁻¹ GO band (a), 1540 cm ⁻¹ Co ^{III} TRP(H ₂ dcbpy) band (b) and convoluted Co ^{III} TRP(dcbpy)-Ni/GO composite image (c).....	155
Figure 80. Schematic structure of isoniazid (a), cyclic voltammograms with increasing concentration of isoniazid at 100 mV s ⁻¹ (b) and linear behavior of concentration vs peak current (c).....	157
Figure 81. Comparative CVs upon isoniazid (2x10 ⁻⁴ mol L ⁻¹) oxidation of GC (black line), GO (red line) and Co ^{III} TRP(dcbpy)-Ni/GO (blue line) modified electrodes.....	158
Figure 82. Cyclic voltammograms of a 2x10 ⁻⁴ mol L ⁻¹ isoniazid solution over a four day period (a) and CVs peak current behavior over time (b).	159
Figure 83. I-V curve of [Ru ^{II} (McTerpy)(dmbpy)(HTMT)] assembled DSSC....	163
Figure 84. I-V curve of (N-Bu ₄)[Ru ^{II} (McTerpy)(dmbpy)(TMT)] assembled DSSC.....	163
Figure 85. Schematic representation of 5,15-diisopentiloxyporphyrin.	168

Figure 86. ^1H NMR spectrum of 5,15-diisopentiloxyporphyrin in acetone- d_6	169
Figure 87. Schematic representation of 5,15-diisopentiloxyporphyrin-10-bromoporphyrin.	170
Figure 88. ESI mass spectra of Br-DIPP. Nebulizer: 0.8 Bar, Dry Gas: 5 L min^{-1} , Temp: $200 \text{ }^\circ\text{C}$, HV: 4500 V.	171
Figure 89. ^1H NMR spectrum of Br-DIPP in acetone- d_6	172
Figure 90. Schematic representation of 5,15-diisopentiloxyporphyrin-10,20-dibromoporphyrin.	172
Figure 91. ESI mass spectra of Br_2 -DIPP. Nebulizer: 0.8 Bar, Dry Gas: 5 L min^{-1} , Temp: $200 \text{ }^\circ\text{C}$, HV: 4500 V.	173
Figure 92. ^1H NMR spectrum of Br_2 -DIPP in chloroform- d	174
Figure 93. Schematic representation of 5,15-dioctyloxyphenylporphyrin.	175
Figure 94. Schematic representation of 1,3-dioctyloxybenzene synthesis. ...	176
Figure 95. ^1H NMR spectrum of 1,3-dioctyloxybenzene in chloroform- d	176
Figure 96. Schematic representation of 2,6-dioctyloxybenzaldehyde synthesis.	177
Figure 97. ^1H NMR spectrum of 2,6-dioctyloxybenzaldehyde in chloroform- d	178
Figure 98. ^1H NMR spectrum of DOPP in acetone- d_6	179

ABBREVIATIONS

Ac: Acetate

ACN: Acetonitrile

AFM: Atomic Force Microscopy

BF₃: Trifluoroborate

BIA: Batch Injection Analysis

Bpy: 2,2'-bipyridine

DCM: Dichloromethane

DDQ: 2,3-Dichloro-5,6-dicyano-p-benzoquinone

Dmbpy: 4,4'-dimethyl-2,2'-bipyridine

DMF: N,N-Dimethylformamide

DMPO: 5,5-dimethyl-1-pyrroline N-oxide

DNA: Deoxyribonucleic Acid

DPV: Differential Pulse Voltammetry

Dpypn: 1,3-di(4-pyridyl)propane

DSSCs: Dye Sensitized Solar Cells

EDTA: 2,2',2'',2'''-(Ethane-1,2-diyldinitrilo)tetra acetic acid

EIS: Electrochemical Impedance Spectroscopy

EPR: Electron Paramagnetic Resonance

ESI-MS: Electrospray Ionization Mass Spectrometry

FF: Fill Factor

FIA: Flow Injection Analysis

FTO: Fluorine-doped Tin Oxide

GC: Glassy Carbon

GO: Graphene Oxide

H₂dcbpy: 4,4'-dicarboxylic-2,2'-bipyridine acid

HOMO: Highest Occupied Molecular Orbital

IPCE: Incident Photon to electron Conversion Efficiency

J_{sc}: Short Circuit Current

LB: Langmuir-Blodgett

LMCT: Ligand to Metal Charge Transfer

LOD: Limit of Detection

LOQ: Limit of Quantification

LUMO: Lower Unoccupied Molecular Orbital

McTerpy: [2,2':6',2''-terpyridine]-4'-carboxylic acid

MLCT: Metal to Ligand Charge-Transfer

MOF: Metal-Organic Framework

NBS: N-Bromosuccinimide

NIR: Near Infrared

NMR: Nuclear Magnetic Resonance

OER: Oxygen Evolution Reaction

ORR: Oxygen Reduction Reaction

PCE: Power conversion efficiency

PDT: Photodynamic therapy

Phen: 1,10-phenanthroline

PMA: Phosphomolybdic acid

PPh₃: Triphenylphosphine

PSC: Perovskite solar cell

Py: Pyridine

RDE: Rotating Disk Electrode

rGO: Reduced Graphene Oxide

RRDE: Rotating Ring and Disk Electrode

TAS: Transient Absorption Spectroscopy

TBA: Tetrabutylammonium

TCP: Tetraclusterporphyrin

Tcterpy: [2,2':6',2"-terpyridine]-4,4',4"-tricarboxylic acid

Terpy: 2,2':6',2"-terpyridine

TFMS: Trifluoromethanesulfonate ion

TMT: 2,4,6-trimercapto-1,3,5-triazine

TPP: 5,10,15,20-Tetraphenylporphyrin

TPyP: 5,10,15,20-Tetrapyritylporphyrin

TRP: Tetra-ruthenated Porphyrin

V_{oc}: Open Circuit Voltage

XRPD: X-Ray Powder Diffraction

β-CD: Beta-cyclodextrin

TMEDA: N,N,N',N'-Tetramethylethylenediamine

THF: Tetrahydrofuran

INTRODUCTION

Ruthenium

Ruthenium is a chemical element with an atomic number of 44 and a molar mass of $101.07 \text{ g mol}^{-1}$. It has been classified as a transition metal and has seven isotopes (^{96}Ru , ^{98}Ru , ^{99}Ru , ^{100}Ru , ^{101}Ru , ^{102}Ru , ^{104}Ru) being the last four the most important ones due to their higher natural abundance.¹ This silvery colored metal was discovered by Karl Karlovich Klaus in 1844 at Kazan State University and possesses a wide variety of oxidation states (8, 6, 4, 3, 2, 0, -2) being Ru(IV), Ru(III) and Ru(II) the most common states involved in polypyridine complexes.

Natural abundance of ruthenium poses a major drawback for its commercial applications due to its scarcity, placing this metal among the rarest metals on earth. Nevertheless, ruthenium is found in some platinum minerals but its industrial obtainment comes from nickel purification waste.

This transition metal has found its way into many useful applications; among them we can cite electronics, especially in chip resistors and electrical contacts. As we will further discuss, its oxides are the most commonly employed compounds for anode coating in electrochemical cells alongside with platinum.

Ruthenium electronic configurations for its 2+ and 3+ oxidation states are $[\text{Kr}]4d^6$ and $[\text{Kr}]4d^5$ respectively. This means that Ru(III) complexes are paramagnetic species since the electronic configuration for the d orbitals is $(t_{2g})^5(e_g)^0$, however the diversity of the Ru(III) complexes is strikingly rich with many anionic, cationic and neutral compounds reported to be kinetically inert.² As an example of this reactivity we found the ammine based complexes such as $[\text{Ru}^{\text{III}}(\text{NH}_3)_6]\text{Cl}_3$ and $[\text{Ru}^{\text{III}}(\text{NH}_3)_5\text{Cl}]\text{Cl}_2$, the former complex needs extreme reaction conditions (conc. HCl

and high temperature) in order to introduce the chloride ligand into its coordination sphere affording the latter complex. At the same time, $[\text{Ru}^{\text{III}}(\text{NH}_3)_5\text{Cl}]\text{Cl}_2$ requires the formation of the Ru^{2+} species in order to being able to favor the substitution of the chloride ligand.³

$\text{Ru}(\text{II})$ complexes are typically hexacoordinated low spin (diamagnetic) species exhibiting relatively strong spin-orbit coupling. The higher reactivity makes $\text{Ru}(\text{II})$ complex interesting species towards catalytic applications. In particular, its six-coordination sphere may be tuned by substrates X and Y in molecular formulas like RuL_5X , RuL_4Y , where L are ancillary ligands. Catalytic studies encompass hydrogenation of ketones,⁴ bond activation including H-H, C-C, C-H among others,⁵ alkene additions (i.e. Kharasch reaction),⁶ hydroformylations and so on.⁷

In between the two oxidation states, $[\text{Ru}(\text{II})$ and $\text{Ru}(\text{III})]$, we can find the intervalence (IT) compounds. These molecules bear generally two metal centers capable of exchanging electrons upon light absorption. In order for this effect to be observed, one metal atom must be in a low oxidation state, acting as an electron donor, and the other metallic ion must be in a high oxidation state, acting as electron acceptor. This IT charge transfer is commonly identified by a broad absorption band localized typically in the NIR region but it can occasionally appear in the visible range. It has been shown that orbital overlap or some electronic delocalization must take place for the IT transition to occur, and the π -conjugated nature of the bridging ligand and its length can play an important role.⁸ However, Kubiak et al. reported IT charge transfer between two μ_3 -oxoruthenium acetate clusters bridged by hydrogen bonds from the isonicotinic acid residues present.⁹ Before this report, Kaifer et al showed remarkable electronic coupling between two identical ferrocene moieties

separated about 10 Å and only connected by four hydrogen bonds, this IT was spotted approximately at 1200 nm in the absorption spectra.¹⁰

One of the most famous IT complexes was reported by Creutz and Taube in 1969.¹¹ This complex shown in Figure 1 has a global charge of 5+, meaning that individual ruthenium oxidation states must be 2.5 due to high electronic coupling. As found out by Creutz and Taube, formal reduction potentials for two consecutive electrochemical processes can be observed at -0.40 and -0.76 V, instead of a single potential, this difference has been ascribed to the electronic coupling between the ruthenium centers, making them nonequivalent after the first electron transfer. The authors found out an electronic absorption around 1570 nm for this specific combination of oxidation states. whereas for the Ru^{II}/Ru^{II} and Ru^{III}/Ru^{III} configurations no band in the NIR range was spotted. They estimated that this energy doesn't involve the promotion of the electron from the ground to the excited state in the molecule, but rather an energy required for the electron exchange between the Ru^{II}/Ru^{III} to Ru^{III}/Ru^{II} configuration. It was debated how the metallic centers can possess the same coordination sphere, while their environments in the new configuration (Ru^{II}/Ru^{III}) are typical of 2+ and 3+ ions respectively.

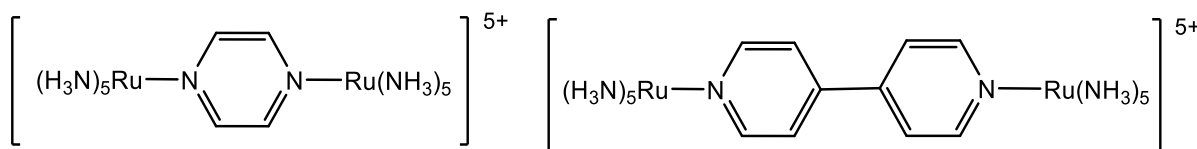


Figure 1. Schematic representation of the Creutz-Taube class III ion (left) and $[\{\text{Ru}(\text{NH}_3)_5\}_2(\mu\text{-4,4'-bpy})]^{5+}$ class II ion (right).

Not only inner coordination sphere intervalence electron transfers have been documented. Surprisingly, in 1980 Toma reported a series of outer-sphere mixed valence ruthenium-iron complexes with the general formula

$[\text{Ru}(\text{NH}_3)_6][\text{Fe}(\text{CN})_5\text{L}\cdot n\text{H}_2\text{O}]$ with L being a ligand ranging from CO, CN to pyrazine and pyridine. His results showed IT absorption bands within the visible region depending upon ligand L nature (π -accepting strength),¹² involving an electron tunneling effect, rather than an electronic delocalization in the bridging system.

Ruthenium Clusters

As expected for electron deficient and electron rich metal ions, Ru(III) and Ru(II) tend to form polynuclear compounds with the interesting formation of metal-metal bonds. As shown in Figure 2 right, the Ru(III) species associates in a μ_3 -oxoruthenium cluster with six bridging carboxylate residues with R substitutes ranging from H to C_8H_{16} and three L ligands, typically H_2O , PPh_3 , CO and N-heterocycles. The electronic and magnetic properties of this cluster depend upon the metals oxidation states that range from $\text{Ru}^{\text{II}}/\text{Ru}^{\text{II}}/\text{Ru}^{\text{II}}$ to $\text{Ru}^{\text{IV}}/\text{Ru}^{\text{IV}}/\text{Ru}^{\text{III}}$ the potentials associated with every monoelectronic process vary depending on the ligand L and substituent R nature. It was observed that when the cluster is in their mixed valence states (i.e. $\text{Ru}^{\text{III}}/\text{Ru}^{\text{III}}/\text{Ru}^{\text{II}}$) it is a diamagnetic species, whereas as homo valence system (i.e. $\text{Ru}^{\text{III}}/\text{Ru}^{\text{III}}/\text{Ru}^{\text{III}}$) it behaves in a paramagnetic fashion.¹³ Due to this interesting electronic and magnetic properties this type of polymetallic clusters have been studied as hydrogenation,^{14,15} hydrogen transfer,¹⁶ and oxidation catalysts¹⁷ among others.

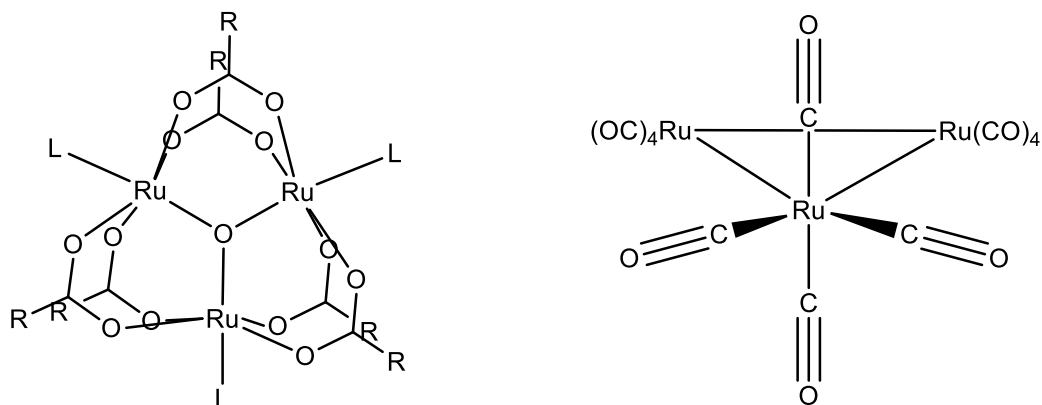


Figure 2. Schematic representations of $[\text{Ru}_3\text{O}(\text{RCO}_2)_6\text{L}_3]_n$ (left) and $\text{Ru}_3(\text{CO})_{12}$ (right).

Figure 2 (right), shows the wire structure of the neutral triruthenium dodecacarbonyl cluster, being one of the well-known polymetallic ruthenium compounds bearing formal Ru-Ru bonds, with a D_{3h} symmetry, displaying three Ru(0) atoms disposed in the vertices of an equilateral triangle coordinated by four carbonyl (CO) ligands each (two axial and two equatorial). The reactivity of this carbonyl cluster has been studied by the coordination of halogens (Cl, Br, I) forming the $\text{Ru}_3(\text{CO})_{12}\text{X}_6$ species. Compounds resulting from reactions with thiols were also performed with no observations of the trimetallic compound being formed.¹⁸ On the other hand, substitution reactions with phosphines (mainly PPh_3 or tertiary phosphines) and N-heterocyclic ligands (bpy) have successfully been carried out. Unfortunately, air and water susceptibility make the vast majority of these carbonyl cluster derivatives easily decomposed and not suitable for many applications. Decomposition is usually initiated by the Ru-Ru bond cleavage and CO loss.

Ruthenium Polypyridine Complexes

One of the most studied areas has been the photochemistry of the polypyridine ruthenium complexes.¹⁹ The star complex is the $[\text{Ru}^{\text{II}}(\text{bpy})_3]^{2+}$ species and its analogues with phenanthroline and terpyridine (Figure 3) drawing special

attention to the studies by Sutin's group in 1979, showing the excited state lifetimes of polypyridine Fe(II), Ru(II) and Os(II) complexes. He outlined the importance of the higher excited state lifetimes in ruthenium complexes when compared to its iron and osmium analogues, performing photochemical conversion and storage reactions with suitable redox quenchers and charge scavenger such as halopentaamincobalt(III) complexes.²⁰

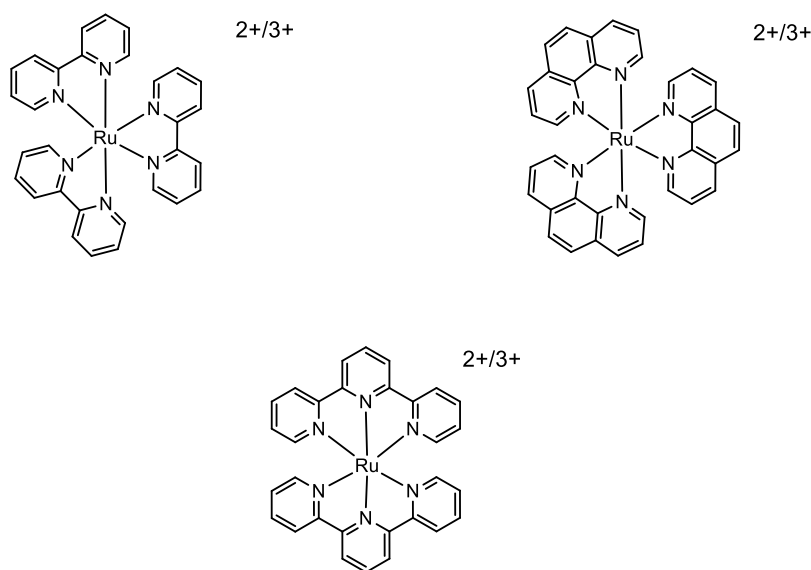
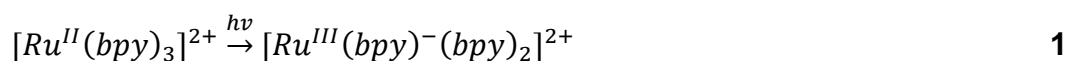


Figure 3. Schematic representations of the $[\text{Ru}(\text{bpy})_3]^{2+/3+}$ (top left), $[\text{Ru}(\text{phen})_3]^{2+/3+}$ (top right) and $[\text{Ru}(\text{terpy})_2]^{2+/3+}$ (bottom).

Since Sutin's work, the crystalline structure of $[\text{Ru}^{\text{II/III}}(\text{bpy})_3]^{2+/3+}(\text{PF}_6)_{2/3}$ has been elucidated at low temperature (105 K) by Röhr and coworkers showing some differences for the Ru(II) species in its crystalline packing when compared with room temperature measurements.²¹ Also the similarities between the Ru(II) and Ru(III) bond lengths with the nitrogen atoms from bpy corroborate the high electronic self-exchange rate obtained in their experiments between these two species. This property will be of remarkable use when attempting to design suitable DSSCs dyes since $\text{Ru}^{\text{II/III}}$ species are continuously being cycled.

This last inquiry was carried on by McKuster et al. in 1997 with femtosecond dynamics of the $[Ru^{II}(bpy)_3]^{2+}$ excited state, observing a process completion (excited state formation) in approximately 300 femtoseconds after excitation, taking into consideration that its excited state lifetime is about 1 μ s.²² It is established that the visible light absorption in this molecule relies on the strong metal to ligand charge transfer, in which an electron located in the metal d orbitals is promoted to a π^* orbital of one of the bpy ligands (MLCT $d\pi \rightarrow p\pi^*$) as shown in equation 1.



This transition occurs from the electronic ground state to the first electronic excited state, initially being a singlet state (¹MLCT) that suffers an ultrafast intersystem crossing to the low lying triplet excited state(³MLCT) in about 15 fs²³ becoming responsible for both oxidative and reductive behavior of the $[Ru^{III}(bpy)^-(bpy)_2]^{2+}$ species.^{24,25}

High excited state lifetimes of polypyridine ruthenium complexes continue to draw scientist's attention due to their application in photochemical processes in solution (PDT). In this manner, eq 1 proves the usefulness of ruthenium compounds since as we will further discuss, polypyridine ligands are commonly modified with functional groups capable of establishing electronic communication with other molecules or materials facilitating the electronic transfer from the excited state $[Ru^{III}(bpy)^-(bpy)_2]^{2+}$.²⁶

In DSSC applications, ruthenium polypyridine complexes have been widely used. The most employed and well-known are N3, N719 and Black Dye (Figure 4).^{27,28,29} N3 was prepared as a series of ruthenium complexes by Grätzel and coworkers with the general formula $Ru^{II}L_2X_{2-n}H_2O$ with $L = H_2dcbpy$ and $X = Cl^-, Br^-$,

I⁻, CN⁻ and SCN⁻.³⁰ Performance of these dyes when deposited on nanocrystalline TiO₂ films was verified, being the isocyanate derivative the device with the most outstanding efficiency, reaching 10 % overall conversion under AM 1.5 sunlight radiation. These results with the SCN⁻ ligand are owed to a series of effects both electronic (molecular) and structural. First of all, isocyanate residues were proved to red shift the absorption maxima in the UV-vis spectra and promotes a higher oscillator strength of the electronic transitions which accounts for a better exploitation of the solar spectrum. Secondly, both steric hindrance and electrostatic repulsion are more effective for impeding dark current increase by recombination with the I₃⁻ species in the electrolyte media.

Moreover, the higher excited state lifetime (59 ns) at room temperature when compared with the cis-dihalogen and cis-diaquo complexes favors the electron injection towards the TiO₂ CB, affording an IPCE as high as 85 % in the 500-600 nm range.

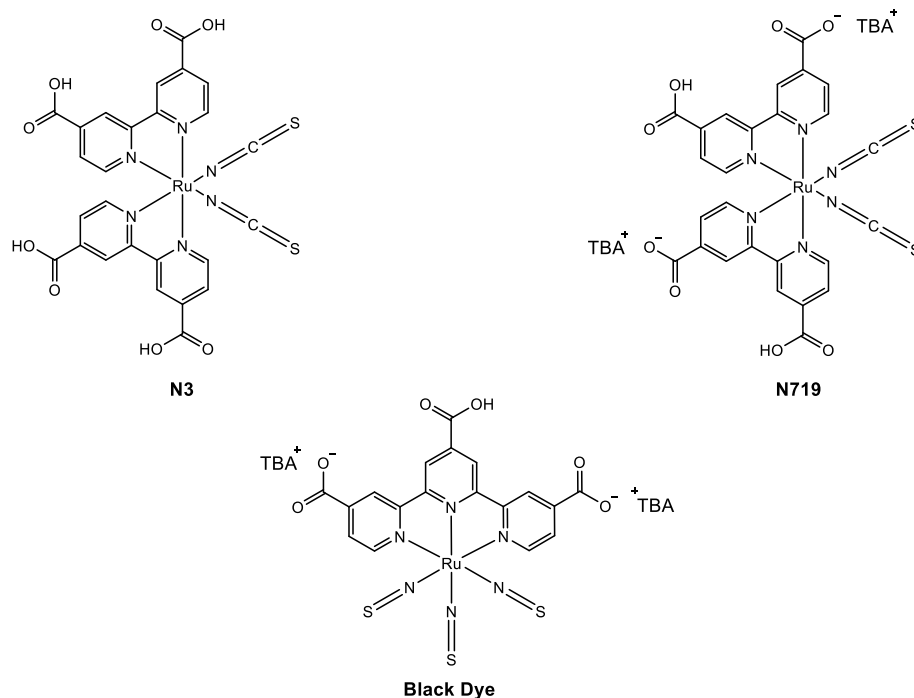


Figure 4. Schematic structures of commonly employed dyes for DSSCs.

Since the N3 complex exhibits four carboxylic residues capable of interacting with the TiO_2 nanoparticles, it was clear since the beginning that not all of these moieties could take part in this interaction at the same time and a coordination approximation must direct the anchoring of the ruthenium species. Accordingly, in 1999 Grätzel and coworkers studied the protonation effect on the charge transfer in this complex when used for solar cell sensitization.³¹

It was found a blue-shift in the absorption and emission spectra; an effect derived from the protonation degree in the dcbpy ligand that increases the π^* orbital energy. In order to being able to generate the different protonation isomers a spectrophotometric titration was employed to identify the pK_a of the equilibria. N3 dye shows four carboxylic groups capable of undergo four acid-base equilibria but the question remained as if all of them would take place in this step by step or one step fashion. Interestingly they found two separate equilibria as pointed out by the

absorbance change in the electronic spectra upon pH variation giving two pK_a values ($pK_{a1} = 3 \pm 0.1$ and $pK_{a2} = 1.5 \pm 0.1$) suggesting nonequivalent pyridyl subunits within the dcbpy ligands as observed in $^1\text{H-NMR}$ spectra.

Photoaction measurements (IPCE) shown a better performance of the deprotonated species $(\text{Bu}_4\text{-N})_2[\text{Ru}^{\text{II}}(\text{dcbpyH})(\text{NCS})_2]$ named N719 by simply increasing the monochromatic efficiency in the 400 to 800 nm range.

In 2001 and with the aim of increasing the spectral absorption range of ruthenium polypyridine complexes, Grätzel and coworkers synthesized a series of panchromatic compounds derived from the protonation of the Black Dye (Figure 4) with the general formula $\{(\text{C}_2\text{H}_5)_3\text{NH}\}_x[\text{Ru}^{\text{II}}(\text{H}_{(3-x)+1}\text{tcterpy})(\text{NCS})_3] \cdot n\text{H}_2\text{O}$ with x varying from 1 to 3.³² Particularly the isomer with $x = 3$ showed the better results in agreement with the study of deprotonation in the dcbpy ligand for its ruthenium complex mentioned above. In this study spectrophotometric studies were performed and confirmed that the central pyridyl residue possess a differentiated acid-base equilibrium than that of the peripheral pyridines within tcterpy, this is due to the trans influence of the NCS ligand, which is a better σ -donor than pyridine augmenting the central pyridyl ring basicity.

IPCE measurements of DSSCs assembled using black dye showed remarkable spectral range affording up to 80 % efficiency in the visible region and giving an additional current generation up to 920 nm (NIR); moreover, authors claim a nearly quantitative current generation (95 % efficiency) that is lowered due to light losses due to optical interfaces in the conducting glass.

As it has been pointed out that a thorough design of ruthenium polypyridyl complexes must be done in order to obtain the desired electronic and structural

properties that make a dye suitable for DSSCs. Some of these properties are thermal stability, anchoring carboxylate or phosphonate groups, bulky and charged ancillary ligands, long excited state life times, wide spectral absorption range and adequate HOMO/LUMO energies that match the electrolyte redox potential and TiO₂ CB energies respectively.

Metallated and Polymetallated Porphyrins

Porphyrins are organic tetrapyrrolic macrocycles bridged by methine groups (Figure 5). They have been widely studied due to their remarkable structural and electronic properties, which emerge from the π -electrons in the conjugated aromatic structure, allowing the electronic transitions to occur in the visible region of the electromagnetic spectrum. The porphyrin electronic absorption spectra are dominated by intense bands originated by the $\pi \rightarrow \pi^*$ ring transitions. These bands correspond to the Soret (B) and Q bands which are typically located between 380-500 nm and 500-700 nm respectively. The energy, quantity and intensity of these bands has been shown to be influenced by conjugation and symmetry and a rather simple explanation has been performed by the four orbital model (two HOMOs and two LUMOs) proposed by Gouterman in 1959.^{33,34}

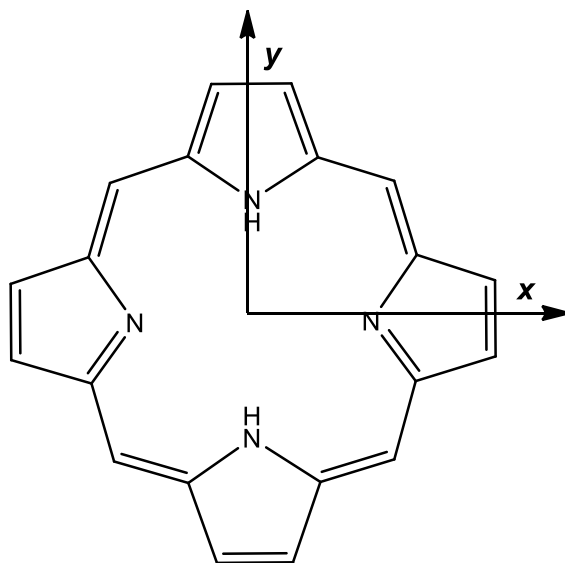


Figure 5. Schematic representation of a porphin ring.

The four orbitals involved in the electronic transitions are represented by the a_{1u} and a_{2u} HOMOs and a degenerate e_g LUMO.³⁵ Ring substituents and metal ions can promote symmetry and electronic changes breaking the LUMOs degeneracy. For the free base porphyrins, the protonated ring leads to a C_{2v} symmetry, where the x and y axes involve different dipole transition moments (Figure 5). However, for the metallated porphyrin, the D_{4h} symmetry turns these two components equivalent, decreasing number of Q bands from four (Figure 6a) to just two as shown in Figure 6b for the TPYP free base and its zinc (II) derivative.

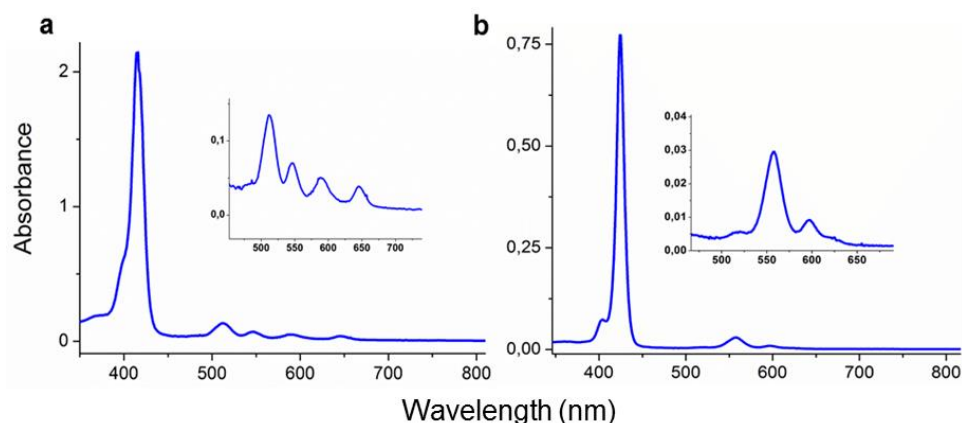


Figure 6. UV-vis spectra of H₂TPyP (a) and ZnTPyP (b).

Soret band involves an electronic transition between the ground state to the second electronic excited state, or $S_0 \rightarrow S_2$. In the case of free base porphyrins, there are also four labeled as Q_{0x} , Q_{1x} , Q_{0y} and Q_{1y} from lower to higher energy respectively. The zero (0) sub-index indicates a purely electronic transition from the ground state (S_0) to the first excited state (S_1) whereas sub-index one (1) shows the same electronic transition with a vibrational component involved hence denoted as vibronic coupling. Sub-indexes x and y denote the polarization of the electric component of the electromagnetic radiation absorbed.³⁶

Porphyrins encompassing suitable substituents in their structure can be synthesized by a varied of methods. However, the most widely employed has been proposed by Lindsey and coworkers in 1986 and extended in 1987,^{37,38} after the classical paper by Rothmund (1941)³⁹ and Adler-Longo (1964).⁴⁰ This route is performed under relatively mild conditions, according to a two-step reaction path involving an aldehyde, pyrrole and an acid catalyst such as trifluoroacetic acid or BF₃ using dry dichloromethane or chloroform under inert atmosphere (N₂) at room temperature. Once the equilibrium condition is reached, an oxidant such as DDQ or *p*-chloranil is added to the reaction in order to convert the porphyrinogen to the

desired porphyrin. This synthetic method provides an adequate path for heat-sensitive aldehydes to generate porphyrins with typical yields of about 46% for 10^{-2} mol L⁻¹ reactant concentration. Figure 7 summarizes the Lindsey general method for *–meso* substituted porphyrins and the multiple variations that can be exploited to make “trans” substituted porphyrins via dipyrromethane formation.

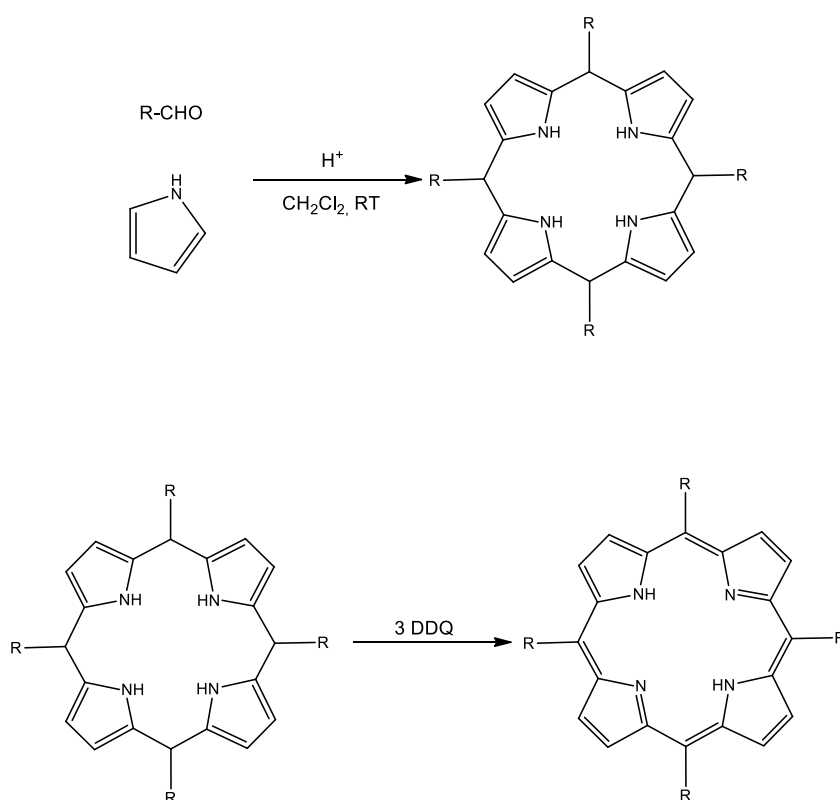


Figure 7. Synthetic pathway for *–meso* substituted porphyrins.

Porphyrins are widespread species in nature, occurring in association with proteins or enzymes as prosthetic groups exemplified by the *heme* center in the photosynthetic apparatus in plants. Structural richness arises from their ability to incorporate metal ions in the macrocycle center generating metalloporphyrins. One example is the photosystem II and I located in green pigment chlorophyll, bearing a magnesium (II) porphyrin in its photoactive sites modified with a saturated

hydrocarbon tail.⁴¹ Different types of substituents in the porphyrin ring give rise to several kind of chlorophylls (a, b, c, d).⁴²

In addition, there are two axial positions which can be occupied by ligands such as H₂O, nitrogen bases (e.g. imidazole, pyridine) and sulfur ligands (thiol, thioether). Such axial positions are relatively labile, and provide the reactive sites for catalysis, modulated by the nature of the metal ion, as well as by the existing ligands and the chemical environment. In the heme proteins, the nature of the axial ligands modulates the redox potentials of the iron center. For instance, thiol groups (e.g. from cysteine) decrease the redox potentials to very negative potentials. This effect facilitates electron transfer with O₂, in order to generate a ferryl group, Fe^{IV}=O, making the powerful oxidizing center of cytochrome P-450.

Metalloporphyrins can also be found performing transport roles such as the hemoglobin protein which carries oxygen and carbon dioxide in the bloodstream using the prosthetic *heme* group. In this case, there is an iron (II) protoporphyrin stabilized by a proximal histidine residue in each of its four subunits, being able to bind up to four oxygen molecules per hemoglobin protein. Oxygen uptake-release has been extensively studied, showing a strong dependence with oxygen partial pressure and pH, upon oxygen coordination the iron atom changes its electronic state to Fe(III) promoting a structural change along hemoglobin favoring the oxygen uptake by the other deoxygenated subunits, process known as allosteric collaboration. Electronic properties of this protoporphyrin are enhanced by the iron (II) center coordination chemistry, which induces symmetry shifts and therefore changes in the electronic state, readily observed by the notable the color difference

between oxygenated (arterial) and deoxygenated (venous) blood, going from red to violet.⁴³

The versatility of the *heme* group is not only restricted to transport mechanisms but to catalytic and transduction processes as well, such cases are illustrated by cytochromes P450, cytochrome C oxidase, cytochrome (a, b, c), catalases and peroxidases. In all of these enzymes, the coordination chemistry of the iron (II) center is ruled by the axial ligands, one of them being typically an amino acid residue of the peptide chain, playing a key role by triggering/preventing the different mechanisms involved in the catalysis, transport or electron transfer processes. Such fine tuning of the Fe(II) redox environment made by the coordinated axial ligands could lead to multiple effects in enzyme activity as shown by Pletneva et al. by removing the glycine residue from the Fe(II) coordination sphere in a cytochrome C clone, lowering the iron reduction potential and accelerating electron transfer kinetics with suitable redox partners.⁴⁴

Supramolecular Porphyrins

Supramolecular porphyrins have been widely studied since early 1990's by Toma and coworkers. This kind of super molecules bears a TPyP (Figure 8) core which is capable of coordinating four metal complexes with its pyridine moieties. As it will be further discussed, the nature of this peripheral complexes (metal oxidation state and ligands) will dictate the properties exhibited by the metal porphyrin core.

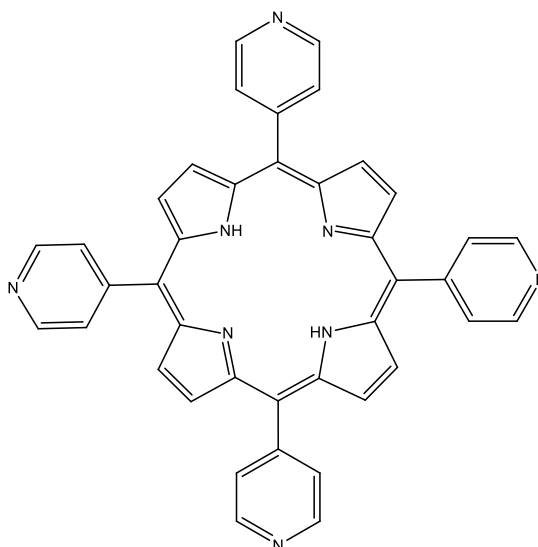


Figure 8. Schematic representation of 5,10,15,20-tetrapyrridylporphyrine (TPyP).

Ruthenium rich coordination chemistry towards N-heterocyclic ligands allowed the synthesis and purification of TPyPs decorated with $[\text{Ru}_3\text{O}(\text{Ac})_6(\text{py})_2]^+$ (further denoted as TCPs), a trinuclear μ_3 -oxoruthenium acetate cluster affecting the chemistry of the metal within the porphyrin core, which is heavily influenced by the ruthenium oxidation states. Thus, zinc became object of interest due to the ability to fine tune their axial coordination chemistry as shown by Toma and coworkers employing a ZnTCP.⁴⁵ For this case its electrochemical and binding properties were of special interests due to the lack of zinc based redox processes in the working potential window allowing a direct correlation between the ruthenium clusters electronic density and its effect on the metal porphyrin center coordination chemistry. In this manner, spectrophotometric titrations were carried out in DCM employing ACN, pyridine and imidazole as coordinating agents. Variations in the Soret band absorptions showed bathochromic shifts ranging from 4 to 10 nm, furthermore all of the titrations exhibited a well-defined isosbestic point proving an equilibrium of two species. Association constants for these N-donor ligands were found to be larger than those for the ZnTPP and ZnTPyP confirming the electron withdrawing nature of

the $[\text{Ru}_3\text{O}(\text{Ac})_6(\text{py})_2]^+$ residues, decreasing the electronic density in the porphyrin ring and therefore augmenting the acidic behavior of the Zn(II) ion.

The bulky nature of the μ_3 -oxoruthenium clusters was further investigated by Toma and his group and a direct effect in the electronic coupling was observed when two TPyP isomers were employed.⁴⁶ For instance, molecular calculations pointed out a difference between the $\text{H}_2(3\text{-TCP})$ and $\text{H}_2(4\text{-TCP})$ (structures shown in Figure 9) of three possible conformations for the former isomer and just one linear conformation for the latter. Also, the molecular diameters differ by 0.4 nm going from 3 nm in the 3-TCP to 3.4 nm in the 4-TCP isomer. Electronic spectra afford interesting information for the 3-TCP species with a low Soret band broadening along with narrow bandwidths indicating poor electronic coupling due to the steric hindrance of the ruthenium clusters towards the bridging pyridine rotation. This behavior is confirmed by the IPCE spectra of DSSCs assembled with these supramolecules, exhibiting poor monochromatic efficiency in the NIR wavelengths by the 3-TCP isomer and comparable performance in the visible range with the 4-TCP species, proving that mainly the porphyrin moiety is responsible for electron injection in the TiO_2 conduction band.

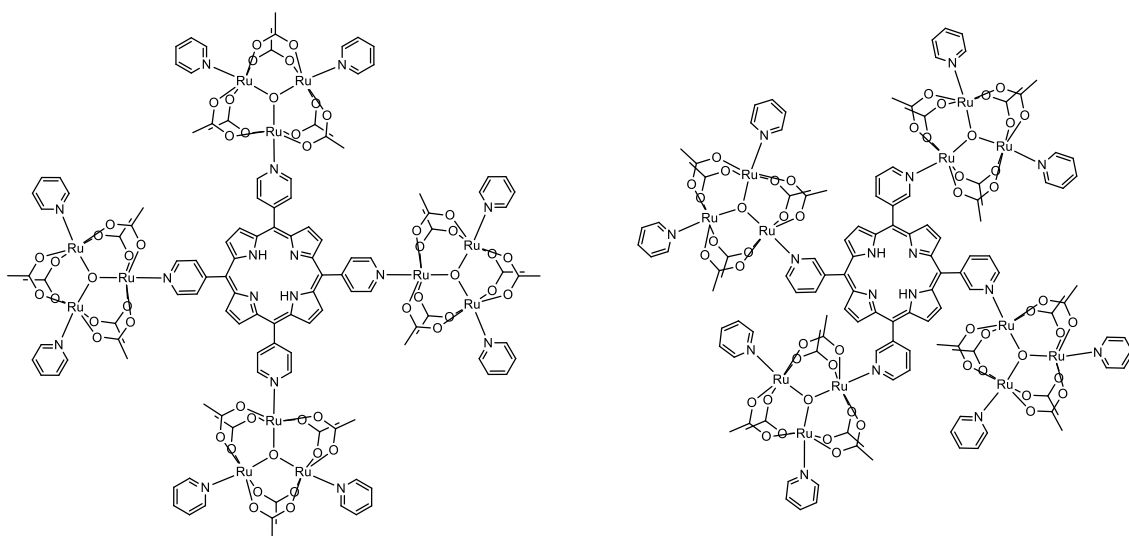


Figure 9. Schematic representation of H2(4-TCP) left and H2(3-TCP) right.

The interest generated by these types of supramolecular porphyrins brought new synthetic and characterization challenges for researchers. For that reason, new techniques and simultaneous combination of them have been brought to help and resolve structural issues.

Travelling wave ion mobility mass spectrometry (TWIM-MS) managed to resolve isomeric polyruthenated porphyrins bearing $[\text{Ru}^{\text{II}}(\text{bpy})_2\text{Cl}]^+$ complexes as shown by Eberlin and coworkers.⁴⁷ These isomers varied from *meta/para* (position of the nitrogen atom in the coordinating pyridine), *cis/trans* for diruthenated porphyrins and multi ruthenation ranging from 1 to 4 ruthenium complexes around the porphyrin core. The results showed very interesting features about the spatial organization of the *meta/para* isomers with the former presenting shorter drift times due to its more compact structure. Ruthenation degree also plays an important role when the species are injected into the travelling wave column, since increasing the complexes increases the net charge by 1+, this is evidenced by shorter drift times with increasing complexation.

Polymetallated Porphyrins in Photochemistry and Photobiology

The outstanding electron transfer properties in porphyrins have been targeted by multiple studies trying to mimic natural photosynthesis. Since chlorophylls are well organized structures some researchers have tried to approach electron transfer systems by fixing porphyrins in defined networks, in this manner Hupp and coworkers,⁴⁸ synthesized two MOFs bearing two different Zn-porphyrin moieties named DA-MOF and F-MOF showing significantly anisotropic electron transfer along the crystalline network with an exciton hop distance of 2000 and 8 chromophores respectively. This difference in exciton migration was attributed to low electronic symmetry and enhanced linear conjugation which translates in higher oscillator strengths and absorption-emission spectra overlap favoring a better dipolar coupling making this material interesting for solar harvesting energy devices.

Following this reasoning, conscious porphyrin design could lead to very efficient structures and arrangements for dye sensitized solar cells (DSSCs).^{49,50,51} In this manner, Grätzel and coworkers,⁵² designed a push-pull Zn-porphyrin (SM315) achieving 13 % overall cell efficiency surpassing their previous record of 11.9 % with the YD2-o-C8 porphyrin based dye.⁵³ Within its structure, a bulky amine donor group was proved compatible with $\text{Co}^{\text{III}}/\text{Co}^{\text{II}}$ electrolytes yielding high open circuit photovoltages. The acceptor moiety a benzothiadiazole benzoic acid residue afforded good panchromatic behavior without co-sensitization by broadening the Soret band and red-shifting it in order to absorb higher wavelengths.

Hybrid materials for solar conversion devices have attracted much attention since metalloporphyrin's spectral and electron transfer properties can be exploited in a synergistic path,⁵⁴ an example with Perovskites is shown by Vasilopoulou and

coworkers,⁵⁵ by depositing a Zn-Porphyrin based layer between the nanocrystalline TiO₂ layer and the MAPbI₃ film. This modification to the PSC improved the maximum power conversion efficiency (PCE) from 15.01 % in the reference cell to 16.87 % in the porphyrin device. Also, a stability increase was observed in the modified cell with retention of 86% of the initial PCE after 200 h of irradiation.

These organic based dyes drew attention and paved the way for coordination-based porphyrins. Such as observed in the electron transfer from the [Ru^{II}(dmbpy)₂Cl]⁺ complexes to a ZnTPyP core, these ruthenium species were used as electronic pumps by Toma et al. to increase the overall cell efficiency when compared to non ruthenated porphyrin dyes.⁵⁶ The structural design of this supramolecule led to an electronic asymmetry favoring the electron injection from the dye into the TiO₂ CB. Consequently, generating some cooperative effects such as aggregation inhibition and electron-hole pair effective separation due to HOMO-LUMO spatial parting within the molecular structure.

Biological applications supramolecular porphyrins have also been pursued as shown by Ravanat and coworkers in 1998,⁵⁷ with the supramolecular μ -[meso(tetrapyrrolyl)porphyrin] tetrakis[bis(bipyridine)(chloro) ruthenium(II)] and its metallated zinc analogue as potential photosensitizers for PDT, aiming for DNA damage using 2'-deoxyguanosine as model. Since two degradation pathways may take place: radical (Type I) or singlet oxygen (Type II) mechanisms different decomposition/oxidation products were monitored, showing a preference for the latter path by both the free base and zinc tetra-ruthenated porphyrins.

With such promising results, Araki et al. in 2000 performed studies with this tetra-ruthenated ZnTPyP (ZnTRP) in order to bind and produce a photoinduced

oxidation of calf-thymus DNA.⁵⁸ With this scope, UV-vis and luminescence experiments were carried out showing two types of interaction between the tetraruthenated porphyrin and DNA depending on the latter concentration. This being a less specific interaction among the $[\text{Ru}^{\text{II}}(\text{bpy})_2\text{Cl}]^+$ residues with DNA in the low concentration range due to higher proportion of the supramolecular ZnTRP species, but at increasing DNA concentrations the interactions become more specific since the porphyrin molecules approach DNA grooves in a fashion where only two vicinal $[\text{Ru}^{\text{II}}(\text{bpy})_2\text{Cl}]^+$ complexes can interact. 2'-deoxyguanosine was the chain residue targeted, showing a preferential oxidative pathway upon $\text{O}_2(^1\Delta_g)$ generation under light conditions with better performance when compared with the isolated 2'-deoxyguanosine.

Polymetallated Porphyrins in Redox Catalysis

Activation of small molecules has been of remarkable interest thru porphyrins rich coordination chemistry.⁵⁹ Rhodium has offered a powerful chemistry in C-H bond activation and hydroformylations among others.^{60, 61, 62} Therefore, its coordination compounds with porphyrins have been widely studied and one of the most interesting examples are the bimetallated porphyrin species bearing two rhodium (II) centers within the same porphyrin ring forming the compound $(\text{TTP})\text{Rh}_2(\text{CO})_4$, since the hollow between the pyrrole rings cannot contain both rhodium atoms, they are disposed above and under the porphyrin plane coordinated by two pyrrole rings each.⁶³

Porphyrin mediated catalysis have also taken part in the quest for cleaner and greener fuels among the reactions aimed by researchers we can cite water splitting (oxidation) or OER, being cobalt,^{64,65} nickel⁶⁶ and manganese⁶⁷ porphyrins one of

the most extensively studied. However, the four-electron transfer along with the oxygen-oxygen bond formation lay a challenge both kinetically and thermodynamically. This can be identified in the large overpotentials required for oxygen evolution to occur, typically ranging from 1.0 V to 1.3 V depending upon metal oxidation state and working pH.^{64, 66, 67, 68} Several approaches both electrochemical or photo induced electrochemical processes have been tested ever since Fujishima and Honda introduced their photoelectrochemical cell for water oxidation back in 1972,⁶⁹ in order to improve faradaic efficiency and catalyst stability due to singlet oxygen formation.⁷⁰

If water splitting is important towards generating solar fuels, the reverse reaction must be efficiently catalyzed in order to benefit from the hydrogen oxidation energy release. Following the same reasoning, porphyrin catalysts towards oxygen reduction reaction (ORR) must be capable of transferring four electrons to the dioxygen molecule at low overpotentials with effective proton coupled transfers. In this manner, the electronic states of the metals in the porphyrin core must be fine-tuned in order to meet the reaction requirements.⁷¹ Knowing that pH is a key parameter when attempting to improve catalytic response,⁷² certain metals have shown better responses such as iron,⁷³ cobalt,^{74,75} and manganese⁷⁶ once again being the four electron transfer and oxygen-oxygen bond cleavage the determining steps.

One of the first tetraruthenated porphyrins was published by Toma and Araki in 1991.⁷⁷ Describing a novel polynuclear cobalt (III) tetrapyridylporphyrinate decorated with four ruthenium(III)-EDTA ions coordinated to the pyridyl residues with interesting electrochemical behavior towards dioxygen reduction below -0.4 V. The

number of electrons transferred by the polymetallated porphyrin was found to be 1.6 ± 0.2 , suggesting the formation of hydrogen peroxide. This catalytic activity was improved when compared with the free $[\text{Ru}^{\text{III}}(\text{EDTA})(\text{H}_2\text{O})]^-$ complex. Concentration dependent catalytic experiments and stopped-flow kinetic experiments showed a synergistic effect between the cobalt center and the ruthenium complexes for the effective regeneration of the Co(II) active species.

As discussed for the water oxidation catalysts, cofacial porphyrins are also employed in the ORR as reported by Cook and coworkers⁷⁸ by a coordination chemistry approach. They manage to assemble two cobalt (II) tetra(meso-4-pyridyl)porphyrinate (CoTPyP) moieties employing four arene-ruthenium complexes as clips for porphyrin parallel (cofacial) positioning, favoring multielectronic catalysis and enhancing the cobalt (II) catalytic activity when compared with its monomeric analogue. Their study showed and enhanced turnover frequency of the dimeric compound (66 h^{-1}) and a good selectivity towards oxygen formation (90 %) over hydrogen peroxide.

Direct effect of protic and aprotic solvent in the proton coupled electron transfer (PCET) was published by Dey and coworkers⁷⁹ as they synthesized four triazole functionalized ferrocene units bound to an iron (II) porphyrin core. Their finds show an electronic pumping from three ferrocene moieties, being the fourth electron provided by the $\text{Fe}^{\text{II}}/\text{Fe}^{\text{III}}$ process in the porphyrin core when approximately three equivalents of a Brønsted acid is added in aprotic organic solvent. For aqueous media, a potential anticipation dependence upon pH variation is observed in the window used. Moreover, all catalytic responses follow the Koutecky-Levich equation

providing a fit for a four-electron process being the oxygen-oxygen bond cleavage the rate determining step rather than oxygen binding.

These findings encouraged scientist to pursue novel polymetallic TPyP based porphyrins for ORR in fuel cells. Anson and coworkers,⁸⁰ that aiming to the electron transfer from the peripheral groups to the cobalt center used the $[\text{Ru}^{\text{II}}(\text{NH}_3)_5]^{2+}$ complexes as electron donors in order to favor the tetra electronic process involved. Rotating disk electrode experiments showed predominantly formation of water over hydrogen peroxide in the polymetallated species proving remarkable improvement over the non-ruthenated cobalt porphyrin. Their electrochemical measurements from the tetraruthenated porphyrin and its tetra osmium coordinated analogue were crucial to determine the electron transfer mechanism, proved as a back-bonding from the ruthenium to the π -accepting orbitals of the coordinating residue rather than a fast intramolecular electron transfer from the complexes.

Anson's research group continued their electronic inquiries in these series of tetraruthenated cobalt TPyPs and the role of the $[\text{Ru}^{\text{II}}(\text{NH}_3)_5]^{2+}$ complexes in the multielectronic reduction of oxygen. Therefore, they performed several femtosecond analyses in order to stablish the electron transfer kinetics. They confirmed the back-bonding nature of the electronic transfer involving the ruthenium/porphyrin/cobalt moieties and proved the necessity of conjugation between the porphyrin core and the ruthenium complex for effective electron transfer.⁸¹

A glimpse in ORR of a CoTCP was given in 2001 by Araki et al.⁸² when modifying GC electrodes by dip-coating. These electrodes showed outstanding mechanical stability for a multilayered film according to coulometric measurements affording a surface concentration of $3.9 \times 10^{-10} \text{ mol cm}^{-2}$. Reduction of dioxygen to

water was studied employing CV, RDE and RRDE experiments, affording a reduction potential of 0.2 V and a tetra electronic process ($n = 4$) revealed by the Levich plot. Finally, some mechanistic insights were provided by RDE and RRDE measurements exhibiting that reaction rate is not limited by either mass transport or electron diffusion in the film, and no significant ring current indicating that almost all dioxygen molecules were reduced to water. It was brought to their attention that high reaction rates and high current densities arose from the activation of the cobalt core by the peripheral ruthenium clusters and their role in the solid state packing, which may favor O_2 diffusion thru the film due to the clusters bulkiness.

TCPs showed interesting electrochemical properties due to the possibility to control the electronic density over the ruthenium clusters with an applied potential.⁸³ This type of control will reflect in a strong shift in the metal center character (oxidizing or reductant) and in the net charge of the supramolecule making it prone to ion pairing with other species such as phthalocyanines and other porphyrins.

After the synthesis of the free base TCPs, the manganese (III) metallated species (MnTCP) was obtained by Toma and coworkers,⁸⁴ with the aim to control the Mn-porphyrin core electronic properties with the ruthenium oxidation state in the peripheral clusters and its use as a potential mimic of cytochrome P-450. Significant electronic coupling was observed by means of CV and spectroelectrochemistry when the four ruthenium clusters were oxidized to their Ru(IV,III,III) state at $E_{1/2} = 1.167$ V and corroborated by the unusually $E_{1/2} = 0.20$ V found for the $Mn^{2+/3+}$ process, shifted towards more positive potentials when compared with nonruthenated MnTPyP. Catalytic activity of MnTCP and MnTPyP was tested towards epoxidation of

cyclooctene and oxidation of cyclohexane employing iodosylbenzene as oxygen atom donor.

Interestingly for cyclooctene epoxidation, MnTCP and MnTPyP showed similar performance based on iodosylbenzene yield around 80%. Whereas for cyclohexane oxidation MnTPyP catalyzed the formation of cyclohexanone and cyclohexanol with 13% and 27% yield respectively. On the other hand, MnTCP produced only cyclohexanol (45%). Moreover, the possible action of a high valence $O=Mn^V$ TCP species was also studied using a flow-cell device and UV-vis spectra, shedding lights of a formal potential for the $O=Mn^V$ TCP/ $O=Mn^{IV}$ TCP higher than 1.17 V meaning that all peripheral clusters are in their oxidized $Ru^{IV}Ru^{III}Ru^{III}$ state, suggesting a mechanism where oxygen and electron transfer processes are concerted.

Not only oxygen and water were aimed as potential substrates for catalysis. Promising results fueled the search for new polymetallated porphyrins bearing different types of peripheral complexes, one of them was $[Ru^{II}(bpy)_2Cl]^+$ as reported in 1995 by Araki et al.⁸⁵ for its use in modified electrodes towards reducing analytes sensing. These electrodes were employed in nitrite and sulfite sensing by means of cyclic voltammetry and FIA experiments showing very good results with detection limits ranging from 2×10^{-7} to 8×10^{-7} mol L⁻¹ for nitrites and 2×10^{-6} to 8×10^{-6} mol L⁻¹ for sulfites at 0.93 V. It was noticeable that potentials shifts took place depending on the anion tested, suggesting specific interactions between the analyte and the CoTPyP.

Polymetallated Hetero-Hybrid Catalysts

Composites bearing porphyrins as active components within their structures have been studied as heterogeneous water oxidation catalysts for increased stability and catalytic activity as shown by Chen and coworkers⁸⁶ by incorporating a

sulfonated Mn-porphyrin into a poly(terthiophene) layer. The sole manganese porphyrin is inactive towards OER, but its close interaction with its relatives within the polymer chains triggers the catalytic activity suggesting a Mn-Mn mediated catalysis; furthermore, experiments performed employing saltwater showed preference towards oxygen (O₂) evolution rather than chlorine (Cl₂) making it a possible material for water splitting using sea water.

Moreover, hybrid materials (composites) have been targeted as potential replacements for Pt based cathodes for fuel cells. Being graphene oxide an attractive candidate as shown by Loh and coworkers,⁸⁷ synthesizing an iron (II) tetracarboxyphenyl porphyrin (TCPP) MOF on a pyridine functionalized reduced graphene oxide (rGO) sheet. When compared to the bare glassy carbon (GC) electrode and non-functionalized GO and rGO composites containing the same Fe(II)TCPP subunit, the pyridine based composite showed a better crystallinity (depending upon pyridine functionalization percentage) favoring a four electron process and an enhanced stability towards methanol poisoning when tested in a direct methanol fuel cell.

Tetraruthenated porphyrin ion pairing films for modified electrodes suitable for FIA tests were assembled as hetero-hybrid catalysts by Toma and coworkers.⁸⁸ This approach yielded mechanically strong and stable films over glassy carbon electrodes when employed the μ -meso(tetrapyrindyl)porphyrinatecobalt(III)tetrakis[bis(bipyridine)(chloro)ruthenium(II)] as the cationic moiety and meso-tetra(4-sulphonatephenyl)porphyrinatezinc(II) as the anionic counterpart. These electrostatically assembled films showed the same detection limits for sulfite (10^{-6} mol L⁻¹) and nitrites (10^{-7} mol L⁻¹) as previously

reported, but the ion pair film modified electrodes performed without sensitivity losses for a week due to higher mechanical stability and lower solubility in the working media.

Recently free base TPyP has been used by He and coworkers⁸⁹ in LB films employing PMA for modified electrodes showing results towards organic dye (methyl orange) degradation and photocurrent generation, although some stability improvements over the electrode surface must be performed to avoid porphyrin solubilization in aqueous media.

In 2015 electropolymerization of a tetraruthenated nickel(II) TPyP (NiTRP) over a GC electrode was elucidated employing EPR and Raman spectroelectrochemistry proving useful characterization techniques.⁹⁰ UV-vis spectrophotometry of a deposited film of electro polymerized NiTRP pointed a π -stacked material from the bands bathochromic shifts. Therefore, to clarify the formation mechanism, electrochemical CV measurements led to the hypothesis of hydroxyl radical formation, species involved in the electropolymerization process. EPR experiments became handy for proving this hypothesis, since hydroxyl radicals can be trapped using DMPO and their adduct clearly detected by the experiments performed sustaining the idea of radical output due to a $[\text{Ru}^{\text{III}}(\text{bpy})_2\text{Cl}(\text{pyp})]^{2+}$ mediated process. In order to identify the linking residue responsible for polymeric chain growth Raman spectroscopy raised answers about the possibility of μ -peroxo bridges as peaks at 1234 and 206 cm^{-1} appeared as the polymerization cycles proceeded.

As scientists, once a molecule structural nature is unveiled, a proper application that exploits its features is easier to find. This is why not long after the

elucidation of the poly-NiTRP structure Angnes and coworkers showed linear electro oxidation behavior when the μ -peroxo polymetallated porphyrin polymer was employed as an amperometric BIA sensor for folic acid with high reproducibility and a detection limit as low as $7.37 \times 10^{-7} \text{ mol L}^{-1}$.⁹¹

This literature search pointed out the importance in attempting the resemblance of nature compounds with the molecules being synthesized in the laboratory. In this manner, we focused our efforts to mimic electrocatalytic supramolecular porphyrins employing polypyridine ruthenium complexes as electronic tuning moieties for the cobalt (III) porphyrin core. By doing this conscious design we manage to obtain compounds capable of reducing dioxygen in a four electron fashion and oxidizing isoniazid, showing promising performance for device building.

OBJECTIVES

In the development of this thesis, several complexes and supramolecular compounds were synthesized and studied in terms of their chemistry, photochemistry, electrochemistry and electronic properties. In total four molecules being one mononuclear ruthenium complex with molecular formula $[\text{Ru}^{\text{II}}(\text{McTerpy})(\text{dmbpy})(\text{TMT})]\text{PF}_6$, a mixed-valence complex $[\text{Ru}^{\text{III}}(\text{NH}_3)_5(\mu_2\text{-dpypn})][\text{Fe}^{\text{II}}(\text{CN})_5]$ and two supramolecular tetraruthenated porphyrins $\{[\text{Ru}^{\text{II}}(\text{dmbpy})\text{Cl}]_4\text{Co}^{\text{II}}\text{TPyP}\}(\text{TFMS})_5$ and $\{[\text{Ru}^{\text{II}}(\text{dcbpy})\text{Cl}]_4\text{Co}^{\text{II}}\text{TPyP}\}\text{Cl}_5 \cdot 12\text{H}_2\text{O}$ were studied.

The mononuclear ruthenium complex $[\text{Ru}^{\text{II}}(\text{McTerpy})(\text{dmbpy})(\text{TMT})]\text{PF}_6$ was synthesized for its application in DSSCs. Ligand choice was done with the aim of promoting a vectorial electron transfer to the TiO_2 CB and wider spectral absorption for the McTerpy and dmbpy, this bipyridine was employed also to introduce steric hindrance hence avoiding undesirable electronic recombination with electrolyte species. TMT played an electronic role of widening the spectral absorption range of the complex towards lower energies.

$[\text{Ru}^{\text{III}}(\text{NH}_3)_5(\mu_2\text{-dpypn})][\text{Fe}^{\text{II}}(\text{CN})_5]$ was synthesized as a challenge my advisor Professor Toma brought to me. The scope of this complex was to prove the existence of an IT between the ruthenium/iron couple and the mechanism involved (inner or outer sphere transfer). For this purpose, dpypn ligand played a major electronic and structural role.

The $\{[\text{Ru}^{\text{II}}(\text{dmbpy})\text{Cl}]_4\text{Co}^{\text{II}}\text{TPyP}\}(\text{TFMS})_5$ supramolecular porphyrin was synthesized to exploit the electron injecting properties of the ruthenium complexes with the aim to make the cobalt (II) center suitable for oxygen reduction.

$\{[\text{Ru}^{\text{II}}(\text{dcbpy})\text{Cl}]_4\text{Co}^{\text{III}}\text{TPyP}\}\text{Cl}_5 \cdot 12\text{H}_2\text{O}$ inversely to the dmbpy porphyrin was designed to be active towards oxidative catalysis finding good results towards isoniazid (antibiotic) sensing.

In general terms, the project of these five years of research had the following scopes:

- Synthesize and characterize the polypyridine ligand McTerpy.
- Synthesize and characterize polypyridine ruthenium complexes employing the ligands McTerpy, dmbpy, dcbpy and TMT.
- Assemble and test DSSCs with the ruthenium dye prepared.
- Synthesize and characterize the pentaaminruthenium complexes with formula $[\text{Ru}^{\text{II}}(\text{NH}_3)_5\text{L}](\text{PF}_6)_2$ with L = dpypn.
- Synthesize and characterize the heteronuclear Ru-L-Fe complex, L = dpypn.
- Synthesize and characterize the homonuclear Ru-L-Ru and Fe-L-Fe complexes with L = dpypn
- Synthesize and characterize the $\text{Co}^{\text{III}}\text{TPyP}$ complex.
- Synthesize and characterize the supramolecular porphyrin $\{[\text{Ru}^{\text{II}}(\text{dmbpy})\text{Cl}]_4\text{Co}^{\text{III}}\text{TPyP}\}(\text{TFMS})_5$.
- Assemble and testing of the nanocomposite between $\{[\text{Ru}^{\text{II}}(\text{dmbpy})\text{Cl}]_4\text{Co}^{\text{III}}\text{TPyP}\}(\text{TFMS})_5$ and GO.
- Synthesize and characterize the supramolecular porphyrin $\{[\text{Ru}^{\text{II}}(\text{dcbpy})\text{Cl}]_4\text{Co}^{\text{III}}\text{TPyP}\}\text{Cl}_5 \cdot 12\text{H}_2\text{O}$.
- Synthesize and characterize the nanocomposite bearing the coordination polymer $\{[\text{Ru}^{\text{II}}(\text{dcbpy})\text{Cl}]_4\text{Co}^{\text{III}}\text{TPyP}\}\text{Cl}_5 \cdot 12\text{H}_2\text{O}$ -Ni with GO.
- Test the nanocomposite $\{[\text{Ru}^{\text{II}}(\text{dcbpy})\text{Cl}]_4\text{Co}^{\text{III}}\text{TPyP}\}\text{Cl}_5 \cdot 12\text{H}_2\text{O}$ -Ni/GO.

EXPERIMENTAL SECTION

Equipment

CHN analyses were obtained in a Perkin Elmer – CHN 2400 instrument from the institute's Analytical Center.

FTIR spectra was recorded in a Bruker (Germany) spectrophotometer model Alpha (Project FAPESP 2009/08584-6), equipped with four sampling modules. Transmittance, Attenuated Total Reflectance (ATR, with Ge or ZnSe crystal), Multi-ATR (with a 50x5 mm slit and ZnSe crystal) and DRIFT.

In the transmittance module, KBr ($\geq 99.0\%$) tablets dried to 0.5 % m/m and homogenized with an agate pestle and mortar. Tablets were pressed with 8 ton cm^{-2} for 10 minutes under vacuum, yielding 13 mm diameter disks.

UV-vis absorption spectra were recorded in an Agilent HP8453A diode-array spectrophotometer in the 190-1100 nm range and 1 nm resolution.

UV-vis absorption spectroelectrochemistry were performed using a custom-built electrochemical cell consisting of a gold minigrad working electrode, Ag/Ag⁺ reference and a platinum wire auxiliary electrode mounted inside a quartz cuvette with a path length 0.025 mm. Potentials were controlled by an EG&G PAR 173 potentiostat/galvanostat.

Spectrophotometric titrations were performed employing the UV-vis absorption spectrometer described above and employing a 20 mL (0.5 mol L⁻¹ NaCl) solution of the desired complex. pH was swept starting from 13 to 2 employing NaOH and HCl (3 mol L⁻¹) solutions taking care not to alter the total volume. After each NaOH or HCl addition pH was let to stabilize for at least 5 minutes before spectrum collection.

Vis-NIR absorption spectra of solutions and solids were gathered in a spectroradiometer from ASD Inc (USA), FieldSpec3 model equipped with silicon detectors and InGaAs photodiodes. A tungsten source and an optic fiber were employed. This equipment possesses a spectral window from 350 to 2500 nm with a 3 nm resolution.

Electrochemical measurements were collected in an Eco Chemie Autolab PGSTAT30 potentiostat/galvanostat and a conventional three electrode arrange with a GC working electrode, Ag/Ag⁺ and Ag/AgCl (KCl 3 mol L⁻¹ organic media) for aqueous media and a platinum coiled wire as auxiliary electrode. Electrolytes used were tetrabutylammonium hexafluorophosphate and KNO₃ (0.1 mol L⁻¹) for organic and aqueous media respectively.

Raman spectra were obtained in a WITec 300R Alpha confocal microscope, equipped with a suitable laser and an 1800 lines mm⁻¹ grating.

NMR spectra were recorded on a Varian Inova 300 MHz or a Bruker Avance 500 MHz spectrophotometers from the institute's Analytical Center, and using the residual solvent signals as reference.

ESI-MS spectra were acquired in a Bruker Daltonics MicroToF (Institute's Analytical Center) with a direct infusion and 10 kV cone potential.

AFM measurements were collected in a LensAFM (Nanosurf) and a C3000 Controller (Nanosurf) operating at intermittent contact mode, using 190 TAP AI – G cantilevers (Budget Sensors). AFM images were acquired with resolution of 512 pixels per line at a scan rate of 2 Hz, and 60 % of free amplitude vibration as setpoint. These images were processed and analyzed using the Gwyddion software.

I-V curves were obtained from a solar simulator ORIEL (AM 1.5, IEC, JIS, ASTM) with a power calibrated to 100 mW cm^2 employing a Si cell (VLSI standards, Oriel P/N 91150 V).

IPCE measurements were recorded from a Spectro illuminator Oriel 69070 and a multimeter (Wavetek Meterman 5XL).

Emission spectra were collected on a PTI QuantaChrome 300 spectrophotometer employing a 4 faced cuvette at room temperature.

SYNTHESES

Reagents and solvents employed in the following syntheses are analytic grade and purchased from commercial sources (Sigma-Aldrich, Synth, Cromoline, Acros). They were employed as received without any further purifications unless stated otherwise in the individual synthetic procedures.

The McTerpy ligand was synthesized in the laboratory due to its simplicity and straightforward synthetic path.

Synthesis of [2,2':6',2''-terpyridine]-4'-carboxylic acid (McTerpy)

This polypyridine ligand was obtained following the existing methodology.⁹² In a 125 mL round bottom reaction flask equipped with a magnetic bar, 3.44 mL of furfural (0.042 mol) and 9.44 mL of 2-acetylpyridine (0.084 mol) were poured together. Right away, 5.2 g of KOH and 60 mL of NH₄OH (28-30 %) were added to the reaction flask and the reaction was left to proceed for 19 hours under reflux. A dark brown solid was filtered out and recrystallized from an ethanol-water mixture giving a white solid in about 50 % yield. This white solid was filtered and washed with water and diethyl ether and dried under vacuum.

4'-(2-furyl)-2,2':6',2''-terpyridine (FuTerpy) was used as obtained for the next reaction step which is an oxidation of the furyl group employing KMnO₄. In a 200 mL reaction flask equipped with a magnetic stirrer, 1.0105 g of FuTerpy (3.3×10^{-3} mol) were suspended in 100 mL of deionized water and pH was adjusted to 13 using NaOH 99 %. 2.15 g of KMnO₄ (1.34×10^{-2} mol) were added to the slurry and let to reflux for four hours.

After reflux ended, 1.72 g $\text{Na}_2\text{S}_2\text{O}_3$ were added to reduce unreacted permanganate and the MnO_2 was filtered off. Supernatant pH was adjusted to 4 with HCl (36.5-38 %) using a pHmeter to precipitate [2,2':6',2''-terpyridine]-4'-carboxylic acid which was centrifuged and washed three times with pH 4-5 deionized water. The white solid was dried under vacuum affording 0.61 g (67%). Figure 10 summarizes the synthetic pathway followed.

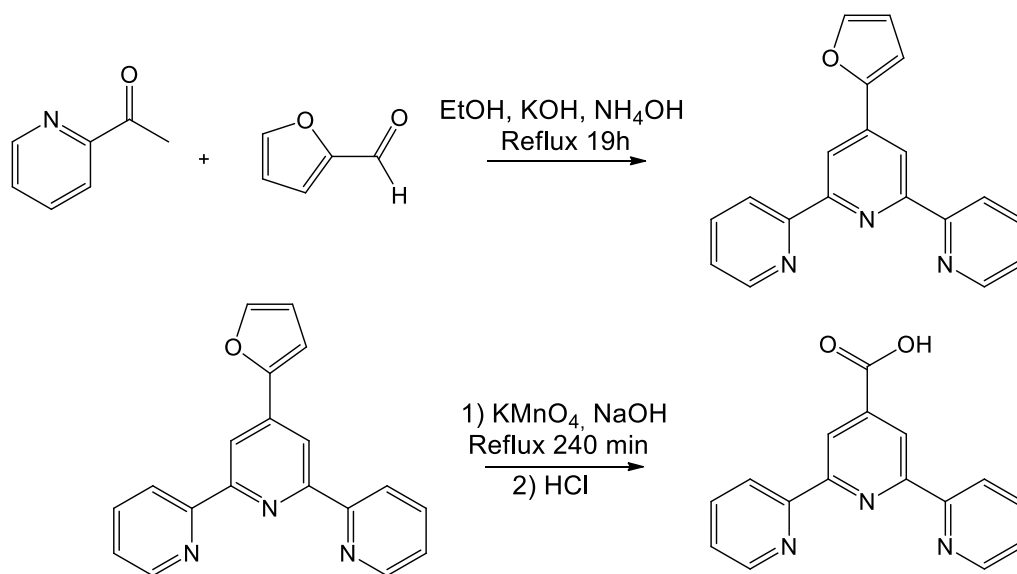


Figure 10. Schematic representation of the synthetic pathway for McTerpy.

Synthesis of $[\text{Ru}^{\text{II}}(\text{McTerpy})(\text{H}_2\text{O})\text{Cl}_2]\cdot\text{H}_2\text{O}$

This complex was synthesized dissolving 1.1064 g of $\text{RuCl}_3\cdot 3\text{H}_2\text{O}$ (4.2×10^{-3} mol) in dinitrogen purged ethanol contained in a 125 mL reaction flask equipped with a magnetic bar. Under a stream of dinitrogen, 1.1765 g of McTerpy (4.2×10^{-3} mol) were added and the reaction mixture was let to reflux for 4 hours. Upon cooldown to room temperature, a red-brown solid precipitated. This solid was centrifuged and washed three times with cold ethanol and an 82 % yield affording 1.9503 g of complex. Figure 11 summarizes the path followed.

%CHN analysis: Exp(Calc) - %C 39.56(39.60) %H 3.19(3.12) %N 7.91(8.66)

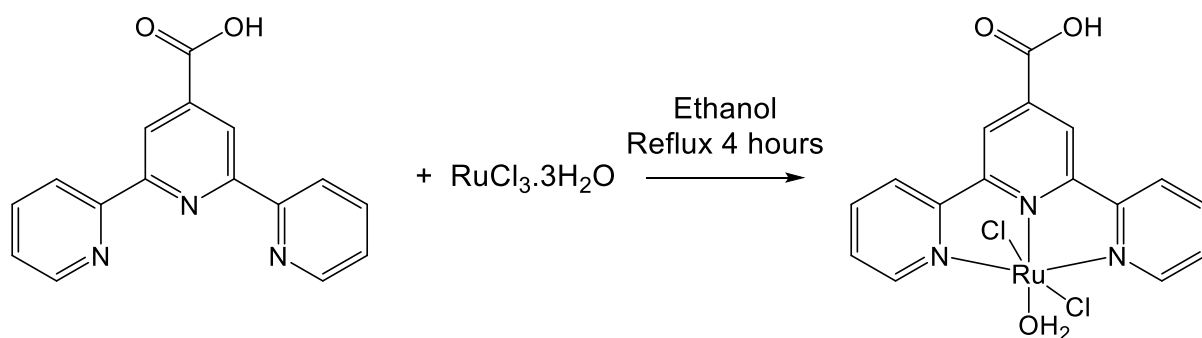


Figure 11. Schematic representation of $[\text{Ru}^{\text{II}}(\text{McTerpy})(\text{H}_2\text{O})\text{Cl}_2]\cdot\text{H}_2\text{O}$ synthesis.

Synthesis of $[\text{Ru}^{\text{II}}(\text{McTerpy})(\text{dmbpy})\text{Cl}]\text{Cl}$

Figure 12 exhibits the synthetic pathway followed. In a 50 mL round bottom flask equipped with a magnetic bar, 174.1 mg (4.1 mmol) LiCl, 200.1 mg (0.41 mmol) $[\text{Ru}^{\text{II}}(\text{McTerpy})(\text{H}_2\text{O})\text{Cl}_2]\cdot\text{H}_2\text{O}$ and 0.5 mL 4-ethylmorpholine were dissolved in 15 mL of methanol/water 5:1 mixture. 76.0 mg (0.41 mmol) dmbpy were added to the stirred solution, and brought to reflux for three hours in the dark. The solution was let to cooldown to room temperature and the crude was dried employing a rotary evaporation. The purple solid was dissolved and loaded into a silica gel column, acetone/methanol/water (3:1:1) saturated with LiCl. The purple fraction was collected and concentrated in the rotary evaporator and 3 mL of concentrated HCl were added, a purple solid precipitated, centrifuged and washed three times with 1 mol L^{-1} HCl. The solid was left to completely dry under vacuum overnight. Yield 45 %.

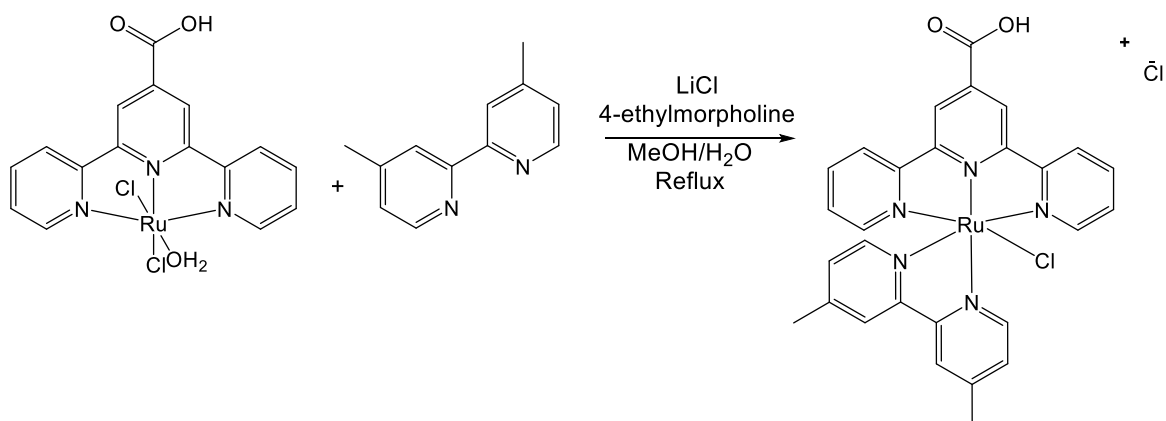


Figure 12. Schematic representation of $[\text{Ru}^{\text{II}}(\text{McTerpy})(\text{dmbpy})\text{Cl}]\text{Cl}$ synthesis.

Synthesis of $[\text{Ru}^{\text{II}}(\text{McTerpy})(\text{dmbpy})(\text{H}_2\text{O})](\text{PF}_6)_2$

Reaction procedure is shown in Figure 13. 150.0 mg (0.24 mmol) of $[\text{Ru}^{\text{II}}(\text{McTerpy})(\text{dmbpy})\text{Cl}]\text{Cl}$ were dissolved in deionized water and 81.2 mg (0.48 mmol) of AgNO_3 were added slowly over the course of four hours under reflux. AgCl formed was centrifuged and discarded after cooling down the reaction mixture. Supernatant was concentrated and the complex precipitated with the addition of NH_4PF_6 , the solid was filtered out, washed carefully with cold water and dried under vacuum overnight. This complex was used without further characterization.

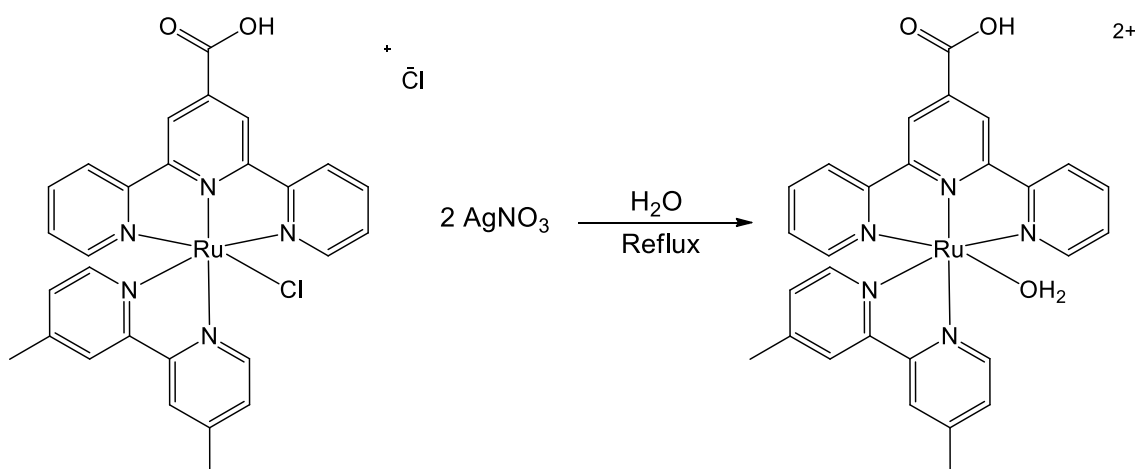


Figure 13. Schematic representation of $[\text{Ru}^{\text{II}}(\text{McTerpy})(\text{dmbpy})(\text{H}_2\text{O})](\text{PF}_6)_2$ synthesis.

Synthesis of $[Ru^{II}(McTerpy)(dmbpy)(TMT)]PF_6$

100.0 mg (0.12 mmol) of $[Ru^{II}(McTerpy)(dmbpy)(H_2O)](PF_6)_2$ were dissolved in 15 mL ethanol and 21.1 mg (0.12 mmol) of TMT were added to the stirred solution and refluxed for 4 hours in the dark. After cooling down, the solvent was removed in the rotary evaporator and the solid dissolved in the minimum amount of DMF. This was added dropwise to a concentrated NH_4PF_6 aqueous solution, the precipitated solid was filtered off and washed carefully with cold water and ether and dried under vacuum.

Further purification was achieved in Sephadex LH-20 column chromatography using methanol as eluent. The solid was loaded and four fractions eluted from the column being the last one to come out the desired complex. The fraction was dried under reduced pressure in the rotary evaporator and overnight under high vacuum. Figure 14 summarizes the procedure followed.

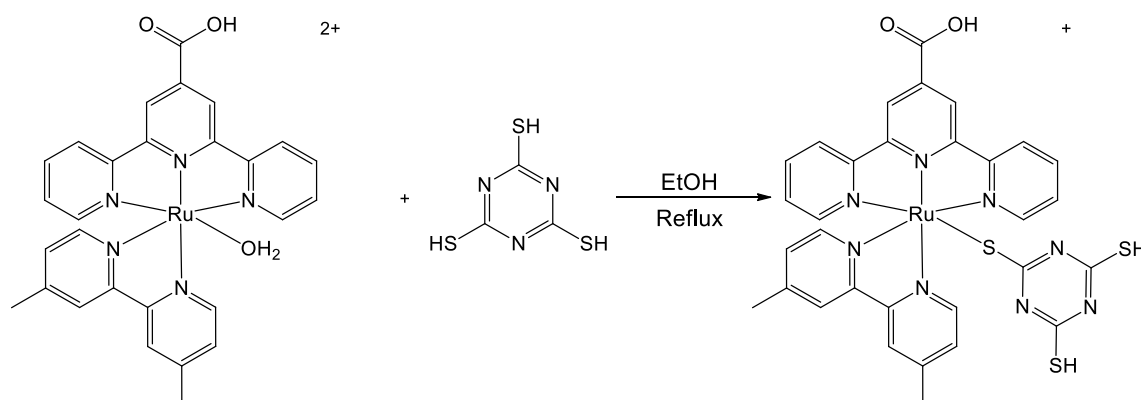


Figure 14. Schematic representation of $[Ru^{II}(McTerpy)(dmbpy)(H_2TMT)]PF_6$ synthesis.

Preparation of $[Ru^{II}(McTerpy)(dmbpy)(H_2TMT)]PF_6$ deprotonated species

Spectrophotometric titration afforded three pKa values in the pH window employed. Therefore, deprotonation species of $[Ru^{II}(McTerpy)(dmbpy)(H_2TMT)]PF_6$

were prepared by adjusting the pH of an aqueous solution of this complex with $(\text{Bu}_4\text{N})_4\text{OH}$ and the species precipitated upon ether addition.

Synthesis of $[\text{Ru}^{\text{II}}(\text{NH}_3)_5(\text{dpypn})](\text{PF}_6)_2 \cdot 3\text{H}_2\text{O}$

The ruthenium and iron precursors $[\text{Ru}^{\text{II}}(\text{NH}_3)_6]\text{Cl}_2$, $[\text{Ru}^{\text{III}}(\text{NH}_3)_5\text{Cl}]\text{Cl}_2$, and $\text{Na}_3[\text{Fe}^{\text{II}}(\text{CN})_5(\text{NH}_3)]$ were synthesized as previously described.^{3,93}

In a two-necked reaction flask equipped with a magnetic bar, 150.0 mg (0.51 mmol) of $[\text{Ru}^{\text{III}}(\text{NH}_3)_5\text{Cl}]\text{Cl}_2$ were dissolved in 15 mL of deionized water and purged with N_2 for 10 min. Then, Hg/Zn amalgam pellets were added to the reaction flask under stirring and N_2 purging. After 5 min, 306.1 mg (1.54 mmol) of dpypn were added and the reaction was allowed to proceed for 12 hours in the dark, after which the amalgam was removed by filtration and the product precipitated by addition of NH_4PF_6 . The yellow solid product was filtered off and washed several times with cold deaerated water and dried in vacuum. Figure 15 exhibits the condensed reaction path followed.

% CHN analysis: Exp(Calc) - %C 20.51(21.43) %H 4.55(4.84) %N 13.35(13.46).

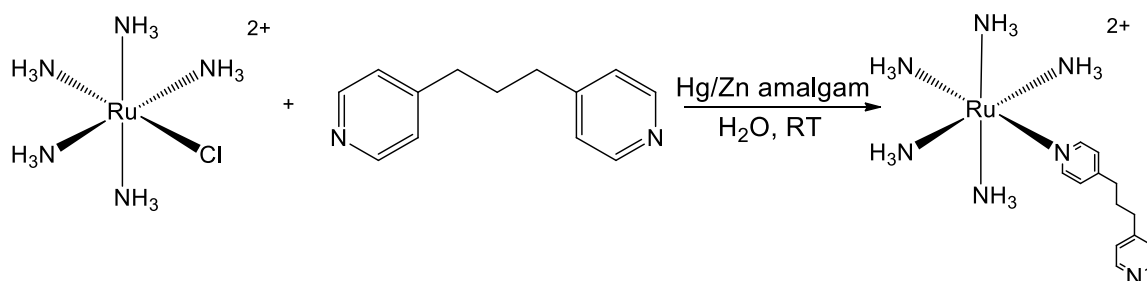


Figure 15. Schematic representation of $[\text{Ru}^{\text{II}}(\text{NH}_3)_5(\text{dpypn})](\text{PF}_6)_2 \cdot 3\text{H}_2\text{O}$ synthesis.

Synthesis of $[\text{Ru}^{\text{III}}(\text{NH}_3)_5(\mu\text{-dpypn})\text{Fe}^{\text{II}}(\text{CN})_5] \cdot 4\text{H}_2\text{O}$

In a two-necked reaction flask equipped with a magnetic bar, 50.1 mg of $[\text{Ru}^{\text{II}}(\text{NH}_3)_5(\text{dpypn})](\text{PF}_6)_2$ (0.069 mmol) were added to 10 mL of deionized water

degassed with N₂. After 5 min, 22.4 mg of Na₃[Fe(CN)₅(NH₃)]·H₂O (0.077 mmol) were added and the mixture was kept under stirring and N₂ atmosphere. After 30 min, the N₂ flow was interrupted and the reaction was let to continue in the presence of air. The initially yellow solution turned into green and then a green solid started to form within ~5 minutes. After the solid was filtered off and washed several times with water and ethyl ether, the final product was dried overnight in vacuum. Attempts to grow single crystals for X-ray studies have been unsuccessful. Figure 16 exemplifies the pathway followed.

% CHN analysis: Exp(Calc) - %C 33.56(33.65) %H 5.71(5.80) %N 23.09(26.16).

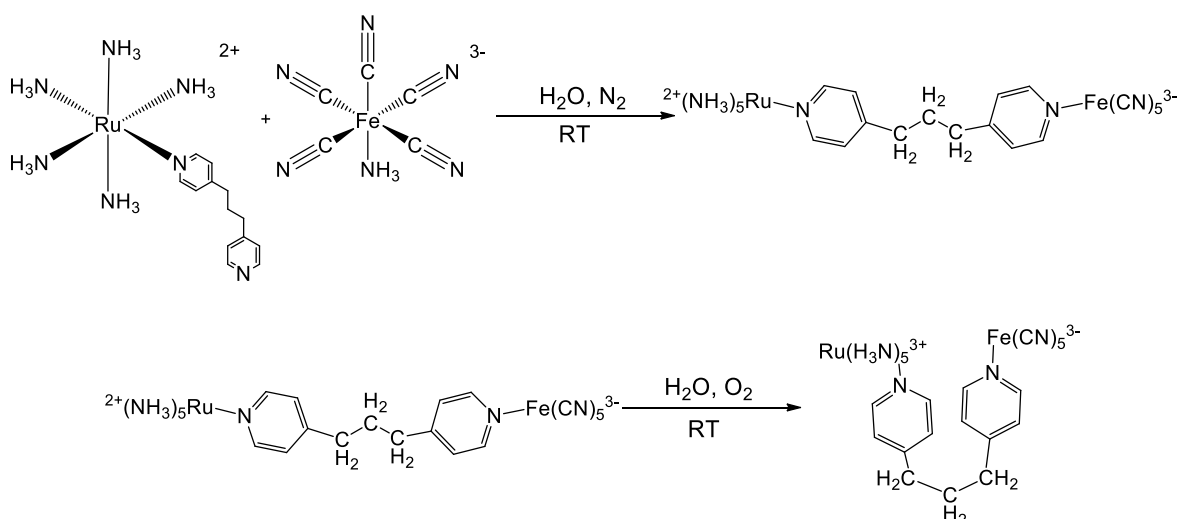


Figure 16. Schematic representation of $[\text{Ru}^{\text{III}}(\text{NH}_3)_5(\mu\text{-dpypn})\text{Fe}^{\text{II}}(\text{CN})_5] \cdot 4\text{H}_2\text{O}$ synthesis.

Synthesis of $[\text{Ru}^{\text{III}}(\text{NH}_3)_5\{\mu\text{-(dpypn}\cdot\beta\text{-CD)}\}\text{Fe}^{\text{II}}(\text{CN})_5]$

The inclusion complex with β -cyclodextrin (β -CD) was prepared *in situ*. Starting with an aqueous solution of $[\text{Ru}^{\text{II}}(\text{NH}_3)_5(\text{dpypn})]^{2+}$ (5.0 mmol L⁻¹) in N₂ atmosphere, an excess of β -CD (10 mmol L⁻¹) was added and the mixture was kept under stirring for 2 h. Then, an stoichiometric amount of $[\text{Fe}^{\text{II}}(\text{CN})_5(\text{NH}_3)]^{3-}$ (5.0 mmol L⁻¹) was added and the mixture was kept under stirring for additional 2 h, in the

presence of air. The reaction yields a stable yellow product that remains fully soluble in water (note that the heterobinuclear complex precipitates in the absence of β -CD). Figure 17 summarizes the procedure performed.

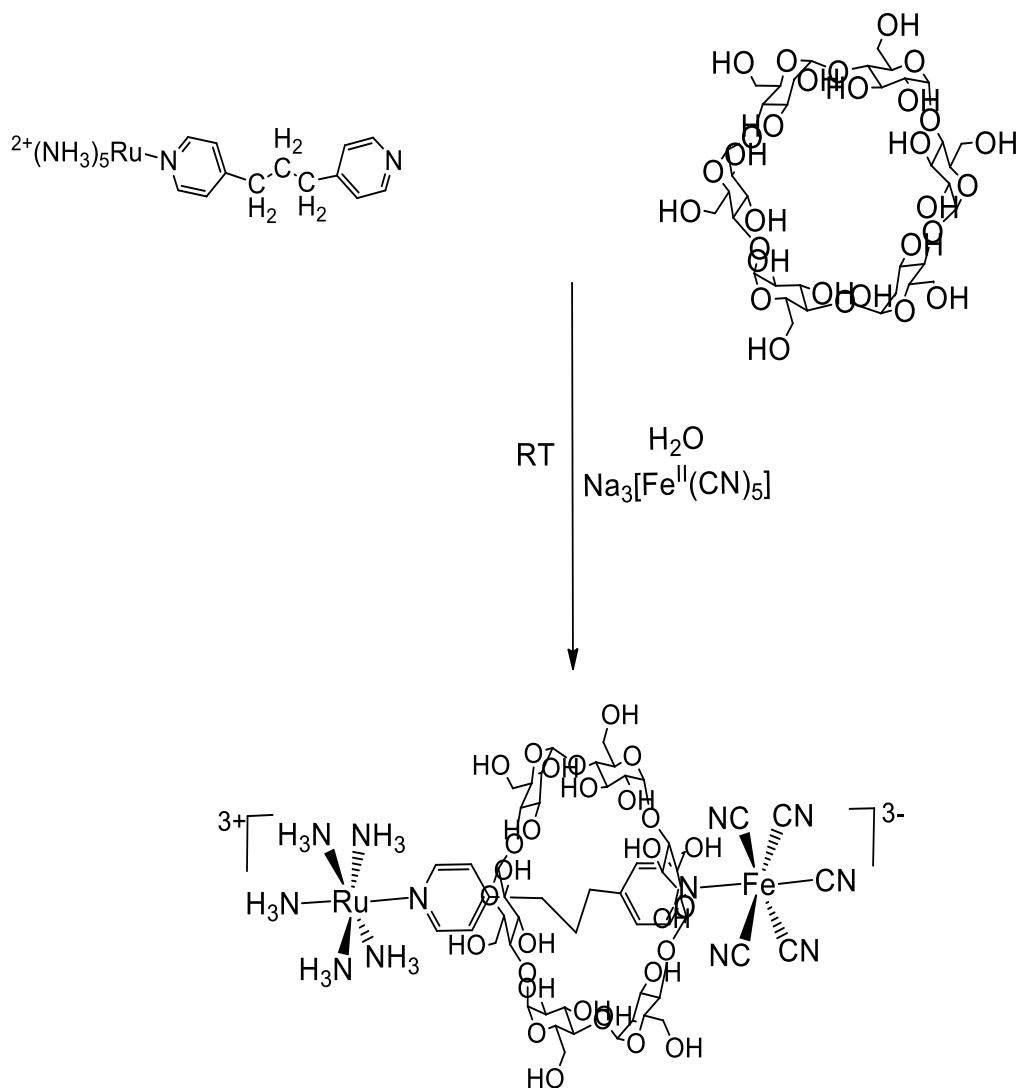


Figure 17. Schematic representation of $[\text{Ru}^{\text{III}}(\text{NH}_3)_5\{\mu\text{-}(\text{dpypn})\cdot\beta\text{-CD}\}]\text{Fe}^{\text{II}}(\text{CN})_5]$ synthesis.

Synthesis of $[\text{Ru}^{\text{II}}(\text{NH}_3)_5(\mu\text{-dpypn})\text{Ru}^{\text{II}}(\text{NH}_3)_5](\text{PF}_6)_4$

In a two-necked reaction flask equipped with a magnetic bar, 150.1 mg (0.51 mmol) of $[\text{Ru}^{\text{III}}(\text{NH}_3)_5\text{Cl}]\text{Cl}_2$ were dissolved in 15 mL of deionized water and purged with N_2 for 10 min. Then, Hg/Zn amalgam pellets were added to the reaction flask under stirring and N_2 purging. After 5 min, 51.0 mg (0.25 mmol) of dpypn were

added and the reaction was allowed to proceed for 12 hours in the dark, after which the amalgam was removed by filtration and the product precipitated by addition of NH_4PF_6 . The yellow solid product was filtered off and washed several times with cold deaerated water and dried in vacuum. Figure 18 exhibits the condensed reaction path followed.

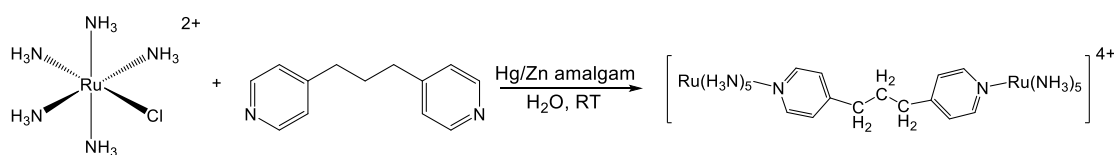


Figure 18. Schematic representation of $[\text{Ru}^{\text{II}}(\text{NH}_3)_5(\mu\text{-dpypn})\text{Ru}^{\text{II}}(\text{NH}_3)_5](\text{PF}_6)_4$ synthesis.

Synthesis of $\text{Na}_6[\text{Fe}^{\text{II}}(\text{CN})_5(\mu\text{-dpypn})\text{Fe}^{\text{II}}(\text{CN})_5]$

In a two-necked reaction flask equipped with a magnetic bar, 150.1 mg (0.52 mmol) of $\text{Na}_3[\text{Fe}^{\text{II}}(\text{CN})_5(\text{NH}_3)]$ were dissolved in 15 mL of deionized water and purged with N_2 for 10 min. After 5 min, 52.0 mg (0.26 mmol) of dpypn were added and the reaction was allowed to proceed for 30 minutes. The yellow solution was employed to perform the desired experiments. Figure 19 exhibits the condensed reaction path followed.

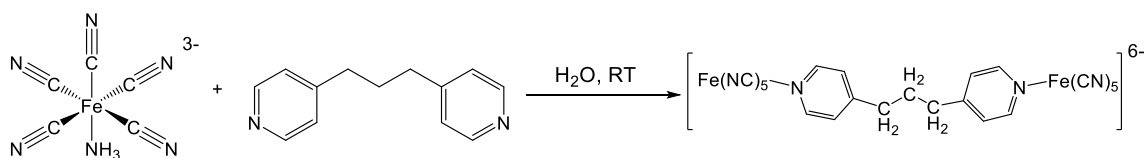


Figure 19. Schematic representation of $\text{Na}_6[\text{Fe}^{\text{II}}(\text{CN})_5(\mu\text{-dpypn})\text{Fe}^{\text{II}}(\text{CN})_5]$ synthesis.

Synthesis of *cis*- $[\text{Ru}^{\text{II}}(\text{dmbpy})_2\text{Cl}_2]$

In a round bottom reaction flask equipped with a magnetic bar, 1.3441 g LiCl (3.2×10^{-2} mol) were dissolved in 35 mL DMF purged with N_2 . With constant stirring, 0.6013 g $\text{RuCl}_3 \cdot 3\text{H}_2\text{O}$ (2.7×10^{-3} mol) and 0.9788 g *dmbpy* (5.3×10^{-3} mol) were added

to the solution. After all the reagents were fully dissolved, mixture was refluxed for 8 hours in the dark under nitrogen atmosphere.

The reaction mixture was left to cooldown at room temperature, and the solvent was removed by rotary evaporation. The violet solid was purified by alumina column chromatography with a dichloromethane/Methanol (20:1) eluent. Solvent was removed in a rotary evaporator and the violet fraction was dried under vacuum, yielding 0.3622 g (50%).

Also, a simpler and effective purification was performed as follows: reaction mixture was left to cooldown at room temperature, and the crude was concentrated by rotary evaporation to its minimum volume. This slurry was added dropwise to an erlenmeyer containing acetone, a purple solid precipitated, it was filtered off employing a sintered glass crucible and washed gently with cold acetone and water. The solid is then dried under vacuum overnight. Procedure is summarized in Figure 20.

% CHN analysis: Exp(Calc) - %C 53.18(53.34) %H 5.06(4.48) %N 10.17(10.37).

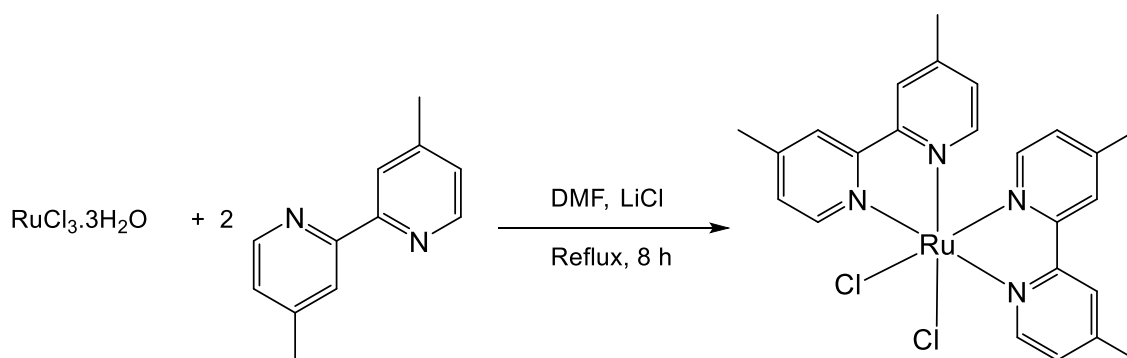


Figure 20. Schematic representation of cis-[Ru^{II}(dmbpy)₂Cl₂] synthesis.

Synthesis of *cis*-[Ru^{II}(H₂dcbpy)₂Cl₂]

In a round bottom reaction flask equipped with a magnetic bar, 1.3446 g LiCl (3.2x10⁻² mol) were dissolved in 35 mL DMF purged with N₂. With constant stirring, 0.6031 g RuCl₃·3H₂O (2.7x10⁻³ mol) and 1.2912 g H₂dcbpy (5.3x10⁻³ mol) were added to the solution. After all the reagents were fully dissolved, mixture was refluxed for 8 hours in the dark under nitrogen atmosphere. The solvent was removed with a rotary evaporator and the solid dissolved in glacial acetic acid and further refluxed for another hour. The crude was dried under vacuum and the remaining solid dissolved/suspended in methanol and magnetically stirred overnight in the dark. The violet precipitate was filtered off and washed gently with cold methanol and ether and let dry under vacuum. Yield 1.5063 g (84%) of the complex. Figure 21 exhibits the condensed reaction pathway.

% CHN analysis for *cis*-[Ru^{II}(H₂dcbpy)₂Cl₂].DMF: Exp(Calc) - %C 43.42(44.21) %H 3.55(3.16) %N 10.10(9.55).

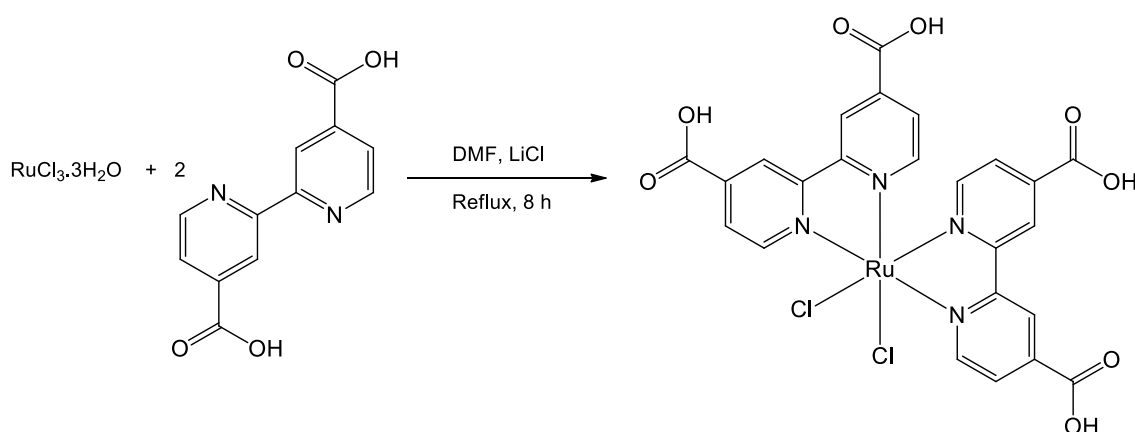


Figure 21. Schematic representation of *cis*-[Ru^{II}(H₂dcbpy)₂Cl₂] synthesis.

Synthesis of Co^{II}TPyP

Figure 22 exhibits the reaction pathway for Co^{II}TPyP synthesis. In a two necked reaction flask equipped with a magnetic bar, 50 mL of DMF were employed

to dissolve 200.1 mg (0.32 mmol) of TPyP, once all the porphyrin was soluble 200.2 mg (0.80 mmol) of cobalt (II) acetate were added to the reaction mixture purged with dinitrogen and refluxed for four hours. The crude reaction was let to cooldown and the solvent was removed using a rotary evaporator, the remaining solid was washed gently with deionized water several times in order to remove cobalt (II) acetate excess. The purple solid was dried under vacuum overnight.

% CHN analysis: Exp(Calc) - %C 70.53(71.11) %H 3.78(3.58) %N 16.15(16.59).

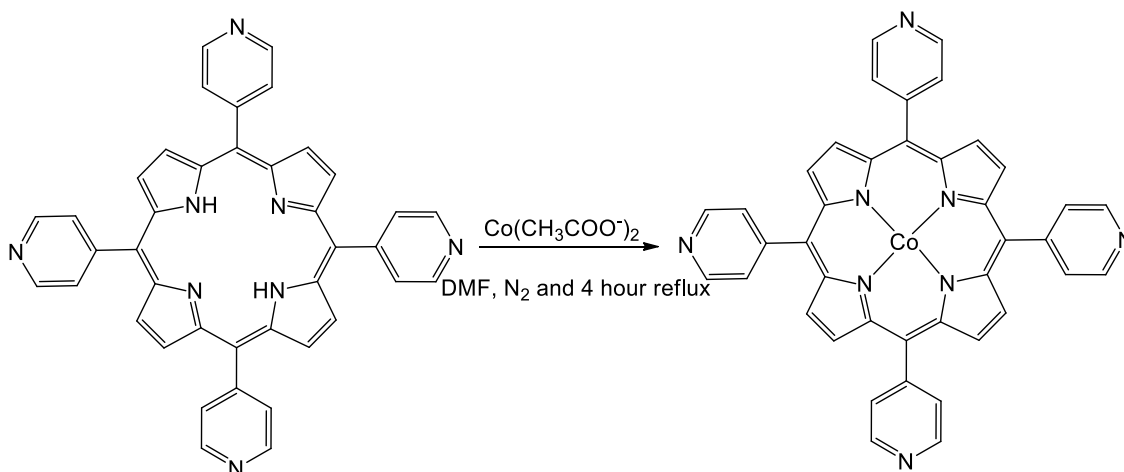


Figure 22. Schematic representation of Co^{II}TPyP synthesis.

Synthesis of Co^{III}TRP(dmbpy)

Supramolecular Co^{III}TRP(dmbpy) species was synthesized as described in literature and shown in Figure 23.⁸⁵ In a round bottom reaction flask equipped with a magnetic bar, 200.2 mg (0.30 mmol) of Co^{II}TPyP were dissolved in 30 mL of glacial acetic acid. Once the porphyrin was in solution, 681.0 mg (1.26 mmol) of *cis*-[Ru^{II}(dmbpy)₂Cl₂] was added to the reaction mixture and refluxed for one hour. The solvent was removed employing a rotary evaporator and the residue redissolved in methanol and refluxed for another hour. Solvent was taken out with the rotary evaporator and the solid redissolved in the minimum amount of DMF this solution

was added dropwise to a saturated LiTFMS aqueous solution. The precipitated dark brown solid was filtered off and washed gently with cold water.

For purification, the $\text{Co}^{\text{III}}\text{TRP}(\text{dmbpy})$ species bearing the TFMS^- counterion was dissolved in the minimum amount of methanol and precipitated by addition to a saturated LiCl acetone solution. The solid was washed with cold acetone and successive anion exchange between TFMS^- and Cl^- was performed in order to remove $\text{cis-}[\text{Ru}^{\text{II}}(\text{dmbpy})_2\text{Cl}_2]$ excess. The final $\text{Co}^{\text{III}}\text{TRP}(\text{dmbpy})$ compound exhibits five TFMS^- counterions.

% CHN analysis for $\{[\text{Ru}^{\text{II}}(\text{dmbpy})_2\text{Cl}]_4\text{Co}^{\text{III}}\text{TPyP}\}(\text{TFMS})_5 \cdot 4\text{H}_2\text{O}$: Exp(Calc) - %C 47.82(48.21) %H 3.84(3.67) %N 9.75(9.57).

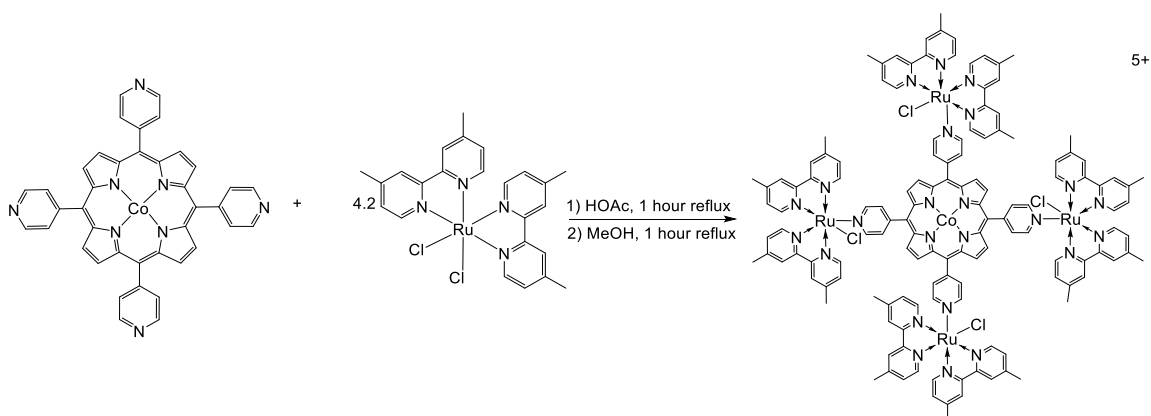


Figure 23. Schematic representation of $\text{Co}^{\text{III}}\text{TRP}(\text{dmbpy})$ synthesis.

Synthesis of $\text{Co}^{\text{III}}\text{TRP}(\text{H}_2\text{dcbpy})$

Supramolecular $\text{Co}^{\text{III}}\text{TRP}(\text{H}_2\text{dcbpy})$ species was synthesized as described in literature and shown in Figure 24.⁸⁵ In a round bottom reaction flask equipped with a magnetic bar, 200.0 mg (0.30 mmol) of $\text{Co}^{\text{II}}\text{TPyP}$ were dissolved in 30 mL of glacial acetic acid. Once the porphyrin was in solution, 821.1 mg (1.24 mmol) of $\text{cis-}[\text{Ru}^{\text{II}}(\text{H}_2\text{dcbpy})_2\text{Cl}_2]$ was added to the reaction mixture and refluxed for one hour. The

solvent was removed employing a rotary evaporator and the residue redissolved in methanol and refluxed for another hour. The reaction mixture was allowed to cool down to room temperature forming a dark brown precipitate. This solid was filtered off, washed several times with methanol and dried under vacuum overnight.

% CHN analysis for $\{[Ru^{II}(H_2dcbpy)_2Cl]_4Co^{III}TPyP\}Cl_5 \cdot 12H_2O$: Exp(Calc) - %C 45.74(45.77) %H 3.90(3.16) %N 9.69(9.42).

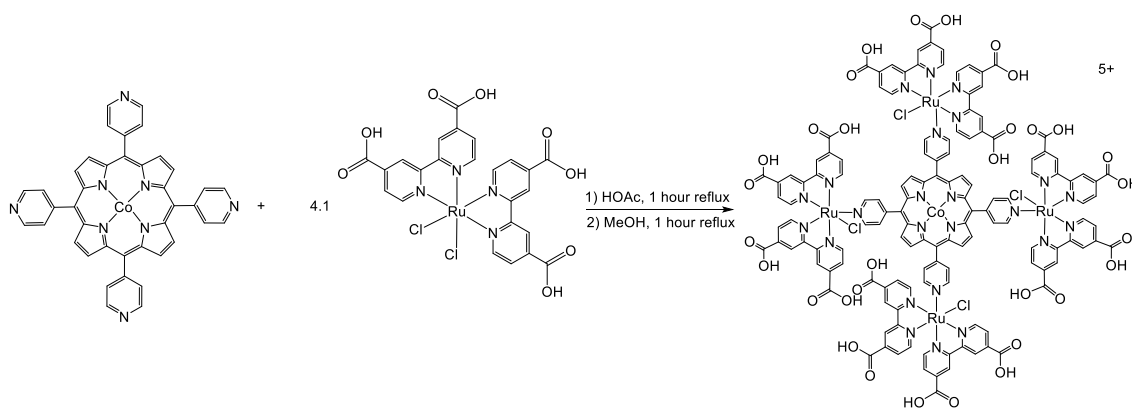


Figure 24. Schematic representation of $Co^{III}TRP(H_2dcbpy)$ synthesis.

Preparation of GO dispersion

Concentrated H_2SO_4 (115 mL) was added to a mixture of graphite flakes (5.0 g) and $NaNO_3$ (2.5 g). Then, $KMnO_4$ (15.0 g) was slowly added while the reaction mixture was kept at 50 °C under stirring for 6 h. The reaction mixture was carefully diluted with 400 mL of deionized-water and then cooled in a water bath before further reaction with 20 mL of H_2O_2 solution (30% v/v). After 30 min, the reaction mixture was centrifuged (5000 rpm, 10 min), and the supernatant decanted away. The solid material was then successively washed and centrifuged (5000 rpm for 10 min) with 800 mL of 30% HCl solution, and then with 400 mL of ethanol. The black solid was resuspended in 400 mL of diethyl ether, filtered out with a 0.45 mm PTFE membrane, and dried overnight at room temperature, in a desiccator under vacuum. GO was

employed as very stable dark brown suspension, by exfoliating 500 mg of graphite oxide in 500 mL of deionized water in an ultrasonic bath for two hours, while the pH was adjusted to 9.0 by adding a concentrated KOH solution.

Preparation of Co^{III}TRP(dmbpy)/nGO composite

The Co^{III}TRP(dmbpy)/nGO (being n the mass ratio of GO relative to Co^{III}TRP(dmbpy)) composites were prepared by mixing 10 mL of an aqueous Co^{III}TRP(dmbpy) solution (1 mg mL⁻¹) and a GO suspension (2.0 mg mL⁻¹) in order to study the right proportion between the porphyrin and GO. In this manner, 5, 10, 20 and 30 mL of GO suspension were employed and poured into 10 mL of Co^{III}TRP(dmbpy) solution each. The solid was filtered out and washed with water yielding the composites Co^{III}TRP(dmbpy)/GO, Co^{III}TRP(dmbpy)/2GO, Co^{III}TRP(dmbpy)/4GO and Co^{III}TRP(dmbpy)/6GO.

Preparation of Co^{III}TRP(dcbpy)-Ni/ GO composite

5 mL of GO suspension in DMF (1 mg mL⁻¹) was poured into a reaction flask equipped with a magnetic bar. While being purged, 38.3 mg (134.4 μ mol) of nickel (II) acetate were added to the suspension and warmed to 30 °C under a stream of dinitrogen. Meanwhile, 20 mg (5.0 μ mol) of Co^{III}TRP(H₂dcbpy) were dissolved in 5 mL DMF by adding a NH₄OH solution dropwise until complete solubilization. After ten minutes of degassing, the solution containing the [Co^{III}TRP(dcbpy)]¹⁺ species was added slowly to the GO/Ni dispersion and let it to react for 72 hours at 30 °C. After this time, the solid was centrifuged and washed several times with DMF until supernatant came out colorless. This solid was resuspended in 5 mL of ethanol and used in this manner for electrode modification: 50 μ L of this ethanolic suspension were diluted with 450 μ L of ethanol, 5 μ L of Nafion[®] were added and the volume completed to 1 mL with water.

Electrode modification with Co^{III}TRP(dmbpy)/nGO composite

A GC electrode was polished with a polishing cloth using 0.05 µm alumina powder and cleaned in an ultrasound bath for 5 minutes. Afterwards, 50 µL of Co^{III}TRP(dmbpy)/nGO dispersion were drop casted on the electrode surface and allowed to dry in air for 4 hours.

Electrode modification with Co^{III}TRP(H₂dcbpy)-Ni/ GO composite

A GC electrode was polished with a polishing cloth using 0.05 µm alumina powder and cleaned in an ultrasound bath for 5 minutes. Afterwards, 16 µL of the Co^{III}TRP(H₂dcbpy)-Ni/ GO dispersion in water/ethanol/Nafion® were drop casted on the electrode surface and let to dry in air.

Anatase TiO₂ nanoparticles synthesis

Anatase TiO₂ nanoparticles were synthesized according to the published methodology and standardized in our laboratory.⁹⁴ 12.5 mL of titanium (IV) isopropoxide were stabilized in 3.5 mL of isopropanol, this mixture was added dropwise to an acetic acid (27 mL) – deionized water (84 mL) solution at 3 °C under magnetic stirring. Soon after complete addition, the crude mixture was heated to 80 °C for 8 hours under stirring. The resulting slurry mixture was transferred to an autoclave and brought to 230 °C for 12 hours. The dispersion obtained was poured into a round bottom flask and concentrated in a rotary evaporator and centrifuged at 4800 rpm for 30 minutes. The obtained solid was washed several times with ethanol.

The paste employed for electrode manufacturing was prepared by adding 8.71 mL of α-terpineol and 15 mL of an 81.3 mg mL⁻¹ ethanolic ethyl cellulose solution were added. This mixture was exposed to several sonication and magnetic stirring

processes for homogenization. The solvent was gradually removed by a rotary evaporator until a viscose paste was obtained.

TiO₂ electrode preparation

FTO conducting glass was employed as support for the TiO₂ anodes preparation. This glass was carefully cleaned employing sonication in water/Extran[®] mixture for 20 minutes, rinsed and further sonicated in deionized water for another 20 minutes. The glass was cut in 1x2 cm pieces and an electrode area of 0.25 cm² was delimited employing adhesive tape. TiO₂ paste was deposited on this area and the film was formed by spin coating technique. Upon adhesive tape removal, the films were let to rest for 1 hour and put into an oven at 150 °C for 60 minutes. Right after this primary drying, the electrodes were sintered at 450 °C for 20 minutes.

TiO₂ film dye functionalization

The desired dye was dissolved in 5 mL *tert*-butanol and acetonitrile 1:1 affording a 2x10⁻⁴ mol L⁻¹ solution. TiO₂ films were soaked in this solution for 36 hours and washed with ethanol to remove dye excess prior to DSSC assemble.

Counter electrode preparation

FTO conducting glass plates of 1x2 cm were cleaned as described before and 10 µL of a 0.005 mol L⁻¹ H₂PtCl₆ solution in isopropanol were deposited on its surface and let to dry in air. The dry electrodes were heated to 400 °C for 20 minutes to sinter the platinum coating.

Electrolyte preparation

Iodine based electrolytes are composed by a 3-metoxipropionitrile solution bearing 0.5 mol L⁻¹ of *tert*-butylpyridine, 0.6 mol L⁻¹ of tetrabutylammonium iodide, 0.1 mol L⁻¹ of lithium iodide and 0.1 mol L⁻¹ of iodine.

DSSCs assemble

DSSCs were assembled by joining together a TiO₂ sensitized electrode and a Pt coated cathode employing Surlyn[®] as both spacer and sealer. Sealing was performed heating the sandwich type DSSC to 110 °C for 15 minutes.

After cooling down the cells, I⁻/I₃⁻ electrolyte was injected by a pre-drilled hole in the counter electrode and sealed with Surlyn[®] in the same fashion as described before. Figure 25 shows a photograph of fully functional DSSCs manufactured with the process described.

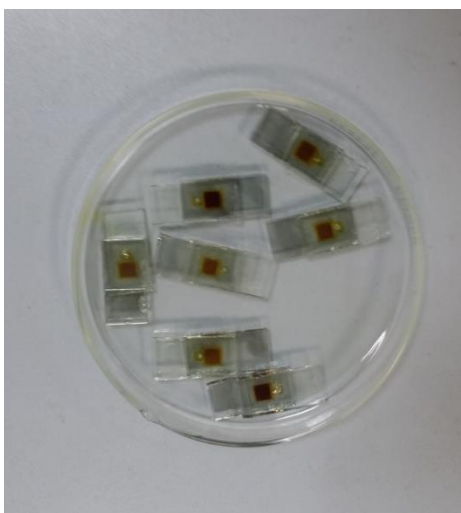


Figure 25. Image of assembled DSSCs employing N719 and a porphyrin-based dye.

RESULTS AND DISCUSSION

In the present work was explored the efficiency of a novel polypyridine ruthenium complex as sensitizer and its application in dye sensitized solar cells (DSSCs) was performed. Its deprotonated species were tested as well in search for improved performance.

An outer sphere intervalence transfer (IT) was observed in a novel mixed valence $\text{Ru}^{\text{II}}/\text{Fe}^{\text{III}}$ complex exhibiting ligand conformational dependence for the IT to occur.

A novel tetraruthenated cobalt porphyrin was synthesized and employed for dissolved oxygen sensing with a four-electron mediated mechanism and its stability over time was monitored.

A novel tetraruthenated cobalt porphyrin was synthesized and employed for isoniazid sensing with a possible four-electron mediated mechanism.

CHAPTER I: Synthesis and Characterization of [Ru^{II}(McTerpy)(dmbpy)(TMT)]PF₆ and DSSC Application.

McTerpy characterization

NMR spectroscopy is one of the most powerful techniques that a synthetic chemist can exploit in order to unveil the structural features of his molecules. This is due to the information about magnetic environments or interactions between carbon and hydrogen atoms (there are many other nuclei with magnetic resonance effect) within the molecular frame.⁹⁵

This technique gives a glimpse about the purity of the compounds analyzed and the discussion will take place when necessary.

This ligand was obtained as a white solid, which showed a perfect signal match in the ¹H-NMR spectrum (Figure 26), exhibiting five signals between 8.5 and 7.4 ppm. The spectrum was recorded in deuterium oxide and 0.15 mL sodium deuterioxide (Aldrich, 30 wt. % in D₂O, 99 atom % D). Signals were unequivocally assigned due to their coupling constants and the simplicity of the spectrum. The signal corresponding to the hydrogens in the central pyridyl ring denoted as **a** served as integration reference.

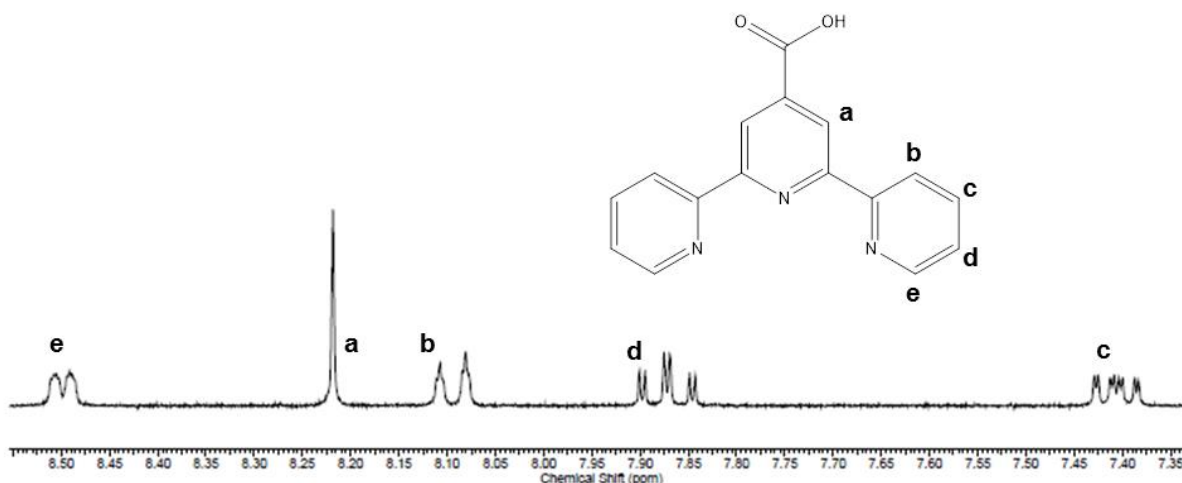


Figure 26. ^1H -NMR spectrum of MCTerpy in $\text{D}_2\text{O}/\text{NaOD}$.

^1H NMR (300 MHz, DEUTERIUM OXIDE/ NaOD) δ ppm 7.41 (2 H, ddd, $J=7.62, 4.91, 1.25$ Hz) 7.87 (2 H, td, $J=7.76, 1.76$ Hz) 8.09 (2 H, d, $J=7.91$ Hz) 8.22 (2 H, s) 8.50 (2 H, d, $J=4.98$ Hz).

[Ru^{II}(McTerpy)(H₂O)Cl₂].H₂O characterization

The complex formed by the coordination of the tridentate ligand Terpy and its analogues is commonly reported as being $\text{Ru}^{\text{III}}(\text{Terpy})\text{Cl}_3$, it is believed that due to the lack of a reducing agent in the reaction media, the ruthenium center does not undergo a redox process during the complex formation.^{96,97,98,99}

However, as we will further discuss there are several experiments that led us to believe that the ruthenium (II) species may be formed under the reaction conditions employed.

^1H -NMR spectra

The first hint about a low spin $\text{Ru}(\text{II})$ species was given by the ^1H -NMR spectrum shown in Figure 27. Despite some little impurities, the spectrum exhibits five well-defined signals exhibiting symmetry and lack of broadening typical of a diamagnetic metal center favoring slower nuclear relaxation times whereas

paramagnetic species (metal centers or organic radicals) tend to speed up this process.¹⁰⁰ Figure 27 allowed the assignment of a highly symmetrical Ru(II) complex (inset) and the singlet in 8.98 ppm enabled the integration of every signal acting as reference. Coupling constants permitted the correlation between nuclei thanks to the *-orto*, *-meta* and *-para* values.

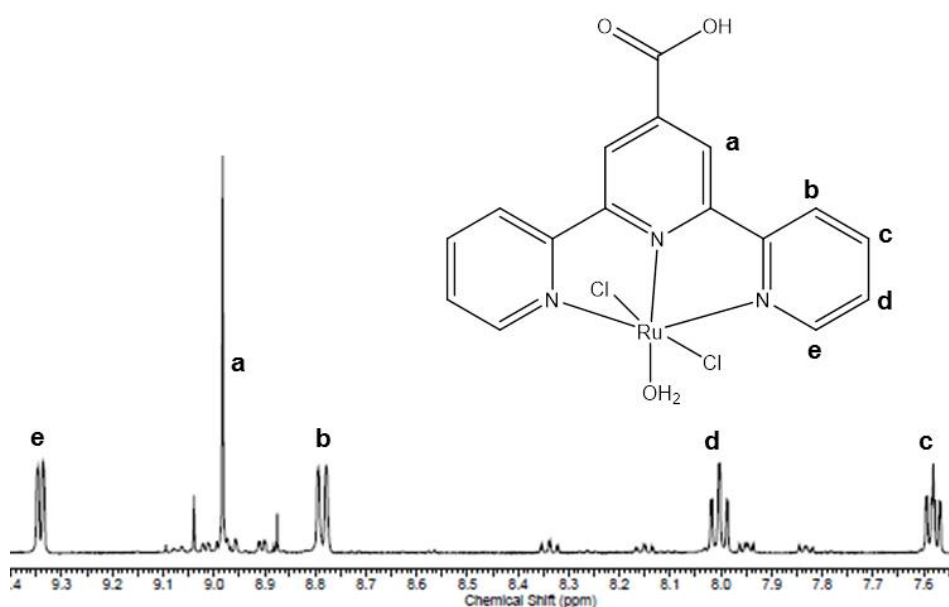


Figure 27. ¹H-NMR spectrum of [Ru^{II}(McTerpy)(H₂O)Cl₂].H₂O in DMSO-*d*₆.

¹H-NMR (500 MHz, DMSO-*d*₆) δ ppm 7.58 (2 H, ddd, *J*=7.40, 5.72, 1.22 Hz) 8.00 (2 H, td, *J*=7.78, 1.53 Hz) 8.79 (2 H, d, *J*=7.32 Hz) 8.98 (2 H, s) 9.34 (2 H, dd, *J*=5.49, 0.92 Hz).

Since [Ru^{II}(McTerpy)(H₂O)Cl₂].H₂O ¹H-NMR spectrum was recorded in dmsO-*d*₆ and the free ligand was collected employing D₂O/NaOD, a direct comparison between chemical shifts upon coordination is not suitable, hence it was noted from literature,¹⁰¹ that this ¹H-NMR values differ from the free ligand as depicted in Table I. It is noteworthy that almost all of the signals have been shifted to lower field values typical of deshielding nucleus upon coordination to an electron deficient metal center.

Table I. Chemical shifts in ppm from free ligand to [Ru^{II}(McTerpy)(H₂O)Cl₂].H₂O complex for dmsO-d₆ solvent.

Free Ligand (multiplicity)	Complex (multiplicity)
7.54(t)	7.58(ddd)
8.04(t)	8.00(td)
8.66(d)	8.79(d)
8.76(d)	8.98 (s)
8.86 (s)	9.34(dd)

Although, ¹H-NMR spectra gave us a hint about the oxidation state of the ruthenium center, spin delocalization across the whole complex may be poor enough to enable a good NMR signal.¹⁰²

EPR spectra

EPR experiments were carried out to verify the ruthenium center oxidation state. As shown in the spectrum recorded (Figure 28) no signal of unpaired electrons for a Ru(III) (4d⁵ configuration) state was observed when compared with reported EPR studies of Ru(III) complexes, therefore indicating a low spin Ru(II) center.¹⁰³

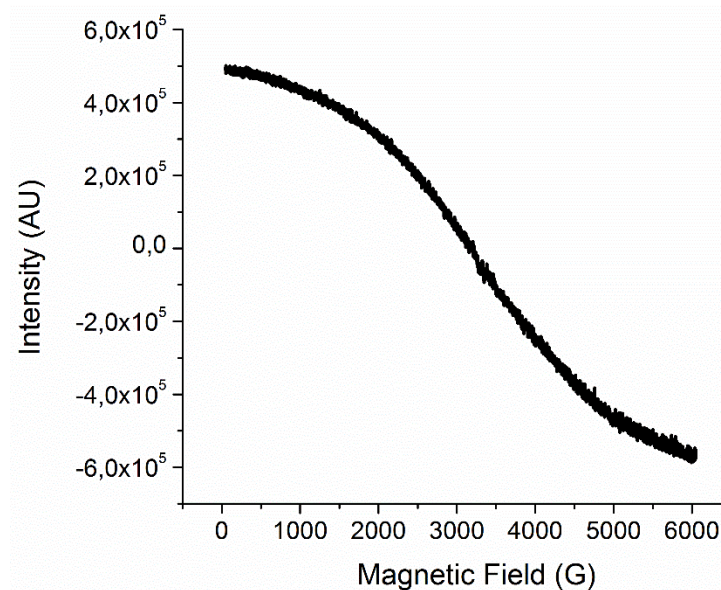


Figure 28. EPR spectra of $[\text{Ru}^{\text{II}}(\text{McTery})(\text{H}_2\text{O})\text{Cl}_2]\cdot\text{H}_2\text{O}$ in DMF at 77 K.

Mass spectrometry

Further characterization experiments such as ESI-MS were performed and showed in Figure 29. The molecular ion peak was observed at 449.2 m/z affording a good match for the ion $[\text{Ru}^{\text{II}}(\text{McTery})\text{Cl}_2(\text{H}^+)]^+$ 449.93 m/z. Additional peak for successive ligand loss is visible at 414.0 m/z for the $[\text{Ru}^{\text{II}}(\text{McTery})\text{Cl}]^+$ ion.

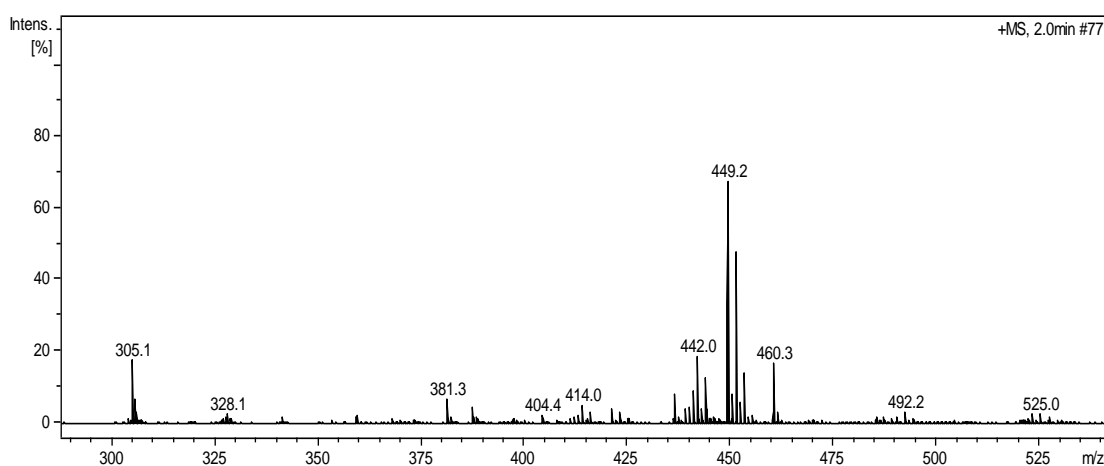


Figure 29. ESI-MS from $[\text{Ru}^{\text{II}}(\text{McTery})(\text{H}_2\text{O})\text{Cl}_2]\cdot\text{H}_2\text{O}$. Nebulizer: 0.8 Bar, dry gas: 5 L min^{-1} , temp: $200 \text{ }^\circ\text{C}$, HV: 4500 V and formic acid.

UV-Vis spectra

Polypyridine ruthenium complexes have rich electronic spectra in which all of the characteristic transitions can be readily assigned due to their characteristic energies. As observed in Figure 30, three types of transitions can be observed within the spectral working window (200-800 nm). The highest energy transitions are those centered in the ligands or intraligand (IL) which involves the $\rho\pi$ filled and the $\rho\pi^*$ empty orbitals. These types of absorptions occur in the UV region for small conjugated organic molecules such as bpy and terpy. Metal centered transitions (d-d) that occur between the t_{2g} and e_g d -orbitals are forbidden (less prone to occur) due to symmetry for an octahedral complex, nevertheless vibronic coupling and geometry distortion lead to this selection rule relaxation. These d-d absorptions take place in the visible region but due to the selection rules its molar extinction coefficient is low and they are usually overlapped by the stronger MLCT or LMCT bands.¹⁰⁴ Finally MLCT bands are located in the visible region of the spectrum involving the $d\pi$ filled metal orbitals and the empty $\rho\pi^*$ ligands orbitals, this is the case for π -accepting ligands such as polypyridines.

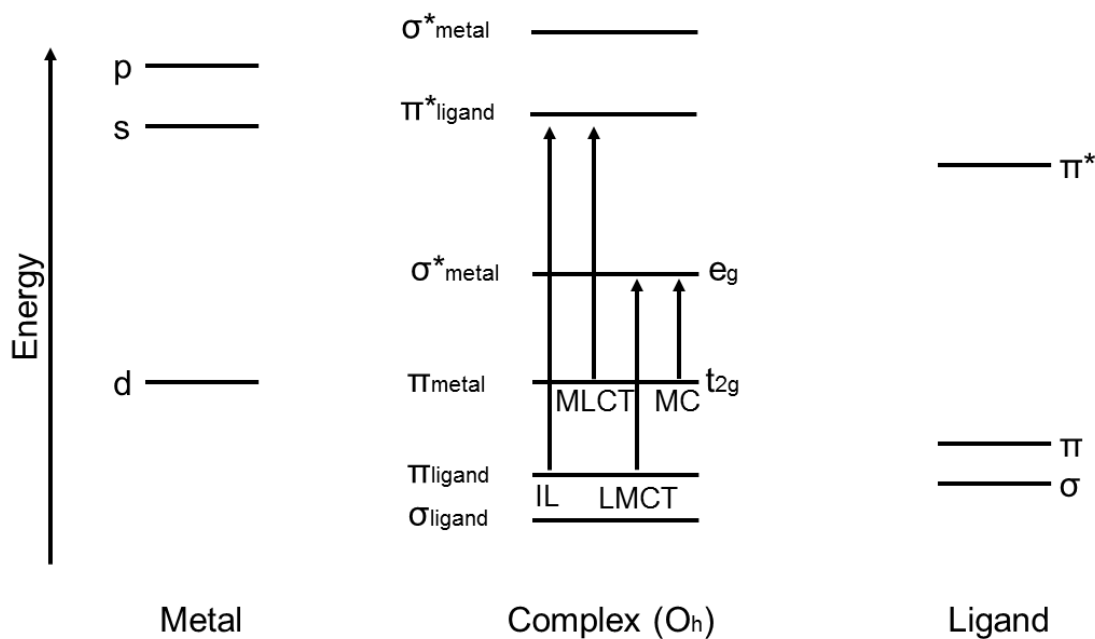


Figure 30. Molecular orbital energy diagram for octahedral RuL_6 complexes.

Figure 31 exhibits the absorption spectrum of $[Ru^{II}(McTerpy)(H_2O)Cl_2] \cdot H_2O$ with three bands in the spectral window. The bands at 275 and 326 nm are assigned to IL ($p\pi \rightarrow p\pi^*$) from the McTerpy ligand and the band located at 489 nm is ascribed as a charge transfer from the $Ru(II)$ center to the ligand ($d\pi \rightarrow p\pi^*$).

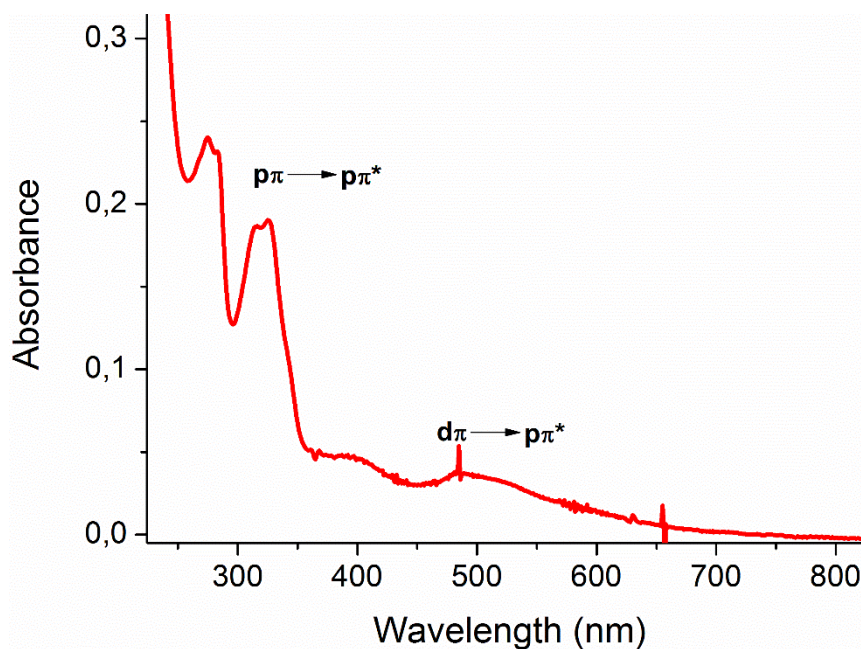


Figure 31. UV-vis absorption spectra of $[Ru^{II}(McTerpy)(H_2O)Cl_2] \cdot H_2O$ in DMF.

Due to the afforded experimental evidences we believe that ethanol employed as solvent is acting as the reducing agent in the RuIII/RuII process. This assumption is supported by reports of assisted reductions of metal ions using ethanol.^{105,106}

[Ru^{II}(McTerpy)(dmbpy)Cl]Cl characterization

¹H-NMR spectra

This experiment provided sufficient evidence about complex formation and purity, affording 13 signals between 2.37 and 9.99 ppm expected for a symmetric terpy with 5 signals and an unsymmetrical dmbpy ligand due to the electronic *trans* effect of the chloride to one of the pyridyl rings, making them magnetically inequivalent, therefore, every ring in dmbpy gives rise to four signals each as shown in Figure 32. Labeling has been kept for McTerpy for comparison and further labeling was adopted for dmbpy hydrogens.

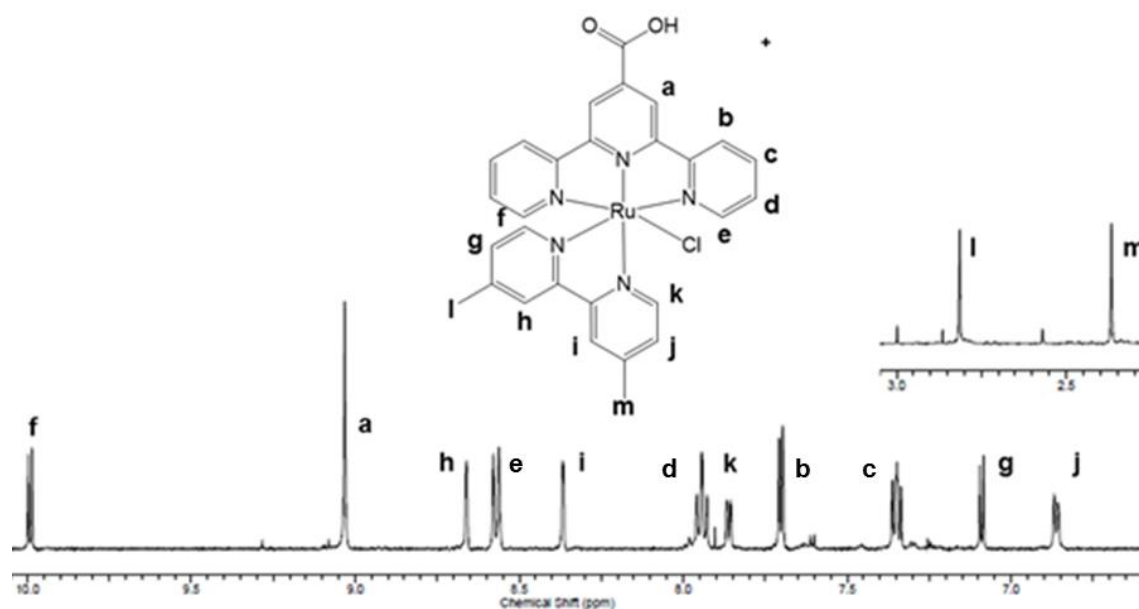


Figure 32. ¹H-NMR spectra of [Ru^{II}(McTerpy)(dmbpy)Cl]Cl in MeOD-*d*₄.

¹H NMR (500 MHz, METHANOL-*d*₄) δ ppm 2.37 (s, 3 H) 2.81 (s, 3 H) 6.86 (d, *J*=7.05 Hz, 1 H) 7.09 (d, *J*=5.76 Hz, 1 H) 7.33 - 7.37 (m, 2 H) 7.70 (d, *J*=5.55 Hz, 2 H)

7.86 (d, $J=6.83$ Hz, 1 H) 7.94 (t, $J=8.43$ Hz, 2 H) 8.37 (s, 1 H) 8.57 (d, $J=7.90$ Hz, 2 H) 8.66 (s, 1 H) 9.03 (s, 2 H) 9.99 (d, $J=5.76$ Hz, 1 H).

UV-vis spectra

Figure 33 shows the electronic absorption spectrum of $[\text{Ru}^{\text{II}}(\text{McTerpy})(\text{dmbpy})\text{Cl}]\text{Cl}$ in MeOH exhibiting a dominance of the $\rho\pi \rightarrow \rho\pi^*$ transitions from the McTerpy ligand with a little contribution from the dmbpy moiety due to the resemblance of its pattern with the spectrum shown in Figure 31. On the other hand, the MLCT ($d\pi \rightarrow \rho\pi^*$) transitions afforded a notorious change upon dmbpy coordination with its band centered in 523 nm displaying a stronger absorption when compared with the $[\text{Ru}^{\text{II}}(\text{McTerpy})(\text{H}_2\text{O})\text{Cl}_2]$ species spectrum.

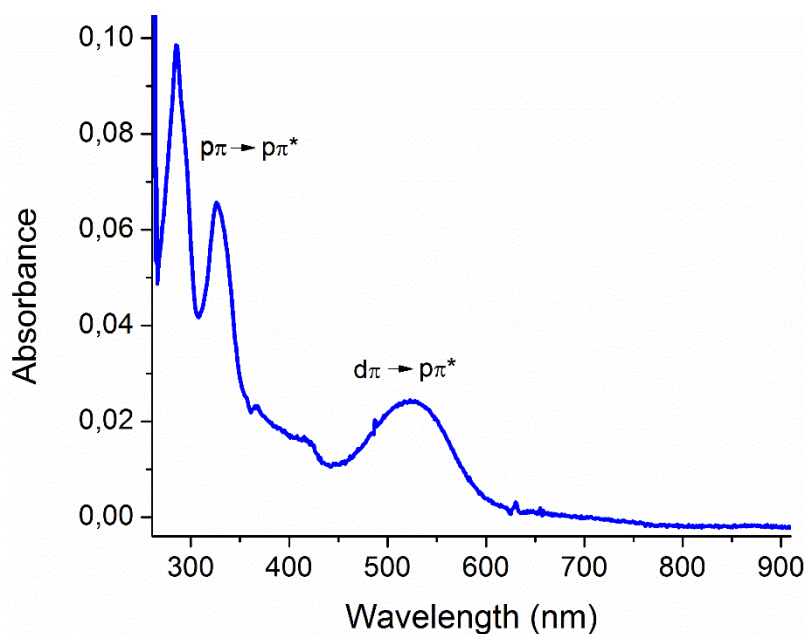


Figure 33. UV-vis absorption spectra of $[\text{Ru}^{\text{II}}(\text{McTerpy})(\text{dmbpy})\text{Cl}]\text{Cl}$ in MeOH.

$[\text{Ru}^{\text{II}}(\text{McTerpy})(\text{dmbpy})(\text{H}_2\text{TMT})]\text{PF}_6$ characterization

$^1\text{H-NMR}$ spectra

The spectrum of the $[\text{Ru}^{\text{II}}(\text{McTerpy})(\text{dmbpy})(\text{H}_2\text{TMT})]\text{PF}_6$ complex is shown in Figure 34 and due to the use of protic solvent (MeOD-d_4) isotopic exchange takes

place with the thiol residues making these hydrogens non visible in the spectrum. Nevertheless, chemical shifts for the eleven signals found between 6.94 and 9.79 ppm differ substantially from those found for the $[\text{Ru}^{\text{II}}(\text{McTery})(\text{dmbpy})\text{Cl}]^+$ precursor as shown in Table II, allowing us to infer the coordination of the TMT ligand although more analyses were performed to confirm this hypothesis.

^1H NMR (500 MHz, $\text{METHANOL-}d_4$) δ ppm 2.38 (s, 3 H) 2.79 (s, 3 H) 6.94 (dd, $J=5.95, 1.07$ Hz, 1 H) 6.98 - 7.00 (m, 1 H) 7.34 (ddd, $J=7.32, 5.80, 1.22$ Hz, 2 H) 7.80 (dd, $J=5.80, 1.22$ Hz, 1 H) 7.86 (dd, $J=5.65, 0.76$ Hz, 2 H) 7.91 (td, $J=7.78, 1.53$ Hz, 2 H) 8.39 (s, 1 H) 8.57 (d, $J=7.93$ Hz, 2 H) 8.63 (s, 1 H) 9.04 (s, 2 H) 9.79 (d, $J=5.80$ Hz, 1 H).

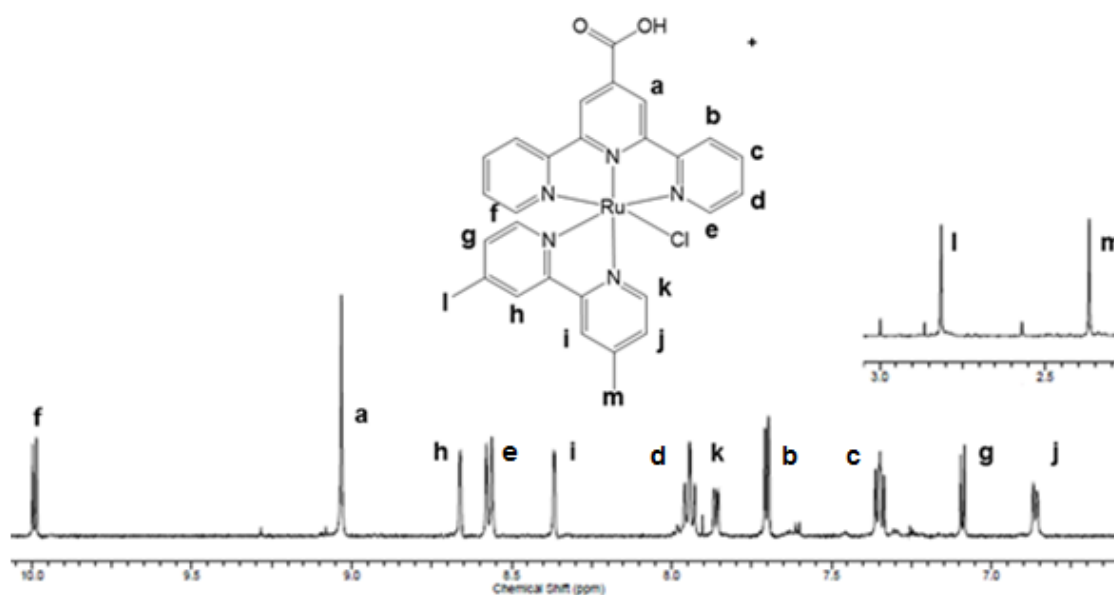


Figure 34. ^1H -NMR spectra of $[\text{Ru}^{\text{II}}(\text{McTery})(\text{dmbpy})(\text{H}_2\text{TMT})]\text{PF}_6$ in $\text{MeOD-}d_4$.

It is noteworthy the low magnetic effect over the majority of the hydrogens environments but those closer to the triazine ring show the most evident shifts this is due to the ligand electronic properties such as π -accepting character and an intrinsic ring current due to the delocalized π -electrons.

Table II. Chemical shifts comparison from $[\text{Ru}^{\text{II}}(\text{McTerpy})(\text{dmbpy})\text{Cl}]^+$ and $[\text{Ru}^{\text{II}}(\text{McTerpy})(\text{dmbpy})(\text{H}_2\text{TMT})]^+$ species.

Signal	Chemical Shift (ppm)	
	$[\text{Ru}^{\text{II}}(\text{McTerpy})(\text{dmbpy})\text{Cl}]^+$	$[\text{Ru}^{\text{II}}(\text{McTerpy})(\text{dmbpy})(\text{H}_2\text{TMT})]^+$
a	9.03	9.04
b	7.70	7.34
c	7.35	8.57
d	7.94	7.86
e	8.57	7.91
f	9.99	9.79
g	7.09	6.98
h	8.66	8.63
i	8.37	8.39
j	6.86	6.94
k	7.86	7.80
l	2.81	2.79
m	2.37	2.38

Mass spectrometry

ESI mass spectra was recorded in the positive ion mode affording a total m/z ratio of 739.03 for the molecular ion $[\text{Ru}^{\text{II}}(\text{McTerpy})(\text{dmbpy})(\text{H}_2\text{TMT})]^+$ with a

matching isotopic distribution for a one ruthenium center species (Figure 35). There is a peak preserving this isotopic distribution at 761.01 m/z which we assign as the $[M+Na]^+$ ion. Interestingly a peak at 598.06 m/z is present and is ascribed to the $[Ru^{II}(McTery)(dmbpy)Cl]^+$ species, we infer that this comes from the little impurities observed in the 1H -NMR spectrum meaning a much higher stability during ionization-separation processes in the mass spectrometer of this chloride species.

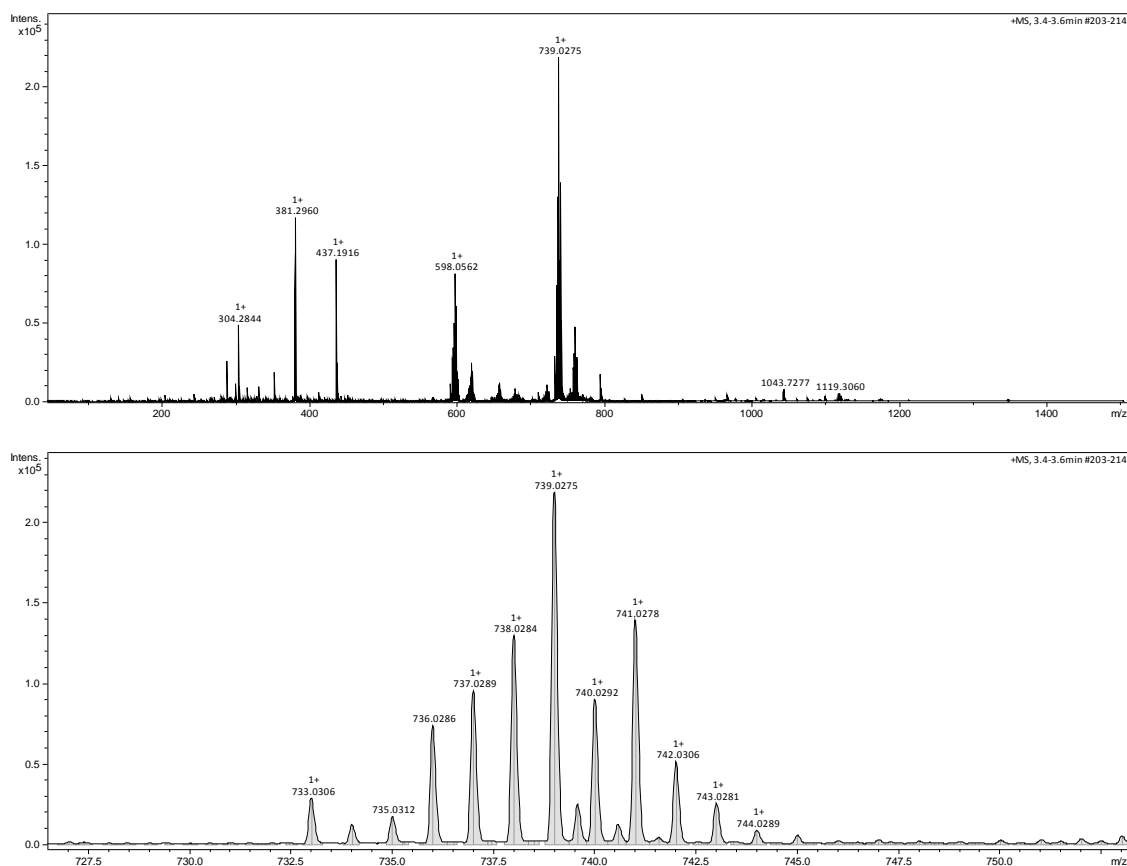


Figure 35. ESI-MS from $[Ru^{II}(McTery)(dmbpy)(H_2TMT)]PF_6$. Nebulizer: 0.4 Bar, dry gas: 4 L min^{-1} , temp: 200 °C, HV: 4500 V.

UV-Vis spectra

Electronic spectra of the $[Ru^{II}(McTery)(dmbpy)(H_2TMT)]PF_6$ complex in methanol (Figure 36) exhibits typical IL transitions in the region below 400 nm. At 224 nm is located the first transition assigned to be a $p\pi \rightarrow p\pi^*$ from the TMT ligand due to the smaller size of its conjugated structure when compared to McTery and

dmbpy. At 281 nm is located an intense band with a shoulder in 317 nm which are ascribed to both dmbpy and McTerpy IL transitions ($\rho\pi \rightarrow \rho\pi^*$). In the visible region (above 400 nm) there are located two distinguishable MLCT bands at 435 and 497 nm being the former assigned to the $\text{Ru}^{\text{II}} d\pi \rightarrow \text{TMT} \rho\pi^*$. The latter transition is assigned to a contribution from $\text{Ru}^{\text{II}} d\pi \rightarrow \text{McTerpy} \rho\pi^*$ and $\text{Ru}^{\text{II}} d\pi \rightarrow \text{dmbpy} \rho\pi^*$. Molar extinction coefficients were estimated and are presented in appendix 1.

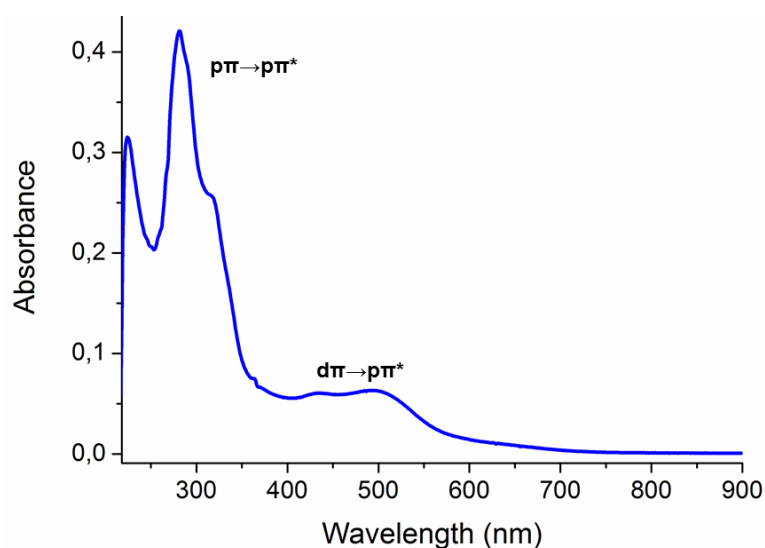


Figure 36. UV-vis spectra from $[\text{Ru}^{\text{II}}(\text{McTerpy})(\text{dmbpy})(\text{H}_2\text{TMT})]\text{PF}_6$ in MeOH.

Electrochemistry

Cyclic voltammetry shown in Figure 37 exhibits five redox processes in the potential window employed. The anodic region presents one monoelectronic process assigned to the $\text{Ru}^{\text{II}}/\text{Ru}^{\text{III}}$ oxidation at $E_{1/2} = 1.03$ V anodically shifted (when compared with other ruthenium complexes) due to the π -accepting character of all ligands stabilizing the ruthenium lower oxidation state, thus making it harder to oxidize. The anodic peak of this process ($E_{\text{pa}} = 1.07$ V) manifested a higher current than the cathodic peak ($E_{\text{pc}} = 1.00$ V) evidencing some kind of catalytic reaction with the media. The cathodic region is much richer since it displays all of the electrochemical processes of the ligands. At $E_{\text{pc}} = -0.98$ V for the McTerpy ligand followed by the

reduction of the TMT at $E_{pc} = -1.31$ V and the stepwise reduction of the dmbpy rings at $E_{pc} = -1.51$ and -1.77 V, these four processes match their current intensities for a one electron process each in agreement with previously reported polypyridine ruthenium complexes.^{85,107,108} All of these reduction reactions are irreversible and their anodic waves appear with low current intensities implying that a coupled chemical reaction depleted the reduced species.

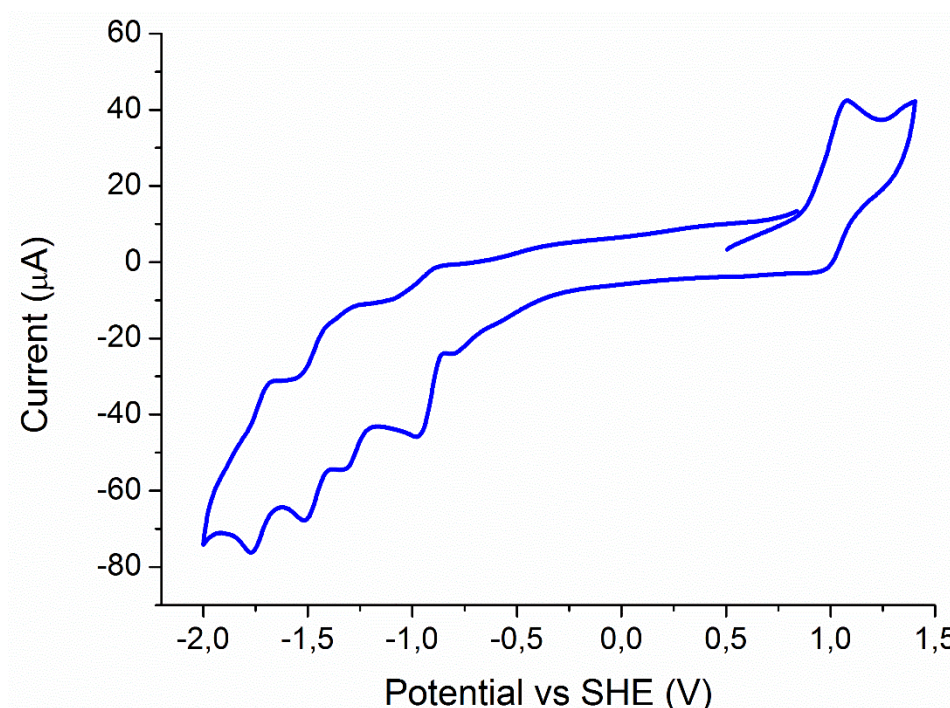


Figure 37. Cyclic voltammetry of $[\text{Ru}^{\text{II}}(\text{McTerpy})(\text{dmbpy})(\text{H}_2\text{TMT})]\text{PF}_6$ in CH_3CN , 100 mV s^{-1} .

Spectroelectrochemistry

Spectroelectrochemistry shown in Figure 38 highlighted the role and contribution of the ruthenium center to the electronic structure of the complex since all of the absorption's intensities are diminished when the potential sweep is made between 0.89 and 1.15 V. The MLCT region described in the UV-vis discussion had an outstanding impact upon ruthenium oxidation. MLCT bands diminish is an indicative of the absence of electron density over the ruthenium center impeding

these transitions to occur, confirming the assignment performed in the UV-vis spectrum.

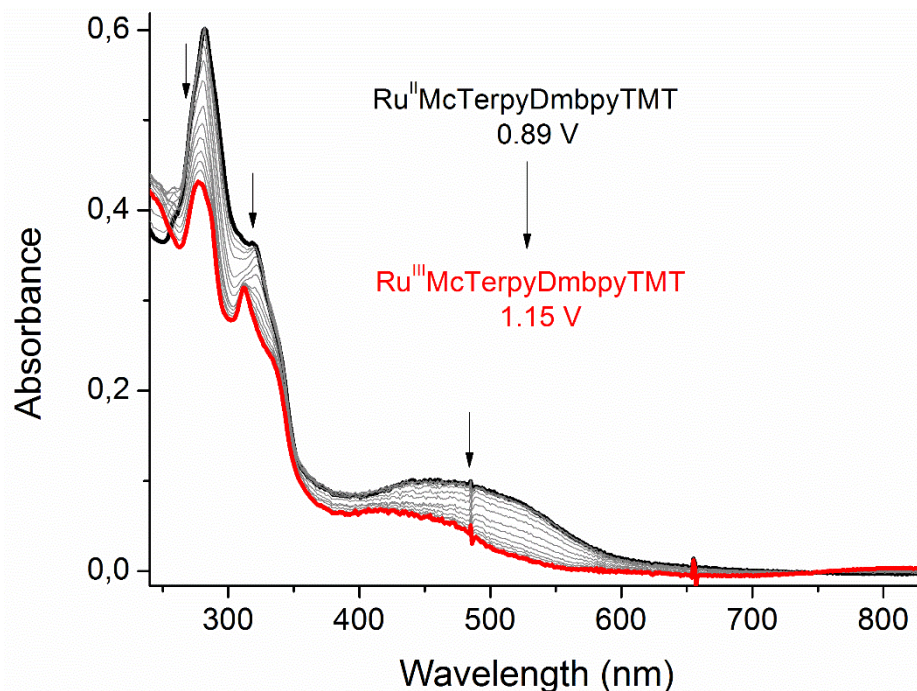


Figure 38. Spectroelectrochemistry spectrum from $[\text{Ru}^{\text{II}}(\text{McTerpy})(\text{dmbpy})(\text{TMT})]\text{PF}_6$ in DMF.

Spectrophotometric Titration

Due to the proposed structure of the $[\text{Ru}^{\text{II}}(\text{McTerpy})(\text{dmbpy})(\text{TMT})]\text{PF}_6$ complex there are several functional groups capable of undergoing acid-base equilibria. Determining these pK_a values is crucial since coordination chemistry (for anchoring into TiO_2 nanoparticles), electronic properties (HOMO/LUMO energies) and electrostatic interactions are governed by the degree of protonation in the complex. Therefore, the possible protonation isomers must be isolated in order to study the effect in the efficiency of the assembled DSSCs as shown by R. Guimarães in his thesis.¹⁰⁹

There are two methods capable of affording pK_a values of chemical species in solution. The first one is the potentiometric titration and the second and most employed is the spectrophotometric titration since prior knowledge of the species

concentrations is not mandatory as they can be easily calculated employing the spectrum absorbance. This can be better understood when looking at the dissociation constant of an acid in aqueous media:



From this equilibrium we can deduce the HA acid strength by means of its dissociation constant K_a expressed as:

$$K_a = \frac{[H_3O^+][A^-]}{[HA]} \quad \mathbf{3}$$

It is in this point where the concentration of the species $[A^-]$ and $[HA]$ becomes relevant and the spectrophotometric method facilitates their calculation through the absorption intensities, employing the Lambert-Beer equation **4**, where l is the optic path length, C is the concentration of the desired species and ε is the molar absorption coefficient.

$$A = l C \varepsilon \quad \mathbf{4}$$

For this instance, we have three possible scenarios that have to be evaluated in order to determine the relative concentrations and the total concentration of the species in solution. The first one is when the acid species predominate (i.e. low pH):

$$A_{HA} = l C_T \varepsilon_{HA} \quad \mathbf{5}$$

When basic species predominate in solution (i.e. high pH) we have:

$$A_{A^-} = l C_T \varepsilon_{A^-} \quad \mathbf{6}$$

where C_T is total concentration.

The case where both species are present in relatively equal amounts (equilibrium point), total absorbance (A_T) is given by a contribution of all of them as follows:

$$A_T = l C_{HA} \varepsilon_{HA} + l C_{A^-} \varepsilon_{A^-} \quad \mathbf{7}$$

And taking into account that the total concentration (C_T) at this point is given by:

$$C_T = C_{HA} + C_{A^-} \quad \mathbf{8}$$

Introducing equations **5** and **6** into **7**, the following expression is obtained;

$$A_T = \frac{A_{HA}}{C_T} C_{HA} + \frac{A_{A^-}}{C_T} C_{A^-} \quad \mathbf{9}$$

After rearranging terms and replacing eq **8** into eq **9** we obtain expression **10**:

$$A_T(C_{HA} + C_{A^-}) = A_{HA}C_{HA} + A_{A^-}C_{A^-} \quad \mathbf{10}$$

Dividing by C_{HA} and rearranging terms we get to the equation **11**:

$$\frac{[A^-]}{[HA]} = \frac{C_{A^-}}{C_{HA}} = \frac{A_T - A_{HA}}{A_{A^-} - A_T} \quad \mathbf{11}$$

Equation **3** can be further exploited for graphical purposes by being expressed as:

$$\log K_a = \log[H_3O^+] + \log \frac{[A^-]}{[HA]} \quad \mathbf{12}$$

Combination of equations **11** and **12** yields the following expression:

$$\log \left(\frac{A_T - A_{HA}}{A_{A^-} - A_T} \right) = pH - pK_a \quad \mathbf{13}$$

In this manner, pK_a values can be ideally obtained by plotting $\log (A_T - A_{HA}) / (A_{A^-} - A_T)$ vs pH where the y-axis intercept affords the negative value of pK_a . However, plotting the absorbance at a determined wavelength vs pH yields a sigmoidal curve in

which the inflection point corresponds to the pK_a value that can be more accurately calculated through the second derivative of a properly fitted curve.^{110,111}

Following this reasoning, complex $[Ru^{II}(McTerpy)(dmbpy)(TMT)]PF_6$ was spectrophotometrically titrated employing an $H_2O/MeOH$ 20:1 solution containing 0.5 mol L^{-1} of $NaCl$ supporting electrolyte in order to maintain and control the ionic force. All of the spectra were collected at room temperature ($25 \text{ }^\circ\text{C}$) starting in pH 13 and acidified stepwise with HCl (3 mol L^{-1}) solution until pH 2.

Figure 39 (left) shows the collection of spectra in the 13-7 pH window. It is noteworthy a bathochromic shift of the $\pi\pi \rightarrow \pi\pi^*$ transitions, this is due to the stabilization of the π^* molecular orbital of the TMT ligand upon protonation lowering its energy whereas the MLCT bands in the visible range exhibit minimum variation throughout the titration due to this π^* stabilization and d-orbital destabilization.

Figure 39 (right) displays spectra collected between pH 7-2 and once again the main and most noticeable variations are in the $\pi\pi \rightarrow \pi\pi^*$ transitions, with a bathochromic shift owed to the stabilization of the π^* McTerpy orbital upon protonation. Indicating a much greater contribution of the McTerpy ligand to the IL overall band.

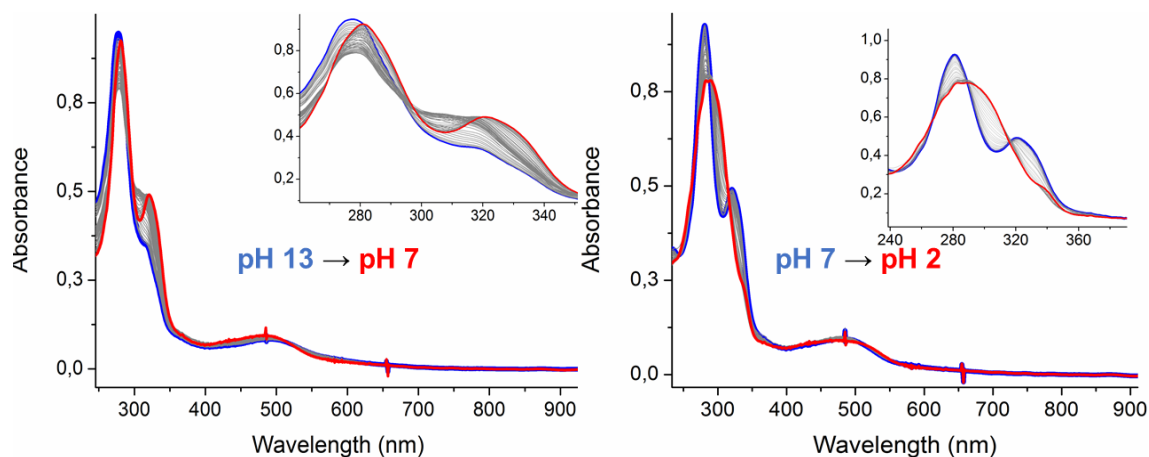


Figure 39. Spectrophotometric titration of $[\text{Ru}^{\text{II}}(\text{McTerpy})(\text{dmbpy})(\text{H}_2\text{TMT})]\text{PF}_6$ complex in basic (left) and acid (right) pH window.

In order to determine the number of acid-base equilibrium present in the titration, a plot of the absorbance at 302 nm, which was the band with the greater variation along the experiment, versus pH is presented in Figure 40a. It displays three distinguishable sigmoidal regions pH 2-7, 7-10 and 11-13. Each of these regions was plotted separately as shown in Figure 40b (for pH 2-7) and fitted to a sigmoidal function affording an $r^2 = 0.99979$ meaning a really good match between the experiment and the fitting equation. Is this equation that allowed us to determine the pK_a value for this equilibrium employing its second derivative and taking the pH value when the function equals zero. Since this is the only pK_a present in acid conditions we assigned it to be from the carboxylic group in the McTerpy ligand.

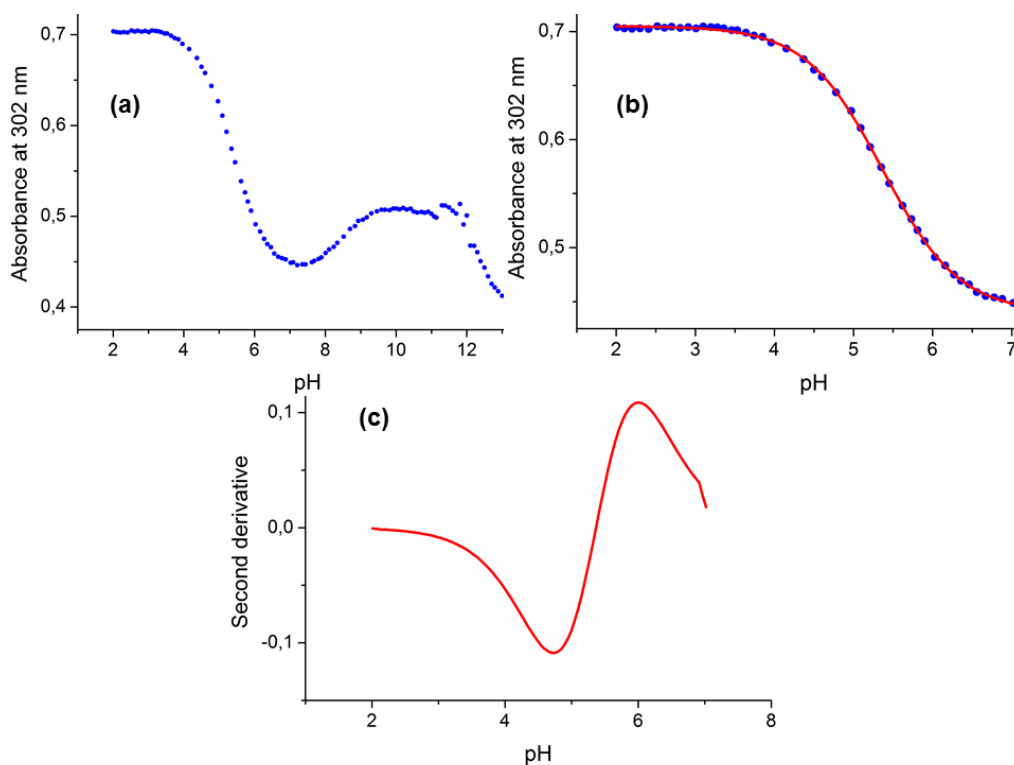


Figure 40. Absorbance at 302 nm vs pH (a), sigmoidal fitting for the first equilibrium (b) and second derivative for the fitting (c).

Table III shows the pK_{as} calculated from this spectrophotometric titration and the comparison with the reported pK_a values for the free ligands. It is noticeable that only two equilibria were found for the TMT ligand meaning that the third thiol (-SH) group already underwent deprotonation in order to coordinate the Ru(II) center. This supports our assumption of a sterically hindered sixth coordination position in the ruthenium allowing the bonding of the TMT ligand thru one of the thiol residues instead of the nitrogen in the bulky triazine ring.

Table III. pK_as for [Ru^{II}(McTerpy)(dmbpy)(H₂TMT)]PF₆ complex and their comparison with free ligand values.

Compound	pK _{a1}	pK _{a2}	pK _{a3}
McTerpy	4-5	-	-
TMT	5.71 ^b	8.36 ^b	11.38 ^b
[Ru ^{II} (McTerpy)(dmbpy)(H ₂ TMT)]PF ₆	5.35	8.49	12.32

b: adapted from ¹¹²

Once all of the pK_a were determined, the deprotonation species were prepared and isolated as described in the materials and methods section.

Emission and excitation studies

For DSSC application the dyes must fulfill some electronic requirements as mentioned before, so in order to estimate the energies of the HOMO/LUMO orbitals and the E₀₋₀ in the complex emission/excitation experiments were carried out. Figure 41 displays the electronic spectrum (blue) for the [Ru^{II}(McTerpy)(dmbpy)(TMT)]PF₆ complex and its fluorescence spectrum (red) in methanol. Upon excitation in the MLCT band at 496 nm, the spectrofluorimeter detected an emission process with its maximum located at 583 nm, with these processes the energy gap between HOMO and LUMO orbitals (E₀₋₀) was calculated in the point where the two spectra cross at 516 nm and employing equation 14 the energy is 2.39 eV.

$$E = \frac{hc}{\lambda}$$

14

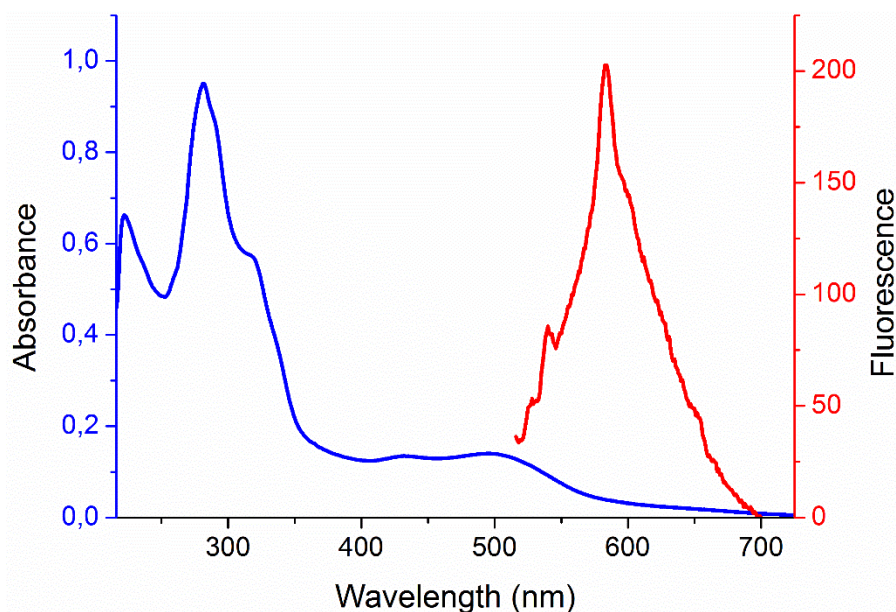


Figure 41. Absorption (blue) and emission spectra (red) of $[\text{Ru}^{\text{II}}(\text{McTeryp})(\text{dmbpy})(\text{H}_2\text{TMT})]\text{PF}_6$ in MeOH.

With the energy gap obtained it is necessary to calculate either HOMO or LUMO energy for comparison with the energy levels of the conduction band (CB) in nanocrystalline anatase TiO_2 and redox potential of the I^-/I_3^- couple found in literature.¹¹³ For this endeavor, CV experiments performed allowed calculation of either of the frontier orbitals in the complex, with the first oxidation potential affording information of the ionization potential. This means that the oxidation potential for the $\text{Ru}^{\text{II}}/\text{Ru}^{\text{III}}$ process yields the energy of the HOMO orbital employing equation 15.^{114,115}

$$I_p = -(E_{ox} + 4.44) \text{ eV}$$

15

Where E_{ox} is the onset potential for the $\text{Ru}^{\text{II}}/\text{Ru}^{\text{III}}$ process versus an SHE reference electrode and the value 4.44 is the vacuum level potential of the normal hydrogen electrode potential. The calculated values are shown in Figure 42 for better appreciation and a straightforward comparison, it is observed that the HOMO energy in the complex is in good position with respect to the iodide redox potential meaning an advantageous condition for the proper regeneration of the oxidized dye when the

electron is injected into the TiO₂ CB, furthermore, the energy of the LUMO is well placed above the TiO₂ CB favoring the electron injection.

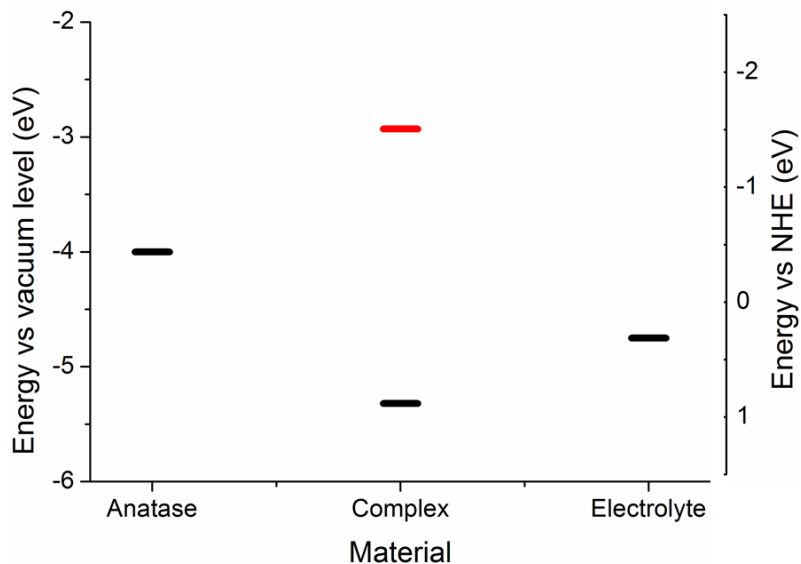


Figure 42. Energy diagram comparison for anatase TiO₂, [Ru^{II}(McTerpy)(dmbpy)(H₂TMT)]PF₆ and I⁻/I₃⁻ redox couple.

All of these experimental evidence suggest a good electronic structure for the utilization of the [Ru^{II}(McTerpy)(dmbpy)(TMT)]PF₆ complex as a sensitizer for DSSCs.

Efficiency and IPCE measurements

A total of three DSSCs were assembled for each ruthenium species [Ru^{II}(McTerpy)(dmbpy)(H₂TMT)]⁺, [Ru^{II}(McTerpy)(dmbpy)(HTMT)], [Ru^{II}(McTerpy)(dmbpy)(TMT)]⁻ and comparative reference cells mounted with N719 as sensitizer were employed, a picture of the TiO₂ dyed anodes is presented in Figure 43 bearing an average electrode surface of 0.25 cm².

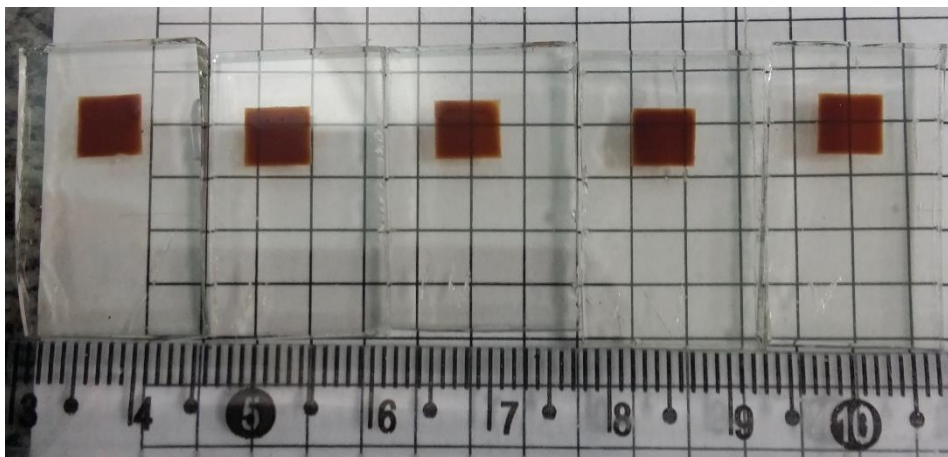


Figure 43. Image of anatase TiO₂ sensitized anodes.

Figure 44 shows the I-V curves obtained for the [Ru^{II}(McTerpy)(dmbpy)(H₂TMT)]PF₆ (left) and N719 (right) DSSCs exhibiting very low values of V_{oc} and J_{sc} for the novel dye probably due to undesired recombination processes, also the pronounced curvature in the I-V curve for our dye led us to think of low FF values.

V_{oc} can be extracted from the curves when the current density thru the circuit is zero and it is a measure of the difference between the Fermi level when the dye is injecting electrons into the CB and the electrolyte redox potential.¹¹⁶ J_{sc} is obtained when the potential applied to the circuit is zero and depends solely on the electrode area and the illumination power. On the other hand, FF and efficiency (η) were calculated employing equations **16** and **17** and the results for all of the three dyes and the reference (N719) appear in Table IV.

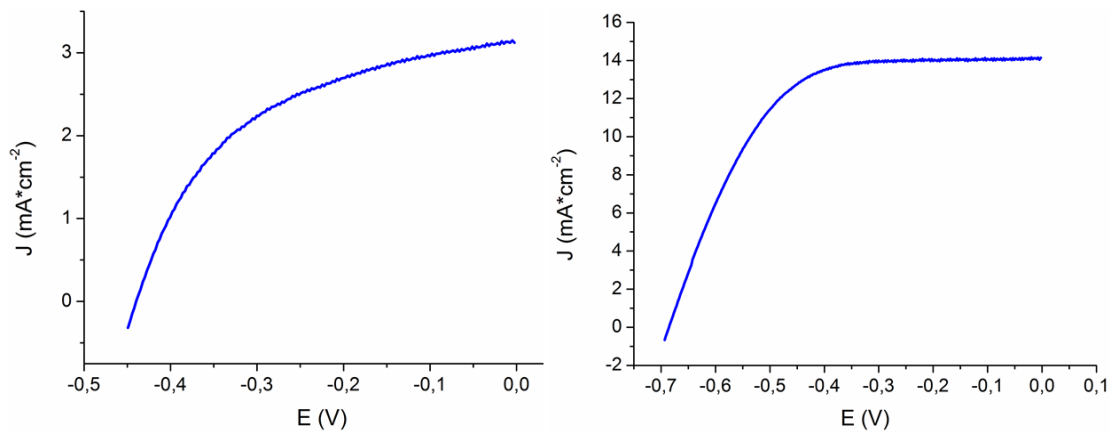


Figure 44. I-V curves for $[\text{Ru}^{\text{II}}(\text{McTerpy})(\text{dmbpy})(\text{H}_2\text{TMT})]\text{PF}_6$ (left) and N719 (right) assembled DSSCs.

$$FF = \frac{J_{pmax} * V_{pmax}}{J_{sc} * V_{oc}} \quad \mathbf{16}$$

$$\eta = \frac{P_{dssc}}{P_{lamp} * A} * 100 \quad \mathbf{17}$$

The fill factor (FF) in a DSSC indicates how far from an ideal cell (FF = 1) it is, this includes assembling processes and electronic transport behavior as well, in equation **16** J_{pmax} and V_{pmax} are the maximum current density and the maximum voltage afforded by the cells within the I-V curve (the highest area rectangle under the I-V curve). For equation **17**, P_{dssc} is the maximum power outcome from the DSSC under illumination, P_{lamp} is the power afforded by the lamp (100 mW cm^{-2}) and A is the electrode surface area.

Table IV. Performance data from the assembled DSSCs.

Compound	Power (mW)	FF	J _{sc} (mA cm ⁻²)	V _{oc} (V)	η (%)
[Ru ^{II} (McTerpy)(dmbpy)(H ₂ TMT)]PF ₆	0.175	0.49	3.12	0.44	0.7
[Ru ^{II} (McTerpy)(dmbpy)(HTMT)]	8.59 x10 ⁻²	0.58	1.71	0.36	0.35
(N-Bu ₄)[Ru ^{II} (McTerpy)(dmbpy)(TMT)]	4.79 x10 ⁻²	0.50	1.33	0.33	0.19
N719	1.32	0.60	14.14	0.69	5.28

From Table IV, it is noticeable the low values for the current density and the open circuit voltage which are accounted for the low power and efficiency of the assembled DSSCs. Due to the reference value obtained for the N719 cells, poor performance of the DSSCs sensitized with [Ru^{II}(McTerpy)(dmbpy)(H₂TMT)]PF₆ complexes is not owed to lack of manufacturing skills as shown by the relatively similar FF values. In order to clarify if it's a low electronic injection from the dye into the TiO₂ CB, monochromatic photo injection measurements were performed.

IPCE measurements

Figure 45 exhibits the monochromatic photo injection properties of the three ruthenium species prepared. It was observed that all three species IPCE followed the shape of their absorption spectra with an injection efficiency peaking around 490 nm where the MLCT $d\pi \rightarrow p\pi^*$ bands are located, the lack of absorption bands in lower energies (higher wavelengths) diminished the electronic injection. [Ru^{II}(McTerpy)(dmbpy)(H₂TMT)]PF₆ photo injection properties shown in Figure 45a proved to be the most efficient among the three species isolated with a maximum of 23% of the incident photons converted into current. On the other hand, efficiency

decreased with increasing negative charge in the TMT ligand ([Ru^{II}(McTerpy)(dmbpy)(HTMT)] Figure 44b and (N-Bu₄)[Ru^{II}(McTerpy)(dmbpy)(TMT)] Figure 44c) contrary to what was initially supposed with the electrostatic repulsion between the negatively charged TMT residue and the I₃⁻ ion.

In order to rule out the possibility of low sensitization by the species employed, desorption and quantification of the loaded [Ru^{II}(McTerpy)(dmbpy)(H₂TMT)]PF₆ complex on to DSSC anode was performed spectrophotometrically. Desorption was performed with a 0.1 mol L⁻¹ NaOH aqueous solution and diluted with deionized water to the desired volume. A value of 9.3x10¹⁶ molecules cm⁻² was found, this value is in agreement with those reported by Guimaraes in his thesis for similar ruthenium complexes.¹⁰⁹

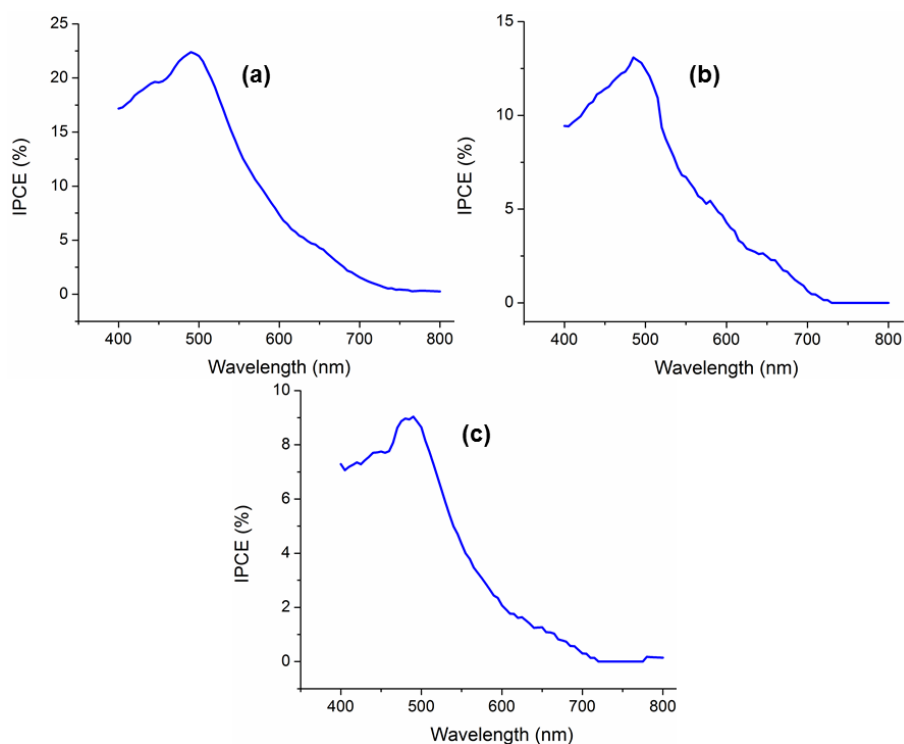


Figure 45. IPCE measurements of [Ru^{II}(McTerpy)(dmbpy)(H₂TMT)]PF₆ (a), [Ru^{II}(McTerpy)(dmbpy)(HTMT)] (b) and (N-Bu₄)[Ru^{II}(McTerpy)(dmbpy)(TMT)] (c).

By the time these experiments were performed a second bibliographic search shed light in a possible explanation for the low efficiency observed in the assembled DSSCs with our novel ruthenium dyes. Nazeeruddin and coworkers observed higher V_{oc} and FF values for sulfur containing ligands but TAS and EIS experiments showed that the sulfur atoms favored recombination lowering the conversion efficiencies of the devices by catalyzing the reduction of the I_3^- ion, concluding that sulfur containing aromatic rings should be avoided as ligands for sensitizers in DSSCs when the iodide electrolyte is employed.¹¹⁷

Chapter I conclusions

Synthesis and characterization of the $[Ru^{II}(McTerpy)(dmbpy)(TMT)]PF_6$ complex was successfully performed through conscious electronic design aiming for better absorption properties and a wider spectral absorption range as observed by PhD Robson in his doctoral research. A step by step process was followed since one of the three ligands was synthesized in the lab and every intermediary complex was characterized to ensure a proper approach to the desired complex.

Working DSSCs were assembled employing the laboratory's established protocols and tested in a solar simulator to generate electric power.

Due to the afforded experimental evidence and supported by the literature we conclude that the low efficiency of the assembled DSSCs accounts for the sulfur-triiodide interaction via lower electron recombination lifetimes.

CHAPTER II: Synthesis and Characterization of [Ru^{III}(NH₃)₅(μ-dpypn)Fe^{II}(CN)₅].4H₂O Complex.

[Ru^{II}(NH₃)₅(dpypn)](PF₆)₂.3H₂O characterization

UV-vis spectra

Electronic spectra for the species [Ru^{III}(NH₃)₅Cl]Cl₂ and [Ru^{II}(NH₃)₅(dpypn)](PF₆)₂.3H₂O (Ru^{II}L) are shown in Figure 46 in the 10⁻³ mol L⁻¹ range. The spectra are rather simple due to the low number of transitions observed which were assigned by comparison between them. For the ruthenium (III) species (black line) a really strong band is located below 200 nm assigned to possible n→σ* transitions of the NH₃ ligands and a weak LMCT transition from the chloride to the ruthenium center (pπ→dπ) at 327 nm.¹¹⁸ On the other hand, the Ru^{II}L complex (red line) displays a pπ→pπ* ascribed to IL transitions of the dpypn ligand while preserving the n→σ* band now above 200 nm due to dpypn contribution.

Reduction of the metal center provoked ligand exchange between chloride and dpypn which bears a π conjugated system capable of accepting charge from the Ru(II) ion emerging an MLCT band centered at 415 nm.

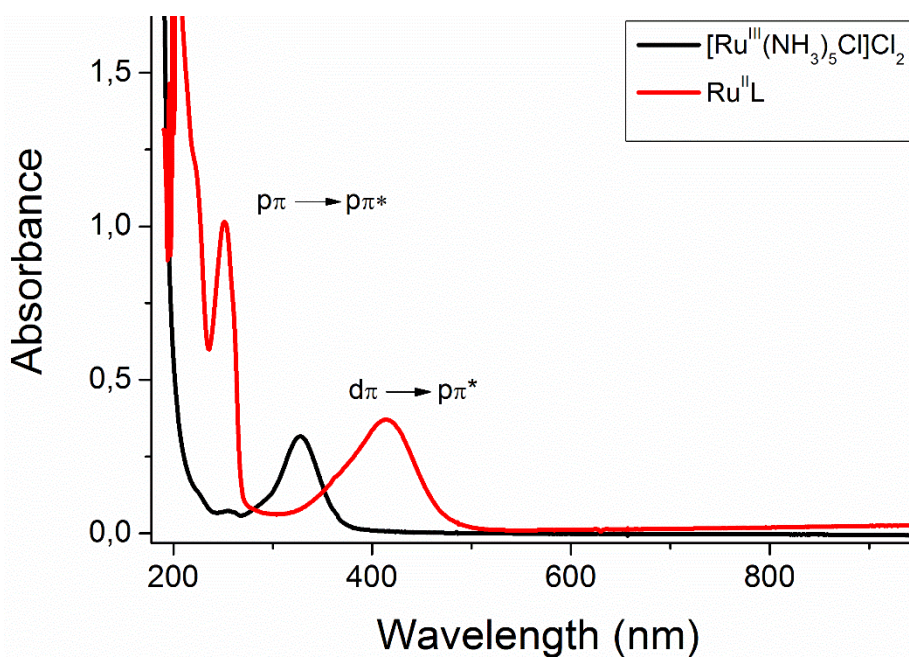


Figure 46. UV-vis spectra from $[\text{Ru}^{\text{III}}(\text{NH}_3)_5\text{Cl}]\text{Cl}_2$ (black line) and $[\text{Ru}^{\text{II}}(\text{NH}_3)_5(\text{dpypn})](\text{PF}_6)_2 \cdot 3\text{H}_2\text{O}$ (red line) in water.

Mass spectrometry

ESI mass spectra for the $[\text{Ru}^{\text{II}}(\text{NH}_3)_5(\text{dpypn})](\text{PF}_6)_2 \cdot 3\text{H}_2\text{O}$ complex is shown in Figure 47 displaying a base peak at 199.12 m/z assigned to the ion $[\text{dpypn}+\text{H}]^+$ higher mass to charge ratio peaks exhibit low intensity due to their low ionization efficiency when compared to the dpypn ion. Nevertheless, expansion of the 225 to 400 m/z region displays a succession of peaks bearing isotopic distribution for species containing one ruthenium atom. Molecular ion $[\text{M}]^+$ was assigned to the $[\text{Ru}(\text{NH}_3)_5(\text{dpypn})]^+$ species at 387.12 m/z and a calculated value of 385.15 m/z, some kind of charge neutralization/exchange phenomena must be taking place in order to afford a 1+ species (i.e. hydride transfer). Following this peak, there are five peaks product of successive loss of ammonia as follows: $[\text{Ru}(\text{NH}_3)_4(\text{PyC3Py})]^+$ 368.13 m/z found at 369.09 m/z, $[\text{Ru}(\text{NH}_3)_3(\text{PyC3Py})]^+$ 351.10 m/z found at 352.06 m/z, $[\text{Ru}(\text{NH}_3)_2(\text{PyC3Py})]^+$ 334.07 m/z found at 336.04 m/z, $[\text{Ru}(\text{NH}_3)(\text{PyC3Py})]^+$ 317.05 m/z found at 316.03 and $[\text{Ru}(\text{PyC3Py})]^+$ 300.02 m/z found at 299.01 m/z.

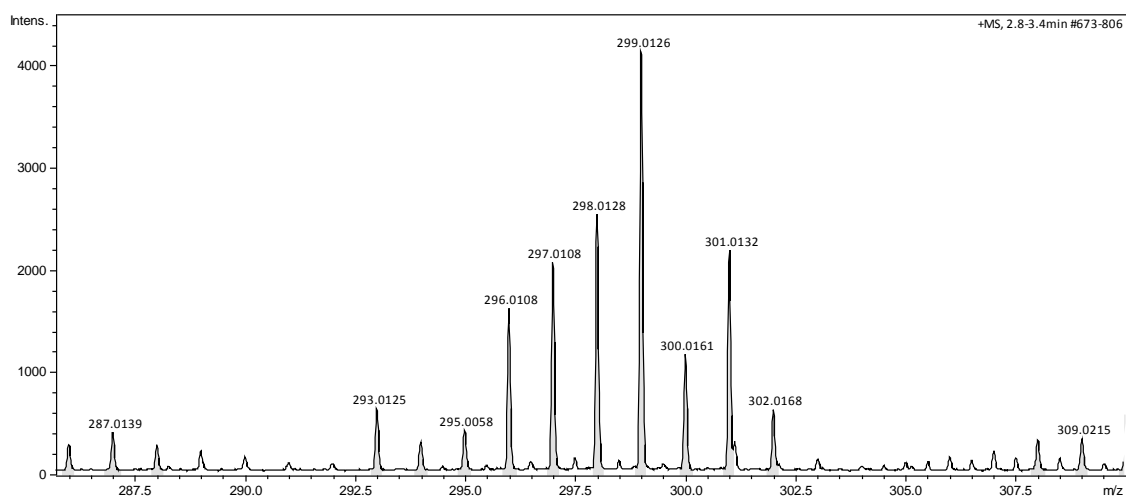
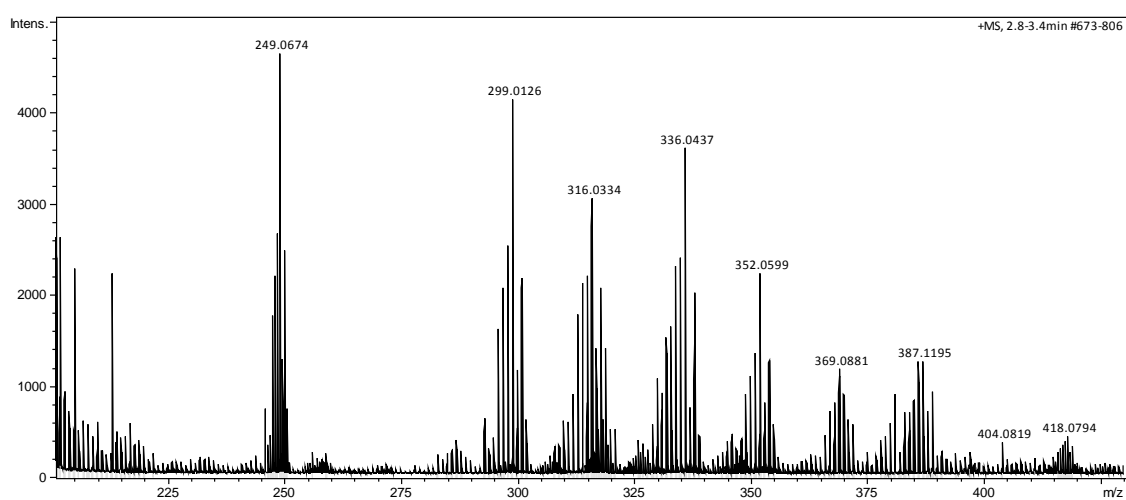
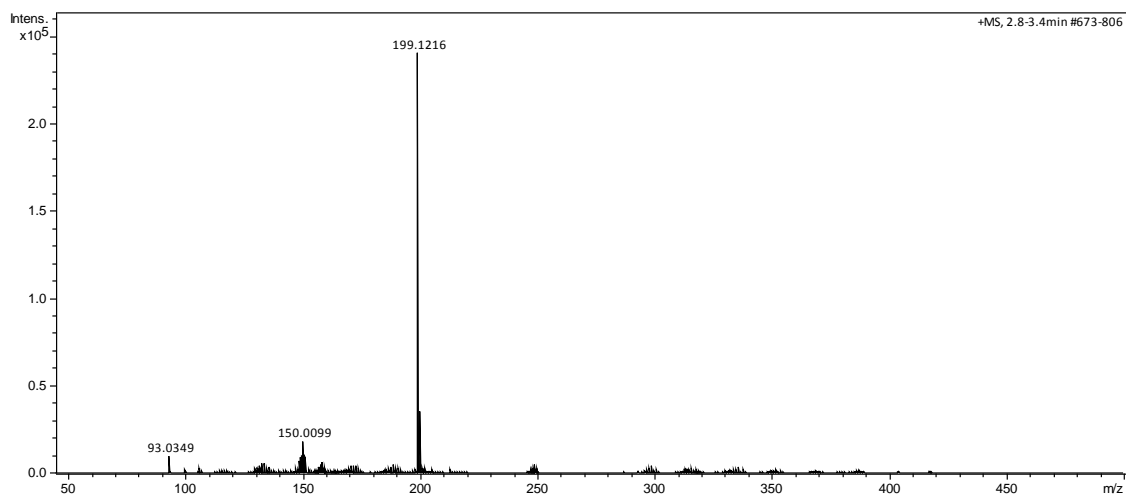


Figure 47. ESI-MS from $[\text{Ru}^{\text{II}}(\text{NH}_3)_5(\text{dpypn})](\text{PF}_6)_2 \cdot 3\text{H}_2\text{O}$. Nebulizer: 0.4 Bar, dry gas: 4 L min⁻¹, temp: 200 °C, HV: 4500 V.

[Ru^{III}(NH₃)₅(μ-dpypn)Fe^{II}(CN)₅].4H₂O characterization

FTIR spectroscopy

Figure 48 displays the FTIR spectrum of the [Ru^{III}(NH₃)₅(μ-dpypn)Fe^{II}(CN)₅].4H₂O complex labeled as Ru^{III}LFe^{II}, being L = dpypn. Vibrational modes are assigned and described within the figure being the most noteworthy the stretching modes for NH₃ ligands (ν-NH₃) at 3445 and 3240 cm⁻¹.³ The characteristic ν-CN peak for the pentacyanoferrate moiety allowed us to conclude and assign the metal oxidation states in the mixed-valence complex. This vibrational mode appeared at 2044 cm⁻¹ pointing out a reduced state of a Fe(II) center.^{119,120} Whereas for the oxidized Fe(III) species this vibrational mode is shifted to higher frequencies above 2150 cm⁻¹.

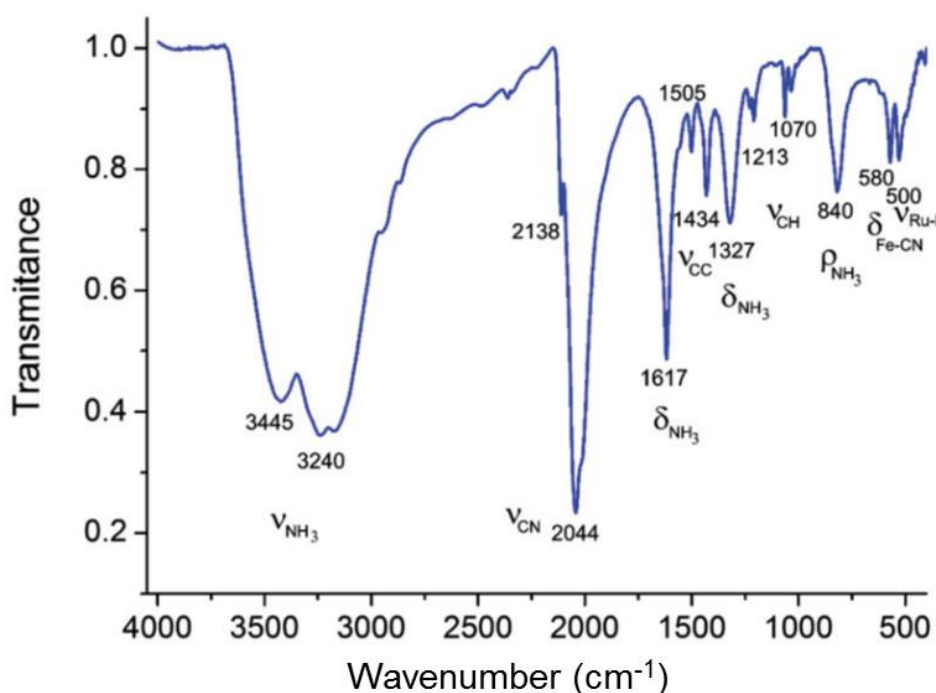


Figure 48. FTIR spectrum of the mixed-valence complex [Ru^{III}(NH₃)₅(μ-dpypn)Fe^{II}(CN)₅].4H₂O in KBr pellets.

Electrochemistry

Cyclic voltammetry combined with differential pulse voltammetry shown in Figure 49 confirm the formation of the heteronuclear mixed-valence complex denoted as Ru^{III}LFe^{II}. Figure 49a exhibits the CV of the homoleptic Ru^{II}LRu^{II} and Fe^{II}LFe^{II} complexes with a single Ru^{III/II} and Fe^{III/II} processes at E_{1/2} 0.26 and 0.44 V respectively. The fact just one redox event is observable for both ruthenium and iron homonuclear species evidences the lack of electronic coupling between the metal centers thru the bridging dpypn ligand.

These E_{1/2} values confirmed the easier oxidizable nature of the ruthenium moiety over the iron center supporting the hypothesis of the ruthenium undergoing the redox process in presence of dioxygen in the heteronuclear complex synthesis. This was further sustained by the CV (Figure 48b) acquired while the reaction between Ru^{II}L and [Fe^{II}(NH₃)(CN)₅]³⁻ was taking place under inert atmosphere the E_{1/2} values were exactly the same as for the homonuclear complexes (0.26 and 0.44 V) confirming no electronic coupling even in the Ru^{II}LFe^{II} species. Furthermore, DPV experiments (Figure 48c) allowed direct comparison of the current values for both Ru^{III/II} and Fe^{III/II} processes showing an expected 1:1 ratio between them.

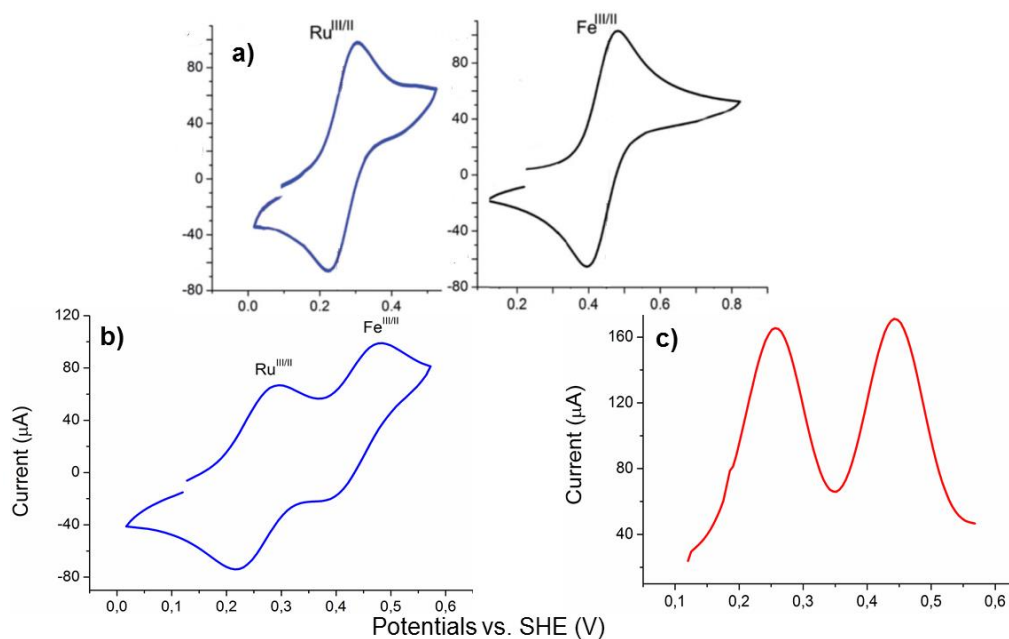


Figure 49. CV measurements of Ru^{II}LRu^{II} and Fe^{II}LFe^{II} (a), Ru^{II}LFe^{II} (b) and DPV of Ru^{II}LFe^{II} (c) at 50 mV s⁻¹ in aqueous 0.1 mol L⁻¹ KCl.

UV-vis spectra

UV-vis spectra for the Ru^{II}LFe^{II} species was obtained in water and under inert atmosphere in order to avoid precipitation of the mixed-valence complex thus avoiding scattering issues. Figure 50 compares the electronic spectra of the heteronuclear (Ru^{II}LFe^{II}), mononuclear ruthenium and iron (Ru^{II}L and Fe^{II}L) species. It should be noted that the IL ($p\pi \rightarrow p\pi^*$) transition at 251 nm of the dpypn ligand remains stable for the three complexes whereas the MLCT band for the Ru^{II}LFe^{II} complex is broadened and located right in between the Ru-dpypn and Fe-dpypn MLCT bands at 376 nm, suggesting an overlap between these bands in the heteronuclear species, shedding light of the presence of the two metal centers within the complex. Also, if UV-vis was possible to be taken for the mixed-valence complex Ru^{III}LFe^{II}, ruthenium MLCT band would not appear due to its oxidation state.

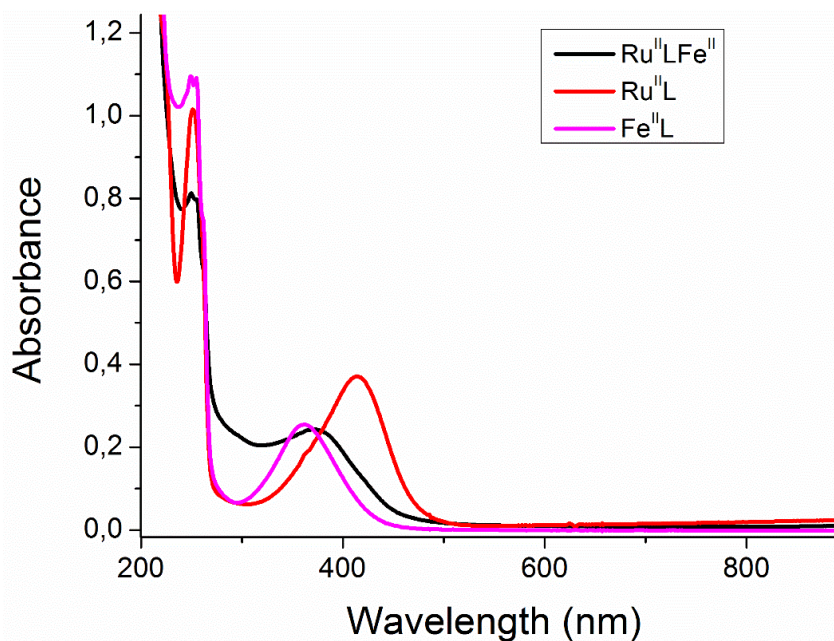


Figure 50. UV-vis spectra from $[\text{Ru}^{\text{II}}(\text{NH}_3)_5(\mu\text{-dpypn})\text{Fe}^{\text{II}}(\text{CN})_5]^-$ ($\text{Ru}^{\text{II}}\text{LFe}^{\text{II}}$), $[\text{Ru}^{\text{II}}(\text{NH}_3)_5(\text{dpypn})]^{2+}$ ($\text{Ru}^{\text{II}}\text{L}$) and $[\text{Fe}^{\text{II}}(\text{CN})_5(\text{dpypn})]^{3-}$ ($\text{Fe}^{\text{II}}\text{L}$) in water.

A more comprehensive comparison was performed including the electronic spectra for the homonuclear species shown in Figure 51. Figure 51a exhibits the UV-vis spectra of the iron species $\text{Fe}^{\text{II}}\text{L}$ and $\text{Fe}^{\text{II}}\text{LFe}^{\text{II}}$ and Figure 51b presents the electronic spectra for the ruthenium complexes $\text{Ru}^{\text{II}}\text{L}$ and $\text{Ru}^{\text{II}}\text{LRu}^{\text{II}}$ both Figure 51a and 51b follow the same band assignment performed for Figure 49. Nevertheless, there are some details to observe in this figure. First of all, MLCT bands for the mononuclear and homonuclear species (Figure 51a and 51b) are located at the same wavelength 365 nm for the $\text{Fe}^{\text{II}}\text{L}$ and $\text{Fe}^{\text{II}}\text{LFe}^{\text{II}}$ complexes and 415 nm for $\text{Ru}^{\text{II}}\text{L}$ and $\text{Ru}^{\text{II}}\text{LRu}^{\text{II}}$, further supporting the electrochemical evidence suggesting no electronic coupling mediated by the dpypn ligand. IL transfers exhibit a pattern of just one band for the homonuclear $\text{Fe}^{\text{II}}\text{LFe}^{\text{II}}$ and $\text{Ru}^{\text{II}}\text{LRu}^{\text{II}}$ species and two bands for the mononuclear $\text{Fe}^{\text{II}}\text{L}$ and $\text{Ru}^{\text{II}}\text{L}$ complexes. This behavior is due to higher symmetry of the homonuclear compounds.

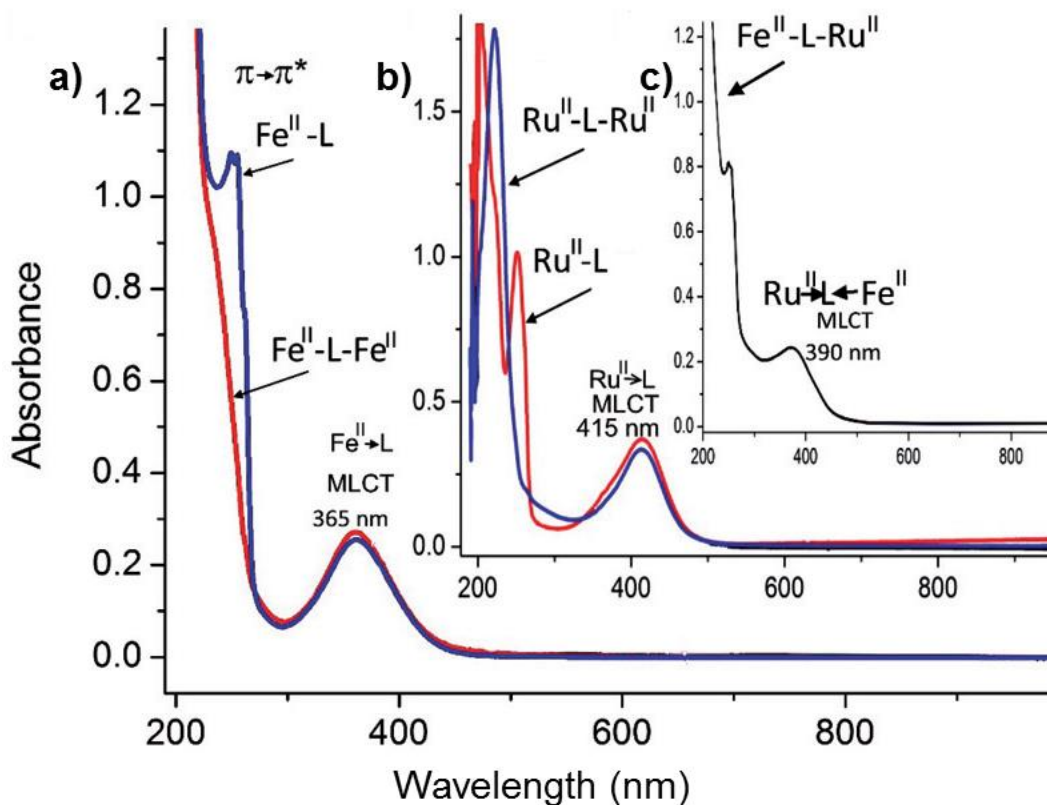


Figure 51. UV-vis spectra from Fe^{II}L and Fe^{II}LFe^{II} (a), Ru^{II}L and Ru^{II}LRu^{II} (b) and Ru^{II}LFe^{II} in water under N₂ atmosphere.

Vis-NIR spectra

Visible to near infrared spectra (Vis-NIR) shown in Figure 52 clarifies the nature and the goal behind this mixed-valence complex, an intervalence (IT) transition between the two metal centers. Due to the non-conjugated nature of the bridging dpypn ligand the IT must be from an outer sphere regime facilitated by the proximity of the metal ions owed to the electrostatic attraction and bending of the dpypn moiety. This electronic transfer appears in the Ru^{III}LFe^{II} spectrum with a maximum absorption between 1100 and 1400 nm expected for an IT Fe^{II}→Ru^{III}. The broadness nature of this band suggests a localized mixed-valence complex with some kind of lattice distortion on the basis of Hush's theoretical $\Delta\nu_{1/2}$ relationships.¹²¹ This strong IT band was tested chemically in order to dismiss any kind of artifact from the equipment. Therefore, reduction with hydrazine hydrate in order to reduce the

$\text{Ru}^{\text{III}} \rightarrow \text{Ru}^{\text{II}}$ center was observed immediately by the disappearance of the IT band (black line in Figure 52) and visually by the changing color from green to yellow.

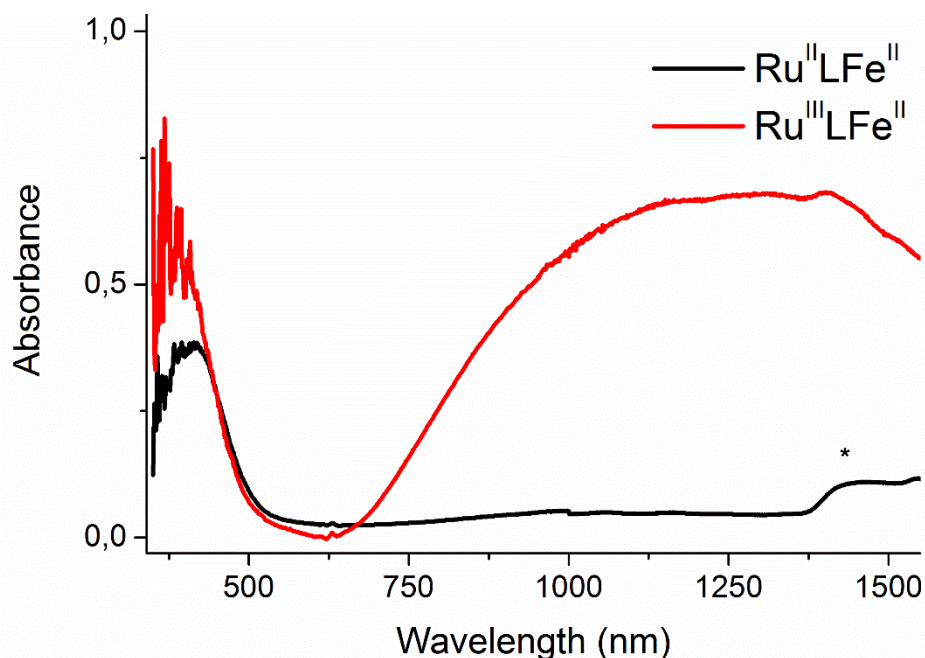


Figure 52. Vis-NIR spectra of $\text{Ru}^{\text{II}}\text{LFe}^{\text{II}}$ (black line) and $\text{Ru}^{\text{III}}\text{LFe}^{\text{II}}$ (red line) in the solid state. *Instrumental artifact.

Mechanical hindrance employing β -CD through an inclusion compound $[\text{Ru}^{\text{III}}(\text{NH}_3)_5\{\mu\text{-(dpypn}\cdot\beta\text{-CD)}\}\text{Fe}^{\text{II}}(\text{CN})_5]$ shown in Figure 17 was also used in order to prove the outer-sphere IT. Figure 53 shows the comparison between the mixed-valence complex (black line) spectrum with its IT band centered at 1250 nm due to the bent configuration of the dpypn ligand and the inclusion species (red line) with β -CD, in this case is observable the absence of the IT band, supporting the hypothesis of an outer-sphere electronic transition mechanism owed to the lack of proximity between the two metal centers. The marked absorbance difference between the two species is owed to the fact that the $\text{Ru}^{\text{III}}\text{LFe}^{\text{II}}$ spectrum was acquired from the solid complex whereas the $[\text{Ru}^{\text{III}}(\text{NH}_3)_5\{\mu\text{-(dpypn}\cdot\beta\text{-CD)}\}\text{Fe}^{\text{II}}(\text{CN})_5]$ species was obtained by concentrating the compound over the measuring surface with successive drying processes.

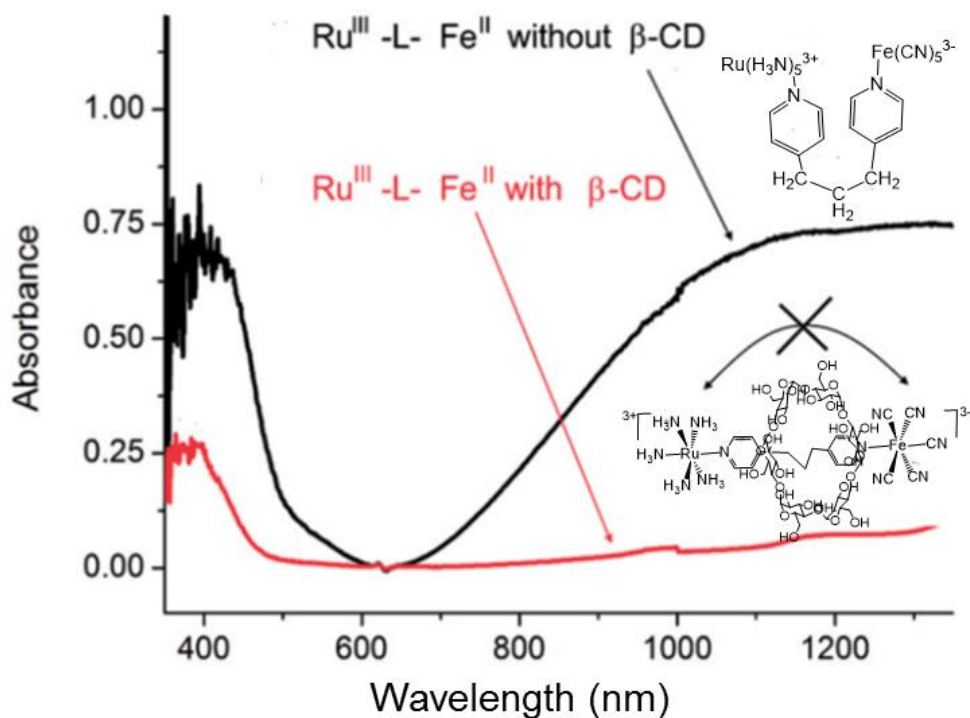


Figure 53. Vis-NIR spectra of $\text{Ru}^{\text{III}}\text{LFe}^{\text{II}}$ (black line) and $[\text{Ru}^{\text{III}}(\text{NH}_3)_5\{\mu\text{-}(\text{dpypn } \beta\text{-CD})\}\text{Fe}^{\text{II}}(\text{CN})_5}]$ (red line).

DFT calculations

All of these experimental evidences were supported by DFT calculations that showed effective bending of the dpypn ligand in the mixed-valence complex (Figure 54a) with the spin density fully localized in the Ru center as expected for a Ru(III) configuration making this a class II intervalence complex.¹²²

On the other hand, homonuclear species $\text{Fe}^{\text{II}}\text{LFe}^{\text{II}}$ and $\text{Ru}^{\text{II}}\text{LRu}^{\text{II}}$ (Figure 54b and 54c respectively) afforded linear configurations probably as consequence of electrostatic repulsion of the equally charged metal residues. Consequently, spin density plots showed spin localization for their hypothetical mixed-valence forms in just one of the metal moieties, indicating no communication between them.

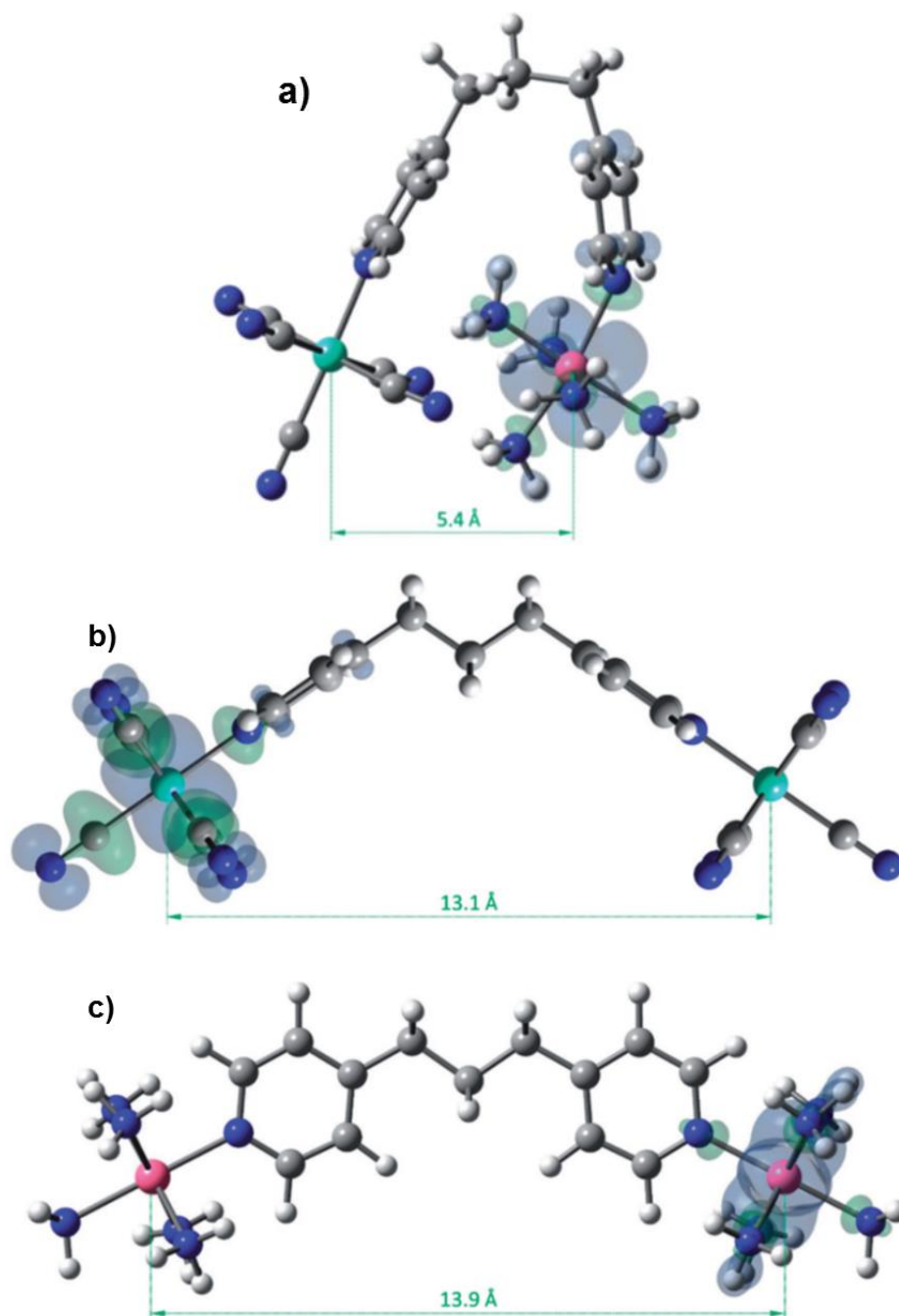


Figure 54. DFT structures of $\text{Ru}^{\text{III}}\text{LFe}^{\text{II}}$ (a), $\text{Fe}^{\text{II}}\text{LFe}^{\text{II}}$ (b) and $\text{Ru}^{\text{II}}\text{LRu}^{\text{II}}$ (c).

Chapter II conclusions

Synthesis and characterization over a series of mononuclear Fe(II) and Ru(II)/Ru(III) complexes were successfully performed, along with homonuclear and heteronuclear complexes bearing the non-conjugated dpypn bridging ligand.

Experimental results proved the existence of an IT electronic transfer from the Fe(II) to the Ru(III) center in the heteronuclear species. Furthermore, this electron transfer ceased upon chemical reduction of the Ru(III) to a Ru(II) state using hydrazine. And by physical hindrance with β -CD by forming an intercalation compound with the dpypn ligand preventing electrostatic mediated bending.

These experimental results were supported by DFT and TDDFT calculations performed by PhD Reginaldo C. Rocha at Los Alamos National Laboratory in the USA.

CHAPTER III: Synthesis and Characterization of $\text{Co}^{\text{III}}\text{TRP}(\text{dmbpy})$ and its GO Composite for Dissolved Oxygen Sensors.

$\text{cis-}[\text{Ru}^{\text{II}}(\text{dmbpy})_2\text{Cl}_2]$ characterization

UV-vis spectra

UV-vis spectrum of $\text{cis-}[\text{Ru}^{\text{II}}(\text{dmbpy})_2\text{Cl}_2]$ complex (Figure 55) displays an IL band from the dmbpy $\rho\pi \rightarrow \rho\pi^*$ transition at 297 nm along with two MLCT bands from the $\text{d}\pi \rightarrow \rho\pi^*$ transitions at 413 nm and 569 nm.

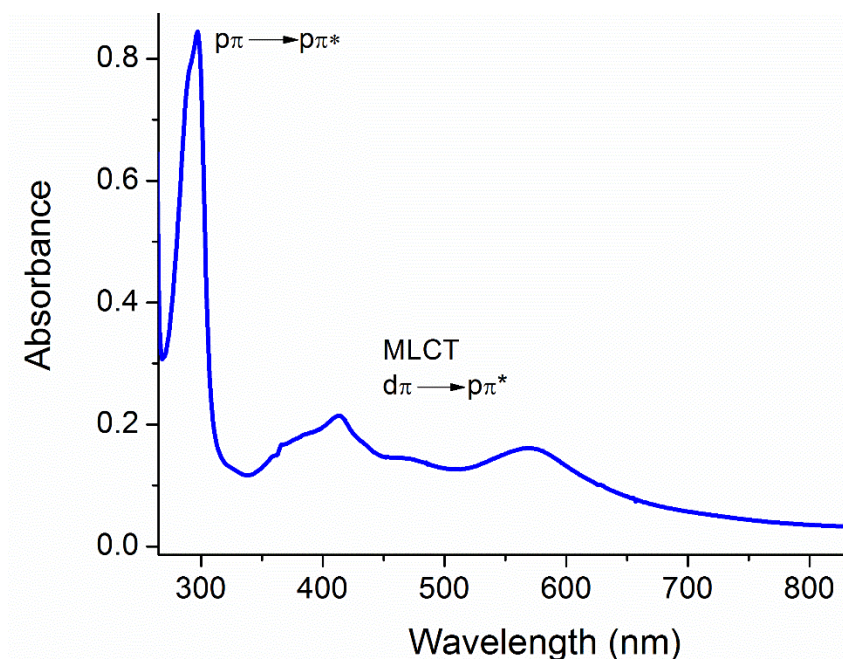


Figure 55. UV-vis spectra of the $\text{cis-}[\text{Ru}^{\text{II}}(\text{dmbpy})_2\text{Cl}_2]$ complex in MeOH.

$\text{Co}^{\text{II}}\text{TPyP}$ characterization

UV-vis spectra

Electronic spectrum of $\text{Co}^{\text{II}}\text{TPyP}$ shown in Figure 56 exhibits just two bands. The first one located at 413 nm (Soret) and the second at 533 nm (Q_{0-0}). This band

pattern and transition energies are typical of a Co^{II} metallated porphyrin as reported in literature.^{123,124} As we will be further observed for the supramolecular porphyrins in which Co^{II} TPyP was employed, the cobalt oxidation state will be $\text{Co}(\text{III})$ for the catalytic and sensing purposes. For this particular synthesis the desired oxidation state was $\text{Co}(\text{II})$ to facilitate purification.

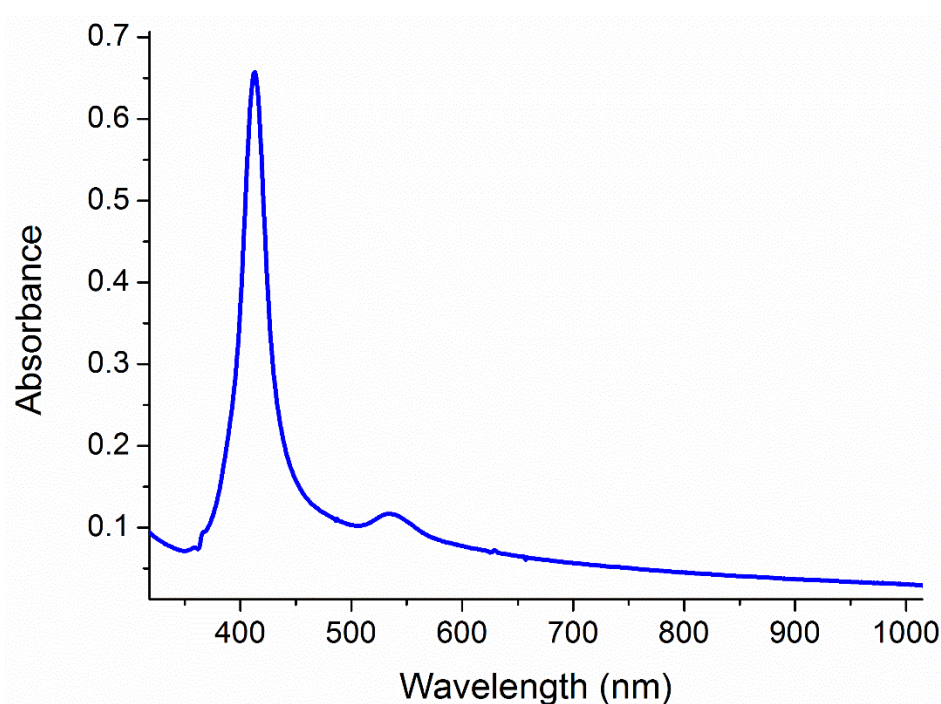


Figure 56. UV-vis spectra of Co^{II} TPyP in DMF.

Co^{III} TRP(dmbpy) characterization

UV-vis spectra

UV-vis spectrum shown in Figure 57 and the resemblance with Figures 55 and 56 stands out. The overall spectrum for the Co^{III} TRP(dmbpy) species is the additive overlap of its constituents' spectra starting by the IL $\rho\pi \rightarrow \rho\pi^*$ transition from the dmbpy at 292 nm slightly shifted towards higher energy.

The Soret band is found at 436 nm shifted towards lower energies when compared to the non-ruthenated cobalt porphyrin this is probably due to orbital

stabilization from the electron donating *cis*-[Ru^{II}(dmbpy)₂Cl₂] complexes. Broadening of this band is noticeable and is attributed to the effect of the MLCT bands from the ruthenium complexes.

Q band region now displays two absorptions located at 545 and 594 nm assigned as the Q₁₋₀ and Q₀₋₀ transitions, indicating an oxidation state change for the cobalt center being now Co(III). This is due to the purification processes performed without inert atmosphere.

Moreover, the absorption spectrum exhibits broad bands at 366 nm and 497 nm ascribed to the peripheral ruthenium complexes MLCT Ru dπ → ππ* dmbpy.

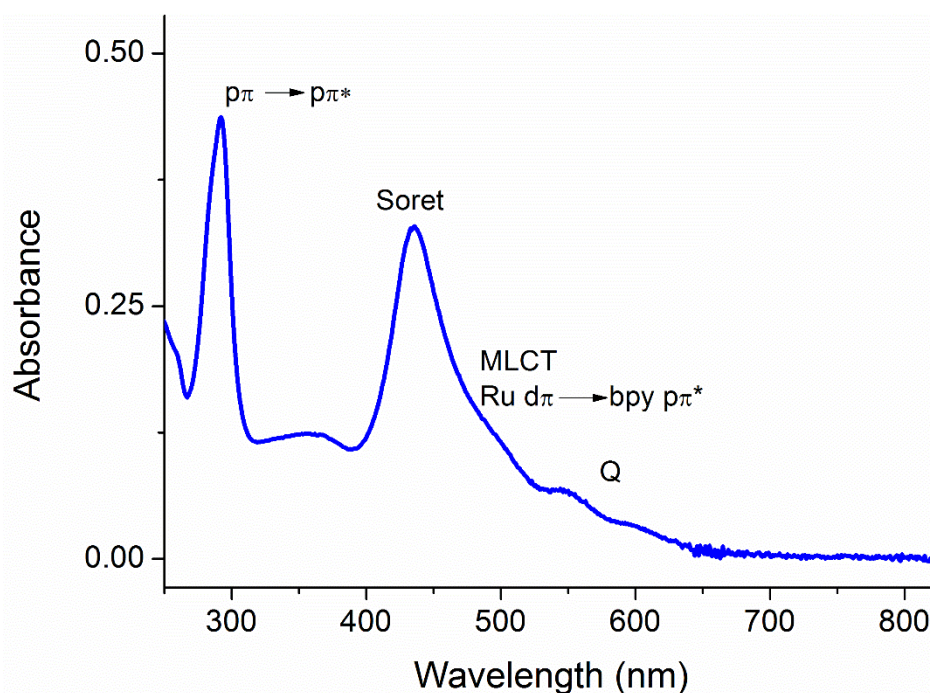


Figure 57. UV-vis spectra of Co^{III}TRP(dmbpy) in MeOH.

Raman spectra

Raman spectra for the Co^{III}TRP(dmbpy) compound is shown in Figure 58 and collected employing the 488 nm Ar laser as excitation source. This spectrum displays typical frequencies for the functional groups present within the supramolecule. The

1020 cm^{-1} peak is assigned to pyridines and pyrrole breathing modes and deformation $\delta(\text{py})$ at 1213 cm^{-1} . $\nu(\text{C-CH}_3)$ is ascribed to the peak at 1316 cm^{-1} and 1369 cm^{-1} is assigned as $\delta(\text{CH}_3)$ mode. On the other hand, the peaks at 1544 and 1606 cm^{-1} are from the $\nu(\text{C=N})$ and $\nu(\text{C=C})$ respectively.

It must be taken into account that these attributions are merely tentative due to the complexity of the $\text{Co}^{\text{III}}\text{TRP}(\text{dmbpy})$ supramolecule, therefore contribution of several vibrational modes is advised, promoting broadening in the mentioned peaks.

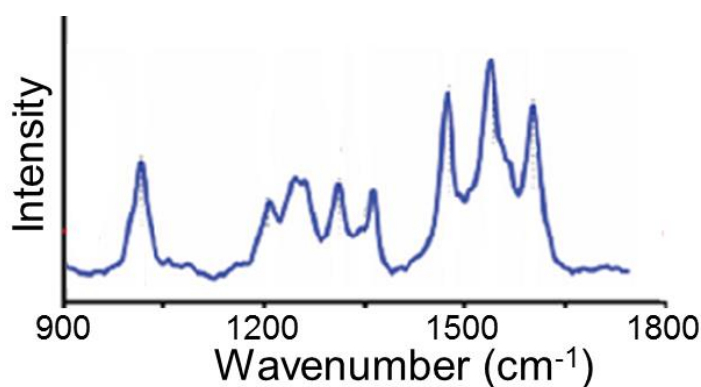


Figure 58. Raman spectra of $\text{Co}^{\text{III}}\text{TRP}(\text{dmbpy})$.

Electrochemistry

CV experiments in DMF and water as solvents shown in Figure 59a and 59b respectively exhibit a reversible process for the $\text{Ru}^{\text{III}}/\text{Ru}^{\text{II}}$ at $E_{1/2} = 0.91$ V in agreement with polypyridyl substituted ruthenium centers. The fact that only one process is observed indicates a weak electronic communication among the ruthenium moieties within the supramolecular porphyrin structure.

The cathodic region of the CV (Fig 59a), only displays the successive reduction events for the porphyrin ring at $E_{\text{pc}} = -1.05$ and -1.21 V. Unfortunately, due to catalytic currents the reduction processes for the dmbpy ligand are not visible and should appear at approximately $E_{1/2} = -1.5$ and -1.7 V. Figure 59b presents a quasi-

reversible wave at $E_{1/2} = -0.59$ V that has been assigned to the $\text{Co}^{\text{III/II}}\text{TRP}(\text{dmbpy})$ process.⁸⁵

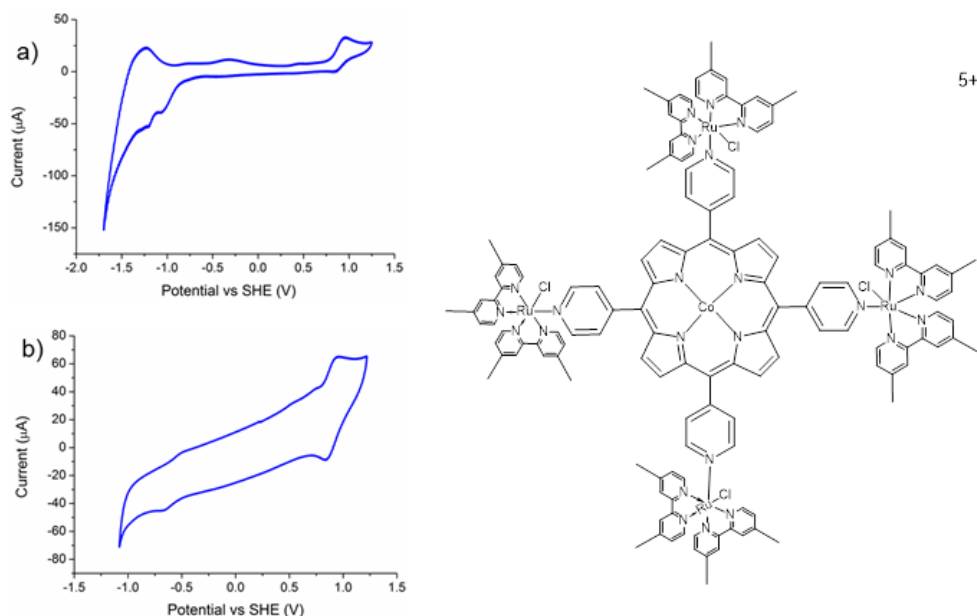


Figure 59. Cyclic voltammograms of $\text{Co}^{\text{III}}\text{TRP}(\text{dmbpy})$ in DMF (a) and water (b).

Spectroelectrochemistry

This technique was employed in order to study the behavior of the absorption spectra with applied potential and confirm the band assignment performed. It was also vital for confirmation of the cobalt center presence since the process was not observable during CV experiments due to its low heterogeneous electron transfer kinetics.⁸⁵

Figure 60 presents the spectroelectrochemistry performed in the 0.717 V to 1.017 V potential window. The first noticeable change is the IL band ($\rho\pi \rightarrow \rho\pi^*$) diminishing at 292 nm and shifting towards lower energy at 310 nm. Soret band (436 nm) is affected by ruthenium oxidation even though its transition is not linked to the ruthenium complexes since it involves orbitals centered in the porphyrin ring. This intensity change is owed to the MLCTs bands ($d\pi \rightarrow \rho\pi^*$) disappearance at 413 and

569 nm due to the higher oxidation state of the ruthenium center neglecting the electronic transfer from the metal to the ligand orbitals. It is worth mentioning that Soret band profile resembles that of the non-ruthenated Co^{II} TPyP in Figure 56.

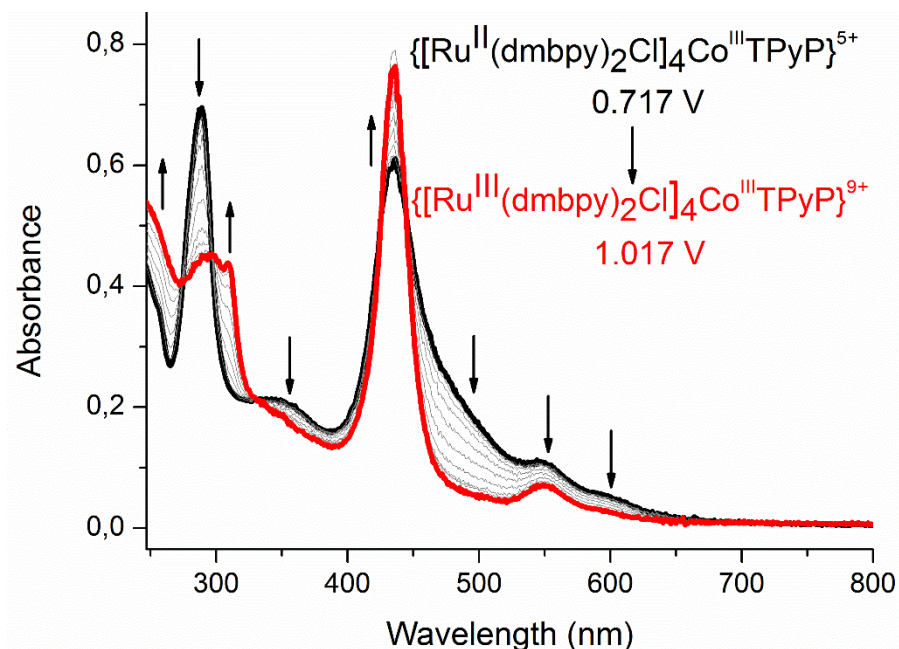


Figure 60. Spectroelectrochemistry spectra of Co^{III} TRP(dmbpy) in DMF.

Figure 61 shows the spectroelectrochemical behavior over the potential window -0.105 to 0.277 V these were the probed potentials in which the $\text{Co}^{\text{III/II}}$ process is located in structurally similar TRPs.^{82,85}

IL band ($\rho\pi \rightarrow \rho\pi^*$) from dmbpy shows little changes in the potential sweep confirming no influence from the cobalt center into its transitions. The most outstanding alterations were observed in the Soret and Q bands. In the case of the Soret band, its maximum absorption wavelength shifted from 436 nm to 416 nm in the Co^{II} form generating a very well defined isosbestic point which allowed the calculation of the $E_{1/2} = 0.19$ V for the $\text{Co}^{\text{III/II}}$ process employing the Nernst equation

19.

$$E_{app} = E_{1/2} + \frac{RT}{nF} \ln \frac{[Ox]}{[Red]}$$

19

In this case, E_{app} is the applied potential, $E_{1/2}$ is the half-wave potential in which 50% of the porphyrin species are oxidized and the other 50% are reduced, R is the gas constant ($J K^{-1} mol^{-1}$), T is temperature in K, n indicates the number of electrons transferred in the process, F is the Faraday constant and $[Ox]$ and $[Red]$ are the concentrations of oxidized and reduced species.¹²⁵

Q bands present in the $Co^{III}TRP(dmbpy)$ supramolecule are diminished and become a single Q band in the $Co^{II}TRP(dmbpy)$ species. These shifts from Soret and Q bands are in agreement with the electronic spectra for the $Co^{II}TPyP$ complex shown in Figure 56.

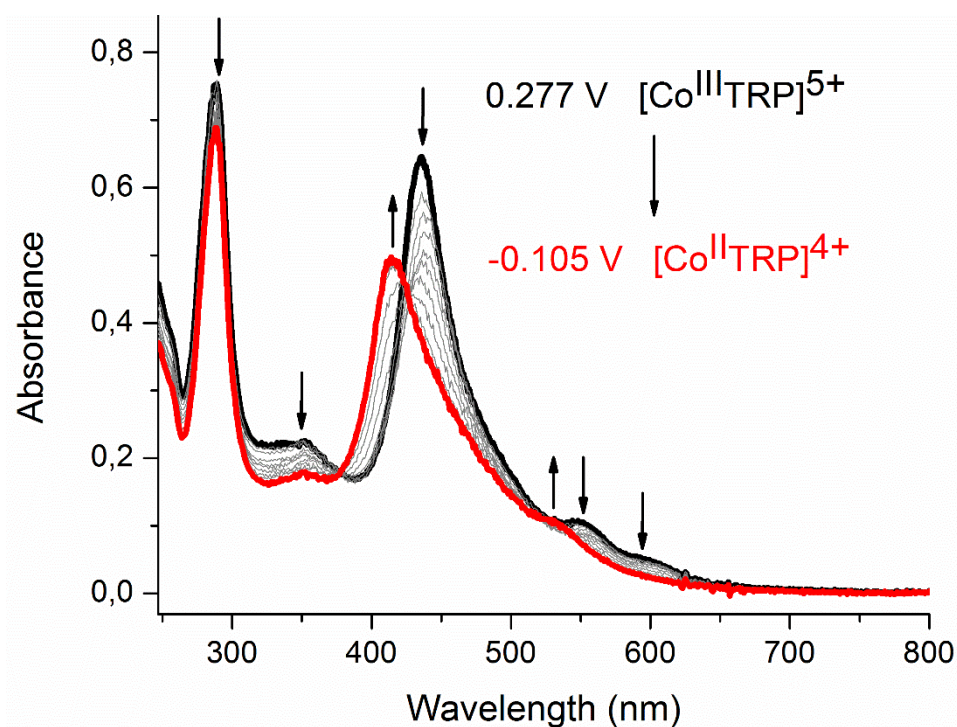


Figure 61. Spectroelectrochemistry spectra of $Co^{III/II}TRP(dmbpy)$ in DMF.

Co^{III}TRP(dmbpy)/4GO composite characterization

UV-vis spectra

Comparative absorption/scattering spectra for the Co^{III}TRP(dmbpy)/4GO composite and its isolated constituents GO and Co^{III}TRP(dmbpy) is shown in Figure 62. The scattering spectrum profile of the composite (black line) is that of the additive contribution of the GO scattering spectrum (red line) and absorption spectrum of Co^{III}TRP(dmbpy) supramolecule (blue line) indicating weak interaction between them. It is noticeable the presence of the Soret band at 436 nm and the IL dmbpy $\pi\pi \rightarrow \pi\pi^*$ transition at 292 nm. Increasing baseline both in GO and composite spectra indicates the interaction between Co^{III}TRP(dmbpy) and GO ensuring the formation of the desired Co^{III}TRP(dmbpy)/4GO compound.

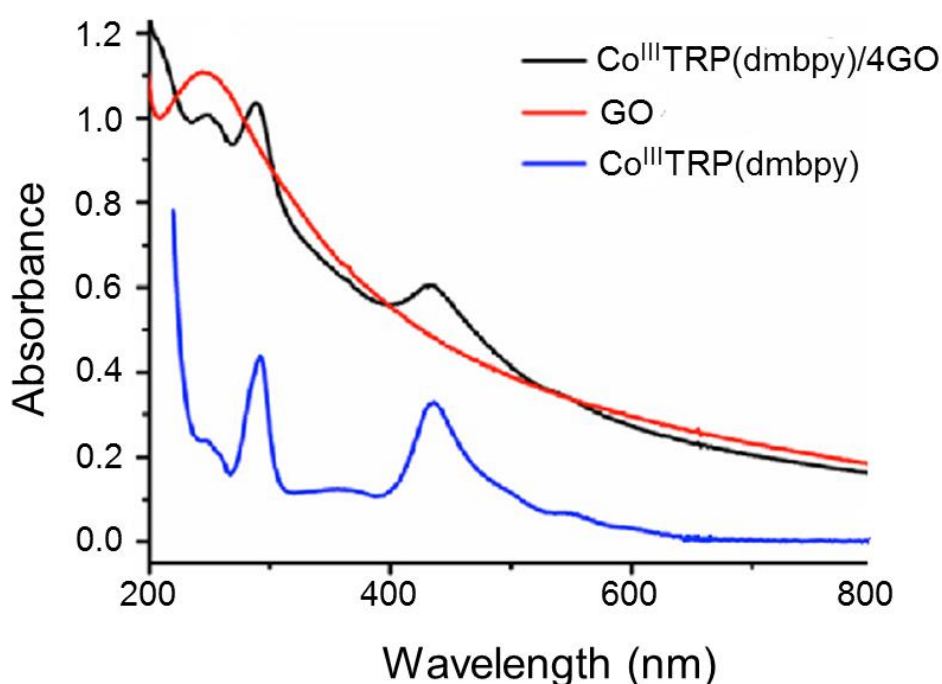


Figure 62. UV-vis/scattering spectra of Co^{III}TRP(dmbpy) (blue line), GO (red line) and Co^{III}TRP(dmbpy)/4GO composite (black line).

Raman spectra

Comparative Raman spectra for the GO, Co^{III}TRP(dmbpy) and Co^{III}TRP(dmbpy)/4GO is shown in Figure 63a. GO spectrum (red line) possess two distinguishable peaks assigned as the symmetric D band at 1353 cm⁻¹ and a G band at 1608 cm⁻¹ from vC=C.

It is observed in the composite spectrum the additive contribution of the peaks of the GO and Co^{III}TRP(dmbpy) constituents without any energy shift in the vibrational modes indicating once again a weak interaction between these two moieties' π-systems.

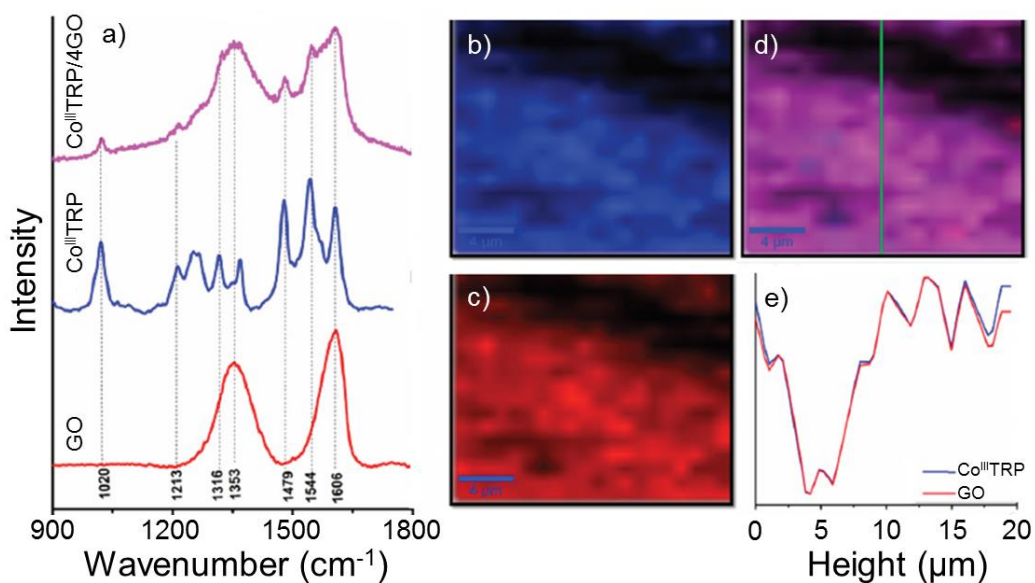


Figure 63. Raman spectra of GO, Co^{III}TRP(dmbpy) and Co^{III}TRP(dmbpy)/4GO (a), confocal Raman images of Co^{III}TRP(dmbpy)/4GO generated from Co^{III}TRP(dmbpy) spectra (b), from GO (c) and convolved image (d). Raman profile contribution of Co^{III}TRP(dmbpy) and GO along

Composite homogeneity is of crucial importance for possible applications. Therefore, confocal Raman images were generated in order to observe the distribution of the Co^{III}TRP(dmbpy) (Fig 63b), GO sheets (Fig 63c) and the overall allocation of the composite along the working surface (Fig 63d). With these chemical mappings, it was observed a homogeneous distribution of both Co^{III}TRP(dmbpy) and

GO along the surface explored, confirmed by the convoluted image in Figure 63d and its Raman profile contribution (Figure 63e) along the green line displaying the binary character of the deposited composite.

Co^{III}TRP(dmbpy)/4GO composite electrochemical behavior

This composite was drop casted over a GC electrode and dried under air with the aim of testing upon oxygen detection through reductive catalysis. These measurements were performed in collaboration with Professor Mauro Bertotti's Laboratory and the CVs are shown in Figure 64 for the cathodic region of a dioxygen saturated aqueous solution. From these experiments we were able to see the anodic shift of the reductive process of the O₂ molecule with an outstanding potential anticipation for the Co^{III}TRP(dmbpy) deposited over the GC electrode (green line) and the Co^{III}TRP(dmbpy)/4GO composite (blue line). This shift was over 800 mV when compared with the bare GC electrode (black line) indicating a synergistic interaction between the Co^{III}TRP(dmbpy) complex and the GO sheets making this a suitable material for dioxygen sensing devices once the reduction mechanism is elucidated.

For this reason, RDE measurements were performed in order to clarify the reduction pathway being performed by the composite. Several voltammograms at different rotation speeds and disk potentials were collected and employed in the corresponding Levich and Koutecky-Levich plots shown in appendant 3 in the published article.¹²⁶ The number of electrons involved in the process (n) was calculated from the slope of the Koutecky-Levich linearizations and compared with the theoretical slopes for n = 2 and 4 for hydrogen peroxide and water formation respectively. It was brought to our attention that the reduction process was

tetraelectronic when the bias potential was more negative than 0.28 V (vs SHE). Conversely, when the potential was more positive than 0.28 V, the rate of electron transfer from the electrode to the composite may be limiting the reaction to a bielectronic reduction.

Analytical performance of the modified electrodes was done by measuring their response in a deaerated solution (Ar) upon O₂ bubbling affording a linear response as a function of dissolved dioxygen concentration with a bias potential of 0.17 V yielding a limit of detection of 5.8×10^{-6} mol L⁻¹.

On the other hand, stability of the modified electrodes and reproducibility of the analytical signal was monitored employing fast cycling of dioxygen concentration. Thus, the response time curve when switching between O₂ saturated to argon saturated solution indicated a rapid and reproducible responses over long periods of time. Moreover, potential physiological interferents such as glucose, urea and ascorbic acid were added and none or very low current variations were observed.

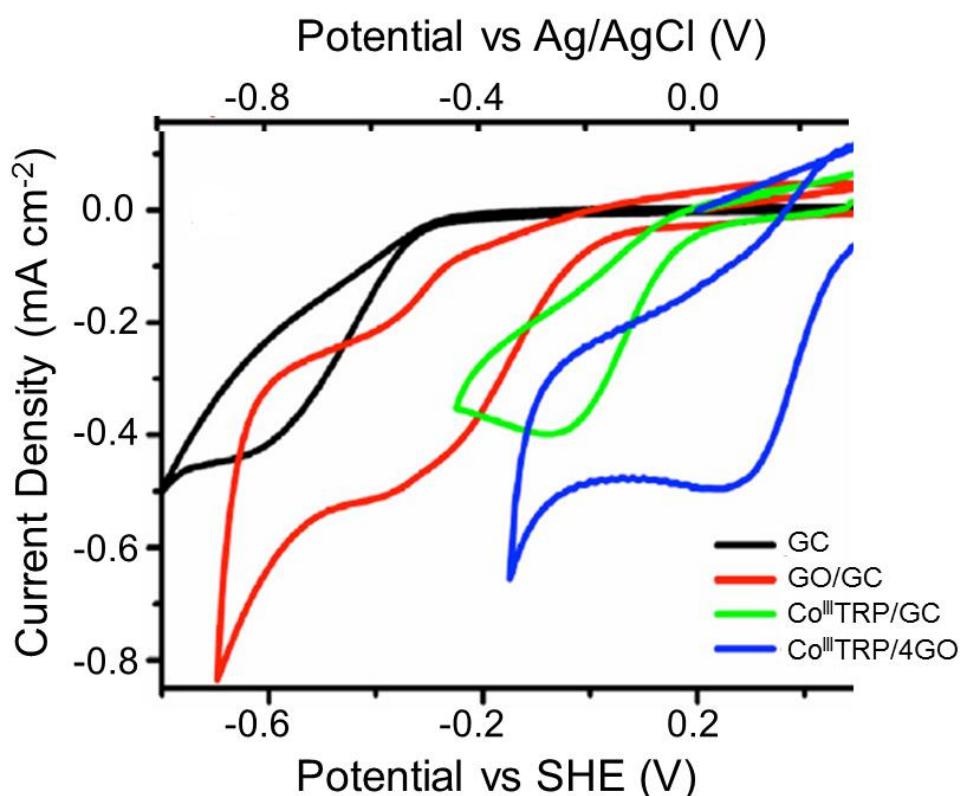


Figure 64. Cathodic region of cyclic voltammograms of GC (black line), GO/GC (red line), $\text{Co}^{\text{III}}\text{TRP}(\text{dmbpy})/\text{GC}$ (green line), $\text{Co}^{\text{III}}\text{TRP}(\text{dmbpy})/4\text{GO}$ (blue line) modified electrodes of an O_2 saturated aqueous solution.

Chapter III conclusions

Supramolecular $\text{Co}^{\text{III}}\text{TRP}(\text{dmbpy})$ complex was successfully synthesized from its minor $\text{cis-Ru}^{\text{II}}(\text{dmbpy})_2\text{Cl}_2$ and $\text{Co}^{\text{II}}\text{TPyP}$ complexes and fully characterized.

The $\text{Co}^{\text{III}}\text{TRP}(\text{dmbpy})/4\text{GO}$ composite was prepared and fully characterized prior to its utilization in modified electrodes.

Modified electrodes employing the $\text{Co}^{\text{III}}\text{TRP}(\text{dmbpy})/4\text{GO}$ composite displayed outstanding activity towards dioxygen reduction in aqueous media with an approximately 800 mV cathodic shift when compared with bare GC electrodes. Furthermore, dioxygen reduction mechanism found for this composite suggests a four-electron transfer when the bias potential is more negative than 0.28 V vs SHE.

Stability measurements exhibited rapid and stable responses overtime with little to no interference from common physiological compounds.

Due to the afforded experimental evidence, it is possible to assemble and develop reliable dissolved dioxygen sensors from the $\text{Co}^{\text{III}}\text{TRP}(\text{dmbpy})/4\text{GO}$ composite.

CHAPTER IV: Synthesis and Characterization of $\text{Co}^{\text{III}}\text{TRP}_{(\text{dcbpy})}\text{-Ni}$ Coordination Polymer and its GO Composite for Isoniazid Sensing.

cis-[Ru^{II}(H₂dcbpy)₂Cl₂] characterization

UV-vis spectra

Electronic spectra for the *cis*-[Ru^{II}(H₂dcbpy)₂Cl₂] complex shown in Figure 65 exhibits a band at 314 nm assigned to the IL $\text{p}\pi \rightarrow \text{p}\pi^*$ transition from the H₂dcbpy ligands and two MLCT bands from $\text{d}\pi \rightarrow \text{p}\pi^*$ at 398 and 543 nm.

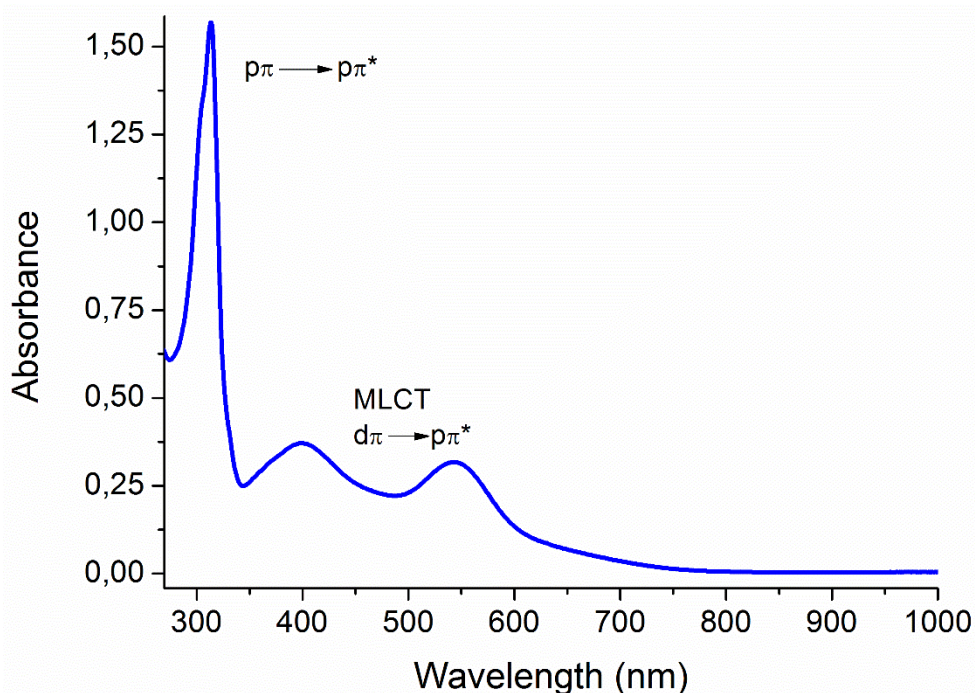


Figure 65. UV-vis spectra from *cis*-[Ru^{II}(H₂dcbpy)₂Cl₂] in DMF.

¹H-NMR spectra

¹H-NMR spectra shown in Figure 66 displays six well-defined signals with some minor impurities from the complex [Ru^{II}(H₂dcbpy)₃]Cl₂ that do not represent any

inconvenient for further synthetic steps. Assignment was made upon coupling constants found (J in Hz).

^1H NMR (500 MHz, $\text{DMSO-}d_6$) δ ppm 7.46 (d, $J=5.80$ Hz, 2 H) 8.19 (d, $J=5.80$ Hz, 2 H) 8.85 (dd, $J=1.53, 0.92$ Hz, 2 H) 8.90 (dd, $J=4.88, 0.92$ Hz, 2 H) 9.03 (s, 2 H) 10.06 (d, $J=5.80$ Hz, 2 H).

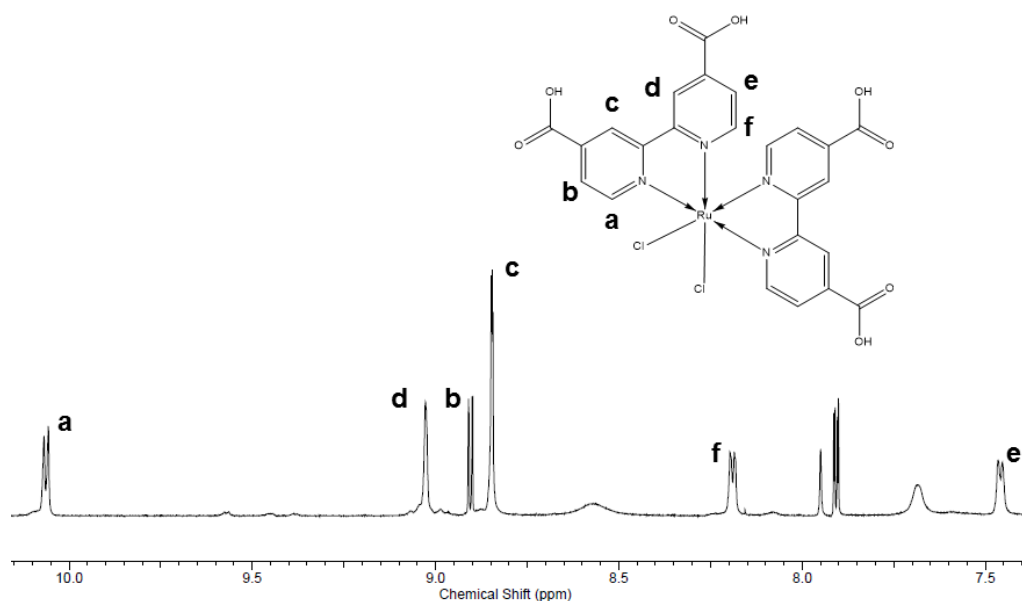


Figure 66. ^1H -NMR spectra of $\text{cis-}[\text{Ru}^{\text{II}}(\text{H}_2\text{dcbpy})_2\text{Cl}_2]$ in $\text{DMSO-}d_6$.

Co^{III}TRP(H₂dcbpy) characterization

^1H -NMR and 2D ^1H - ^1H COSY NMR spectra

Figure 67 displays the ^1H -NMR spectrum of $\text{Co}^{\text{III}}\text{TRP}(\text{dcbpy})$ exhibiting nine signals distributed between the 8.5-11 ppm window. Due to high symmetry of the $\text{Co}^{\text{III}}\text{TPyP}$ moiety, only three signals appear for the pyrrole hydrogens and pyridine *ortho* and *meta* protons. However, low symmetry of the peripheral ruthenium complexes generates different magnetic environments for the protons in the dcbpy rings just like the ^1H NMR spectrum for the $\text{cis-}[\text{Ru}^{\text{II}}(\text{H}_2\text{dcbpy})_2\text{Cl}_2]$ complex. Therefore, it was expected a total of seventy-two hydrogens distributed equally

among nine signals. Due to spin-spin coupling, H_b, H_c, H₁, H₂, H₅ and H₆ protons should appear as doublets and H_a, H₃ and H₄ protons as singlets.

Due to the higher complexity of this tetraruthenated porphyrin, assignment of the signals within the ¹H-NMR spectrum was not straightforward and a homonuclear spin coupling 2D NMR experiment (COSY) shown in Figure 68 was employed to unequivocally allocate the protons in the TRP structure (Figure 67 inset). In this spectrum, appeared couplings of protons H₄-H₅ and H₂-H₃ that were crucial to fully differentiate and assign the “singlets” H₃ and H₄. It was also relevant the coupling between H_b-H_c from the pyridyl group from the Co^{III}TPyP residue.

¹H NMR (500 MHz, D₂O/NaOD) δ ppm 8.67 (d, *J*=5.19 Hz, 8 H) 9.05 (d, *J*=5.80 Hz, 8 H) 9.10 (d, *J*=5.49 Hz, 8 H) 9.29 (d, *J*=5.80 Hz, 8 H) 9.48 (d, *J*=4.88 Hz, 8 H) 10.03 (s, 8 H) 10.23 (s, 8 H) 10.29 (s, 8 H) 10.77 (d, *J*=5.49 Hz, 8 H).

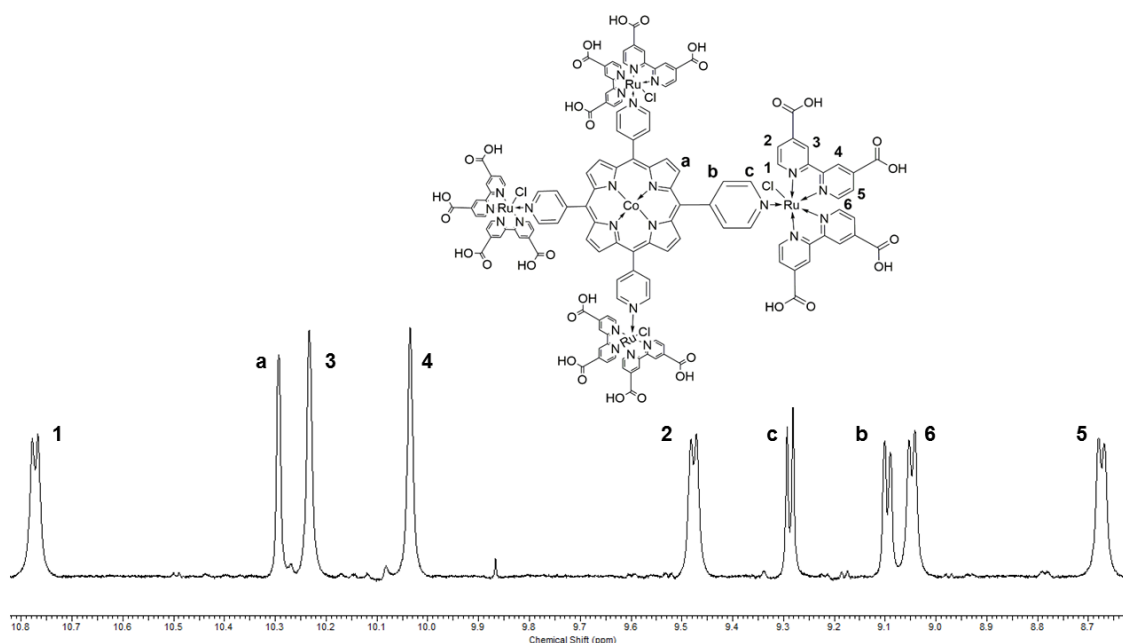


Figure 67. ¹H-NMR spectrum of Co^{III}TRP(dcbpy) in D₂O/NaOD.

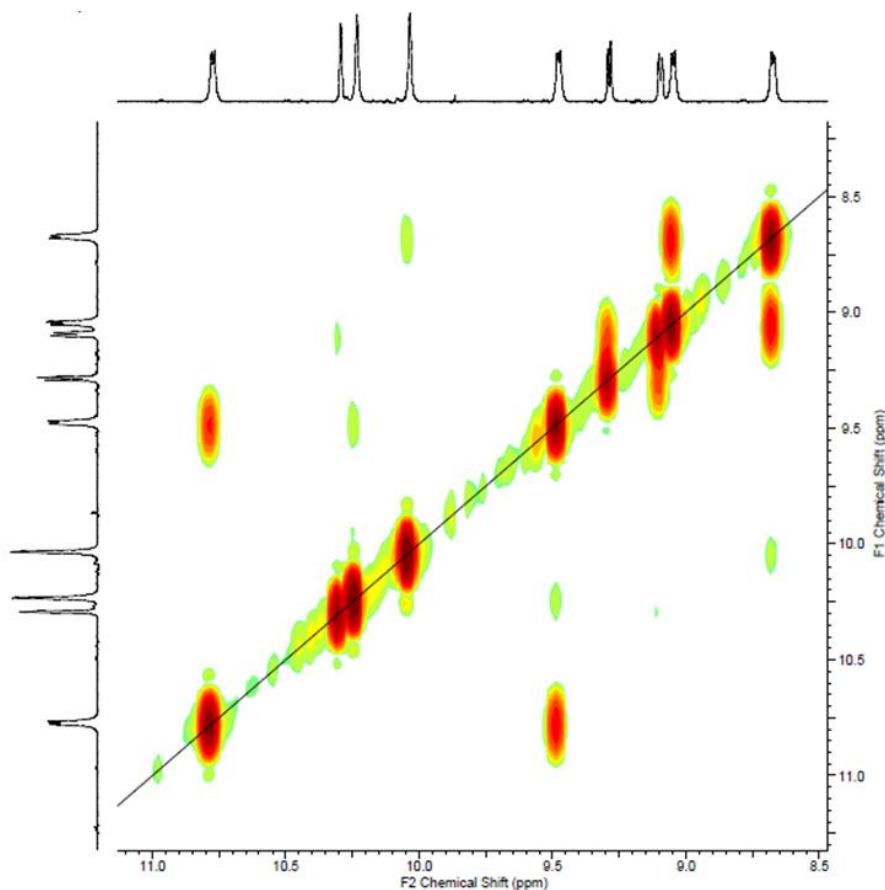


Figure 68. 2D ^1H - ^1H NMR COSY spectrum of $\text{Co}^{\text{III}}\text{TRP}(\text{dcbpy})$ in $\text{D}_2\text{O}/\text{NaOD}$.

UV-vis spectra

Figure 69 displays the UV-vis spectrum of $\text{Co}^{\text{III}}\text{TRP}(\text{dcbpy})$ complex in $\text{MeOH}/\text{H}_2\text{O}/\text{NaOH}$ which highlights the additive nature of its constituents' spectra (Figures 56 and 65). The first transition located at 308 nm was assigned as IL from the $\text{p}\pi \rightarrow \text{p}\pi^*$ in the dcbpy ligands, slightly shifted towards higher energies when compared with the free ruthenium complex due to the formal negative charge in the carboxylic groups which destabilizes the $\text{p}\pi^*$ level. This trend was also observed in the $\text{Co}^{\text{III}}\text{TRP}_{(\text{dmbpy})}$ indicating that destabilization of the $\text{p}\pi^*$ orbital upon coordination of the $\text{Co}^{\text{III}}\text{TPyP}$ moiety may be also taking place.

The Soret band appears at 435 nm, almost the same energy of that for the $\text{Co}^{\text{III}}\text{TRP}(\text{dmbpy})$ supramolecule, indicating that stabilization of the second excited

state (S_2) of the Co^{III} TPyP is affected by the bpy electron donating nature under our experimental conditions.

Q bands are located at 543 nm (Q_{1-0}) and 590 nm (Q_{0-0}) as expected for a $\text{Co}(\text{III})$ porphyrin species. Likewise observed for the Soret band, Q bands in Co^{III} TRP(H_2dcbpy) are located at almost the same energies than those of the Co^{III} TRP(dmbpy) compound indicating that stabilization of the first electronic excited state of the Co^{III} TPyP residue is dependent of the bpy ligand nature for this particular case. As discussed for the Co^{III} TRP(dmbpy) the oxidation of the cobalt center from $\text{Co}(\text{II})$ to $\text{Co}(\text{III})$ is attributed to the reaction with dioxygen in the air exposed solutions.

Moreover, the absorption spectrum exhibits broad bands at 364 nm and 504 nm ascribed to the peripheral ruthenium complexes MLCT $\text{Ru } d\pi \rightarrow p\pi^*$ dcbpy.

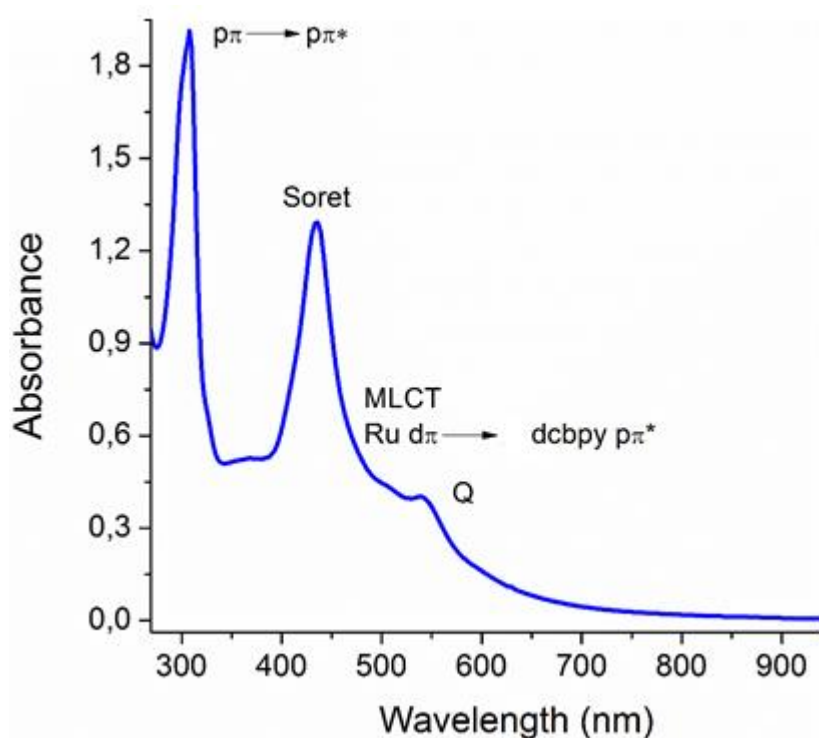


Figure 69. UV-vis spectra of Co^{III} TRP(dcbpy) in $\text{MeOH}/\text{H}_2\text{O}/\text{NaOH}$.

Table V summarizes the electronic transitions of the Co^{III}TRP (dmbpy and dcbpy) and its constituents ruthenium complexes and Co^{III}TPyP.

Table V. Summary of UV-vis spectra transitions from Co^{III}TRP supramolecules and its constituent complexes.

Compound	Band (nm)					
	IL	Soret	MLCT ₁	MLCT ₂	Q ₍₁₋₀₎	Q ₍₀₋₀₎
Co ^{II} TPyP	-	413	-	-	-	533
<i>cis</i> -[Ru ^{II} (dmbpy) ₂ Cl ₂]	297	-	569	413	-	-
<i>cis</i> -[Ru ^{II} (H ₂ dcbpy) ₂ Cl ₂]	314	-	543	398	-	-
Co ^{III} TRP(dmbpy)	292	436	497	366	545	594
Co ^{III} TRP(dcbpy)	308	435	504	364	543	590

Spectrophotometric titration

The spectrophotometric titration of Co^{III}TRP(dcbpy) species was performed sweeping the 13 to 2 pH window. But due to the elevated number of carboxylic groups capable of undergo acid-base equilibriums (sixteen in total) pKa determination was unsuccessful because no well-defined sigmoidal patterns were obtained when monitoring different absorption bands in the basic pH range (pH > 7). On the other hand, results for the acid pH window (pH < 7) were much more congruent and allowed a better understanding of the processes taking place.

Figure 70a displays the spectrophotometric titration of the Co^{III}TRP(dcbpy) species in the 7 to 2 pH window. The first noticeable change is the red-shifting of the IL band from 308 nm to 313 nm upon dcbpy protonation this is in agreement with a

higher stabilization of the π^* orbital owed to the negative charge neutralization in the carboxylic groups. The Soret band is shifted towards lower energies from 436 nm to 441 nm and its absorbance is diminished with a concomitant increasing of the MLCT band absorption induced by the π^* orbital stabilization in the dcbpy ligands.

Monitoring the absorbance at 436 nm yielded the best results in order to establish what is believed to be the first deprotonation process underwent by the supramolecule. This is shown in Figure 70b displaying the sigmoidal fitting performed with a calculated $r^2 = 0.99028$.

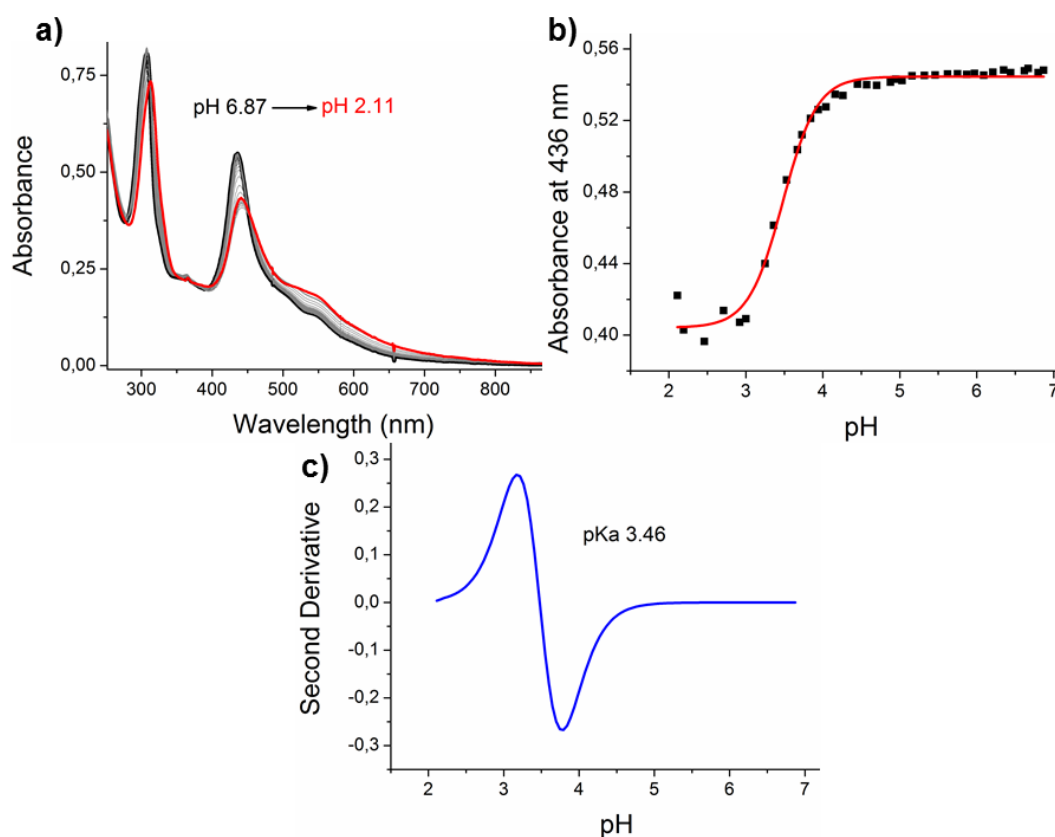


Figure 70. Spectrophotometric titration of $\text{Co}^{\text{III}}\text{TRP}(\text{dcbpy})$ (a), sigmoidal fitting for absorbance at 436 nm (b) and second derivative of the sigmoidal function (c).

As discussed in previous spectrophotometric titrations, the second derivative of the fitted sigmoidal curve afforded the pK_a value for the process when its value

reaches zero. Figure 70c exhibits this second derivative plot with the calculated pK_a 3.46.

FTIR spectra

Figure 71 displays the FTIR spectrum of $\text{Co}^{\text{III}}\text{TRP}(\text{H}_2\text{dcbpy})$ in which appear the very broad νOH stretching band at 3437 cm^{-1} mainly from the $-\text{OH}$ in the carboxylic groups and its hydrogen bond with water molecules. Little shoulders corresponding to the νCH sp^2 from the aromatic rings are visible between 2900 and 3100 cm^{-1} . The carbonyl stretching band ($\nu\text{C}=\text{O}$) appeared at 1726 cm^{-1} .

Unfortunately, unequivocal band assignments cannot be done in this case since the $\text{Co}^{\text{III}}\text{TRP}(\text{H}_2\text{dcbpy})$ species bears similar functional groups within its structure that may result in overlapped absorption bands. Therefore, we will refer to regions in the spectrum where vibrational bands of some functional groups are typically located. Bands at 1612 and 1546 cm^{-1} can be assigned to $\nu\text{C}=\text{C}$ stretching mode of double bonds in aromatic rings. Also, several ring vibration modes (porphyrin ring included) and aromatic ring vibrations can be found in the 1100 to 1500 cm^{-1} region. Finally, $\delta\text{C}-\text{C}-\text{H}$ bending mode associated with the β -pyrrolic hydrogens can be found in the lower energy end of the spectra between 700 to 850 cm^{-1} .^{127,128}

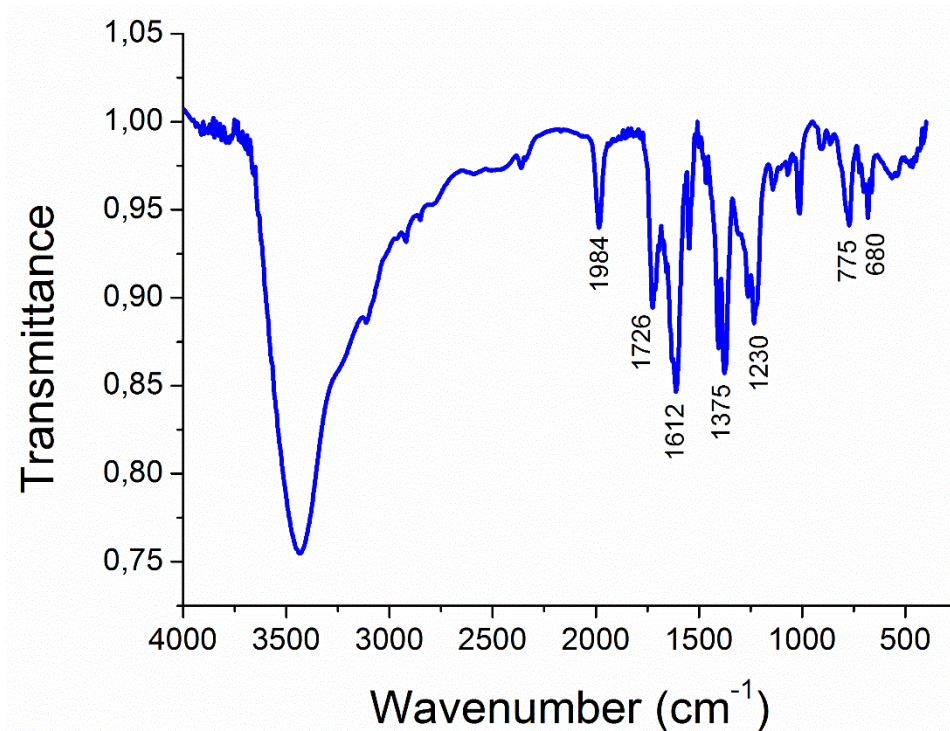


Figure 71. FTIR spectrum of $\text{Co}^{\text{III}}\text{TRP}(\text{H}_2\text{dcbpy})$ in KBr pellet.

Raman spectra

Raman spectra of the $\text{Co}^{\text{III}}\text{TRP}(\text{H}_2\text{dcbpy})$ compound is shown in Figure 72 and collected employing the 532 nm laser as excitation source.

Peaks at 360 and 703 cm^{-1} assigned to the $\phi\text{C-C}$ macrocycle ring deformation ($\delta(\text{porph}) + \delta(\text{py})$) and $\gamma\text{C-H}$ out of plane deformation modes, respectively, whereas the band at 1022 cm^{-1} was attributed to $\nu\text{C-N}$ in-plane stretching mode of py. The peaks at 1261 cm^{-1} $\delta(\text{C}_m\text{-py})$, 1473 cm^{-1} $\nu(\text{C}_\alpha\text{-C}_\beta)$, 1534 cm^{-1} $\nu(\text{C}_\beta\text{-C}_\beta)$ and $\nu(\text{C-C}) + \nu(\text{C-N}) + \delta(\text{CCH})$, 1606 cm^{-1} $\nu(\text{C-C}) + \nu(\text{C-N})$ and 3068 cm^{-1} $\nu(\text{C}_\beta\text{-H})$ were associated with the $\text{Co}^{\text{III}}\text{TRP}(\text{H}_2\text{dcbpy})$ complex.

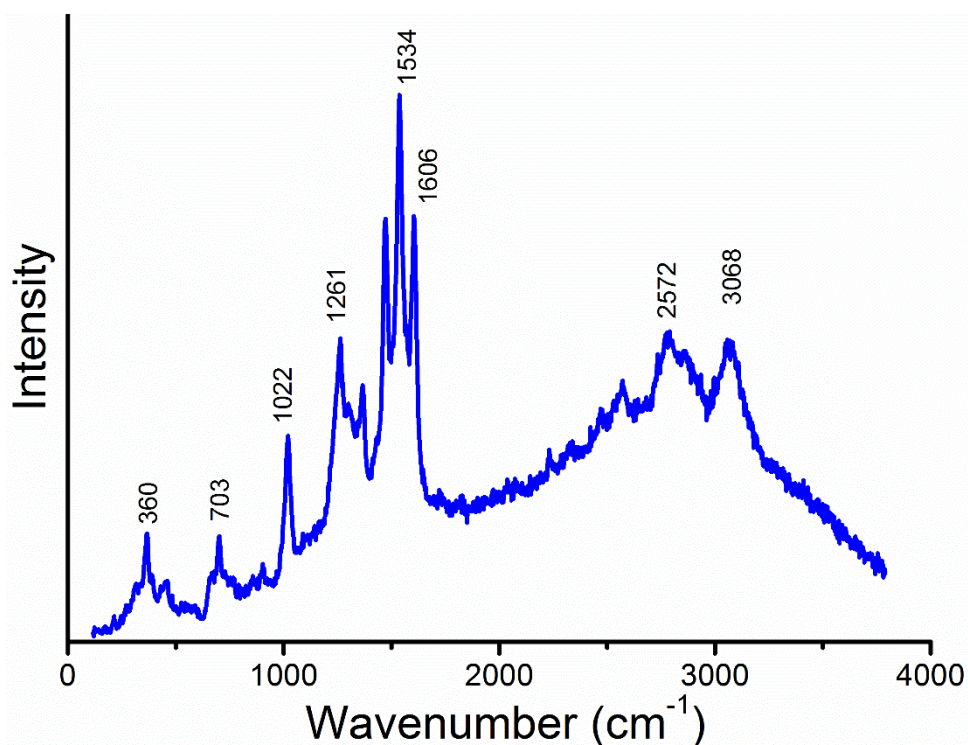


Figure 72. Raman spectra of Co^{III}TRP(H₂dcbpy).

Electrochemistry

CV experiment shown in Figure 73 exhibits redox processes of all the constituents in the Co^{III}TRP(dcbpy) complex. The anodic region displays the Ru^{III}/Ru^{II} wave at $E_{pa} = 1.18$ V as an irreversible process for the four peripheral complexes which is a result of the catalytic current arisen from sample preparation that included an addition of water and sodium hydroxide to fully dissolve the porphyrin. The appearance of only one redox wave for the ruthenium process indicates no electronic communication between the metal centers by acting as independent redox sites.

Cathodic region in the CV possess three distinguishable processes. The first wave at $E_{pc} = -1.18$ V was assigned to the first reduction of the porphyrin ring to the radical anion, while its second reduction to the dianion appeared at $E_{pc} = -1.32$ V. The first reduction of the dcbpy ligand to the radical anion was observed at $E_{pc} = -1.54$ V.

As perceived in the CV for the $\text{Co}^{\text{III}}\text{TRP}(\text{dmbpy})$ species, the $\text{Co}^{\text{III}}/\text{Co}^{\text{II}}$ process did not appear in $\text{Co}^{\text{III}}\text{TRP}(\text{dcbpy})$ voltammogram due to its slow heterogeneous electron transfer kinetics discussed before.

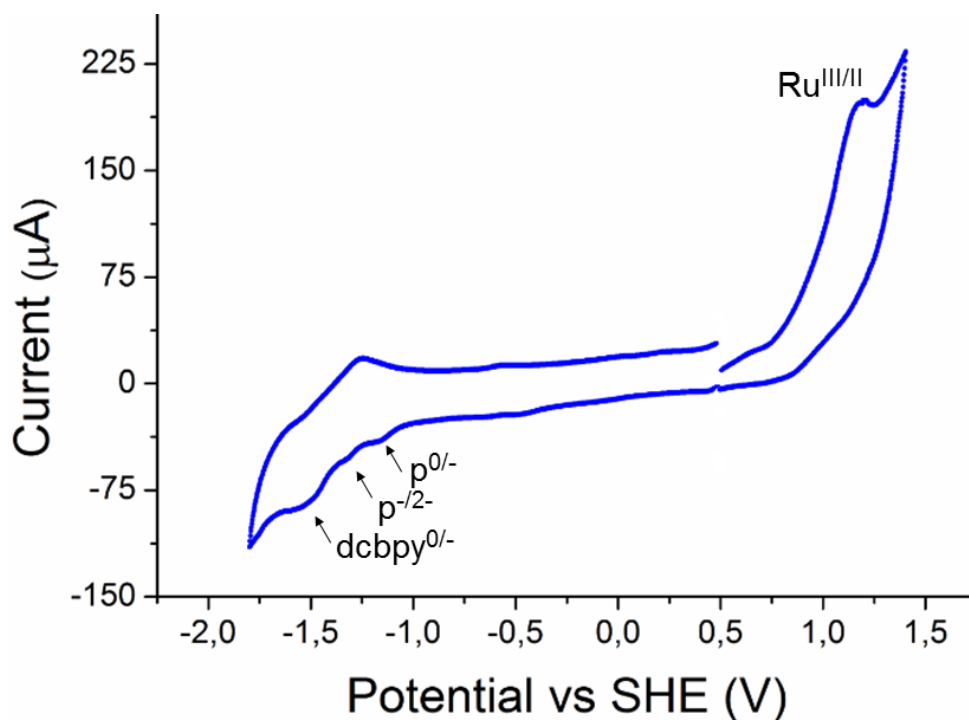


Figure 73. Cyclic voltammogram of $\text{Co}^{\text{III}}\text{TRP}(\text{dcbpy})$ in DMF/ H_2O /NaOH mixture 100 mV s^{-1} .

Spectroelectrochemistry

Figure 74 displays the spectroelectrochemistry spectra performed between 1.03 and 1.27 V for the $\text{Ru}^{\text{III}}/\text{Ru}^{\text{II}}$ process. The most noticeable spectral changes were from the IL $\rho\pi \rightarrow \rho\pi^*$ from the dcbpy ligands lowering its intensity being compensated by broadening at 308 nm. MLCT₂ band at 364 nm is diminished together with the MLCT₁ at 504 nm due to oxidation of the ruthenium center the charge transfer is no longer possible from the metal to the dcbpy ligands owing to the low electronic density over the $d\pi$ orbitals.

Soret and Q bands profiles remain unchanged along with their energies, indicating that in the potential window swept the only electrochemical process involved is that of the ruthenium core.

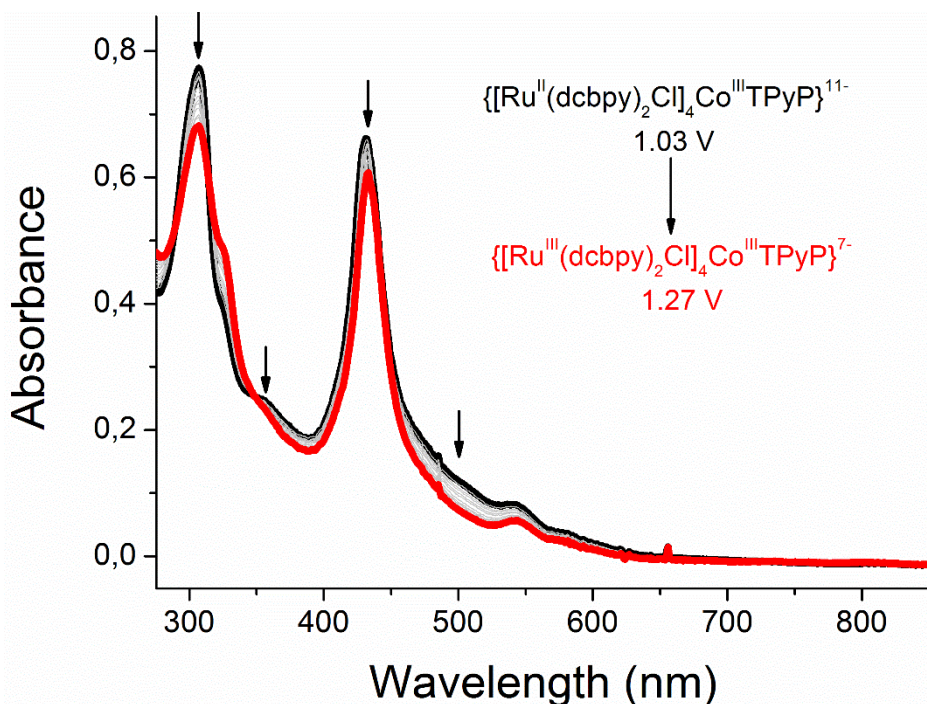


Figure 74. Spectroelectrochemistry spectra of $\text{Co}^{\text{III}}\text{TRP}(\text{dcbpy})$ in DMF.

Spectroelectrochemistry was employed to identify the presence of the $\text{Co}^{\text{III}}/\text{Co}^{\text{II}}$ process and is shown in Figure 75. Therefore, potential sweeping between 0.2 to -0.43 V afforded well-defined UV-vis spectral changes centered in the $\text{Co}^{\text{III/II}}\text{TPyP}$ moiety transitions.

Soret band is red-shifted towards 412 nm upon cobalt reduction corresponding to the wavelength found for the $\text{Co}^{\text{II}}\text{TPyP}$ (Table V). The most outstanding feature observed in this band is the isosbestic point indicating the equilibrium between the $\text{Co}(\text{III})$ and $\text{Co}(\text{II})$ species (Figure 75 inset) affording an estimate $E_{1/2} = 0.05$ V.

Q bands also gave a glimpse of the reduction process taking place within the potential sweep. With a two Q band profile in the $\text{Co}(\text{III})$ species to a single Q band at

531 nm for the Co(II) center which is in agreement with the wavelength found for the Q band in the Co^{II}TPyP complex (Table V).

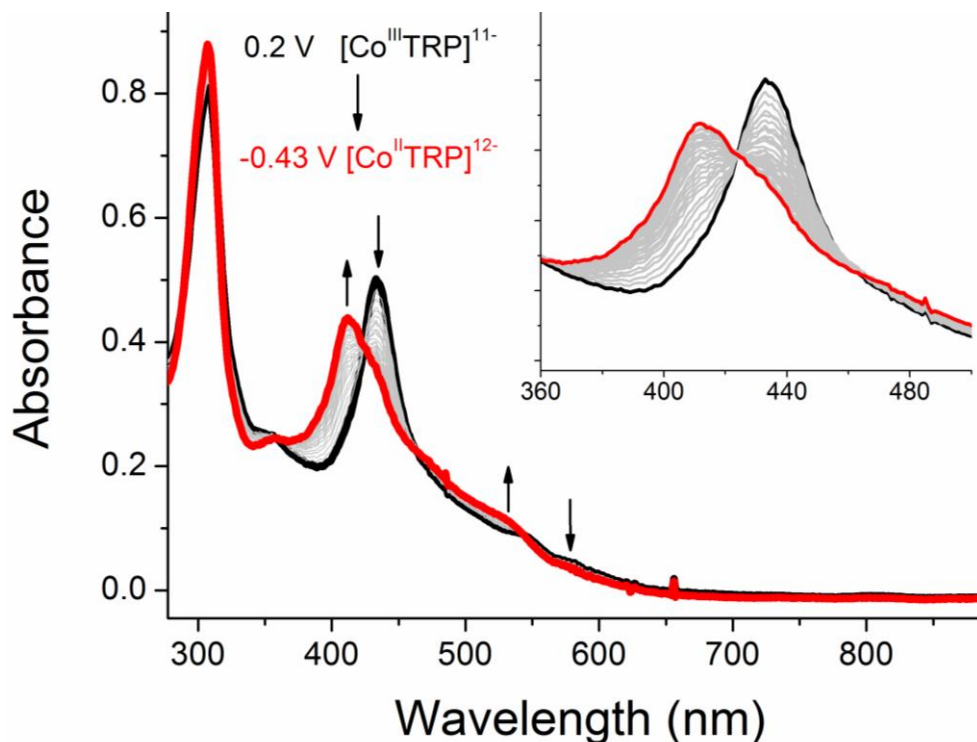


Figure 75. Spectroelectrochemistry spectra of Co^{III/II}TRP(dcbpy) in DMF.

Co^{III}TRP(dcbpy)-Ni/GO composite characterization

The synthetic approach taken for this particular composite demanded a series of requirements in order to facilitate the interaction between the highly negatively charged Co^{III}TRP(dcbpy) species and GO sheets. Previous attempts showed little to no interaction of the GO dispersion with the supramolecular porphyrin by means of UV-vis measurements of the remaining supernatant. Therefore, a coordination polymer exploiting the carboxylate groups in the Co^{III}TRP(dcbpy) complex would reduce the net negative charge to the extent of favoring the interaction with GO. Nickel (II) was the chosen ion to take part into the coordination polymer mainly because its coordination geometry which may favor a 2D arrangement and its charge.

X-ray Powder Diffraction measurement

XRPD experiments shown in Figure 76 displayed significant shift for the 001 reflection plane to lower 2θ values from 11.3° in GO to 6.5° in the composite, confirming a lamellar structure with the $\text{Co}^{\text{III}}\text{TRP}(\text{dcbpy})\text{-Ni}$ coordination polymer intercalated between GO sheets.

Average crystallite size was estimated from the 001 reflection peaks employing the Debye-Scherrer equation **20**.

$$D = K \lambda / B \cos \theta \quad \mathbf{20}$$

Where D is the average crystallite size, λ is the x-ray irradiation wavelength, B is the FWHM in radians and K is the Scherrer constant (0.9). With this equation the crystallite sizes found were 5.6 and 2.5 nm for GO and $\text{Co}^{\text{III}}\text{TRP}(\text{dcbpy})\text{-Ni/GO}$ respectively. In agreement with the interaction and easier dispersibility of the of the $\text{Co}^{\text{III}}\text{TRP}(\text{dcbpy})\text{-Ni/GO}$ composite when compared with GO.

Eq 20 was employed even though the morphology expected for the nanocomposite differs substantially from an sphere ($K = 0.9$), affording an approximate crystallite size which was the objective behind this approximation.

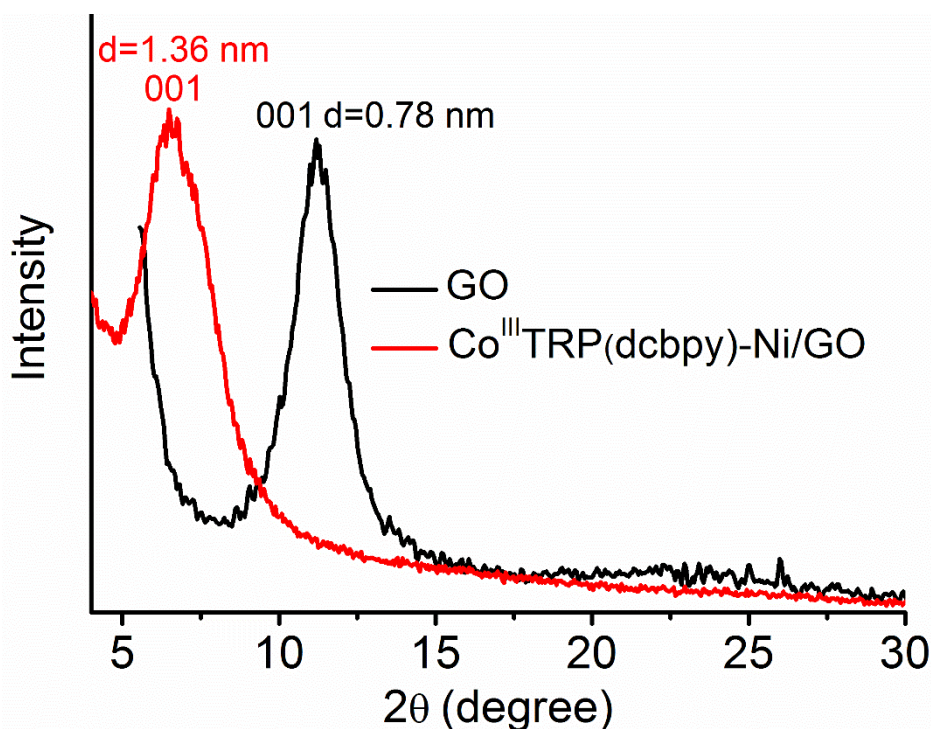


Figure 76. X-ray powder diffractograms of Co^{III}TRP(dcbpy)-Ni/GO (red line) and GO (black line).

FTIR spectra

Comparative FTIR spectra for the Co^{III}TRP(dcbpy)-Ni/GO composite and its constituents are shown in Figure 77. It was observed the additive profile for the composite spectrum (blue line) exhibiting IR bands corresponding to its components such as the 1984 cm⁻¹ band from the Co^{III}TRP(H₂dcbpy) complex and the 1075 cm⁻¹ from the GO typically attributed to stretching modes of the epoxy groups and the 1632 cm⁻¹ band is assigned to the $\nu(\text{C}=\text{C})$ vibration. On the other hand, the disappearance of some bands was attributed to the hindrance of some vibrational modes, as consequence of the interaction of Co^{III}TRP(dcbpy)-Ni with GO, an example of such vibrations are; the out of plane deformations and bending modes.

The absence of the $\nu(\text{C}=\text{O})$ stretching band at 1726 cm⁻¹ in the composite IR spectrum, is ascribed to the coordination of the Ni(II) ions to the carboxylate groups, lowering the C=O bond stretching energy.

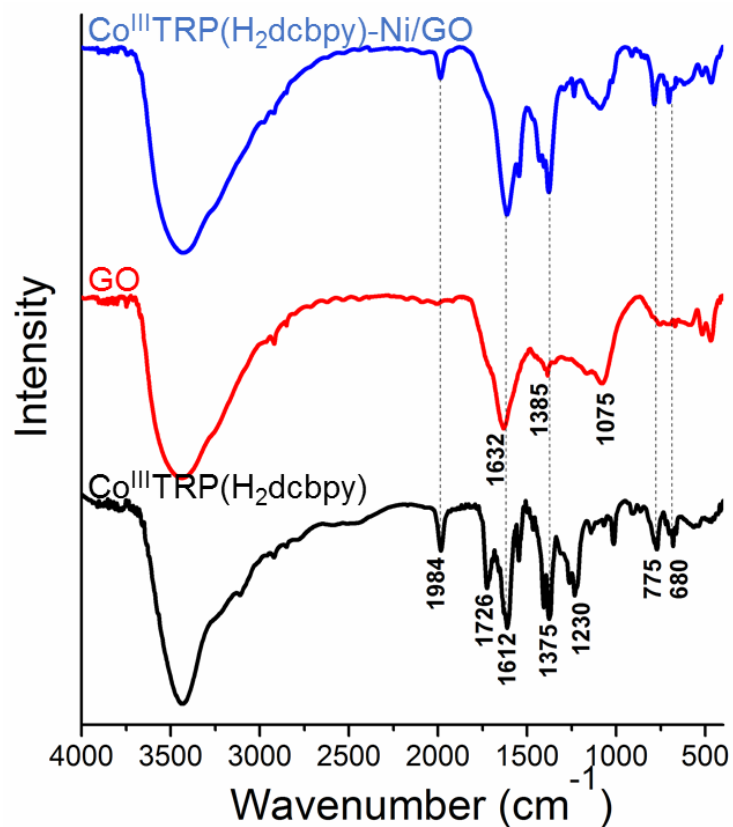


Figure 77. FTIR spectra of Co^{III}TRP(H₂dcbpy) (black line), GO (red line) and Co^{III}TRP(dcbpy)-Ni/GO composite (blue line) in KBr pellets.

Raman spectra

Figure 78 displays the comparative Raman spectra of the Co^{III}TRP(H₂dcbpy) (black line), GO (red line) and Co^{III}TRP(dcbpy)-Ni/GO composite (blue line). GO spectrum exhibited the D band at 1330 cm⁻¹ assigned to the sp² aromatic carbon rings breathing modes in regions where structural disorders and defects are present, and the G band which is ascribed to the first order scattering of E_{2g} phonons of in-plane bond-stretching motions of sp² carbon atoms at 1595 cm⁻¹.¹²⁹

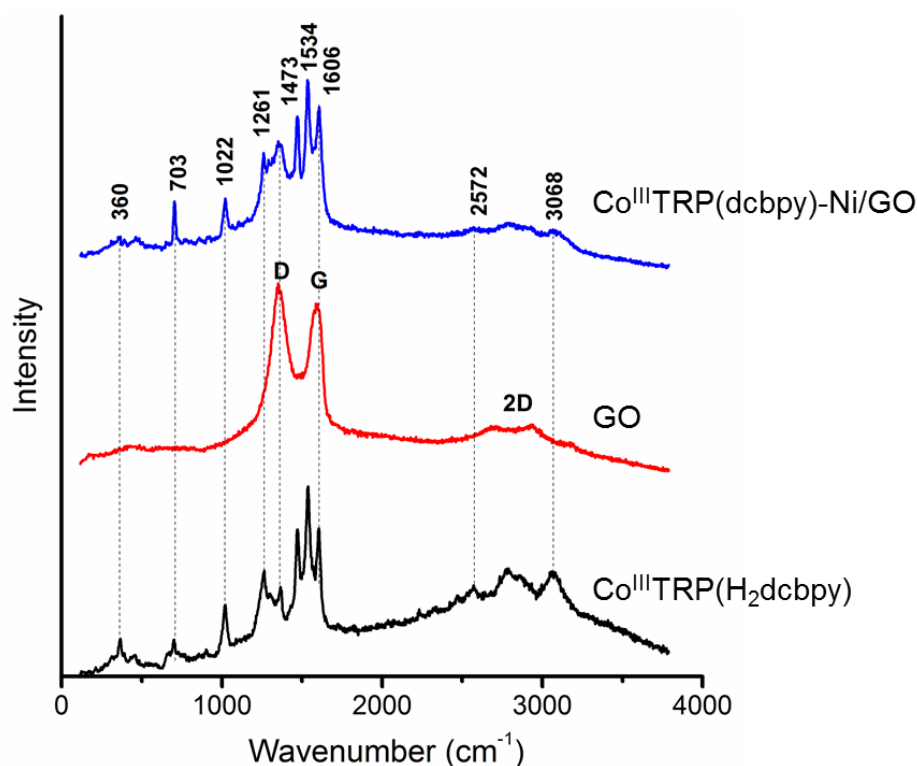


Figure 78. Raman comparative spectra of $\text{Co}^{\text{III}}\text{TRP}(\text{H}_2\text{dcbpy})$ (black line), GO (red line) and $\text{Co}^{\text{III}}\text{TRP}(\text{dcbpy})\text{-Ni/GO}$ composite (blue line) λ_{exc} 532 nm.

Complementarity of the GO and $\text{Co}^{\text{III}}\text{TRP}(\text{H}_2\text{dcbpy})$ spectra leads to easily distinguishable vibration peaks in the composite spectrum facilitating the Raman mapping of the $\text{Co}^{\text{III}}\text{TRP}(\text{dcbpy})\text{-Ni/GO}$ composite shown in Figure 79. The mapping was performed over the same composite aggregate and the images were generated by monitoring the Raman peak at 1350 cm^{-1} of the GO spectrum and presented as the red picture displayed in Figure 79a. Figure 79b was obtained when tracking the peak at 1540 cm^{-1} of the $\text{Co}^{\text{III}}\text{TRP}(\text{H}_2\text{dcbpy})$ spectrum. Both Figures 79a and 79b were convoluted in order to generate an image exhibiting the contribution and therefore the distribution of the GO and $\text{Co}^{\text{III}}\text{TRP}(\text{H}_2\text{dcbpy})$ over the composite aggregate (Figure 79c) confirming a homogeneous distribution of the GO and the tetra-ruthenated porphyrin along the composite as observed by the yellow color.

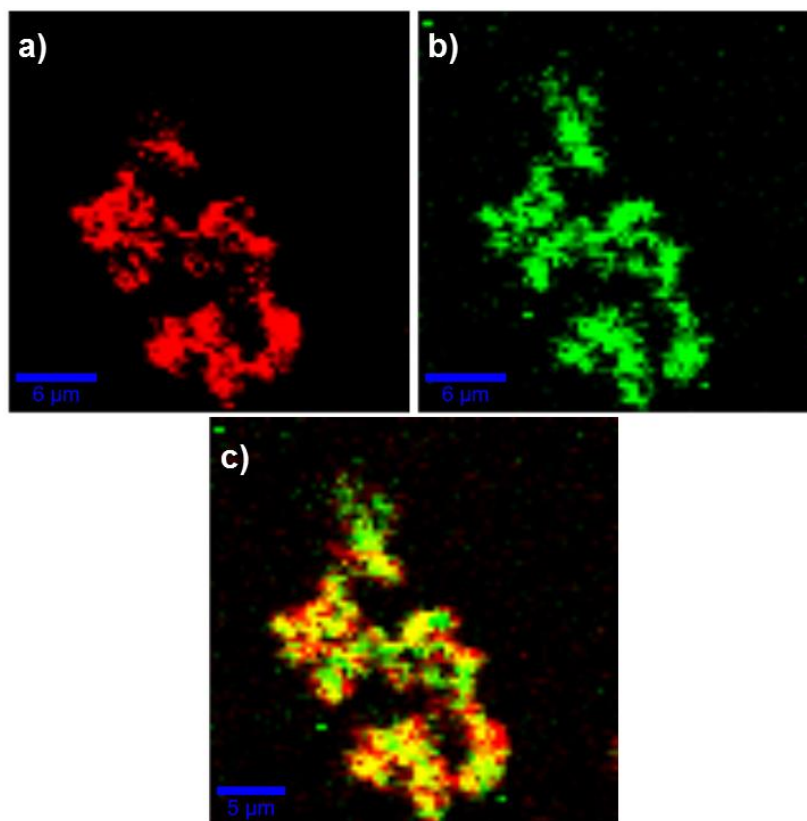


Figure 79. Raman microscopy images from 1350 cm^{-1} GO band (a), 1540 cm^{-1} $\text{Co}^{\text{III}}\text{TRP}(\text{H}_2\text{dcbpy})$ band (b) and convoluted $\text{Co}^{\text{III}}\text{TRP}(\text{dcbpy})\text{-Ni/GO}$ composite image (c).

$\text{Co}^{\text{III}}\text{TRP}(\text{dcbpy})\text{-Ni/GO}$ composite electrochemical behavior

Isoniazid is a heterocyclic compound shown in Figure 80a and widely employed as an antibiotic for tuberculosis treatment. Although it is used together with rifampicin or other antibiotics it could be employed on its own. This molecule's antibiotic properties rely on its ability to disrupt the bacteria's cell wall formation.

However, some undesirable side effects can often appear, mostly when isoniazid blood concentration is not controlled. This side effects include increased blood levels of liver enzymes and hepatotoxicity.¹³⁰

Hence, a reliable, fast and easy method for isoniazid quantification is of high interest. Therefore, the oxidative catalysis observed for $\text{Co}^{\text{III}}\text{TRP}(\text{dcbpy})\text{-Ni/GO}$ composite competes with already published methodologies in the potential observed

for the isoniazid electrochemical process, linear range and LOD. Nevertheless, the ease of sample preparation for our composite stands above the rest because little to no modifications were performed in order to obtain reproducible results. For our quantification experiments isoniazid aqueous solutions with KNO_3 (0.1 mol L^{-1}) as supporting electrolyte were employed successfully.

Figure 80b displays the cyclic voltammograms of increasing isoniazid concentration (1×10^{-4} to $1 \times 10^{-3} \text{ mol L}^{-1}$) at 100 mV s^{-1} . The oxidative catalysis of isoniazid performed by the modified GC electrode with $\text{Co}^{\text{III}}\text{TRP}(\text{dcbpy})\text{-Ni/GO}$ composite appears at E_{pa} between 0.2 and 0.32 V vs SHE. The electrochemical wave was observed as an irreversible process which is explained by the nature of the species generated upon isoniazid oxidation (N_2 and isonicotinic acid). This was confirmed by dinitrogen evolution on the surface of the modified electrode in a deaerated isoniazid solution.

Plotting of concentration vs current peak taken from CVs shown in Figure 80c afforded a linear behavior with increasing concentration with an $r^2 = 0.9979$, indicating a good fitting that could be employed for real sample quantifications as performed by P. Rossini for a commercial tablet used in tuberculosis treatments and shown in the published article.¹³¹

Composite modified electrode performance was compared with bare GC and a GO modified electrode and its electrochemical responses are shown in Figure 81. From that comparative figure the synergistic effect between the GO and $\text{Co}^{\text{III}}\text{TRP}(\text{dcbpy})\text{-Ni}$ polymer stands out with an anodic shift of approximately 400 mV from the bare GC electrode and about 300 mV from the GO modified electrode,

meaning less possible interferences from real samples due to the low applied voltage required to oxidize isoniazid.

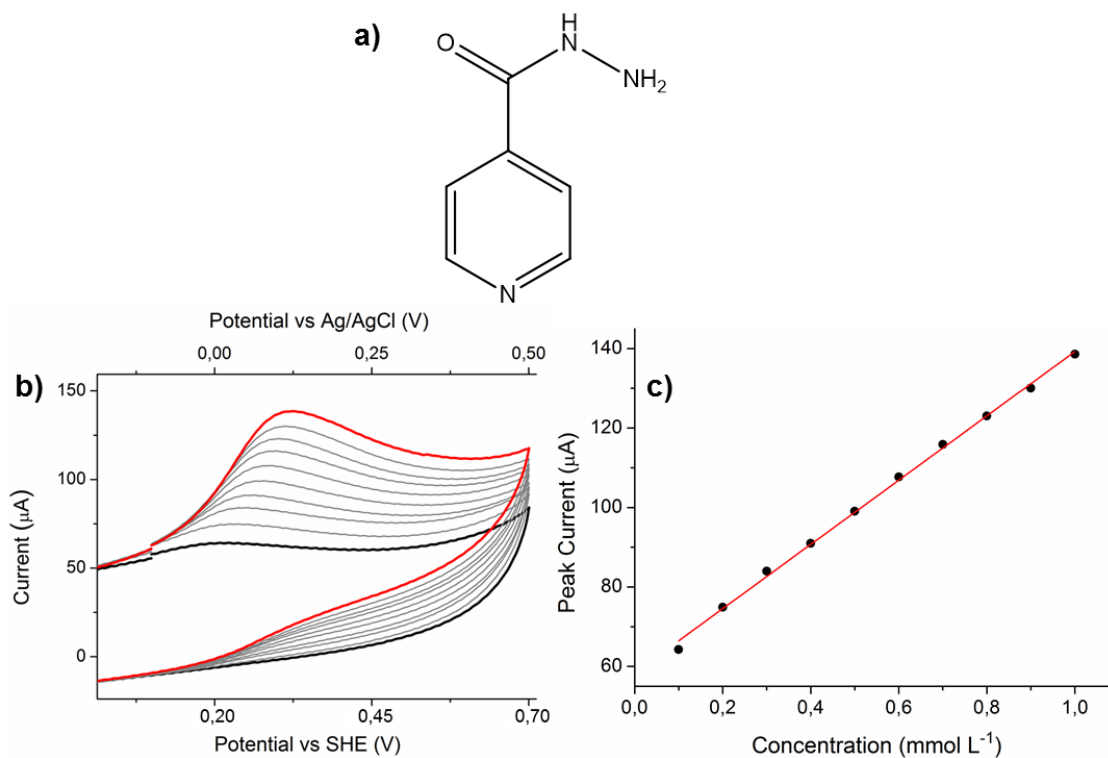


Figure 80. Schematic structure of isoniazid (a), cyclic voltammograms with increasing concentration of isoniazid at 100 mV s^{-1} (b) and linear behavior of concentration vs peak current (c).

Since analytical quantifications are usually performed applying a bias potential (to the working electrode) that is usually above the redox wave observed for the analyte, this linear behavior employing the peak current (Figure 80c) is a valid way of observing current behavior and will not differ from the currents measured in the quantification process due to the higher potential employed.

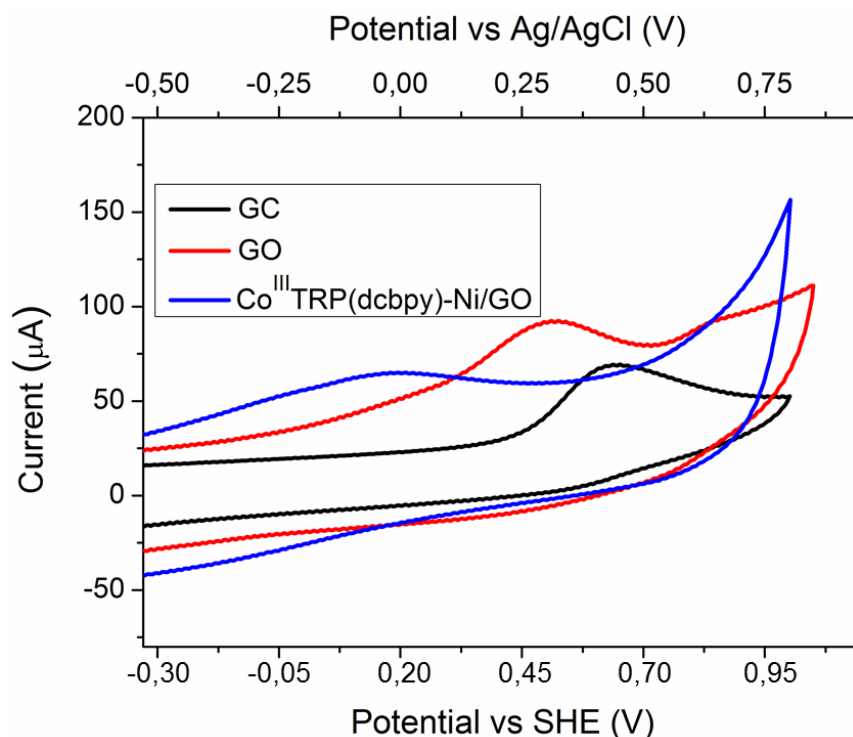


Figure 81. Comparative CVs upon isoniazid ($2 \times 10^{-4} \text{ mol L}^{-1}$) oxidation of GC (black line), GO (red line) and $\text{Co}^{\text{III}}\text{TRP(dcbpy)-Ni/GO}$ (blue line) modified electrodes, 100 mV s^{-1} .

Stability experiments performed over several days displayed an overall good physical adherence of the composite to the GC electrode surface and the electrochemical behavior shown in Figure 82a exhibited a stable response under working conditions, presenting about 90% activity after four days as displayed in Figure 82b. With these results continuous usage of $\text{Co}^{\text{III}}\text{TRP(dcbpy)-Ni/GO}$ modified electrodes is not advise for longer than four days, however as exposed above, ease of sample and electrode modification account for further viability of the proposed sensors.

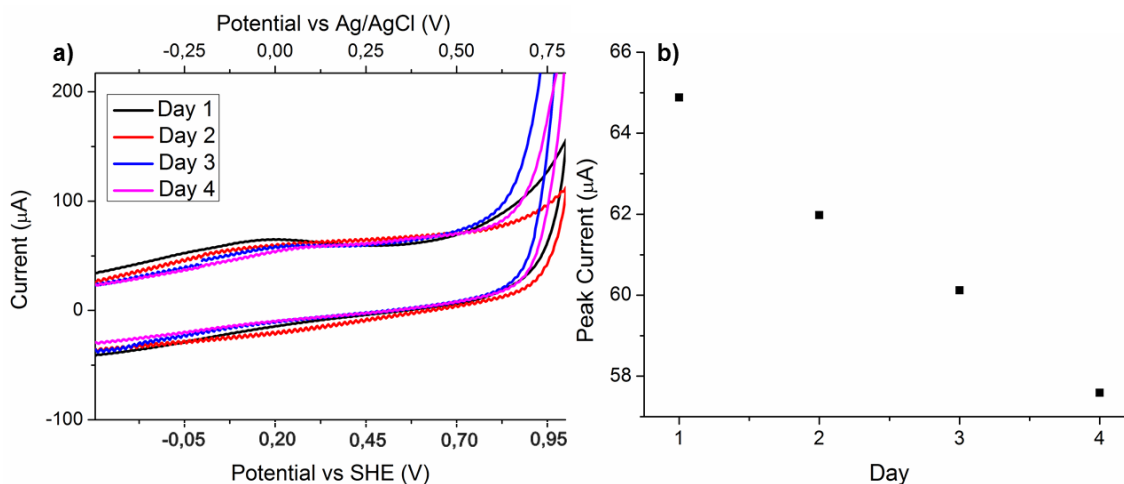


Figure 82. Cyclic voltammograms of a 2×10^{-4} mol L $^{-1}$ isoniazid solution over a four day period (a) and CVs peak current behavior over time (b), 100 mV s^{-1} .

BIA experiments performed by Rossini (Appendix 5) allowed the analytical determination of the LOD and LOQ by using isoniazid solutions between 4.0×10^{-5} to 1.2×10^{-4} mol L $^{-1}$ affording $\text{LOD} = 3.53 \times 10^{-6}$ mol L $^{-1}$ and $\text{LOQ} = 1.18 \times 10^{-5}$ mol L $^{-1}$. This sensitivity is comparable with reported electroanalytical sensors. However, it should be addressed that our modified electrode performs under significant milder conditions (e.g. $E = 0.10 \text{ V vs Ag/AgCl}$ and pH 7) in relation to the methods shown in Table VI.

Moreover, determination of isoniazid in a pharmaceutical sample was performed by BIA experiments and the results were in excellent agreement with the expected values with only a 0.48% higher content in relation to the values afforded in the tablets tested.

Table VI. Comparison of different modified electrodes performance towards oxidative isoniazid detection.

Electrode	Method	Potential (V) vs Ag/AgCl	Detection Limit (μM)	Linear Range (μM)	Buffer (pH)	Reference
CoTRP(dcbpy) ₂ -Ni/GO	BIA	0.10	3.5	100- 1000	KNO ₃ (7)	Present work
75:25, NiCo(OH) ₂	BIA	0.33	0.05	99-950	KOH 1mol L ⁻¹	130
OPPy/GC	CV	0.105	3.15	-	NH ₃ /NH ₄ Cl (9)	132
ARS/GC	LSV	0.5	3.94	10-800	PBS (6)	133
Rh/GC	CV	0.80	13.00	70-130	PBS (7)	134
Ag-HCF/SPE	FIA	0.45	2.6	5-500	(3)	135
Bentonite clay/GC	LSV	0.85	0.80	-	Na ₂ SO ₄ (13.5)	136
GO/GC	LSV	0.307	0.17	2-70	PBS (7)	137
f-MWCNT/GC	CV	0.40	0.27	1-70	AB (4)	138

OPPy = overoxidized polypyrrole; GC = glassy carbon electrode; ARS = Alizarin Red S; PH = poly-L-histidine; HCF = Hexacianoferrate; SPE = Screen Printed Electrode; PBS = Phosphate Buffer Solution; f-MWCNT = Functionalized Multiwalled Carbon Nanotubes.

Chapter V conclusions

Co^{III}TRP(H₂dcbpy) supramolecule was successfully synthesized from its minor cis-Ru^{II}(H₂dcbpy)₂Cl₂ and Co^{II}TPyP complexes and fully characterized by several analytic techniques.

Co^{III}TRP(dcbpy)-Ni coordination polymer was successfully generated in situ in order to promote the Co^{III}TRP(dcbpy)-Ni/GO composite formation.

Co^{III}TRP(dcbpy)-Ni/GO modified electrodes displayed very good activity towards isoniazid oxidative sensing with an anodic shift of approximately 400 mV when compared to a bare GC electrode. Furthermore, linear current response was obtained in the 1×10^{-4} to 1×10^{-3} mol L⁻¹ isoniazid concentration range. Moreover, stability tests showed a 90% activity retention after four days.

Co^{III}TRP(dcbpy)-Ni/GO modified electrodes afforded a LOD = 3.53×10^{-6} mol L⁻¹ and LOQ = 1.18×10^{-5} mol L⁻¹ which are comparable to the values found in literature. Additionally, these modified electrodes allowed isoniazid determination in a commercial tablet employed for tuberculosis treatment with only 0.48% higher content than values reported by manufacturer.

These experimental results point out the viability of device assembling employing Co^{III}TRP(dcbpy)-Ni/GO composite as modifying agent for effective and reliable isoniazid sensors, making them better performers than many reported compounds due to the milder sensing conditions employed (pH 7 aqueous media).

APPENDICES

Appendix 1: $[Ru^{II}(McTerpy)(dmbpy)(TMT)]PF_6$ molar extinction coefficients.

Table VII. Molar extinction coefficients of $[Ru^{II}(McTerpy)(dmbpy)(TMT)]PF_6$

Band (nm)	ϵ (cm^{-1} L mol $^{-1}$)
281	63757
317	38894
435	9167
497	9560

Appendix 2: I-V plots of the $[Ru^{II}(McTerpy)(dmbpy)(HTMT)]$ and $(N-Bu_4)[Ru^{II}(McTerpy)(dmbpy)(TMT)]$ DSSCs.

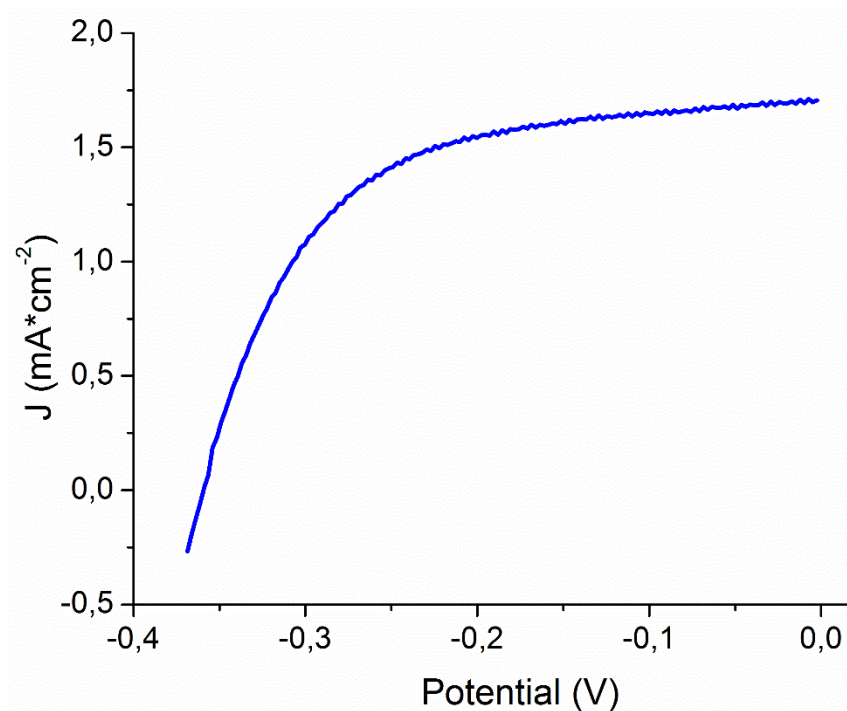


Figure 83. I-V curve of $[Ru^{II}(McTerpy)(dmbpy)(HTMT)]$ assembled DSSC.

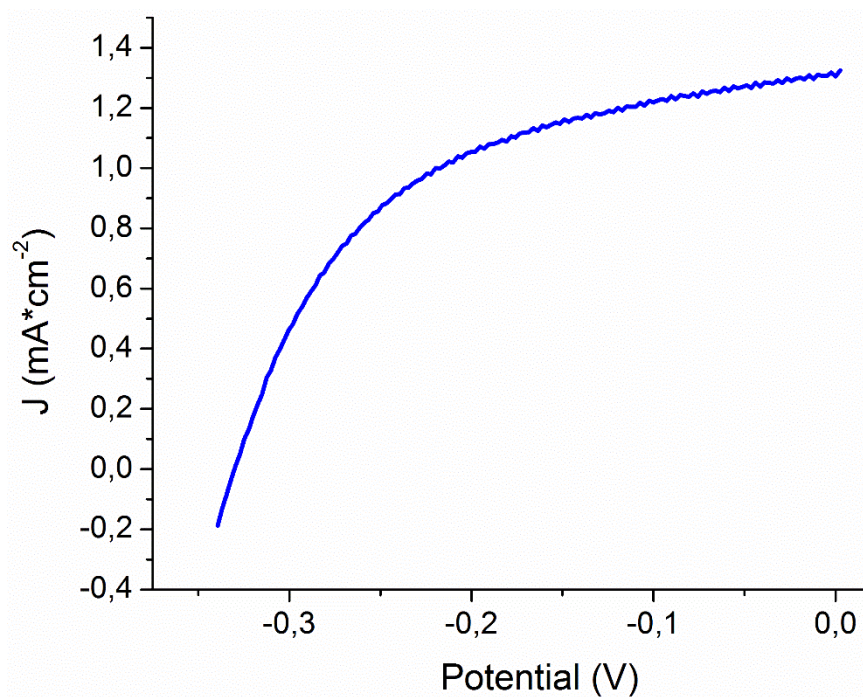


Figure 84. I-V curve of $(N-Bu_4)[Ru^{II}(McTerpy)(dmbpy)(TMT)]$ assembled DSSC.

**Appendix 3: Electrostatic bending and outer-sphere intervalence transfer
in a flexible ligand-bridged ruthenium(III)-iron(II) complex paper first page.**



Journal of Coordination Chemistry



ISSN: 0095-8972 (Print) 1029-0389 (Online) Journal homepage: <http://www.tandfonline.com/loi/gcoo20>

Electrostatic bending and outer-sphere intervalence transfer in a flexible ligand-bridged ruthenium(III)-iron(II) complex

Juan S. Aguirre-Araque, Reginaldo C. Rocha & Henrique E. Toma

To cite this article: Juan S. Aguirre-Araque, Reginaldo C. Rocha & Henrique E. Toma (2018) Electrostatic bending and outer-sphere intervalence transfer in a flexible ligand-bridged ruthenium(III)-iron(II) complex, *Journal of Coordination Chemistry*, 71:11-13, 1778-1790, DOI: [10.1080/00958972.2018.1493725](https://doi.org/10.1080/00958972.2018.1493725)

To link to this article: <https://doi.org/10.1080/00958972.2018.1493725>

 View supplementary material 

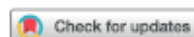
 Accepted author version posted online: 03 Jul 2018.
Published online: 17 Oct 2018.

 Submit your article to this journal 

 Article views: 11

 View Crossmark data 

Full Terms & Conditions of access and use can be found at
<http://www.tandfonline.com/action/journalInformation?journalCode=gcoo20>



Electrostatic bending and outer-sphere intervalence transfer in a flexible ligand-bridged ruthenium(III)-iron(II) complex

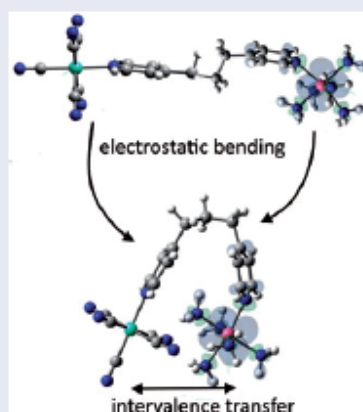
Juan S. Aguirre-Araque^a, Reginaldo C. Rocha^b and Henrique E. Toma^a

^aInstituto de Química, Universidade de São Paulo, São Paulo, Brazil; ^bLos Alamos National Laboratory, Los Alamos, NM, USA

ABSTRACT

In the mixed-valence complex $[\text{Ru}^{\text{III}}(\text{NH}_3)_5(\mu\text{-dpypn})\text{Fe}^{\text{II}}(\text{CN})_5]$ with the flexible bridging ligand 1,3-di(4-pyridyl)propane (dpypn), electrostatic interactions between the $\{\text{Ru}(\text{NH}_3)_5\}^{3+}$ and $\{\text{Fe}(\text{CN})_5\}^{3-}$ moieties drive a strong bending of dpypn and approximation of the Ru^{III} and Fe^{II} centers, from which the enhanced electronic coupling between metal ions produces an intense intervalence-transfer absorption in the near-infrared region. Density functional theory calculations corroborate both the electrostatic bending in this heterobinuclear complex and a linear geometry in the homobinuclear counterparts $[\text{Ru}(\text{NH}_3)_5(\mu\text{-dpypn})\text{Ru}(\text{NH}_3)_5]^{5+}$ and $[\text{Fe}(\text{CN})_5(\mu\text{-dpypn})\text{Fe}(\text{CN})_5]^{5-}$, for which no evidence of electronic coupling was found because of the separation between metal centers. Furthermore, the heterobinuclear species formed an inclusion complex with β -cyclodextrin where the imposed linear geometry prevents significant electronic coupling and intervalence charge transfer between the Ru^{III} and Fe^{II} centers.

GRAPHICAL ABSTRACT



ARTICLE HISTORY

Received 1 February 2018
Revised 26 May 2018
Accepted 6 June 2018

KEYWORDS

Outer-sphere intervalence transfer; electrostatic configurational bending; pentaammineruthenium complexes; pentacyanidoferrate complexes; mixed valency

CONTACT Henrique E. Toma  henetoma@iq.usp.br  Instituto de Química, Universidade de São Paulo, São Paulo, SP 05508-000, Brazil

This article is dedicated to Professor Dan Meyerstein on the occasion of his 80th birthday.

 Supplemental data for this article can be accessed at <https://doi.org/10.1080/00958972.2018.1493725>.

© 2018 Informa UK Limited, trading as Taylor & Francis Group

Appendix 4: CoTRP/Graphene oxide composite as efficient electrode

material for dissolved oxygen sensors paper first page.

Electrochimica Acta 222 (2016) 1682–1690



Contents lists available at ScienceDirect

Electrochimica Acta

journal homepage: www.elsevier.com/locate/electacta



CoTRP/Graphene oxide composite as efficient electrode material for dissolved oxygen sensors



Lucas P.H. Saravia, Anandhakumar Sukeri, Josue M. Gonçalves, Juan S. Aguirre-Araque, Bruno B.N.S. Brandão, Tiago A. Matias, Marcelo Nakamura, Koiti Araki, Henrique E. Toma, Mauro Bertotti*

Department of Fundamental Chemistry, Institute of Chemistry, University of São Paulo, Av. Prof. Lineu Prestes, 748, 05508-000, São Paulo, SP, Brazil

ARTICLE INFO

Article history:

Received 25 July 2016

Received in revised form 22 November 2016

Accepted 27 November 2016

Available online 28 November 2016

Keywords:

Nanocomposite

graphene oxide

oxygen reduction reaction

cobalt porphyrin

four-electron reduction

ABSTRACT

The preparation of the trifluoromethanesulfonate salt of [tetrakis-bisdimethylbipyridine chlororuthenium(II)]-5,10,15,20-tetrapyridylporphyrinate cobalt(II) complex (CoTRP) and its composites with graphene oxide (GO) is described. The CoTRP molecules were found to lie flat on the GO surface, generating nanostructures that are more or less dispersible in aqueous media, depending on the relative amounts of CoTRP and GO. This feature can be used to tune the electrocatalytic activity of the composites in the oxygen reduction reaction (ORR) in neutral media. The material was characterized by transmission electron microscopy, Raman, UV–vis spectroscopy, atomic force microscopy and FT-IR and the results confirmed that CoTRP is strongly supported on GO through electrostatic interactions. The ORR activity of CoTRP/GO was evaluated by electrochemical techniques and a low overpotential (0.05 V) was noticed in the four-electron reduction of dioxygen. This value is dramatically shifted to positive potentials, by 0.88 V in relation to the glassy carbon electrode, and the electrode performance allows its use as effective sensor probe for continuous monitoring of dissolved oxygen (DO). Additionally, analytical parameters such as sensitivity, selectivity, reproducibility, lower detection limit (LOD) and stability were evaluated in order to demonstrate the suitability of the proposed sensor for continuous monitoring of dissolved oxygen.

© 2016 Elsevier Ltd. All rights reserved.

1. Introduction

Oxygen is essential for sustaining animal life in our planet and is a potential electron acceptor in fuel cells owing to its high reduction potential and clean reaction generating water as the only product [1]. However, the poor kinetics of the oxygen reduction reaction (ORR) hinders its use in neutral media. In addition, controlling the mechanism of ORR is very important for several technological applications, especially in fuel cells since their efficiency is strongly dependent on the number of electrons transferred to oxygen ($2e^-$ or $4e^-$). Platinum (Pt) and other noble metals have been extensively employed as $4e^-$ ORR catalyst, but the high cost, scarcity and propensity of poisoning by CO have limited more extensive application, fueling the search for alternative electrocatalytic materials. In this context, since the seminal reports on the properties of cobalt phthalocyanine and

porphyrins [2], several other molecular mediators such as DNA [3], anthraquinone [4,5], polymethylene blue [6], nanostructure peptide [7], cobalt complexes [8–12], iron(II) tetrasulfonated phthalocyanine and iron(II) tetra-(N-methyl-pyridyl) porphyrin [13], magnesium (II) phthalocyanine [14], nickel Salen [15], vitamin B₁₂ [16], ABTS-laccase [17], ZnO doped RuO₂ [18], diamino-*o*-benzoquinone [19], indigo tetrasulfonate [20] and eugenol [21], have been described.

The continuous measurement of oxygen concentration is essential in many medical procedures and applications, technological processes, environmental monitoring and analysis, among other applications. Several electrochemical sensors based on ORR mediators have been proposed for monitoring oxygen dissolved in water [13,22–29], but none of them exhibited the robustness, reproducibility and sensitivity requirements to compete with Clark electrode.

We have recently reported the fabrication of a sensor based on CoTPP modified glassy carbon electrodes for monitoring the oxygen consumption in biological samples [30] by a bioelectronic

* Corresponding author.

E-mail address: mbertotti@iq.usp.br (M. Bertotti).

Appendix 5: GO composite encompassing a tetra-ruthenated cobalt porphyrin-Ni coordination polymer and its behavior as isoniazid BIA sensor
paper first page.

Electrochimica Acta 300 (2019) 113–122



Contents lists available at ScienceDirect

Electrochimica Acta

journal homepage: www.elsevier.com/locate/electacta



GO composite encompassing a tetra-ruthenated cobalt porphyrin-Ni coordination polymer and its behavior as isoniazid BIA sensor



Juan S. Aguirre-Araque, Josué M. Gonçalves, Marcelo Nakamura, Pamela O. Rossini, Lucio Angnes, Koiti Araki, Henrique E. Toma*

Department of Fundamental Chemistry, Institute of Chemistry, University of Sao Paulo, Av. Prof. Lineu Prestes 748, Sao Paulo, SP, 05508-000, Brazil

ARTICLE INFO

Article history:

Received 5 October 2018

Received in revised form

13 December 2018

Accepted 18 January 2019

Available online 21 January 2019

Keywords:

Tetra-ruthenated porphyrin

Graphene oxide composite

Isoniazid

Amperometric sensor

BIA

ABSTRACT

A new cobalt(III) tetrapyrrolylporphyrin species (CoTPyP) coordinated to four ruthenium dicarboxy-bipyridine complexes, $[\text{Ru}(\text{H}_2\text{dcbpy})_2\text{Cl}]^+$ was synthesized and successfully deposited onto graphene oxide (GO) sheets by forming *in situ* a coordination polymer with nickel(II) ions, $[\text{CoTRP}(\text{dcbpy})_2]\text{-Ni}$. Because of the high negative charge of the $[\text{CoTRP}(\text{dcbpy})_2]^{11-}$ species, such strategy helped overcoming the electrostatic repulsion with the carboxylate groups on the GO surface, allowing an effective binding through the available Ni(II) sites. In this way, a stable layered composite material was generated, and its characterization performed by means of spectroscopic, XRD and confocal Raman techniques. The material preserves the characteristics of the supramolecular tetra-ruthenated cobalt porphyrin species, and exhibits an unusual electrocatalytic activity in the oxidation of isoniazid, performing at low potentials in aqueous solution (0.10 V vs Ag/AgCl) and pH 7. The GC electrodes modified with this material were used for isoniazid analysis with the BIA assay, revealing an interesting amperometric sensor capable of working under very mild conditions, with a detection limit of 3.5 μM .

© 2019 Published by Elsevier Ltd.

1. Introduction

Porphyrins and metalloporphyrins have been widely used in supramolecular chemistry because of their interesting catalytic, electrocatalytic [1,2] and photochemical [3] properties. A variety of porphyrin-based supermolecules can be assembled by covalently binding appropriate transition metal complexes such as ruthenium polypyridyl units [4–6] at the ring periphery [7]. Such combination has been pursued, since it can enhance the catalytic and photochemical properties by means of synergistic intramolecular electron and energy transfer processes. In special, cobalt porphyrin derivatives exhibit interesting catalytic properties towards substrates such as water, carbon dioxide and oxygen among others [8,9], modulated by the peripheral functional groups attached to the macrocyclic ring.

Recently, porphyrin/graphene oxide composites have emerged as promising materials for many applications ranging from amperometric sensors to photoelectrochemical devices [10,11]. Porphyrins can harvest light to produce electron and hole couples,

while graphene oxide can improve light induced electron transfer and electrochemical processes. For instance, Saravia et al. [12], have demonstrated that the electrostatic interaction of the cationic [tetrakis-bis(dimethylbipyridine-chlororuthenium(II))]-5,10,15,20-tetrapyrrolyl porphyrinate-cobalt complex (denoted CoTRP) with graphene oxide (GO) generates stable nanocomposite materials, where the electrocatalytic oxygen reduction reaction (ORR) mechanism can be tuned by the CoTRP:GO ratio. In this way, four-electron dioxygen reduction catalysis has been performed, allowing the use in electrochemical sensors for monitoring dissolved oxygen concentration.

In this work, we report on a new tetra-ruthenated porphyrin species, denoted $[\text{CoTRP}(\text{H}_2\text{dcbpy})_2]\text{Cl}_5$, containing a central cobalt(III) tetrapyrrolylporphyrin moiety connected to four $[\text{Ru}(\text{H}_2\text{dcbpy})_2\text{Cl}]^+$ complexes (Fig. 1). The peripheral Ru(II) complexes are expected to enhance the oxidizing catalytic properties of the Co(III) center because of their strong electron withdrawing effects. Its direct association with GO has been pursued for improving the electron transfer properties, however with no success, because of the high negative charge of the deprotonated complex.

In order to overcome this effect, nickel(II) ions were added, generating an *in situ* coordination polymer, $[\text{CoTRP}(\text{dcbpy})_2]\text{-Ni}$, capable of interacting with the GO coordinating groups. In this way,

* Corresponding author.

E-mail address: henetoma@iq.usp.br (H.E. Toma).

Appendix 6: Parallel Collaborations

Bromination of 5,15-diisopentiloxyporphyrin (DIPP) with NBS

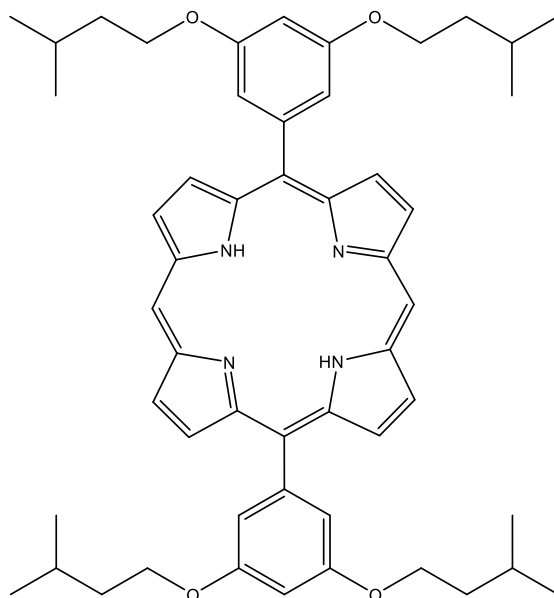


Figure 85. Schematic representation of 5,15-diisopentiloxyporphyrin.

This porphyrin was synthesized by Professor Koiti Araki employing the aldehyde and dipyrromethane route (variation of the Adler-Longo method). The objective with this porphyrin was to synthesize charge separation compounds shielding the porphyrin ring with isolating alkyl chains, placing a physical and energetical barrier between the HOMO and LUMO.⁵²

Figure 86, shows the ¹H-NMR spectrum of DIPP (5,15-diisopentiloxyporphyrin) and its assignments, confirming the purity of the starting material. ¹H NMR (500 MHz, Acetone-d₆) δ ppm 1.01 (d, *J*=6.81 Hz, 24 H) 1.80 (q, *J*=6.81 Hz, 8 H) 1.87 - 1.98 (m, 4 H) 4.29 (t, *J*=6.68 Hz, 8 H) 7.01 (t, *J*=2.32 Hz, 2 H) 7.47 (d, *J*=2.45 Hz, 4 H) 9.20 (d, *J*=4.63 Hz, 4 H) 9.58 (d, *J*=4.63 Hz, 4 H) 10.54 (s, 2 H).

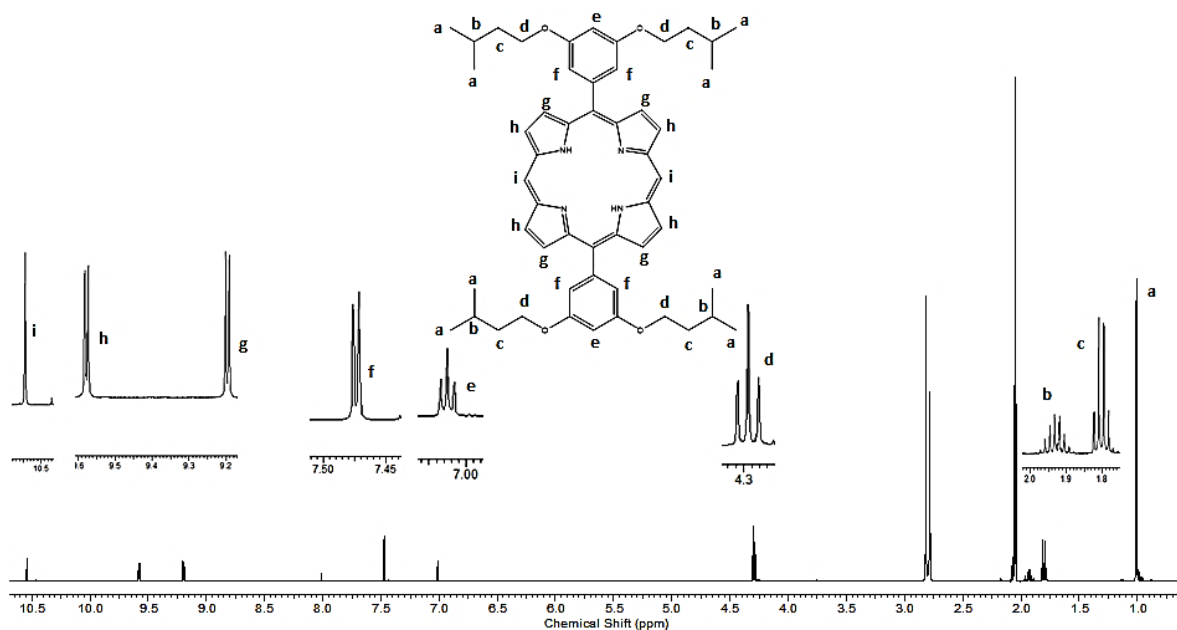


Figure 86. ^1H NMR spectrum of 5,15-diisopentiloxyporphyrin in acetone- d_6 .

Bromination in just one of the free meso positions was achieved by meticulously controlling temperature and stoichiometry of the reaction with NBS. Therefore 1.000 g (1.2 mmol) of DIPP was dissolved in deaerated (N_2) 600 mL of dry CHCl_3 at 0 °C. A purged (N_2) dry CHCl_3 solution of 0.2205 g (1.2 mmol) of NBS was added dropwise over the course of 6 hours using an addition funnel with vigorous stirring. 30 mL of acetone were added to deactivate unreacted NBS and the solution was evaporated under rotary evaporator. Silica column chromatography was performed using a mixture hexane/ CHCl_3 1:1 providing three fractions of the Br_2 -DIPP, Br-DIPP and unreacted DIPP. All the fractions were collected and the brominated compounds characterized.

Characterization of Br-DIPP

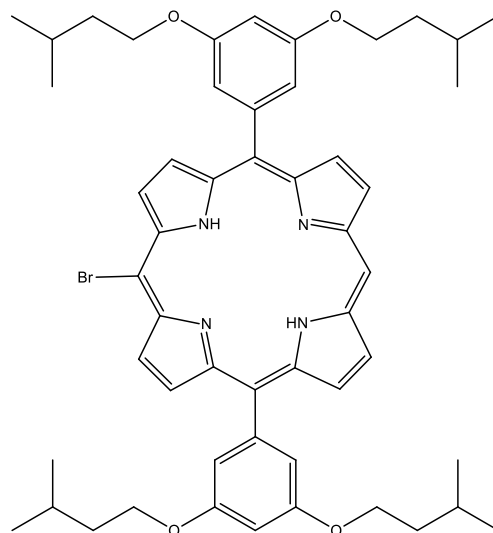


Figure 87. Schematic representation of 5,15-diisopentiloxyphehyl-10-bromoporphyrin.

This porphyrin was the main product of the synthetic route followed before; the objective with this monobromated compound is to asymmetrically functionalize the meso positions 10 and 20 with pyridine or polypyridine type groups with Sonogashira cross couplings in order to coordinate different ruthenium complexes to obtain differentiated and localized HOMO/LUMO regions within the same molecule obtaining larger excited state lifetimes therefore, increasing overall cell efficiencies.

Elemental analysis showed very good match between the experimental and theoretical values:

% CHN analysis: Exp(Calc) % C 70.25(70.49) % H 6.85(6.94) % N 6.33(6.32).

ESI mass spectra Figure 88, shows the molecular ion peak $[M+H]^+$ 887.39 m/z with the isotopic distribution for one bromine atom in the molecule. There is another peak at 909.37 m/z which corresponds to the $[M+23]^+$ ion; those 23 mass units are due to a sodium atom, maintaining the same isotopic distribution of the molecular peak.

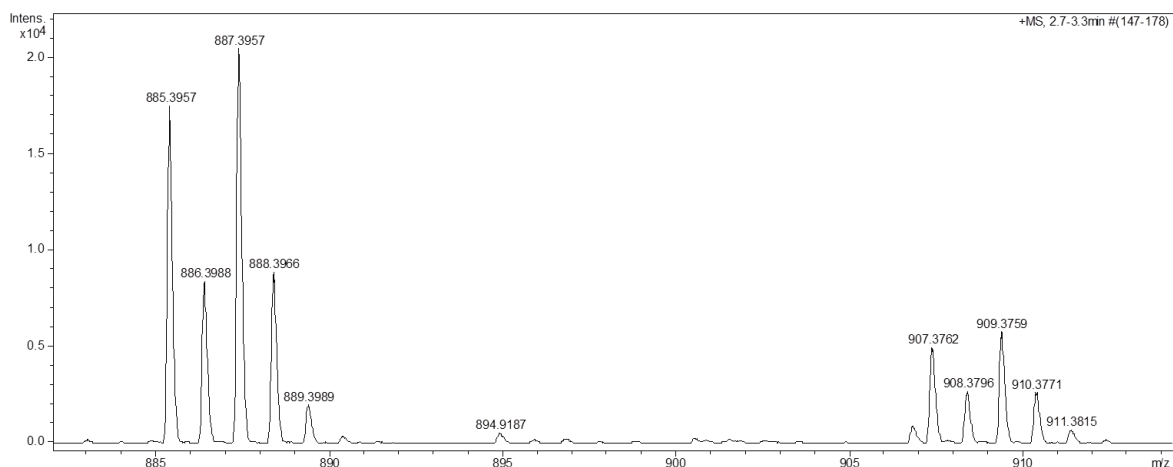


Figure 88. ESI mass spectra of Br-DIPP. Nebulizer: 0.8 Bar, Dry Gas: 5 L min⁻¹, Temp: 200 °C, HV: 4500 V.

¹H NMR spectrum shown in Figure 89 exhibits ten signals for the eleven magnetically different protons present in the molecule, due to the proximity of the signals for the protons *g* and *h*. The presence of the signal for the *meso* hydrogen (*k*) and the signal splitting of the pyrrole protons confirms that this product is the monobromated porphyrin due to symmetry loss.

¹H NMR (500 MHz, Acetone-d₆) δ ppm 1.00 (d, *J*=6.81 Hz, 24 H) 1.79 (q, *J*=6.72 Hz, 8 H) 1.92 (dq, *J*=13.45, 6.69 Hz, 4 H) 4.28 (t, *J*=6.68 Hz, 8 H) 7.01 (t, *J*=2.32 Hz, 2 H) 7.44 (d, *J*=2.18 Hz, 4 H) 9.10 (d, *J*=4.63 Hz, 2 H) 9.12 (d, *J*=4.90 Hz, 2 H) 9.50 (d, *J*=4.63 Hz, 2 H) 9.80 (d, *J*=4.63 Hz, 4 H) 10.45 (s, 1 H).

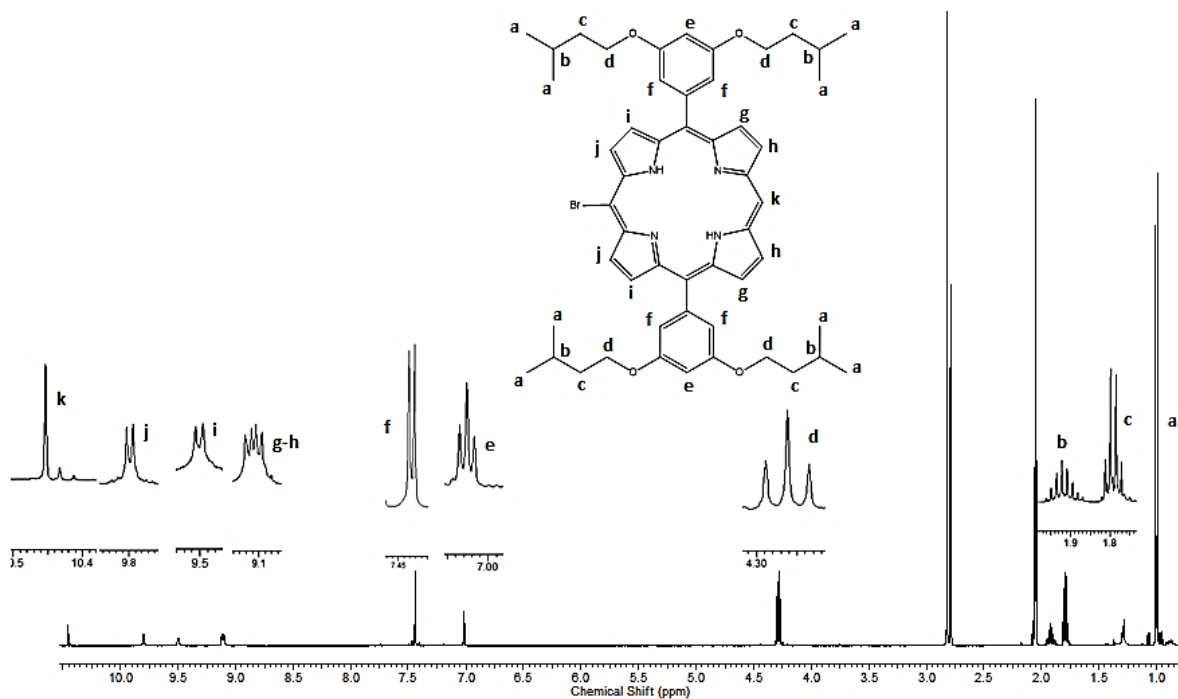


Figure 89. ^1H NMR spectrum of Br-DIPP in acetone- d_6 .

Characterization of Br₂-DIPP

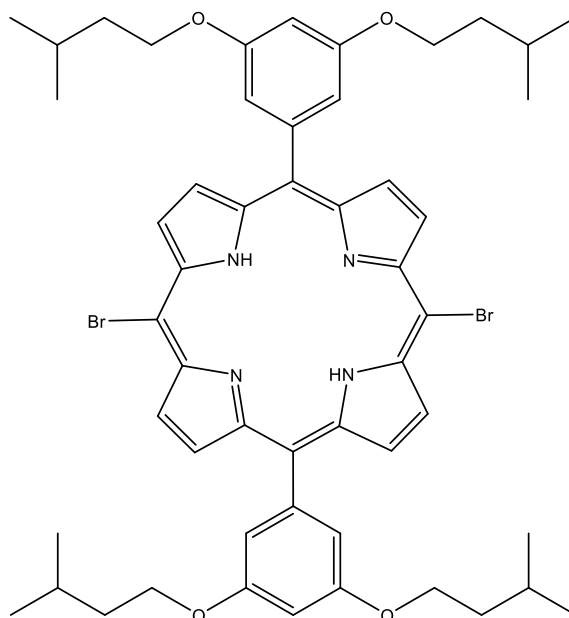


Figure 90. Schematic representation of 5,15-diisopentiloxylphenyl-10,20-dibromoporphyrin.

This porphyrin was obtained as a side product of the bromination described and was recovered because it has some potential use in symmetric compounds that could be useful for coordination polymers.

Elemental analysis showed very good match between the experimental and theoretical values:

% CHN analysis: Exp(Calc) % C 64.86(64.73) % H 6.80(6.27) % N 5.53(5.81).

ESI mass spectra in Figure 91, shows the molecular ion peak $[M+H]^+$ 965.31 m/z with the proper isotopic distribution for a molecule with two bromine atoms. There is another peak at 987.29 m/z which corresponds to the $[M+23]^+$ ion; those 23 mass units are due to a sodium atom, maintaining the same isotopic distribution of the molecular peak.

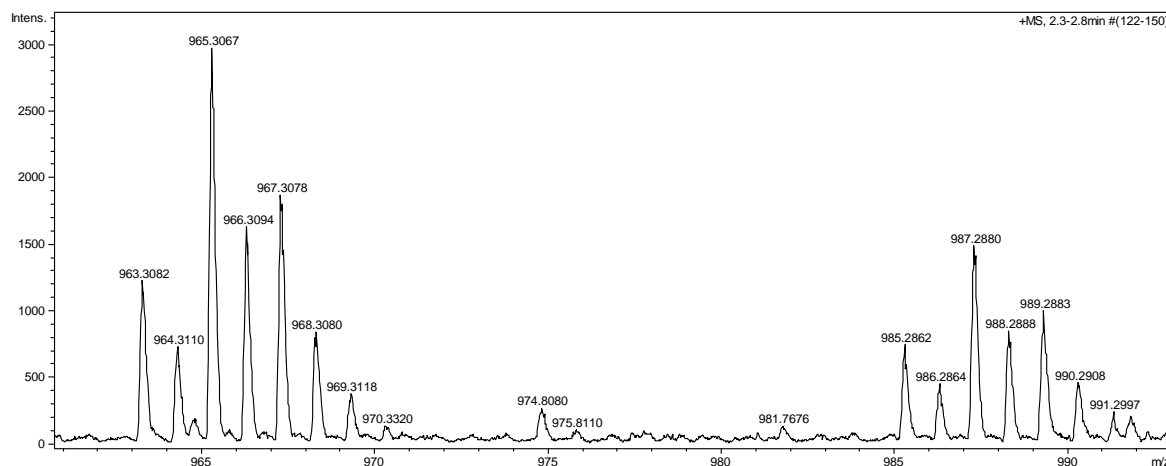


Figure 91. ESI mass spectra of Br₂-DIPP. Nebulizer: 0.8 Bar, Dry Gas: 5 L min⁻¹, Temp: 200 °C, HV: 4500 V.

¹H NMR spectrum in Figure 92, displays eight signals corresponding with the eight magnetically different hydrogens present in Br₂-DIPP. Absence of the 10 and 20 meso protons signal and merging of the pyrrole signals confirm the dibromated character of the product due to symmetry recovery. Solubility issues in acetone led to chloroform usage in this experiment.

^1H NMR (500 MHz, CHLOROFORM-*d*) δ ppm 1.00 (d, $J=6.64$ Hz, 24 H) 1.79 (q, $J=6.64$ Hz, 8 H) 1.86 - 1.94 (m, 4 H) 4.17 (t, $J=6.77$ Hz, 8 H) 6.91 (t, $J=2.30$ Hz, 2 H) 7.33 (d, $J=2.30$ Hz, 4 H) 8.97 (d, $J=4.09$ Hz, 4 H) 9.61 (d, $J=4.85$ Hz, 4 H).

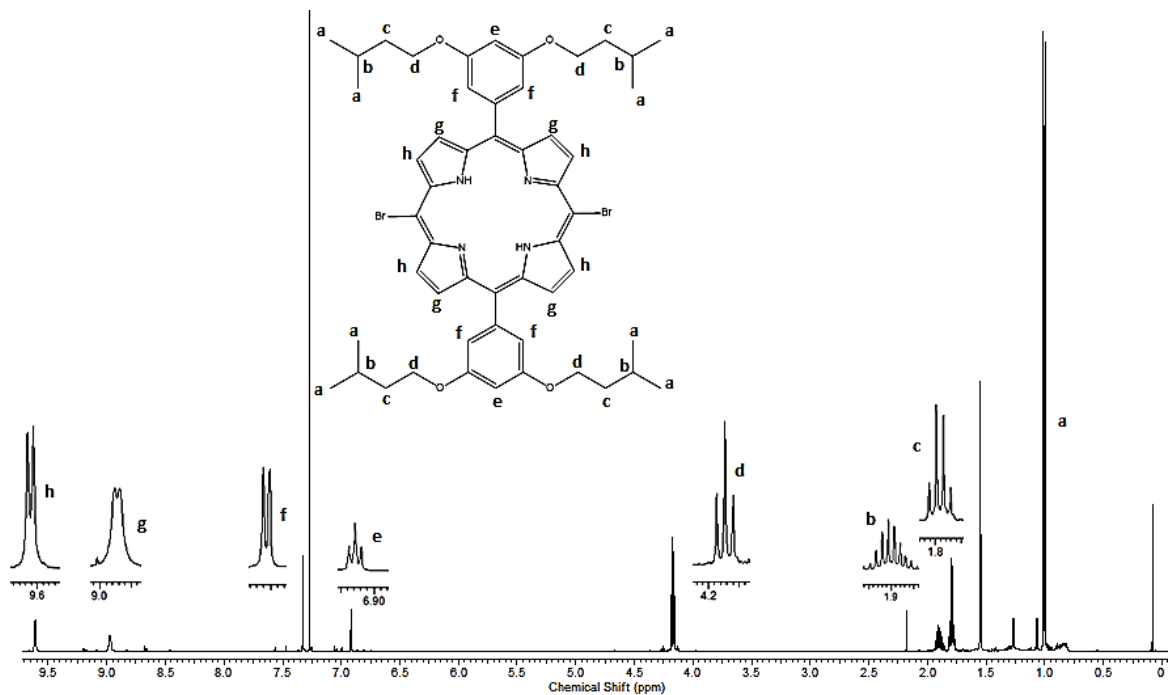


Figure 92. ^1H NMR spectrum of Br₂-DIPP in chloroform-*d*.

Synthesis and characterization of 5,15-dioctyloxyphenylporphyrin (DOPP).

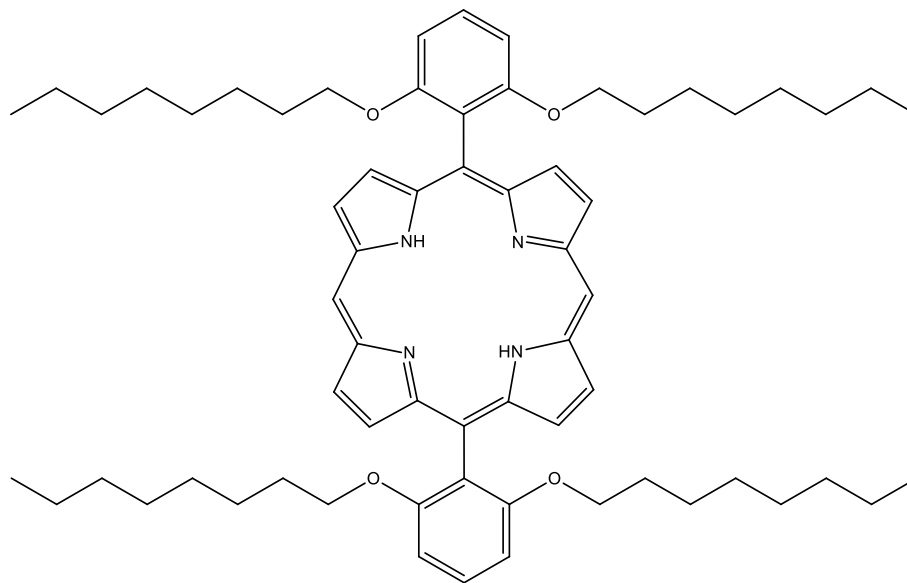


Figure 93. Schematic representation of 5,15-dioctyloxyphenylporphyrin.

This porphyrin was synthesized in collaboration with MSc. Wilmmmer Alexander Arcos from our laboratory employing the aldehyde and dipyrromethane route (variation of the Adler-Longo method).

However, the aldehyde and the dipyrromethane were synthesized from ordinary organic reagents as reported elsewhere:⁵³

Synthesis and characterization of 1,3-dioctyloxybenzene

11 g of resorcinol (0.1 mol), 69.6 mL of 1-bromooctane (0.4 mol) and 69 g of K_2CO_3 (0.5 mol) were refluxed for 96 hours in 500 mL dry acetone. Solvent was removed employing a rotary evaporator and extracted three times with ethyl acetate (100 mL each). The extracts were washed with deionized water and dried employing $CaSO_4$. Solvent was removed under vacuum and the product was purified using silica column chromatography using hexanes/ $CHCl_3$ 5:1 as eluent. Solvent was

removed in the rotary evaporator and the white product was crystallized from the residual slurry by adding acetonitrile and the solid was dried under vacuum overnight.

% CHN analysis: Exp(Calc) % C 78.46(78.99) % H 11.61(11.45) % N

2.26(0).

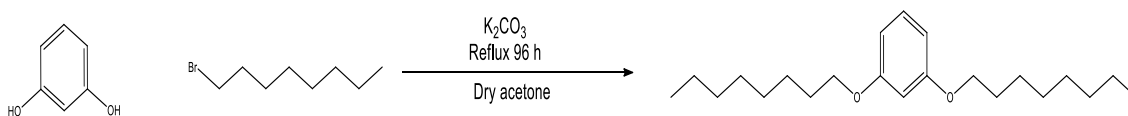


Figure 94. Schematic representation of 1,3-dioctyloxybenzene synthesis.

1H NMR spectrum shown in Figure 95, exhibits well defined signals for the aromatic and nearest protons to the oxygen atoms displaying a higher chemical shift when compared with the other alkyl chain hydrogens.

1H NMR (300 MHz, CHLOROFORM-*d*) δ ppm 0.84 - 0.94 (m, 6 H) 1.20 - 1.52 (m, 20 H) 1.71 - 1.84 (m, 4 H) 3.94 (t, $J=6.59$ Hz, 4 H) 6.45 - 6.49 (m, 2 H) 6.50 (d, $J=2.20$ Hz, 1 H) 7.11 - 7.20 (m, 1 H).

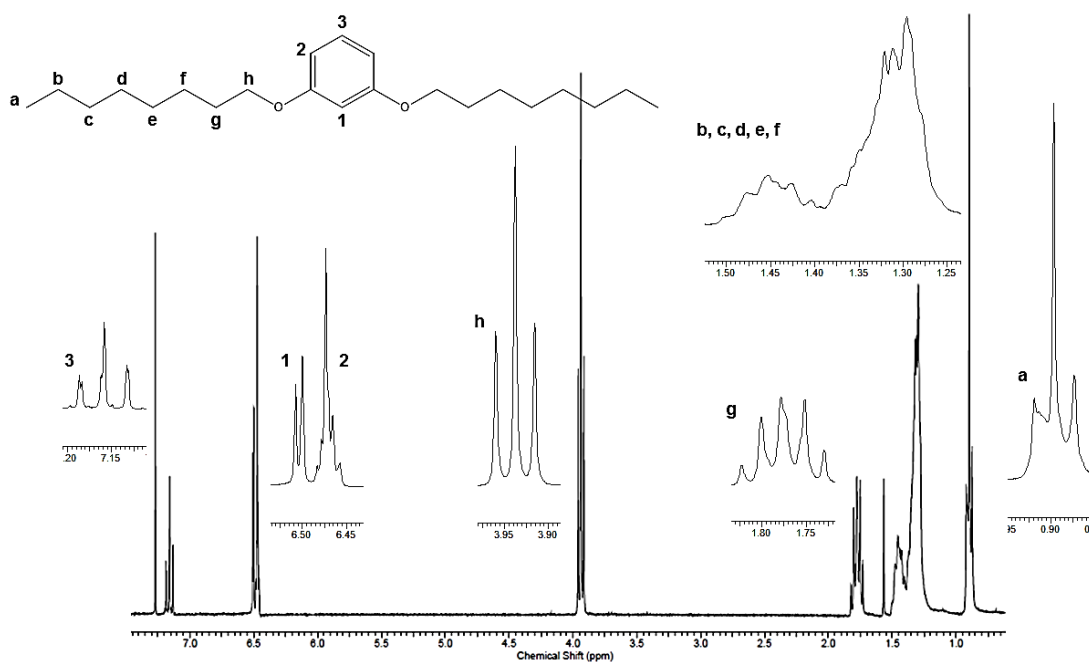


Figure 95. 1H NMR spectrum of 1,3-dioctyloxybenzene in chloroform-*d*.

Synthesis and characterization of 2,6-dioctyloxybenzaldehyde

This synthetic route was performed in the Professor Alcindo Santos' laboratory with the aid of MSc Gisele. 5 g of 1,3-dioctyloxybenzene (15 mmol) and 0.6 mL of freshly distilled TMEDA were dissolved in 50 mL of dry THF employing a three necked flask. The solution was bubbled for 15 minutes with dinitrogen and cooled to 0 °C and 12.0 mL of n-butyllithium (1.6 mol L⁻¹ solution in hexanes) was added dropwise using an addition funnel over 20 min and let to react for 3 hours. The solution was warmed to room temperature and 2.5 mL of freshly distilled DMF were added dropwise and let to react for further 2 hours. The reaction was stopped with water and extracted three times with ether (100 mL each). The combined extracts were dried with brine and CaSO₄ and dried with a rotary evaporator. The solid was recrystallized from hexanes to yield an orange product.

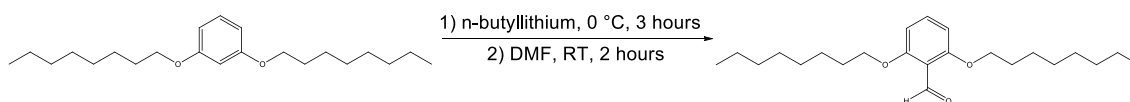


Figure 96. Schematic representation of 2,6-dioctyloxybenzaldehyde synthesis.

As observed in Figure 97, disappearance of proton 1 signal at 6.50 ppm and the appearance of a singlet at 10.55 ppm indicates the formation of an aldehyde group in the benzene ring. The other aromatic signals exhibit minor shifts due to the electronic effect of the aldehyde electron withdrawing nature.

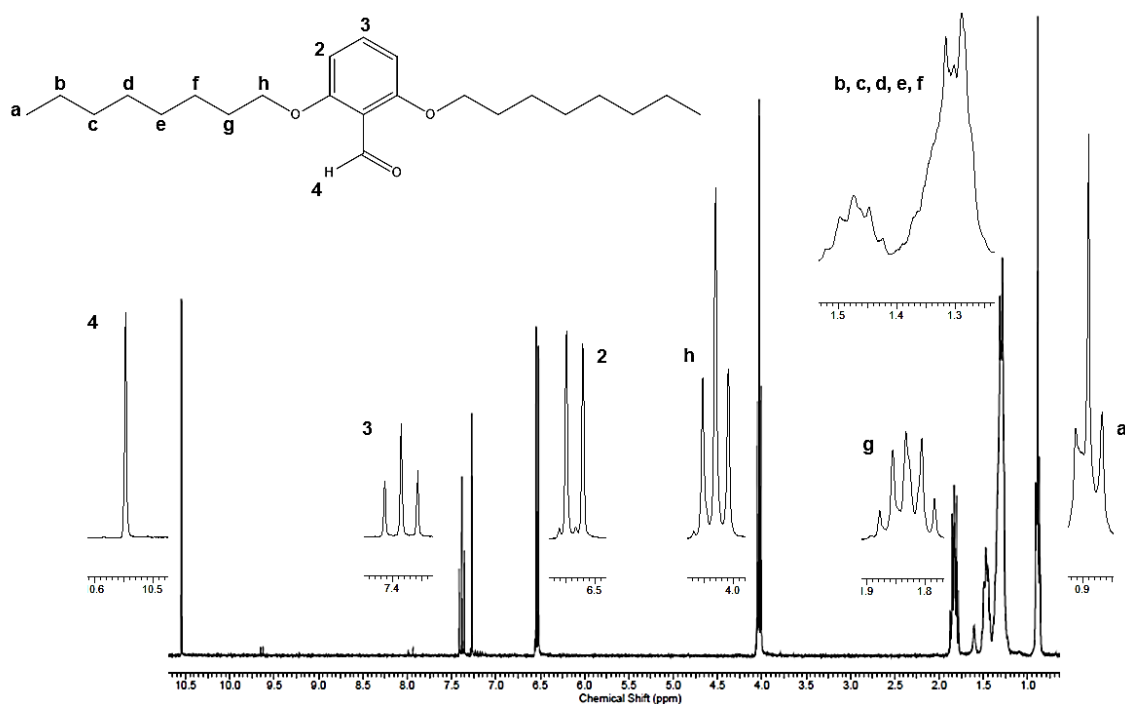


Figure 97. ^1H NMR spectrum of 2,6-dioctyloxybenzaldehyde in chloroform-d.

^1H NMR (300 MHz, CHLOROFORM-*d*) δ ppm 0.84 - 0.94 (m, 6 H) 1.24 - 1.53 (m, 20 H) 1.77 - 1.90 (m, 4 H) 4.03 (t, $J=6.50$ Hz, 4 H) 6.53 (d, $J=8.42$ Hz, 2 H) 7.38 (t, $J=8.42$ Hz, 1 H) 10.55 (s, 1 H).

Synthesis and characterization of DOPP

2.0 g of dipyrromethane (13.8 mmol) and 5.0 g of 2,6-dioctyloxybenzaldehyde (13.8 mmol) were dissolved in 1 L DCM and degassed with dinitrogen for 15 minutes. Right after, 0.96 mL of trifluoroacetic acid (12.4 mmol) were added and the solution was stirred for 4 hours at room temperature. 4.7 g of DDQ (20.7 mmol) were added to the stirring solution and let to react for 1 hour. The mixture was basified employing diethylamine approximately 20 mL and filtered through silica in a glass crucible. Solvent was removed in a rotary evaporator and the remaining solid was purified using silica column chromatography with DCM/Hexanes 1:2 as eluent.

This porphyrin presented solubility issues in chloroform; hence the preferred choice was acetone to collect the spectrum. As observed in Figure 98 there are five well-defined signals in the aromatic region of the spectrum. Being three of them from the pyrrole (**5** and **6**) and 10,20 -meso (**7**) protons, indicating a close resemblance of 5,15-diisopentiloxyporphyrin (DIPP) ¹H NMR spectrum. Nevertheless, the alkyl chains disposition differs in DOPP, positioning them over and under the porphyrin ring as shown by Yella and coworkers in their DFT and TDDFT calculations.⁵² This proximity between them and the porphyrin core ring current, make their magnetic environments unstable, generating multiple signals with poor definition and unmatching integrals.

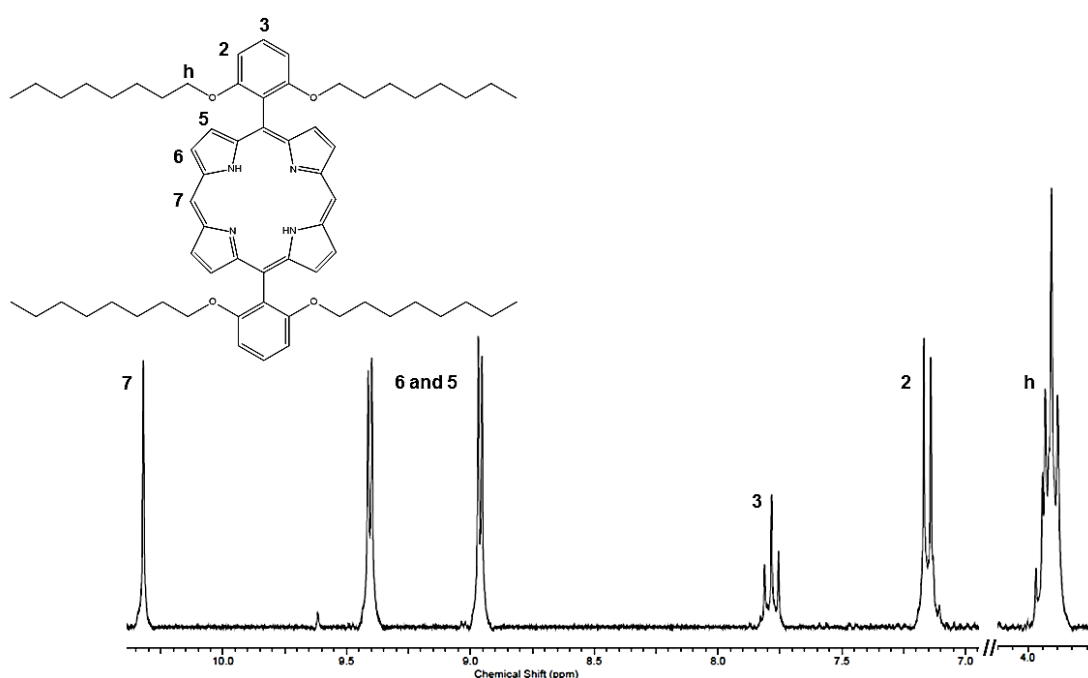


Figure 98. ¹H NMR spectrum of DOPP in acetone-d₆.

¹H NMR (300 MHz, acetone-d₆) δ ppm 3.92 (t, *J*=6.13 Hz, 8 H) 7.15 (d, *J*=8.42 Hz, 4 H) 7.78 (t, *J*=8.33 Hz, 2 H) 8.96 (d, *J*=4.58 Hz, 4 H) 9.41 (d, *J*=4.58 Hz, 4 H) 10.32 (s, 2 H).

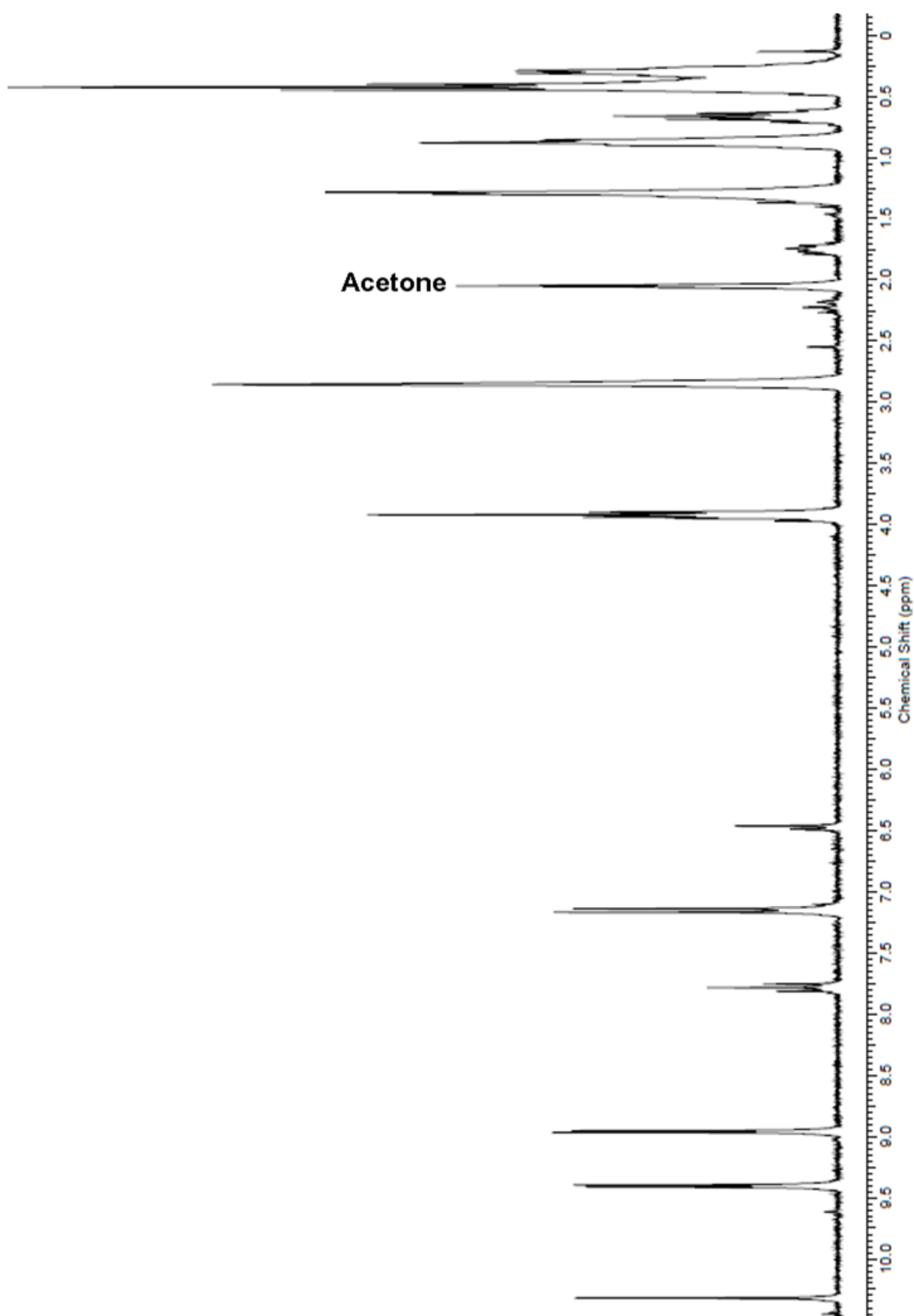
Chapter V conclusions

DIPP was obtained in its pure form from Professor Koiti Araki, it was successfully characterized and functionalized with NBS for further synthetic steps with the aim to create both symmetric and asymmetric porphyrins capable of coordinate two metal centers, opening the possibilities to assemble supramolecular structures able to display catalytic and photochemical among other properties.

DOPP was fully synthesized from resorcinol and pyrrole through several reaction steps. The aim with this porphyrin was to perform a reliable comparison with DIPP for supramolecular porphyrins bearing metal complexes or clusters (i.e. MOFs) and the differences in performance from the sole organic porphyrins reported by Yella and coworkers.

Unfortunately, by not being the main objective of my doctoral research, time ran out and further synthetic steps couldn't be executed. Nevertheless, the objectives being pursued with these porphyrins are attractive enough to other fellow researchers within LQSN continue this endeavor.

Full ^1H NMR spectrum of DOPP



BIBLIOGRAPHY

- (1) Royal Society of Chemistry. Periodic Table: Ruthenium
<http://www.rsc.org/periodic-table/element/44/ruthenium>.
- (2) Seddon, E. A.; Seddon, K. R. Ruthenium(III). In *Topics in Inorganic and General Chemistry*; Clark, R. J. H., Ed.; Elsevier Science, 1984; Vol. 19, pp 155–340. <https://doi.org/10.1016/B978-0-444-42375-7.50016-6>.
- (3) Vogt, L. H.; Lawrence, J.; Wiberley, S. E. The Crystal and Molecular Structure of Ruthenium-Sulphur Dioxide Coordination Compounds. *Inorg. Chem.* **1965**, *4* (8), 1157–1163.
- (4) Jin, W.; Wang, L.; Yu, Z. A Highly Active Ruthenium(II) Pyrazolyl – Pyridyl – Pyrazole Complex Catalyst for Transfer Hydrogenation of Ketones. *Organometallics* **2012**, *31*, 5664–5667.
- (5) Gunanathan, C.; Milstein, D. Bond Activation and Catalysis by Ruthenium Pincer Complexes. *Chem. Rev.* **2014**, *114*, 12024–12087. <https://doi.org/10.1021/cr5002782>.
- (6) Quebatte, L.; Solari, E.; Scopelliti, R.; Severin, K. A Bimetallic Ruthenium Ethylene Complex as a Catalyst Precursor for the Kharasch Reaction. *Organometallics* **2005**, *24*, 1404–1406. <https://doi.org/10.1021/om050027x>.
- (7) Sanchez-delgado, B. R. A.; Bradley, J. S.; Wilkinson, G. Further Studies on the Homogeneous Hydroformylation of Alkenes by Use of Ruthenium Complex Catalysts. *J. Chem. Soc. Dalton Trans.* **1976**, *0*, 399–404.
- (8) Bajaj, H. C.; Shukla, A. D.; Das, A. Intervalence Charge Transfer Transition in Mixed Valence Complexes Synthesized from Ru(III)(EDTA)- and Fe(II)(CN)₅-Cores. *J. Chem. Sci.* **2002**, *114* (4), 431–442.
- (9) Canzi, G.; Goeltz, J. C.; Henderson, J. S.; Park, R. E.; Maruggi, C.; Kubiak, P.

- On the Observation of Intervalence Charge Transfer Bands in Hydrogen-Bonded Mixed Valence Complexes. *J. Am. Chem. Soc.* **2014**, *136* (5), 1710–1713.
- (10) Sun, H.; Steeb, J.; Kaifer, A. E. Efficient Electronic Communication between Two Identical Ferrocene Centers in a Hydrogen-Bonded Dimer. *J. Am. Chem. Soc.* **2006**, *128* (9), 2820–2821.
- (11) Creutz, C.; Taube, H. A Direct Approach to Measuring the Franck-Condon Barrier to Electron Transfer between Metal Ions. *J. Am. Chem. Soc.* **1969**, *91* (14), 3988–3989.
- (12) Toma, H. H. Intervalence Transfer in Outer-Sphere Hexa-Ammineruthenium(III) Pentacyanoferrate(II) Complexes. *J. Chem. Soc. Dalton Trans.* **1980**, *0*, 471–475.
- (13) Alexiou, A. D. P.; Dovidauskas, S.; Toma, H. E. Propriedades e Aplicacoes de Clusters Trinucleares de Carboxilatos de Rutenio. *Quim. Nova* **2000**, *23* (6), 785–793.
- (14) Legzdins, R.; Mitchell, R. W.; Rempel, G. L.; Ruddick, J. D.; Wilkinson, G. The Protonation of Ruthenium- and Rhodium-Bridged Carboxylates and Their Use as Homogeneous Hydrogenation Catalysts for Unsaturated Substances. *J. Chem. Soc. A* **1970**, 3322–3325. [https://doi.org/10.1016/0376-8716\(96\)01221-5](https://doi.org/10.1016/0376-8716(96)01221-5).
- (15) Nicolaidis, C. P.; Coville, N. J. Polymer-Supported Catalysts Part 2. Polymer-Supported Ruthenium Acetate as an Olefin Hydrogenation Catalyst. *J. Mol. Catal.* **1984**, *24* (3), 375–381.
- (16) Sasson, Y.; Rempel, G. L. Oxidative Transfer Dehydrogenation of α,β -Unsaturated Carbinols to α,β -Unsaturated Ketones Catalyzed by Ruthenium

Complexes. *Can. J. Chem.* **1974**, *52* (22), 3825–3827.
<https://doi.org/10.1139/v74-572>.

- (17) Szymanska-Buzar, T.; Ziolkowski, J. J. M₃-Oxotrimetal Hexacarboxylates as Heterogenized Catalysts in Hydroperoxide Decomposition and Olefin Epoxidation Reactions. *J. Mol. Catal.* **1987**, *11* (3), 371–381.
- (18) Johnson, B. F. G.; Johnston, R. D.; Josty, P. L.; Lewis, J.; Williams, I. G. Some Reactions of Triruthenium Dodecacarbonyl. *Nature* **1967**, 901–902.
<https://doi.org/10.1002/jps>.
- (19) Kalyanasundaram, K. Photophysics, Photochemistry and Solar Energy Conversion with Tris(Bipyridyl)Ruthenium(II) and Its Analogues. *Coord. Chem. Rev.* **1982**, *46*, 159–244. [https://doi.org/10.1016/0010-8545\(82\)85003-0](https://doi.org/10.1016/0010-8545(82)85003-0).
- (20) Sutin, N. Light-Induced Electron Transfer Reactions. *J. Photochem.* **1979**, *10* (1), 19–40. [https://doi.org/10.1016/0047-2670\(79\)80035-0](https://doi.org/10.1016/0047-2670(79)80035-0).
- (21) Biner, M.; Burgi, H. B.; Ludi, A.; Rohr, C. Crystal and Molecular Structures of [Ru(Bpy)₃](PF₆)₃ and [Ru(Bpy)₃](PF₆)₂ at 105 K. *J. Am. Chem. Soc.* **1992**, *114*, 5197–5203.
- (22) Damrauer, N. H.; Cerullo, G.; Yeh, A.; Boussie, T. R.; Shank, C. V.; McCusker, J. K. Femtosecond Dynamics of Excited-State Evolution in [Ru(Bpy)₃]²⁺. *Science* (80-.). **1997**, *275*, 54–57.
<https://doi.org/10.1126/science.275.5296.54>.
- (23) Müller, P.; Brettel, K. [Ru(Bpy)₃]²⁺ as a Reference in Transient Absorption Spectroscopy: Differential Absorption Coefficients for Formation of the Long-Lived ³MLCT Excited State. *Photochem. Photobiol. Sci.* **2012**, *11* (4), 632–636.
<https://doi.org/10.1039/c2pp05333k>.
- (24) Belser, P.; von Zelewsky, A.; Frank, M.; Seel, C.; Vögtle, F.; De Cola, L.;

- Balzani, V.; Barigelletti, F. Supramolecular Ru and/or Os Complexes of Tris(Bipyridine) Bridging Ligands. Syntheses, Absorption Spectra, Luminescence Properties, Electrochemical Behavior, Intercomponent Energy, and Electron Transfer. *J. Am. Chem. Soc.* **1993**, *115* (10), 4076–4086. <https://doi.org/10.1021/ja00063a028>.
- (25) Juris, A.; Balzani, V.; Barigelletti, F.; Campagna, S.; Belser, P.; Von Zelewsky, A. Ru(II) Polypyridine Complexes: Photophysics, Photochemistry, Electrochemistry and Chemiluminescence. *Coord. Chem. Rev.* **1988**, *84*, 85–277. [https://doi.org/10.1016/0010-8545\(88\)80032-8](https://doi.org/10.1016/0010-8545(88)80032-8).
- (26) Reynal, A.; Palomares, E. Ruthenium Polypyridyl Sensitisers in Dye Solar Cells Based on Mesoporous TiO₂. *Eur. J. Inorg. Chem.* **2011**, No. 29, 4509–4526. <https://doi.org/10.1002/ejic.201100516>.
- (27) Abbotto, A.; Manfredi, N. Electron-Rich Heteroaromatic Conjugated Polypyridine Ruthenium Sensitizers for Dye-Sensitized Solar Cells. *Dalt. Trans.* **2011**, *40*, 12421–12438. <https://doi.org/10.1039/c1dt10832h>.
- (28) O'Donnell, R. M.; Johansson, P. G.; Abrahamsson, M.; Meyer, G. J. Excited-State Relaxation of Ruthenium Polypyridyl Compounds Relevant to Dye-Sensitized Solar Cells. *Inorg. Chem.* **2013**, *52* (12), 6839–6848.
- (29) Wang, Z.; Yamaguchi, T.; Sugihara, H. Significant Efficiency Improvement of the Black Dye-Sensitized Solar Cell through Protonation of TiO₂ Films. *Langmuir* **2005**, *21* (5), 4272–4276.
- (30) Nazeeruddin, M. K.; Kay, A.; Muller, E.; Liska, P.; Vlachopoulos, N.; Gratzel, M. Conversion of Light to Electricity by Cis-X₂Bis(2,2'-Bipyridyl-4,4'-Dicarboxylate)Ruthenium(II) Charge-Transfer Sensitizers (X = Cl-, Br-, I-, CN-, and SCN-) on Nanocrystalline TiO₂ Electrodes. *J. Am. Chem. Soc.* **1993**, *115*,

6382–6390.

- (31) Nazeeruddin, M. K.; Zakeeruddin, S. M.; Humphry-Baker, R.; Jirousek, M.; Liska, P.; Vlachopoulos, N.; Shklover, V.; Fischer, C.; Grätzel, M. Acid-Base Equilibria of (2,2'-Bipyridyl-4,4'-Dicarboxylic Acid)Ruthenium(II) Complexes and the Effect of Protonation on Charge-Transfer Sensitization of Nanocrystalline Titania. *Inorg. Chem.* **1999**, *38* (26), 6298–6305.
- (32) Nazeeruddin, M. K.; Péchy, P.; Renouard, T. Engineering of Efficient Panchromatic Sensitizers for Nanocrystalline TiO₂-Based Solar Cells. *J. Am. Chem. Soc.* **2001**, *123* (8), 1613–1624.
- (33) Gouterman, M. Study of the Effects of Substitution on the Absorption Spectra of Porphin. *J. Chem. Phys.* **1959**, *30* (5), 1139–1161. <https://doi.org/10.1063/1.1730148>.
- (34) Gouterman, M. Spectra of Porphyrins. *J. Mol. Spectrosc.* **1961**, *6* (C), 138–163. [https://doi.org/10.1016/0022-2852\(61\)90236-3](https://doi.org/10.1016/0022-2852(61)90236-3).
- (35) Giovannetti, R. The Use of Spectrophotometry UV-Vis for the Study of Porphyrins. *Macro To Nano Spectrosc.* **2012**. <https://doi.org/10.5772/38797>.
- (36) Kim, B. F.; Bohandy, J. High-Resolution Spectroscopy of Porphyrins. *Johns Hopkins APL Tech. Dig.* **1981**, *2* (3), 2–12.
- (37) Lindsey, J. S.; Hsu, H. C.; Schreiman, I. C. Synthesis of Tetraphenylporphyrins under Very Mild Conditions. *Tetrahedron Lett.* **1986**, *27* (41), 4969–4970. [https://doi.org/10.1016/S0040-4039\(00\)85109-6](https://doi.org/10.1016/S0040-4039(00)85109-6).
- (38) Lindsey, J. S.; Schreiman, I. C.; Hsu, H. C.; Kearney, P. C.; Marguerettaz, A. M. Rothmund and Adler-Longo Reactions Revisited: Synthesis of Tetraphenylporphyrins under Equilibrium Conditions. *J. Org. Chem.* **1987**, *52*, 827–836. <https://doi.org/10.1021/jo00381a022>.

- (39) Rothemund, P.; Menotti, A. R. The Synthesis of a,b,c,d-Tetraphenylporphine. *J. Am. Chem. Soc.* **1941**, *63*, 267–270.
- (40) Adler, A. D.; Longo, F. R.; Shergalis, W. Mechanistic Investigations of Porphyrin Syntheses. I. Preliminary Studies on Ms-Tetraphenylporphin. *J. Am. Chem. Soc.* **1964**, *86* (15), 3145–3149. <https://doi.org/10.1021/ja01069a035>.
- (41) Royal Society of Chemistry. Photosynthesis <http://www.rsc.org/Education/Teachers/Resources/cfb/Photosynthesis.htm>.
- (42) Green, B. R.; Anderson, J. M.; Parson, W. W. Photosynthetic Membranes and Their Light-Harvesting Antennas. In *Light-Harvesting Antennas in Photosynthesis*; Green, B. R., Parson, W. W., Eds.; Kluwer Academic Publishers: Dordrecht, 2003; pp 1–28.
- (43) Storz, J. F. A Study in Scarlet: The Role of Hemoglobin in Blood Gas Transport. In *Hemoglobin: Insights Into Protein Structure, Function and Evolution*; Oxford, 2019; pp 11–29.
- (44) Deng, Y.; Zhong, F.; Alden, S. L.; Hoke, K. R.; Pletneva, E. V. The K79G Mutation Reshapes the Heme Crevice and Alters Redox Properties of Cytochrome C. *Biochemistry* **2018**, *57*, 5827–5840. <https://doi.org/10.1021/acs.biochem.8b00650>.
- (45) Dovidauskas, S.; Araki, K.; Toma, H. E. Electrochemical and Binding Properties of a Meso-Tetra(4-Pyridyl)Porphyrinatozinc Supramolecule Containing Four m³-Oxo-Triruthenium Acetate Clusters. *J. Porphyr. Phthalocyanines* **2000**, *4*, 727–735.
- (46) Formiga, A. L. B.; Nogueira, A. F.; Araki, K.; Toma, H. E. Contrasting Photoelectrochemical Behaviour of Two Isomeric Supramolecular Dyes Based on Meso-Tetra(Pyridyl)Porphyrin Incorporating Four (M³-Oxo)-Triruthenium(III)

Clusters. *New J. Chem.* **2008**, 32 (7), 1167–1174.
<https://doi.org/10.1039/b709888j>.

- (47) Lalli, P. M.; Iglesias, B. A.; Deda, D. K.; Toma, H. E.; De Sa, G. F.; Daroda, R. J.; Araki, K.; Eberlin, M. N. Resolution of Isomeric Multi-Ruthenated Porphyrins by Travelling Wave Ion Mobility Mass Spectrometry. *Rapid Commun. Mass Spectrom.* **2012**, 26 (3), 263–268. <https://doi.org/10.1002/rcm.5314>.
- (48) Son, H.-J.; Jin, S.; Patwardhan, S.; Wezenberg, S. J.; Jeong, N. C.; So, M.; Wilmer, C. E.; Sarjeant, A. A.; Schatz, G. C.; Snurr, R. Q.; et al. Light-Harvesting and Ultrafast Energy Migration in Porphyrin-Based Metal Organic Frameworks (MOFs). *J. Am. Chem. Soc.* **2013**, 135, 862–869. <https://doi.org/10.1557/opl.2013.987>.
- (49) Cheng, Y.; Yang, G.; Jiang, H.; Zhao, S.; Liu, Q.; Xie, Y. Organic Sensitizers with Extended Conjugation Frameworks as Cosensitizers of Porphyrins for Developing Efficient Dye-Sensitized Solar Cells. *ACS Appl. Mater. Interfaces* **2018**. <https://doi.org/10.1021/acsami.8b12883>.
- (50) Reddy, K. S. K.; Liu, Y.-C.; Chou, H.-H.; Kala, K.; Wei, T.-C.; Yeh, C.-Y. Synthesis and Characterization of Novel β -Bis(N,N-Diarylamino) Substituted Porphyrin for Dye-Sensitized Solar Cells under One Sun and Dim Light Conditions. *ACS Appl. Mater. Interfaces* **2018**. <https://doi.org/10.1021/acsami.8b14457>.
- (51) Song, H.; Tang, W.; Zhao, S.; Liu, Q.; Xie, Y. Porphyrin Sensitizers Containing an Auxiliary Benzotriazole Acceptor for Dye-Sensitized Solar Cells: Effects of Steric Hindrance and Cosensitization. *Dye. Pigment.* **2018**, 155 (January), 323–331. <https://doi.org/10.1016/j.dyepig.2018.03.054>.
- (52) Mathew, S.; Yella, A.; Gao, P.; Humphry-Baker, R.; Curchod, B. F. E.; Ashari-

- Astani, N.; Tavernelli, I.; Rothlisberger, U.; Nazeeruddin, M. K.; Grätzel, M. Dye-Sensitized Solar Cells with 13% Efficiency Achieved through the Molecular Engineering of Porphyrin Sensitizers. *Nat. Chem.* **2014**, *6* (3), 242–247. <https://doi.org/10.1038/nchem.1861>.
- (53) Yella, A.; Lee, H.-W.; Tsao, H. N.; Yi, C.; Chandiran, A. K.; Nazeeruddin, M. K.; Diao, E. W.; Yeh, C.-Y.; Zakeeruddin, S. M.; Gratzel, M. Porphyrin-Sensitized Solar Cells With Cobalt (II/III)-Based Redox Electrolyte Exceed 12 Percent Efficiency. *Science* (80-.). **2011**, *334*, 629–633.
- (54) Düring, J.; Kunzmann, A.; Killian, M. S.; Costa, R. D.; Guldi, D. M.; Gröhn, F. Porphyrins as Multifunctional Interconnects in Networks of ZnO Nanoparticles and Their Application in Dye-Sensitized Solar Cells. *ChemPhotoChem* **2017**, *2*, 213–222. <https://doi.org/10.1002/cptc.201700107>.
- (55) Balis, N.; Verykios, A.; Soultati, A.; Constantoudis, V.; Papadakis, M.; Kournoutas, F.; Drivas, C.; Skoulikidou, M.-C.; Gardelis, S.; Fakis, M.; et al. Triazine-Substituted Zinc Porphyrin as an Electron Transport Interfacial Material for Efficiency Enhancement and Degradation Retardation in Planar Perovskite Solar Cells. *ACS Appl. Energy Mater.* **2018**, *1* (7), 3216–3229. <https://doi.org/10.1021/acsaem.8b00447>.
- (56) Parussulo, A. L.; Iglesias, B. A.; Toma, H. E.; Araki, K. Sevenfold Enhancement on Porphyrin Dye Efficiency by Coordination of Ruthenium Polypyridine Complexes. *Chem. Commun.* **2012**, *48* (55), 6939–6941.
- (57) Ravanat, J.-L.; Cadet, J.; Araki, K.; Toma, H. E.; Medeiros, M. H. .; Di Mascio, P. Supramolecular Cationic Tetraruthenated Porphyrin and Light-Induced Decomposition of 2'-Deoxyguanosine Predominantly Via a Singlet Oxygen-Mediated Mechanism. *Photochem. Photobiol.* **1998**, *68* (5), 698–702.

- (58) Araki, K.; Silva, C. A.; Toma, H. E.; Catalani, L. H.; Medeiros, M. H. G.; Di Mascio, P. Zinc Tetra-ruthenated Porphyrin Binding and Photoinduced Oxidation of Calf-Thymus DNA. *J. Inorg. Biochem.* **2000**, *78* (4), 269–273. [https://doi.org/10.1016/S0162-0134\(00\)00053-2](https://doi.org/10.1016/S0162-0134(00)00053-2).
- (59) Thompson, S. J.; Brennan, M. R.; Lee, S. Y.; Dong, G. Synthesis and Applications of Rhodium Porphyrin Complexes. *Chem. Soc. Rev.* **2018**, *47* (3), 929–981. <https://doi.org/10.1039/c7cs00582b>.
- (60) Vaughan, B. A.; Webster-Gardiner, M. S.; Cundari, T. R.; Gunnoe, T. B. A Rhodium Catalyst for Single-Step Styrene Production from Benzene and Ethylene. *Science* (80-.). **2015**, *348* (6233), 421–424. <https://doi.org/10.1126/science.aaa2260>.
- (61) Jana, R.; Tunge, J. A. A Homogeneous, Recyclable Rhodium(I) Catalyst for the Hydroarylation of Michael Acceptors. *Org. Lett.* **2009**, *11* (4), 971–974. <https://doi.org/10.1021/ol802927v>.
- (62) Tan, M.; Yang, G.; Wang, T.; Vitidsant, T.; Li, J.; Wei, Q.; Ai, P.; Wu, M.; Zheng, J.; Tsubaki, N. Active and Regioselective Rhodium Catalyst Supported on Reduced Graphene Oxide for 1-Hexene Hydroformylation. *Catal. Sci. Technol.* **2016**, *6* (4), 1162–1172. <https://doi.org/10.1039/c5cy01355k>.
- (63) Yoshida, Z.; Ogoshi, H.; Omura, T.; Watanabe, E.; Kurosaki, T. A New Rhodium (I) Porphyrin Complex. *Tetrahedron Lett.* **1972**, *13* (11), 1077–1080.
- (64) Han, A.; Jia, H.; Ma, H.; Ye, S.; Wu, H.; Lei, H.; Han, Y.; Cao, R.; Du, P. Cobalt Porphyrin Electrode Films for Electrocatalytic Water Oxidation. *Phys. Chem. Chem. Phys.* **2015**, No. 16. <https://doi.org/10.1039/c4cp00523f>.
- (65) Liu, B.; Li, J.; Wu, H. L.; Liu, W. Q.; Jiang, X.; Li, Z. J.; Chen, B.; Tung, C. H.; Wu, L. Z. Improved Photoelectrocatalytic Performance for Water Oxidation by

- Earth-Abundant Cobalt Molecular Porphyrin Complex-Integrated BiVO₄ Photoanode. *ACS Appl. Mater. Interfaces* **2016**, *8* (28), 18577–18583. <https://doi.org/10.1021/acsami.6b04510>.
- (66) Han, Y.; Wu, Y.; Lai, W.; Cao, R. Electrocatalytic Water Oxidation by a Water-Soluble Nickel Porphyrin Complex at Neutral pH with Low Overpotential. *Inorg. Chem.* **2015**, *54* (11), 5604–5613. <https://doi.org/10.1021/acs.inorgchem.5b00924>.
- (67) Mohamed, E. A.; Zahran, Z. N.; Naruta, Y. Covalent Bonds Immobilization of Cofacial Mn Porphyrin Dimers on an ITO Electrode for Efficient Water Oxidation in Aqueous Solutions. *J. Catal.* **2017**, *352*, 293–299. <https://doi.org/10.1016/j.jcat.2017.05.018>.
- (68) Yamamoto, K.; Nakazawa, S.; Imaoka, T. Manganese-Cerium Porphyrin Trinuclear Complex as a Catalyst for Water Oxidation. *Mol Cryst Liq Cryst* **2002**, *379*, 407–412. <https://doi.org/10.1080/713738661>.
- (69) Fujishima, A.; Honda, K. Electrochemical Photolysis of Water at a Semiconductor Electrode. *Nature* **1972**, *238*, 37–38. <https://doi.org/10.1038/239137a0>.
- (70) Nakazono, T.; Parent, A. R.; Sakai, K. Improving Singlet Oxygen Resistance during Photochemical Water Oxidation by Cobalt Porphyrin Catalysts. *Chem. - A Eur. J.* **2015**, *21* (18), 6723–6726. <https://doi.org/10.1002/chem.201500716>.
- (71) Kim, S.; Kim, H. Oxygen Reduction Reaction at Porphyrin-Based Electrochemical Catalysts: Mechanistic Effects of pH and Spin States Studied by Density Functional Theory. *Catal. Today* **2017**, *295* (May), 119–124. <https://doi.org/10.1016/j.cattod.2017.05.007>.
- (72) Rigsby, M. L.; Wasylenko, D. J.; Pegis, M. L.; Mayer, J. M. Medium Effects Are

- as Important as Catalyst Design for Selectivity in Electrocatalytic Oxygen Reduction by Iron-Porphyrin Complexes. *J. Am. Chem. Soc.* **2015**, *137* (13), 4296–4299. <https://doi.org/10.1021/jacs.5b00359>.
- (73) He, Q.; Mugadza, T.; Kang, X.; Zhu, X.; Chen, S.; Kerr, J.; Nyokong, T. Molecular Catalysis of the Oxygen Reduction Reaction by Iron Porphyrin Catalysts Tethered into Nafion Layers: An Electrochemical Study in Solution and a Membrane-Electrode-Assembly Study in Fuel Cells. *J. Power Sources* **2012**, *216*, 67–75. <https://doi.org/10.1016/j.jpowsour.2012.05.043>.
- (74) Song, E.; Shi, C.; Anson, F. C. Comparison of the Behavior of Several Cobalt Porphyrins as Electrocatalysts for the Reduction of O₂ at Graphite Electrodes. *Langmuir* **1998**, *14* (15), 4315–4321. <https://doi.org/10.1021/la980084d>.
- (75) Sonkar, P. K.; Prakash, K.; Yadav, M.; Ganesan, V.; Sankar, M.; Gupta, R.; Yadav, D. K. Co(II)-Porphyrin-Decorated Carbon Nanotubes as Catalysts for Oxygen Reduction Reactions: An Approach for Fuel Cell Improvement. *J. Mater. Chem. A* **2017**, *5* (13), 6263–6276. <https://doi.org/10.1039/c6ta10482g>.
- (76) Passard, G.; Dogutan, D. K.; Qiu, M.; Costentin, C.; Nocera, D. G. Oxygen Reduction Reaction Promoted by Manganese Porphyrins. *ACS Catal.* **2018**, *8* (9), 8671–8679. <https://doi.org/10.1021/acscatal.8b01944>.
- (77) Koiti, A.; Toma, H. E. Synthesis and Electrochemical Behavior of a Tetrametallated Cobalt Porphyrin. *Inorganica Chim. Acta* **1991**, *179* (2), 293–296. [https://doi.org/10.1016/S0020-1693\(00\)85891-0](https://doi.org/10.1016/S0020-1693(00)85891-0).
- (78) Oldacre, A. N.; Friedman, A. E.; Cook, T. R. A Self-Assembled Cofacial Cobalt Porphyrin Prism for Oxygen Reduction Catalysis. *J. Am. Chem. Soc.* **2017**, *139* (4), 1424–1427. <https://doi.org/10.1021/jacs.6b12404>.
- (79) Mitra, K.; Chatterjee, S.; Samanta, S.; Dey, A. Selective 4e⁻/4H⁺+O₂reduction

- by an Iron(Tetraferrocenyl)Porphyrin Complex: From Proton Transfer Followed by Electron Transfer in Organic Solvent to Proton Coupled Electron Transfer in Aqueous Medium. *Inorg. Chem.* **2013**, *52* (24), 14317–14325. <https://doi.org/10.1021/ic402297f>.
- (80) Anson, F. C.; Shi, C.; Steiger, B. Novel Multinuclear Catalysts for the Electroreduction of Dioxygen Directly to Water. *Acc. Chem. Res.* **1997**, *30* (11), 437–444. <https://doi.org/10.1021/ar960264j>.
- (81) Yu, H. Z.; Baskin, J. S.; Steiger, B.; Anson, F. C.; Zewail, A. H. Femtosecond Dynamics and Electrocatalysis of the Reduction of O₂: Tetraruthenated Cobalt Porphyrins. *J. Am. Chem. Soc.* **1999**, *121* (2), 484–485. <https://doi.org/10.1021/ja983532c>.
- (82) Araki, K.; Dovidauskas, S.; Winnischofer, H.; Alexiou, A. D. P.; Toma, H. E. A New Highly Efficient Tetra-Electronic Catalyst Based on a Cobalt Porphyrin Bound to Four m³-Oxo-Ruthenium Acetate Clusters. *J. Electroanal. Chem.* **2001**, *498*, 152–160.
- (83) Toma, H. E.; Araki, K.; Silva, E. O. Synthesis and Characterization of a Novel Dodecanuclear Porphyrin Ruthenium Cluster. *Monatshefte fur Chemie* **1998**, *129* (10), 975–984. <https://doi.org/10.1007/PL00010119>.
- (84) Dovidauskas, S.; Toma, H. E.; Araki, K.; Sacco, C.; Iamamoto, Y. Modified By Four M³-Oxo-Triruthenium Acetate Clusters: Synthesis, Characterization, Electrochemical Behavior and Catalytic Activity. *Inorganica Chim. Acta* **2000**, *305*, 206–213.
- (85) Araki, K.; Angnes, L.; Azevedo, C. M. N.; Toma, H. E. Electrochemistry of a Tetraruthenated Cobalt Porphyrin and Its Use in Modified Electrodes as Sensors of Reducing Analytes. *J. Electroanal. Chem.* **1995**, *397*, 205–210.

[https://doi.org/10.1016/0022-0728\(95\)04193-3](https://doi.org/10.1016/0022-0728(95)04193-3).

- (86) Chen, J.; Wagner, P.; Tong, L.; Wallace, G. G.; Officer, D. L.; Swiegers, G. F. A Porphyrin-Doped Polymer Catalyzes Selective, Light-Assisted Water Oxidation in Seawater. *Angew. Chemie - Int. Ed.* **2012**, *51* (8), 1907–1910. <https://doi.org/10.1002/anie.201107355>.
- (87) Jahan, M.; Bao, Q.; Loh, K. P. Electrocatalytically Active Graphene – Porphyrin MOF Composite for Oxygen Reduction Reaction. *J. Am. Chem. Soc.* **2012**, *134*, 6707–6713.
- (88) Azevedo, C. M. N.; Araki, K.; Angnes, L.; Toma, H. E. Electrostatically Assembled Films for Improving the Properties of Tetra-ruthenated Porphyrin Modified Electrodes. *Electroanalysis* **1998**, *10* (7), 467–471. [https://doi.org/10.1002/\(SICI\)1521-4109\(199806\)10:7<467::AID-ELAN467>3.0.CO;2-W](https://doi.org/10.1002/(SICI)1521-4109(199806)10:7<467::AID-ELAN467>3.0.CO;2-W).
- (89) He, W. L.; Chen, J. L.; Chen, M.; Qian, D. J. Interfacial Self-Assembly, Characterization, Electrochemical, and Photo-Catalytic Properties of Porphyrin-Ruthenium Complex/Polyoxometalate Triad Hybrid Multilayers. *Colloids Surfaces A Physicochem. Eng. Asp.* **2016**, *509*, 1–10. <https://doi.org/10.1016/j.colsurfa.2016.08.083>.
- (90) Ferreira, L. M. C.; Grasseschi, D.; Santos, M. S. F.; Martins, P. R.; Gutz, I. G. R.; Ferreira, A. M. C.; Araki, K.; Toma, H. E.; Angnes, L. Unveiling the Structure of Polytetra-ruthenated Nickel Porphyrin by Raman Spectroelectrochemistry. *Langmuir* **2015**, *31* (14), 4351–4360. <https://doi.org/10.1021/acs.langmuir.5b00250>.
- (91) Ferreira, L. M. C.; Martins, P. R.; Araki, K.; Toma, H. H.; Angnes, L. Amperometric Folic Acid Quantification Using a Supramolecular

- Tetraruthenated Nickel Porphyrin μ -Peroxo-Bridged Matrix Modified Electrode Associated to Batch Injection Analysis. *Electroanalysis* **2015**, 27 (10), 2322–2328. <https://doi.org/10.1002/elan.201500251>.
- (92) Cooke, M. W.; Tremblay, P.; Hanan, G. S. Carboxy-Derived (Tpy)₂Ru²⁺ Complexes as Sub-Units in Supramolecular Architectures: The Solubilized Ligand 4'-(4-Carboxyphenyl)-4,4''-Di-(Tert-Butyl)Tpy and Its Homoleptic Ru(II) Complex. *Inorganica Chim. Acta* **2008**, 361 (8), 2259–2269.
- (93) Toma, H. E.; Malin, J. M. Properties and Reactivity of Some Pentacyanoferrate(II) Complexes of Aromatic Nitrogen Heterocycles. *Inorg. Chem.* **1973**, 12 (5), 1039–1045.
- (94) Zaban, A.; Ferrere, S.; Sprague, J.; Gregg, B. A. PH-Dependent Redox Potential Induced in a Sensitizing Dye by Adsorption onto TiO₂. *J. Phys. Chem. B* **1997**, 101 (1), 55–57. <https://doi.org/10.1021/jp962252l>.
- (95) Lambert, J. B.; Mazzola, E. P.; Ridge, C. D. *Nuclear Magnetic Resonance Spectroscopy: An Introduction to Principles, Applications and Experimental Methods*, 2nd ed.; John Wiley & Sons, Inc., 2019.
- (96) Catalano, V. J.; Craig, T. J. Monometallic and Dimetallic Ruthenium (II) – Terpyridine Complexes Employing the Tetradentate Ligands Dipyritylpyrazolyl , Dipyrityloxadiazole , and Their Dimethyl Derivatives. *Inorg. Chem.* **2003**, 42 (2), 321–334.
- (97) Chanda, N.; Mobin, S. M.; Puranik, V. G.; Datta, A.; Niemeyer, M.; Lahiri, G. K. Stepwise Synthesis of [Ru(Trpy)(L)(X)]N⁺ (Trpy = 2,2':6',2''-Terpyridine; L = 2 , 2' -Dipyritylamine; X = Cl⁻ , H₂O , NO₂⁻ , NO⁺ , O₂⁻). Crystal Structure , Spectral , Electron-Transfer , and Photophysical Aspects. *Inorg. Chem.* **2004**, 43 (3), 1056–1064.

- (98) Garza-Ortiz, A.; Maheswari, P. U.; Siegler, M.; Spek, A. L.; Reedijk, J. A New Family of Ru(II) Complexes with a Tridentate Pyridine Schiff-Base Ligand and Bidentate Co-Ligands: Synthesis, Characterization, Structure and in Vitro Cytotoxicity Studies. *New J. Chem.* **2013**, *37*, 3450–3460. <https://doi.org/10.1039/c3nj00415e>.
- (99) Vliet, P. M. Van; Toekimin, S. M. S.; Haasnoot, J. G.; Reedijk, J.; Novakova, O.; Vrana, O.; Brabec, V. Mer-[Ru(Terpy)Cl₃] (Terpy = 2,2':6',2''-Terpyridine) Shows Biological Activity, Forms Interstrand Cross-Links in DNA and Binds Two Guanine Derivatives in a Trans Configuration. *Inorganica Chim. Acta* **1995**, *231*, 57–64.
- (100) Webb, G. A. Nuclear Magnetic Resonance Spectroscopy of Paramagnetic Species. *Annu. Reports NMR Spectrosc.* **1970**, *3*, 211–259.
- (101) Shinpuku, Y.; Inui, F.; Nakai, M.; Nakabayashi, Y. Synthesis and Characterization of Novel Cyclometalated Iridium (III) Complexes for Nanocrystalline TiO₂-Based Dye-Sensitized Solar Cells. *J. Photochem. Photobiol. A Chem.* **2011**, *222* (1), 203–209. <https://doi.org/10.1016/j.jphotochem.2011.05.023>.
- (102) Bren, K. L. Nuclear Magnetic Resonance (NMR) Spectroscopy of Metallobiomolecules. In *Encyclopedia of Inorganic and Bioinorganic Chemistry*; John Wiley & Sons, Inc., 2008; pp 1–27. <https://doi.org/10.1002/9781119951438.eibc0296>.
- (103) Kahn Taqui, M. M.; Srinivas, D.; Kureshy, R. I.; Khan, N. H. Synthesis, Characterization, and EPR Studies of Stable Ruthenium(III) Schiff Base Chloro and Carbonyl Complexes. *Inorg. Chem.* **1990**, *29* (12), 2320–2326.
- (104) Toma, H. E. *Química de Coordenação, Organometálica e Catálise*, 1st ed.;

Sao Paulo, 2013.

- (105) Huba, Z. J.; Carpenter, E. E. Ethanol Assisted Reduction and Nucleation of Ferromagnetic Co and Ni Nanocrystalline Particles. *CrystEngComm* **2013**, *15* (44), 8919–8923.
- (106) Pal, A.; Shah, S.; Devi, S. Microwave-Assisted Synthesis of Silver Nanoparticles Using Ethanol as Reducing Agent. *Mater. Chem. Phys.* **2009**, *114* (2–3), 530–532.
- (107) Araki, K.; Toma, H. Synthesis and Characterization of a Multibridged Porphyrin Complex Containing Peripheral Bis(Bipyridine)- Ruthenium(II) Groups. *J. Coord. Chem.* **1993**, *30* (1), 9–17.
<https://doi.org/10.1080/00958979308022742>.
- (108) Araki, K.; Toma, H. E. Luminescence, Spectroelectrochemistry and Photoelectrochemical Properties of a Tetraruthenated Zinc Porphyrin. *J. Photochem. Photobiol. A Chem.* **1994**, *83*, 245–250.
[https://doi.org/10.1016/1010-6030\(94\)03821-X](https://doi.org/10.1016/1010-6030(94)03821-X).
- (109) GUIMARÃES, R. R. Influência Das Interfaces TiO₂/Corante, TiO₂/Eletrólito e Rutilo/Anatase Sobre a Eficiência de Fotoconversão Das Células de Gratzel, 2016. <https://doi.org/10.1017/CBO9781107415324.004>.
- (110) Kong, X.; Zhou, T.; Liu, Z.; Hider, R. C. PH Indicator Titration : A Novel Fast PKa Determination Method. *J. Pharm. Sci.* **2007**, *96* (10), 2777–2783.
<https://doi.org/10.1002/jps>.
- (111) Vidal Salgado, L. E.; Vargas-Hernandez, C. Spectrophotometric Determination of the PKa , Isosbestic Point and Equation of Absorbance vs . PH for a Universal PH Indicator. *Am. J. Anal. Chem.* **2014**, *5* (December), 1290–1301.
- (112) Henke, K. R.; Hutchison, A. R.; Krepps, M. K.; Parkin, S.; Atwood, D. A.

Chemistry of 2,4,6-Trimercapto-1,3,5-Triazine (TMT): Acid Dissociation Constants and Group 2 Complexes. *Inorg. Chem.* **2001**, *40* (17), 4443–4447. <https://doi.org/10.1021/ic0103188>.

- (113) Gratzel, M. Photoelectrochemical Cells. *Insight Rev. Artic.* **2001**, *414* (November), 338–344. <https://doi.org/10.1038/35104607>.
- (114) Kucur, E.; Riegler, J.; Urban, G. A.; Nann, T. Determination of Quantum Confinement in CdSe Nanocrystals by Cyclic Voltammetry. *J. Chem. Phys.* **2003**, *119* (4), 2333–2337. <https://doi.org/10.1063/1.1582834>.
- (115) Trasatti, S. *Electrified Interfaces in Physics, Chemistry and Biology*; Guidelli, R., Ed.; Kluwer Academic Publishers, 1992.
- (116) Bisquert, J. Dilemmas of Dye-Sensitized Solar Cells. *ChemPhysChem* **2011**, *12* (9), 1633–1636. <https://doi.org/10.1002/cphc.201100248>.
- (117) Aghazada, S.; Gao, P.; Yella, A.; Moehl, T.; Teuscher, J.; Moser, J. E.; Grätzel, M.; Nazeeruddin, M. K. Unraveling the Dual Character of Sulfur Atoms on Sensitizers in Dye-Sensitized Solar Cells. *ACS Appl. Mater. Interfaces* **2016**, *8* (40), 26827–26833. <https://doi.org/10.1021/acsami.6b08882>.
- (118) Rocha, R. C.; Rein, F. N.; Toma, H. E. Ruthenium and Iron Complexes with Benzotriazole and Benzimidazole Derivatives as Simple Models for Proton-Coupled Electron Transfer Systems. *J. Braz. Chem. Soc.* **2001**, *12* (2), 234–242. <https://doi.org/10.1590/S0103-50532001000200018>.
- (119) Rocha, R. C.; Toma, H. E. Intervalence Transfer in a New Benzotriazolate Bridged Ruthenium-Iron Complex. *Can. J. Chem.* **2001**, *79* (2), 145–156. <https://doi.org/10.1139/v00-195>.
- (120) Toma, H. E. Intervalence Transfer in Outer-Sphere Hexa-Ammineruthenium(III) Pentacyanoferrate(II) Complexes. *J. Chem. Soc. Dalton Trans.* **1980**, No. 3,

471–475.

- (121) Hush, N. S. Intervalence-Transfer Absorption. Part 2. Theoretical Considerations and Spectroscopic Data. In *Progress in Inorganic Chemistry*; Cotton, F. A., Ed.; John Wiley & Sons, Inc., 1967; pp 391–444. <https://doi.org/10.1002/9780470166093.ch7>.
- (122) Miessler, G. L.; Tarr, D. A. *Inorganic Chemistry*, 4th ed.; Pearson Prentice Hall, 2011.
- (123) Wolberg, A.; Manassen, J. Electrochemical and Electron Paramagnetic Resonance Studies of Metalloporphyrins and Their Electrochemical Oxidation Products. *J. Am. Chem. Soc.* **1970**, *92* (10), 2982–2991. <https://doi.org/10.1021/ja00713a010>.
- (124) Oldacre, A. N.; Crawley, M. R.; Friedman, A. E.; Cook, T. R. Tuning the Activity of Heterogeneous Cofacial Cobalt Porphyrins for Oxygen Reduction Electrocatalysis through Self-Assembly. *Chem. - A Eur. J.* **2018**, *24* (43), 10984–10987. <https://doi.org/10.1002/chem.201802585>.
- (125) Taboy, C. H.; Bonaventura, C.; Crumbliss, A. L. Anaerobic Oxidations of Myoglobin and Hemoglobin by Spectroelectrochemistry. *Methods Enzymol.* **2002**, *353* (1965), 187–209. [https://doi.org/10.1016/S0076-6879\(02\)53048-2](https://doi.org/10.1016/S0076-6879(02)53048-2).
- (126) Saravia, L. P. H.; Sukeri, A.; Gonçalves, J. M.; Aguirre-Araque, J. S.; Brandão, B. B. N. S.; Matias, T. A.; Nakamura, M.; Araki, K.; Toma, H. E.; Bertotti, M. CoTRP/Graphene Oxide Composite as Efficient Electrode Material for Dissolved Oxygen Sensors. *Electrochim. Acta* **2016**, *222*, 1682–1690. <https://doi.org/10.1016/j.electacta.2016.11.159>.
- (127) Alben, J. O.; Choi, S. S.; Adler, A. D.; Caughey, W. S. Infrared Spectroscopy of Porphyrins. *Ann. N. Y. Acad. Sci.* **1973**, *206* (1), 278–295.

<https://doi.org/10.1111/j.1749-6632.1973.tb43217.x>.

- (128) Garibov, R. E.; Danilenko, E. M.; Sokolov, A. K.; Maravin, G. B.; Ponomarev, G. V. Infrared Spectra of Asymmetrically Substituted Tetraphenylporphyrins. *Theor. Exp. Chem.* **1991**, *27* (1), 103–107. <https://doi.org/10.1007/BF01372934>.
- (129) Adán-Más, A.; Duarte, R. G.; Silva, T. M.; Guerlou-Demourgues, L.; Montemor, M. F. G. Enhancement of the Ni-Co Hydroxide Response as Energy Storage Material by Electrochemically Reduced Graphene Oxide. *Electrochim. Acta* **2017**, *240*, 323–340. <https://doi.org/10.1016/j.electacta.2017.04.070>.
- (130) Martins, P. R.; Ferreira, L. M. C.; Araki, K.; Angnes, L. Influence of Cobalt Content on Nanostructured Alpha-Phase-Nickel Hydroxide Modified Electrodes for Electrocatalytic Oxidation of Isoniazid. *Sensors Actuators, B Chem.* **2014**, *192*, 601–606. <https://doi.org/10.1016/j.snb.2013.11.029>.
- (131) Aguirre-Araque, J. S.; Gonçalves, J. M.; Nakamura, M.; Rossini, P. O.; Angnes, L.; Araki, K.; Toma, H. H. GO Composite Encompassing a Tetra-ruthenated Cobalt Porphyrin-Ni Coordination Polymer and Its Behavior as Isoniazid BIA Sensor. *Electrochim. Acta* **2019**. <https://doi.org/10.1016/j.electacta.2019.01.097>.
- (132) Majidi, M. R.; Jouyban, A.; Asadpour-Zeynali, K. Voltammetric Behavior and Determination of Isoniazid in Pharmaceuticals by Using Overoxidized Polypyrrole Glassy Carbon Modified Electrode. *J. Electroanal. Chem.* **2006**, *589* (1), 32–37. <https://doi.org/10.1016/j.jelechem.2006.01.016>.
- (133) Karimi, M. A.; Hatefi-Mehrjardi, A.; Mazloun Ardakani, M.; Ardakani, R. B.; Mashhadizadeh, M. H.; Sargazi, S. Electrocatalytic Determination of Chlorpromazine Drug Using Alizarin Red S as a Mediator on the Glassy

- Carbon Electrode. *Int. J. Electrochem. Sci.* **2010**, 5 (11), 1634–1648.
<https://doi.org/10.1134/s1023193511010125>.
- (134) Cheemalapati, S.; Chen, S. M.; Ali, M. A.; Al-Hemaid, F. M. A. Enhanced Electrocatalytic Oxidation of Isoniazid at Electrochemically Modified Rhodium Electrode for Biological and Pharmaceutical Analysis. *Colloids Surfaces B Biointerfaces* **2014**, 121, 444–450.
<https://doi.org/10.1016/j.colsurfb.2014.06.035>.
- (135) Oliveira, P. R. De; Oliveira, M. M.; Zarbin, A. J. G.; Marcolino-Junior, L. H.; Bergamini, M. F. Flow Injection Amperometric Determination of Isoniazid Using a Screen-Printed Carbon Electrode Modified with Silver Hexacyanoferrates Nanoparticles. *Sensors Actuators, B Chem.* **2012**, 171–172, 795–802.
<https://doi.org/10.1016/j.snb.2012.05.073>.
- (136) Azad, U. P.; Prajapati, N.; Ganesan, V. Selective Determination of Isoniazid Using Bentonite Clay Modified Electrodes. *Bioelectrochemistry* **2015**, 101, 120–125. <https://doi.org/10.1016/j.bioelechem.2014.08.011>.
- (137) Cheemalapati, S.; Palanisamy, S.; Chen, S. M. Electrochemical Determination of Isoniazid at Electrochemically Reduced Graphene Oxide Modified Electrode. *Int. J. Electrochem. Sci.* **2013**, 8 (3), 3953–3962.
- (138) Chen, W. C.; Unnikrishnan, B.; Chen, S. M. Electrochemical Oxidation and Amperometric Determination of Isoniazid at Functionalized Multiwalled Carbon Nanotube Modified Electrode. *Int. J. Electrochem. Sci.* **2012**, 7 (10), 9138–9149.